STATIONARY HEMISPHERICAL ELECTRODE UNDER SUBMERGED JET IMPINGEMENT AND VALIDATION OF MEASUREMENT MODEL CONCEPT FOR IMPEDANCE SPECTROSCOPY

By

PAVAN KUMAR SHUKLA

A DISSERTATION PRESENTED TO THE GRADUATE SCHOOL
OF THE UNIVERSITY OF FLORIDA IN PARTIAL FULFILLMENT
OF THE REQUIREMENTS FOR THE DEGREE OF
DOCTOR OF PHILOSOPHY

UNIVERSITY OF FLORIDA

2004

ACKNOWLEDGMENTS

I would like to sincerely thank my advisor, Professor Mark E. Orazem, for his technical guidance throughout my graduate research. I will always be grateful for his patience and understanding. I would like to pay special thanks to Dr. Oscar Crisalle for his expertise and guidance in the parameter estimation theory and programming. His time and effort were invaluable to me, especially in understanding transfer function methodology.

I would like to express my gratitude to Dr. Gert Nelissan for his hard work in numerical simulations. His simulation results buttressed my work alongside my experiments.

I gratefully acknowledge OLI Systems, Inc. (108 American Way, Morris Plains, NJ USA, www.olisystems.com) for use of their CorrosionAnalyzer 1.3 software.

I would like to express my appreciation to the members of my committee, Dr. Jason Butler, Dr. Anuj Chauhan and Dr. Darryl Butt, for their contributions in my dissertation defense.

I would like to thank the previous and present members of the electrochemical engineering group, Mike Membrino, Chen Chen Qui, Kerry Allahar, Nellian Perez-Garcia, and Vicky Huang. I was fortunate to be a member of this group.

I would like to express my heartfelt thanks and gratitude to my family members and friends who have always encouraged and facilitated my academic pursuits. I would like to mention my high school physics teacher Mr. Gyanendra Sharma, whose love for physics inspired me to be curious about science.

TABLE OF CONTENTS

page

APPENDIX

LIST OF TABLES

LIST OF FIGURES

Abstract of Dissertation Presented to the Graduate School
of the University of Florida in Partial Fulfillment of the
Requirements for the Degree of Doctor of Philosophy

STATIONARY HEMISPHERICAL ELECTRODE UNDER SUBMERGED JET IMPINGEMENT AND VALIDATION OF MEASUREMENT MODEL CONCEPT FOR IMPEDANCE SPECTROSCOPY

By

Pavan Kumar Shukla

August 2004

Chair: Mark E. Orazem
Major Department: Chemical Engineering

Interpretation of electrochemical impedance measurements requires an adequate understanding of electrode surface phenomena, current distribution, and stochastic error structure. Most importantly, nonuniform current distributions obfuscate impedance analysis using regression. Traditional electrode systems such as the rotating disk electrode have a nonuniform current distribution; therefore, use of the rotating disk electrode is not suitable for impedance studies at high current levels. In this work, a stationary hemispherical electrode under submerged jet impingement is suggested to be an alternative. Primary and secondary current distributions on stationary hemispherical electrode system are uniform, increasing the likelihood of uniform tertiary current distribution. Moreover, electrochemical processes can be monitored *in situ* on a stationary hemispherical electrode. In the present work, a hydrodynamic model was devised using the boundary layer theory and compared to the computational fluid dynamic model developed at Vrije Universiteit Brussel, Belgium. Both models predicted a separation of boundary

layer at the stationary hemispherical electrode under submerged jet impingement. The hydrodynamic model results were used to obtain a solution of convective-diffusion at the mass-transfer limiting condition. Calculations for steady-state current and potential distribution below the mass-transfer limited current were performed to obtain the conditions for uniform current.

Reduction of oxygen and ferricyanide were studied on both the disk and the hemispherical electrode under jet impingement. The objective was to understand the differences in impedance response of the disk and the hemispherical electrodes. Repeated impedances measurements were conducted on both electrode systems. The impedance analysis of ferricyanide reduction showed the evidence of boundary layer separation at the hemispherical electrode.

A systematic study was undertaken to evaluate the measurement model approach for assessing the error structure of electrochemical impedance measurements. The remaining question was whether the error structure obtained with this model was a property of the measurement or depended on the arbitrary selection of a measurement model. Transfer function and Voigt-element based models were used to assess the error structure of impedance measurements. In spite of differences in the fitting errors and numbers of parameters needed for the regression, the values for the frequency-dependent stochastic errors were found to be independent of the measurement model used. These results confirm the measurement model approach for error analysis. The confidence intervals for the parameter estimates differed for the two models. The Voigt-element based model was found to provide the tightest confidence intervals and was more suited for evaluation of consistency with the Kramers-Kronig relations.

CHAPTER 1
INTRODUCTION

Accurate determination of physical properties for electrochemical systems remains a challenge. Electrochemical impedance Spectroscopy (EIS) provides a framework whereby different physical properties of the system can be estimated simultaneously even for complex systems. Interpretation of electrochemical measurements is facilitated when experiments are conducted under well-defined and easily characterized flow conditions. Experimental systems such as the rotating disk electrode (RDE)[1] and the stationary disk electrode under a submerged impinging jet[2,3] have been employed extensively in electrochemical investigations. The rotating and impinging jet disk electrode geometries are attractive because an accurate solution is available for convective diffusion, and the current distribution is uniform at the mass-transfer-limited conditions.

Experimental investigations of electrochemical reaction mechanisms, however, are not generally conducted under mass-transfer limitations. The current and potential distribution on a disk electrode below the mass transfer limited current is not uniform,[4–6] and it has been shown that neglect of the nonuniform current distribution introduces error in estimation of kinetic parameters from steady state (DC) measurements.[7–9]

Even the most complete expressions available for convective diffusion impedance on a rotating disk electrode[10,11] or on a disk electrode under a submerged impinging jet[12] assume that the system may be treated as having a uniform current distribution. Numerical calculations presented by Appel and Newman[13] and Durbha *et al.*[14] illustrated the influence of a non-uniform current distribution

on the impedance response. Orazem *et al.*[15] suggested that the discrepancy between experimental measurements and a detailed mathematical model could be attributed partially to the influence of the non-uniform current distribution below the mass-transfer-limited value. This claim was discussed further by Orazem and Tribollet.[11] Matos *et al.*[16] have demonstrated experimentally that the impedance response on a disk electrode was significantly different than that on a rotating hemisphere electrode (RHE), for which the primary current and potential distributions are uniform.

Current mathematical models for the impedance of a disk electrode with nonuniform current distribution[13,14] are too complex for regression analysis. The preferred approach for experimental investigation of electrode kinetics is to use geometries for which mass-transfer is well-defined and current distribution is uniform at the experimental condition. The rotating hemispherical electrode, introduced by Chin,[17] has a uniform primary current distribution and would therefore be a suitable configuration for experiments conducted under conditions such that the current distribution is not influenced by the non-uniform accessibility to mass transfer. Nisançiöglu and Newman[18] demonstrated that current distribution in the RHE is uniform. This condition of uniformity is achieved when the total current is smaller than 68 percent of the average mass-transfer-limited value. A refined mathematical model for the convective diffusion impedance of a RHE, developed by Barcia *et al.*,[19] provided an excellent match to experimental impedance measurements conducted under these conditions.

Systems that employ a stationary electrode facilitate use of *in situ* observation or surface-analysis techniques. Orazem *et al.*,[12] for example, used *in situ* video microscopy to obtain images of a disk electrode under a submerged impinging jet. These images were then used to interpret impedance measurements in terms of

viscoelastic properties of corrosion product films.[20] Experiments using scanning ellipsometry on a disk electrode under a submerged impinging jet were employed to distinguish between the influence of convective diffusion and hydrodynamic shear.[21] Flow channel experiments have been employed by Alkire and Cangellari[22] to illustrate the role of current distribution on formation of salt films.

To date, no experimental system exists in the literature exhibiting a uniform primary current distribution, a stationary electrode amenable to *in situ* observation, and well defined flow characteristics allowing control of convective diffusion. The objective of the present work was to develop the hydrodynamic, convective diffusion and current distribution calculations for a stationary hemispherical electrode subjected to a submerged impinging jet. The use of a stationary electrode was intended to facilitate *in situ* observation of electrode processes, and the hemispherical electrode geometry was intended to ensure that the primary and secondary current distributions would be uniform.[23] The present work provides a foundation for the design of electrode systems and for development of models for the impedance response.

1.1 History of Electrode Systems

Geometries such as disks, spheres, and cylinders have been widely explored in fluid mechanics, heat, and mass-transfer studies. The idea to employ a disk geometry as an electrochemical experimental tool was envisioned after Levich[24] treated the convective diffusion problem at a rotating disk electrode. Levich showed that the surface of a rotating disk has uniform mass-transfer for the limiting conditions. For a long time it was assumed that the current below the mass-transfer limited value is also uniform for the rotating disk electrode.

Rotating cylinders were suggested to be an alternative to the disk electrode for mass-transfer research as reviewed by Eisenberg *et al.*[25] The disk electrode has

been widely used in numerous studies because of its simple design and ease of operation. The surface of the disk electrode can be easily polished and reused without losing its geometric features. Riddiford[26] provided a detailed account of the evolution of the disk electrode and its use in electroanalytical studies. Newman's[27] treatment of mass-transfer coupled with potential distribution, and electrode kinetics for the rotating disk electrode showed that the current distribution at the electrode surface is highly nonuniform even at current levels slightly below the mass-transfer limited value.

Chin[17] proposed the rotating spherical electrode to be an alternative to the disk electrode for high-rate deposition and dissolution studies. Matlosz and coworkers[28] proposed a hybrid electrode geometry with central disk and a surrounding hemispherical electrode. The resulting electrode was subsequently called a disk-hemispherical electrode. The geometric features of the system allowed the primary current distribution to be finite at the edge of the electrode. Madore *et al.*[29] suggested a cylindrical hull electrode. They calculated the primary current distribution for the system with different cell parameters. Dinan *et al.*[30] proposed a recessed rotating disk electrode. This geometry provided a uniform current distribution; however, uniform accessibility to mass-transfer was lost due to its geometric feature.

1.2 Measurement Model Concept

Measurement model concept was first introduced by Agarwal *et al.*[31–33]The methodology was devised for the following reasons.

1. To estimate stochastic error structure of electrochemical impedance spectroscopy data, and

2. to check for consistency of impedance data with Kramers-Kronig relations.

The proposed measurement model consisted of Voigt elements and a solution resistance connected in series with each other. Agarwal *et al.*[31] showed the applicability of measurement model to various impedance data. The Voigt measurement model with sufficient parameters was able to fit the impedance data within the noise level. Later, Agarwal *et al.*[32] devised a method to filter the replication errors of impedance data in order to distinguish between stochastic errors and deterministic errors. In the subsequent paper, Agarwal *et al.*[33] showed the applicability of Voigt measurement model to assess the consistency of impedance data with Kramers-Kronig relations.

Pauwels *et al.*[34] have recently proposed a transfer function based measurement model. In light of Pauwels's model, the measurement model concept was reevaluated for estimation of stochastic errors. The purpose of this work was to answer the question whether the error structure obtained with Voigt model was a property of the measurement or depended on the arbitrary selection of a measurement model. Both measurement models were applied to estimate stochastic errors in the impedance measurements collected at the rotating disk electrode of ferricyanide reduction. Furthermore, the same data set was also analyzed for Kramers-Kronig consistency check using the two measurement models. The estimated error structure was found to be independent of choice of measurement model even though transfer function model required fewer parameters to fit the impedance data. The confidence intervals for the parameter estimates differed for the two models. The Voigt-element based model was found to provide the tightest confidence intervals. As a result, Kramers-Kronig consistency check was more sensitive for Voigt element based measurement model.

1.3 Scope and Structure of the Thesis

The structure of the thesis can be divided into three parts. The first part of the thesis is presented in Chapters 2, 3, 4, and 5. This part deals with the hydrodynamic models, convective diffusion models, and current distributions calculations for submerged stationary hemispherical electrode under jet impingement and rotating hemispherical electrode. The second part of the thesis presents a study of measurement model concepts for three different measurement models in Chapter 6. The third part deals with experimental investigation of two electrochemical systems in Chapters 7 and 8. A reader can go through the first and third part of this thesis exclusively without losing the continuity. The second part can be read independently.

Chapter 2 provides a rigorous treatment of fluid mechanics for stationary electrode under jet impingement. Two hydrodynamic models were developed for the system. The first model was developed using boundary layer theory, and the governing equations were solved by a series method. The model predicted the separation of boundary layer at an angle of 54.8° from the pole. However, this model is valid up to the point of boundary layer separation, after which the fluid mechanics becomes undefined in the region beyond separation. A computational fluid dynamic model (CFD), developed by Dr. Gert Nelissen at Vrije Universiteit Brussel, Belgium, was used to identify the fluid mechanics over the entire electrode surface. The CFD model predicted vortex formation in the separated part of the boundary layer. The angle of separation was predicted to be 62° by the CFD model. A solution of convective-diffusion equation is provided in Chapter 3. A solution of convective-diffusion was developed with series method which predicted the mass-transfer-limited current until the boundary layer separation point. A complementary CFD model of convective-diffusion, developed by

Dr. Gert Nelissen at Vrije Universiteit Brussel, Belgium, solved the governing equation over the entire surface.

Chapter 4 presents a review of the hydrodynamics and the mass-transfer for a rotating hemispherical electrode. The governing equations were solved using the series solution. The objective of this chapter was to provide a correction to the solution given by Barcia *et al.*[19]

A generalized mathematical model to obtain the current and potential distribution at axisymmetric electrodes was developed in Chapter 5. The model was then applied to calculate the distribution at the submerged stationary disk and hemispherical electrode under jet impingement. A numerical calculation procedure was developed to solve the governing equations. A modified mathematical model was also developed to obtain the current and potential distribution at the rotating hemispherical electrode. This model accounted for correction in the mass-transfer to the electrode due to a finite value of the Schmidt number. An algorithm was developed to solve the governing equations.

Chapter 6 reviews the measurement model concept for estimation of stochastic errors in impedance spectroscopy data. The chapter presents the three different models. Impedance data collected at the rotating disk electrodes for ferricyanide reduction were analyzed for stochastic errors. The data were also analyzed for consistency with Kramers-Kronig relations.

Chapter 7 presents experimental study of oxygen reduction at the nickel electrode. Electrochemical measurements were performed at the disk and hemispherical electrodes. Repeated impedance spectrum were collected at different experimental conditions.

Chapter 8 provides an experimental study of ferricyanide reduction at the disk and hemispherical electrode under submerged jet impingement. Impedance

measurements were carried out at electrodes made of nickel. Analysis of impedance at the stationary hemispherical electrode provided an evidence of boundary layer separation.

Conclusions from this work are provided in Chapter 9, and suggestions for future research is in Chapter 10.

CHAPTER 2
HYDRODYNAMIC MODELS FOR A STATIONARY ELECTRODE UNDER SUBMERGED JET IMPINGEMENT

This chapter presents a detailed description of the hydrodynamics of a stationary submerged hemispherical electrode under submerged jet impingement. The electrode is amenable to *in situ* observation and has a uniform primary and secondary current distribution below the mass-transfer-limited value. The present work is intended to provide a foundation for the design of stationary hemispherical electrode systems and for development of steady state mass transfer and tertiary current distribution calculations for the system.

2.1 Schematic Illustration of the System

A schematic illustration of a stationary hemispherical electrode under a submerged impinging jet is presented in Figure 2-1, where a hemispherical electrode protrudes out of a planar insulating surface and a nozzle is placed above the hemisphere. The center of nozzle is axisymmetric with the hemisphere. The whole system is submerged in an aqueous electrolyte assumed to have uniform fluid properties. The dimensions of the nozzle are sufficiently large and its placement is sufficiently apart from the electrode such that flow field of the fluid coming out nozzle can be described as being a potential flow with uniform axial velocity. A detailed description of flow field generated from the nozzle can be found in the paper by Scholtz and Trass.[35] The walls of the enclosure were assumed to be sufficiently distant that they do not influence the flow patterns near the electrode surface. A spherical polar coordinate system is employed to describe the system, where r represent the radial outward direction, θ represents the colatitude

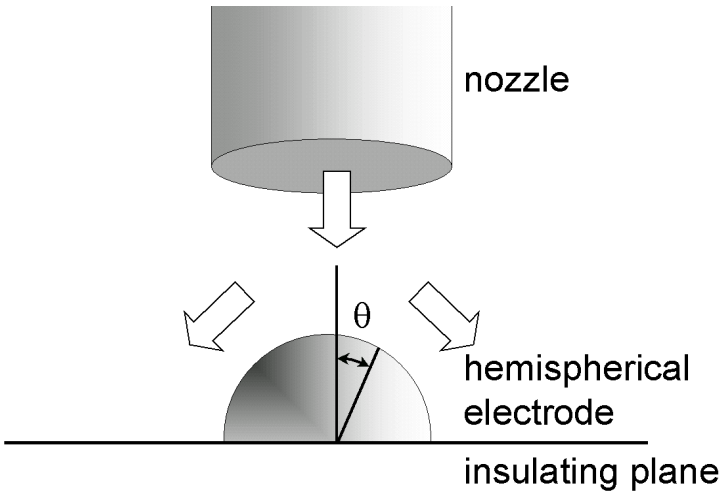

Figure 2-1: Schematic illustration of a stationary hemispherical submerged impinging jet electrode system.

direction, and ϕ is along the body of the revolution. The corresponding fluid field velocity components are v_r, v_θ, and v_ϕ, respectively.

2.2 Governing Equations

The steady-state fluid flow around hemisphere under submerged jet impingement can be treated by dividing the flow field into two regions: the outer or potential flow region, where inertial forces dominate, and the inner or boundary layer region, where viscous and inertial forces are of the same magnitude. The fluid flow in the boundary layer region is described by Navier-Stokes and mass-conservation equations, and the flow in the potential flow region is described by mass-conservation only.

Howarth[36] first derived the governing equations for fluid flow around a rotating sphere in the spherical coordinate system. These equations are valid for high Reynolds numbers, which corresponds to a high rotation speed of the sphere. The equations for fluid flow in the boundary layer can be modified by setting the ϕ component of fluid velocity equal to zero. This is a valid assumption, because the fluid flow around this hemisphere is axisymmetric. Under assumption of constant fluid properties, the equations governing a thin boundary layer on an

axisymmetric body of rotation[37,36] are conservation of momentum in the colatitude direction

$$\frac{v_\theta}{r_0}\frac{\partial v_\theta}{\partial \theta} + v_r\frac{\partial v_\theta}{\partial r} = -\frac{1}{\rho r_0}\frac{\partial p_s}{\partial \theta} + \nu\frac{\partial^2 v_\theta}{\partial r^2} \tag{2-1}$$

and conservation of mass

$$\frac{1}{r_0}\frac{\partial v_\theta}{\partial \theta} + \frac{\partial v_r}{\partial r} + \frac{v_\theta}{r_0}\cot(\theta) = 0 \tag{2-2}$$

The underlying assumptions in deriving the above equations (2-1) and (2-2) are:

1. The fluid flow in the boundary layer is laminar, and the gradients of all quantities are large in the direction normal to the surface: however, their tangential gradients are relatively small.

2. The momentum flow in the r-direction is much smaller than the θ-direction. From this assumption, it can be concluded that the pressure gradient in the r-direction vanishes.

3. The thickness of the momentum boundary layer, δ_0, is much smaller than the radius of the hemisphere.

The governing equation for the potential flow region is

$$\frac{1}{r}\frac{\partial}{\partial r}\left(r^2 v_r\right) + \frac{1}{\sin(\theta)}\frac{\partial}{\partial \theta}\left(\sin(\theta)\, v_\theta\right) = 0 \tag{2-3}$$

which is the continuity equation in the outer flow region. Equations (2-1), (2-2), and (2-3) complete the description of fluid flow around the stationary hemisphere.

The objective is to determine the fluid flow field within the boundary layer. The solution procedure progressed in two stages. First, following the usual boundary layer development for forced flow,[37] a solution was obtained for the potential

flow region. The potential flow solution provided the pressure distribution over the electrode surface and the far-field boundary conditions needed for solution of the boundary layer equations. Second, the boundary layer equation were solved using series expansion discussed by Barcia *et al.*[19] for the rotating hemispherical electrode.

2.3 Potential Flow Calculation

The velocity potential ϕ satisfies Laplace's equation, which can be written in spherical polar coordinates as

$$\frac{\partial}{\partial r}\left(r^2\frac{\partial \phi}{\partial r}\right)+\frac{1}{\sin(\theta)}\frac{\partial}{\partial \theta}\left(\sin(\theta)\frac{\partial \phi}{\partial \theta}\right)=0 \tag{2-4}$$

where the radial component of the fluid velocity is given by

$$v_r=-\frac{\partial \phi}{\partial r} \tag{2-5}$$

the angular or colatitude component of the fluid velocity is given by

$$v_\theta=-\frac{1}{r}\frac{\partial \phi}{\partial \theta} \tag{2-6}$$

and r and θ are the radial and angular components, respectively.

The no-penetration boundary conditions can be expressed as

$$\left.\frac{\partial \phi}{\partial \theta}\right|_{r,\theta=\pi/2}=0 \tag{2-7}$$

for the insulating plane and as

$$\left.\frac{\partial \phi}{\partial r}\right|_{r=r_0,\theta}=0 \tag{2-8}$$

for the electrode surface. A symmetry condition for the centerline can be expressed as

$$\left.\frac{\partial \phi}{\partial \theta}\right|_{r,\theta=0}=0 \tag{2-9}$$

Under the assumption that the flow can be considered to be of uniform velocity towards the insulating plane and the presence of hemisphere does not effect the fluid field far away from the electrode, the velocity potential should approach an asymptotic behavior and can be expressed as

$$\phi|_{r\to\infty,\theta} = \frac{c_\phi r^2}{2}\left(3\cos^2(\theta) - 1\right) \tag{2-10}$$

where c_ϕ is a hydrodynamic constant. Equation (2-10) was previously applied in the development of the potential flow solution for a submerged jet impingement onto a flat disk.[38] Thus, use of equation (2-10) constitutes a statement that, far from the electrode, the influence of the shape of the hemispherical electrode should diminish.

The solution of equation (2-4) subjected to boundary conditions (2-7) to (2-10) is given by

$$\phi = -c_\phi {r_0}^2\left(\frac{1}{2}\frac{r^2}{r_0^2} + \frac{1}{3}\frac{r_0^3}{r^3}\right)\left(3\cos^2(\theta) - 1\right) \tag{2-11}$$

with the corresponding stream function ψ given by

$$\psi = -c_\phi {r_0}^2\left(\frac{r^3}{r_0^3} - \frac{r_0^2}{r^2}\right)\sin^2(\theta)\cos(\theta) \tag{2-12}$$

Computed values for flow trajectories, given as $-\psi c_\phi^{-1} r_0^{-2}$, are presented in Figure 2-2 as a function of dimensionless position scaled by the hemisphere radius r_0. The boundary layer calculation presented in the subsequent section employs the pressure gradient obtained from Bernoulli's equation

$$p + \frac{1}{2}\rho v^2 = \text{constant} \tag{2-13}$$

where the velocity is given by the potential flow solution. Thus, given that $v_r|_{r_0} = 0$ and, from equations (2-11) and (2-6), that

$$v_\theta|_{r_0} = \frac{5cr_0}{2}\sin(2\theta) \tag{2-14}$$

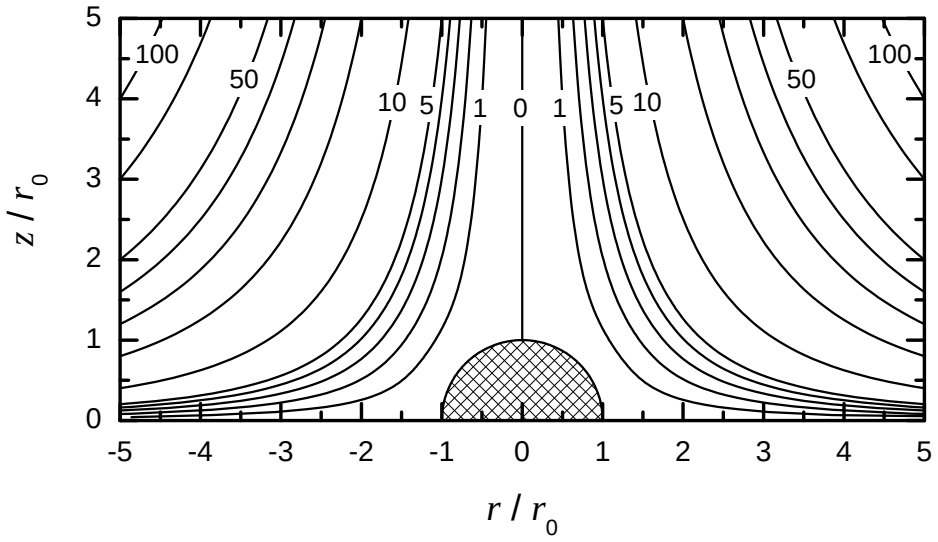

Figure 2-2: Computed flow trajectories corresponding to the potential flow solution, given as equation (2-12), for the hemispherical electrode subjected to a submerged impinging jet system with $-\psi c_{\phi}^{-1} r_0^{-2}$ as a parameter.

the pressure gradient at the electrode surface can be expressed as

$$-\frac{1}{\rho c^2 r_0^2}\frac{\partial p_s}{\partial \theta} = \frac{25}{4}\sin(4\theta) \tag{2-15}$$

The dimensionless pressure gradient along the electrode surface is given in Figure 2-3 as a function of colatitude angle θ. The dimensionless pressure gradient changes sign at a position of $\theta = \pi/4$. As -shown in the subsequent section, the reversal of the pressure driving force for flow induces separation of the velocity boundary layer.

2.4 Boundary Layer Flow Calculation

The solution technique employed to solve equations (2-1) and (2-2) closely follows closely the development presented by Barcia *et al.*[19] for the rotating hemispherical electrode.

Equations (2-1) and (2-2) can be conveniently written in dimensionless form by introducing dimensionless variable ξ, $H(\theta,\xi)$, $F(\theta,\xi)$. The dimensionless momentum and continuity equations are:

$$\frac{1}{4}F(\theta,\xi)\frac{\partial F(\theta,\xi)}{\partial \theta} - H(\theta,\xi)\frac{\partial F(\theta,\xi)}{\partial \xi} = \frac{\sin(4\theta)}{4} + \frac{1}{2}\frac{\partial^2 F(\theta,\xi)}{\partial \xi^2} \tag{2-16}$$

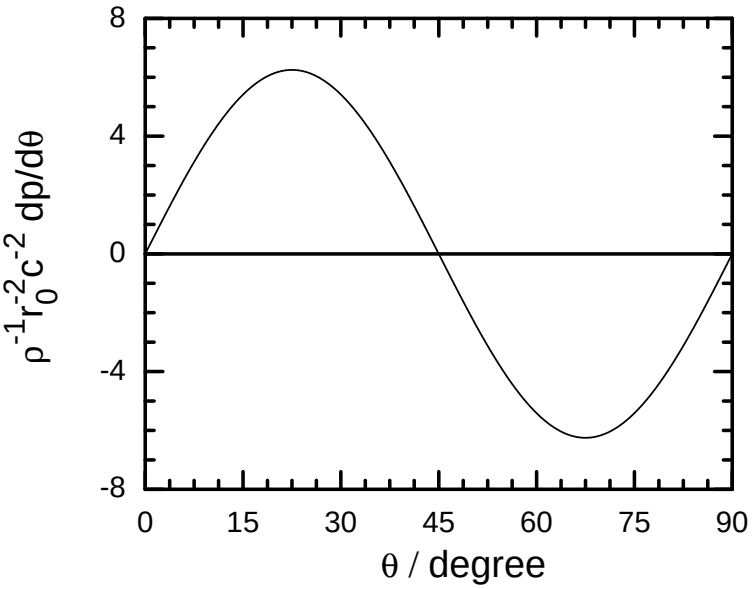

Figure 2-3: Distribution of the dimensionless pressure gradient given as equation (2-15).

and

$$\frac{1}{2}\frac{\partial F(\theta,\xi)}{\partial \theta} - 2\frac{\partial H(\theta,\xi)}{\partial \xi} + \frac{1}{2}F(\theta,\xi)\cot(\theta) = 0 \tag{2-17}$$

respectively, where the pressure gradient was introduced from equation (2-15), ξ is the dimensionless radial position given in terms of the hydrodynamic constant a as

$$\xi = \sqrt{\frac{a}{\nu}}(r - r_0) \tag{2-18}$$

$H(\theta,\xi)$ is the dimensionless radial velocity, such that

$$v_r = -2\sqrt{a\nu}H(\theta,\xi) \tag{2-19}$$

and $F(\theta,\xi)$ is the dimensionless colatitude velocity, such that

$$v_\theta = \frac{ar_0}{2}F(\theta,\xi) \tag{2-20}$$

The no-slip boundary conditions at the electrode surface for the colatitude and radial velocity components can be expressed as

$$F(\theta,\xi)|_{\xi=0} = 0 \tag{2-21}$$

and

$$H(\theta,\xi)|_{\xi=0} = 0 \tag{2-22}$$

respectively. The condition that the flow must approach the potential flow solution far from the surface is expressed by

$$F(\theta,\xi)|_{\xi\to\infty} = \sin(2\theta) \tag{2-23}$$

Comparison between equations (2-23) and (2-14) reveals that $a = 5c_\phi$, which provides that the boundary layer equations corresponding to a jet impinging upon a planar surface are recovered for $\theta = 0$.

Following Howarth,[36] $H(\theta,\xi)$ and $F(\theta,\xi)$ can be expanded in terms of θ and ξ as

$$H(\theta,\xi) = \sum_{i=1}^{n} \theta^{2i-2} H_{2i-1}(\xi) \tag{2-24}$$

and

$$F(\theta,\xi) = \sum_{i=1}^{n} \theta^{2i-1} F_{2i-1}(\xi) \tag{2-25}$$

respectively. The $\sin(4\theta)$ term arising in equation (2-16) from the colatitude pressure gradient can be expanded as

$$\sin(4\theta) = 4\theta - \frac{4^3}{3!}\theta^3 + \frac{4^5}{5!}\theta^5 - \frac{4^7}{7!}\theta^7 + \cdots + \frac{(-1)^{n+1}(4\theta)^{2n-1}}{(2n-1)!} \tag{2-26}$$

and the $\cot(\theta)$ term appearing in equation (2-17) can be expanded as

$$\cot(\theta) = \frac{1}{\theta} - \frac{\theta}{3} - \frac{\theta^3}{45} - \frac{2\theta^5}{945} - \cdots \tag{2-27}$$

The number of terms in the series n can be arbitrarily selected to achieve a desired level of accuracy. In the present work, the number of terms in the expansions (2-24) to (2-27) was limited to $n = 14$ because terms of higher-order in the expansion (2-26) for the colatitude pressure gradient were negligibly small as compared to the largest terms in equation (2-16). Introduction of equations (2-24)-(2-27) into

equations (2-16) and (2-17), and collecting the terms of given orders of θ yields a series of 28 coupled ordinary differential equations for $H_{2i-1}(\xi)$ and $F_{2i-1}(\xi)$. For example, the equation for $H_1(\xi)$ and $F_1(\xi)$ were obtained by collecting the terms of order of θ in the momentum balance. It is represented as

$$\frac{1}{4}F_1^2(\xi) - H_1(\xi)\frac{dF_1}{d\xi} = 1 + \frac{1}{2}\frac{d^2F_1(\xi)}{d\xi^2} \tag{2-28}$$

Similarly, collecting the terms of order θ^0 in the continuity equation yields

$$\frac{1}{2}F_1(\xi) = \frac{dH_1(\xi)}{d\xi} \tag{2-29}$$

The higher order terms of θ in the momentum and the continuity equations, listed in Appendix A, give the governing equations for $H_{2i-1}(\xi)$ and $F_{2i-1}(\xi)$.

The no-slip boundary condition at the electrode surface for v_r and v_θ is related to $H_{2i-1}(\xi)$ and $F_{2i-1}(\xi)$ by the following

$$H_{2i-1}(\xi) = F_{2i-1}(\xi) = 0.0 \quad \text{at} \quad \xi = 0 \tag{2-30}$$

and the far-field boundary condition for v_θ yields

$$F_{2i-1}(\infty) = \frac{(-1)^{i-1}2^{2i-1}}{(2i-1)!} \tag{2-31}$$

Thus, the governing ordinary differential equations for $H_{2i-1}(\xi)$ and $F_{2i-1}(\xi)$ with boundary conditions (2-30) and (2-31) describe the fluid flow within the boundary layer. The solution procedure is described in the next section.

2.4.1 Solution Method

The above set of ordinary differential equations were solved using the BAND algorithm introduced by Newman.[39] The boundary condition (2-31) for the colatitude velocity, *i.e.*, $F_{2i-1}(\xi = \infty)$ was applied at $\xi = 40.0$. The calculation domain ξ was divided into a grid of N nodes. The nodes were spaced at distance of H with each other. The momentum equations were discritized at node J as presented in

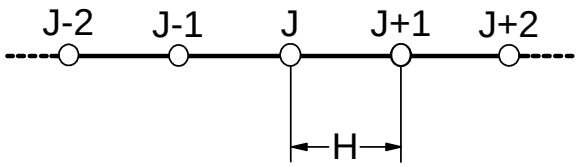

Figure 2-4: Schematic diagram of grid for calculation domain ξ. H is the spacing between adjacent nodes.

Figure 2-4. The corresponding continuity equations were discritized at half point between node J and J $-$ 1. The discretization procedure ensures that the order of resulting equations at each node is of H^2. The disctitized form of continuity and momentum equations for $H_1(\xi)$ and $F_1(\xi)$ (equations (2-28) and (2-29)) are given as

$$G(1) = \frac{(F_1(\mathrm{J}+1) - 2F_1(\mathrm{J}) + F_1(\mathrm{J}-1))}{2\mathrm{H}^2} + 1 + \frac{H_1(\mathrm{J})\,(F_1(\mathrm{J}+1) - F_1(\mathrm{J}-1))}{2\mathrm{H}} - \frac{F_1(\mathrm{J})^2}{4} \tag{2-32}$$

and

$$G(2) = 2\frac{(H_1(\mathrm{J}) - H_1(\mathrm{J}-1))}{\mathrm{H}} - \frac{(F_1(\mathrm{J}) + F_1(\mathrm{J}-1))}{2} \tag{2-33}$$

where $G(1)$ and $G(2)$ are the residuals for the momentum and the continuity equation at node J. The BAND algorithm solves equations (2-33) and (2-32) with boundary conditions (2-30) and (2-31) such that the residuals $G(1)$ and $G(2)$ are effectively equal to zero within the specified tolerance at each node. The same procedure was followed for rest of the equations listed in Appendix A. A FORTRAN code was used to solve the equations. Listing of the code with its main program and subroutines is presented in Appendix C.

2.4.2 Results

The solutions obtained for $H_1(\xi)$ and $F_1(\xi)$ as a function of ξ are presented in Figure 2-5. The results are in agreement with those obtained by Homann[40] for disk electrode under submerged jet impingement. The obtained solution for $H_3(\xi)$, $F_3(\xi)$, $H_5(\xi)$, $F_5(\xi)$, ..., $F_{27}(\xi)$ are presented in Appendix A.2.

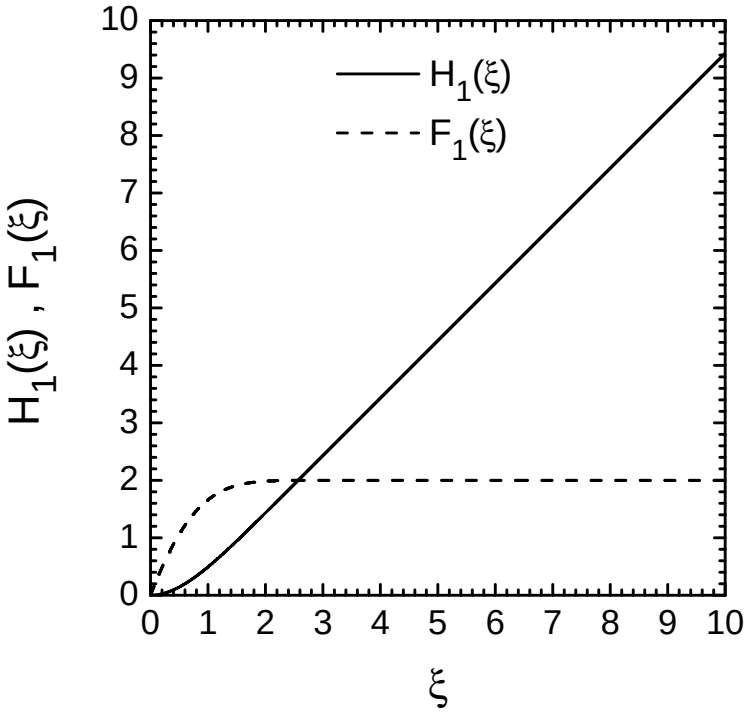

Figure 2-5: Dimensionless radial and colatitude functions $H_1(\xi)$ and $F_1(\xi)$ as a function of ξ (see equations (2-24) and (2-25)).

The velocity distribution near the electrode surface can be approximated by Taylor's series expansions for $F(\theta,\xi)$ and $H(\theta,\xi)$ as

$$F(\theta,\xi) = \left[\sum_{i=1}^{14} \theta^{2i-1} F'_{2i-1}(0)\right] \xi + \frac{1}{2}\left[\sum_{i=1}^{14} \theta^{2i-1} F''_{2i-1}(0)\right] \xi^2 \tag{2-34}$$

and

$$H(\theta,\xi) = \frac{1}{2}\left[\sum_{i=1}^{14} \theta^{2i-1} H''_{2i-1}(0)\right] \xi^2 + \frac{1}{6}\left[\sum_{i=1}^{14} \theta^{2i-1} H'''_{2i-1}(0)\right] \xi^3 \tag{2-35}$$

where the first and second terms of equation (2-34) represent the first and the second order derivative of v_θ with respect to ξ, respectively. Similarly, the first and second terms of equation (2-35) represent the second and the third order derivative of v_r with respect to ξ, respectively. The first order derivative of v_r with respect to ξ is zero because of no penetration condition. Velocity expansions (2-34) and (2-35) provide a convenient way to represent the fluid flow field within the boundary layer. Later, the coefficient of the velocity flow field are utilized in the solution of

convective-diffusion equation. This is a valid approach for convective-diffusion processes with large Sc number, because the mass transfer boundary layer is much thinner compare to the momentum boundary layer, and the fluid velocities v_θ and v_r can be approximated with a quadratic and third-degree polynomial in ξ within the mass transfer boundary layer.

The gradient expressions $F'_{2i-1}(0)$ at the electrode surface were calculated from the obtained solution using three point forward difference method.[41] In order to minimize the influence of finite-difference errors on evaluation of F'_{2i-1} and H''_{2i-1}, the differential equations were approximated to the order of the square of the mesh-size H, and the numerical values were obtained by extrapolation to zero mesh size. Plots $F'_{2i-1}(0)$ vs H^2 are given in Appendix A. The number of digits given in Table 2.1 are consistent with the standard deviation obtained through the regression procedure.

Two methods can be employed in obtaining $H''_{2i-1}(0)$. The first method utilizes the solution of ordinary differential equations and difference schemes. The second method estimates $H''_{2i-1}(0)$ by substituting the calculated values of $F'_{2i-1}(0)$ in the corresponding continuity equations. Most importantly, the second method reduces errors in the evaluation of the expressions $H''_{2i-1}(0)$ by ensuring that the residuals for mass-balance are zero at the electrode surface.

The higher order expressions $F''_{2i-1}(0)$ were obtained by substituting the no-slip condition in the momentum equation (2-16). Thus, the expression for second derivative of $F(\theta,\xi)$ at the electrode surface is given by

$$\left.\frac{\partial^2 F(\theta,\xi}{\partial \xi^2}\right|_{\xi=0} = -\frac{\sin 4\theta}{2} \tag{2-36}$$

After substitution of the series expansion for $F(\theta,\xi)$ (equation (2-25)) and further expansion of $\sin 4\theta$ in terms of θ, values of $F''_{2i-1}(0)$ were obtained. The expressions $H'''_{2i-1}(0)$ were obtained by double differentiating the the continuity equation (2-16)

Table 2.1: Series expansion coefficients $F'_{2i-1}(0)$ and $H''_{2i-1}(0)$ in the equations (2-34) and (2-35) for $H(\theta,\xi)$ and $F(\theta,\xi)$ at $\xi = 0$.

i	$F'_{2i-1}(0)$	$H''_{2i-1}(0)$
1	2.6238754	1.3119377
2	-3.99262600	-4.21128229
3	1.71640917	2.89275550
4	-0.41810335	-0.95844785
5	0.014014149	0.062315385
6	-0.0325842274	-0.0973086579
7	-0.025404936	-0.086129459
8	-0.02354329	-0.09186753
9	-0.0221291	-0.0974599
10	-0.02122090	-0.10411441
11	-0.02068333	-0.11185299
12	-0.02043571	-0.12075969
13	-0.02042491	-0.13093150
14	-0.02061600	-0.14248419

and substituting the second derivative of $F(\theta,\xi)$ at $\xi = 0$. The substitution yields:

$$\left.\frac{\partial^3 H(\theta,\xi)}{\partial\xi^3}\right|_{\xi=0} = -\frac{\cos 4\theta}{2} - \frac{\cos 2\theta \cos^2\theta}{2} \tag{2-37}$$

Again, after substitution of the series expansion for the series expansion for $H(\theta,\xi)$ (see equation (2-24)) and further expansion of trigonometric functions in terms of θ, the values of $F''_{2i-1}(0)$ were obtained. The calculated values for coefficients $F'_{2i-1}(0)$ and $H''_{2i-1}(0)$ for i=1,...,14 are given in Table 2.1. Similarly, values of $F''_{2i-1}(0)$ and $H'''_{2i-1}(0)$ are provided in Table 2.2.

2.5 Boundary Layer Separation

Boundary layer separation takes place at the location where the normal derivative of the colatitude velocity, *i.e.*, $\left.\frac{\partial v_\theta}{\partial\xi}\right|_{r_0,\theta\neq 0}$, has a value equal to zero. Thus, boundary layer separation is observed at the value of θ where the dimensionless shear stress,

$$B(\theta) = \sum_{i=1}^{n} \theta^{2i-1} F'_{2i-1}(0) \tag{2-38}$$

Table 2.2: Series expansion coefficients $F''_{2i-1}(0)$ and $H'''_{2i-1}(0)$ in the equations (2-34) and (2-35) for $H(\theta,\xi)$ and $F(\theta,\xi)$ at $\xi = 0$.

i	$F''_{2i-1}(0)$	$H'''_{2i-1}(0)$
1	-2	-1
2	16/3	11/2
3	-64/15	-41/6
4	512/315	161/45
5	-1024/2853	-641/630
6	8192/155925	2561/14175
7	-32768/6081075	-133/6075
8	262144/638512875	81922/42567525
9	-262144/10854718875	-163841/1277025750
10	2097152/1856156927625	93623/13956067125
11	-8388608/19489647700625	-2621441/9280784638125
12	67108864/49308808782358125	146654/14992036723125
13	-134217728/36981606586768593 75	-5991863/21132346621010625
14	1073741824/1298054391195577640625	335544322/48076088562799171875

has a value equal to zero. The value of θ at which separation was calculated depended slightly on the number of terms retained in the series expansion. The point of separation reached a value of 54.8 degrees for $n = 14$. A plot of $B(\theta)$ is presented in Figure 2-6 as a function of θ, showing clearly the point of boundary layer separation. The corresponding result obtained by Barcia *et al.*,[19] and reproduced in the present work, for the rotating hemisphere is presented in Figure 2-6 to provide comparison. The fluid dynamics calculations of a rotating hemisphere does not predict boundary layer separation, although a small region of is theoretically possible near the singularity where the electrode contacts the insulating plane.

2.6 Numerical Simulation

In the present section, computational fluid mechanics calculations were performed for the stationary hemispherical electrode under jet impingement. The hydrodynamic model developed here involved simultaneous numerical solution

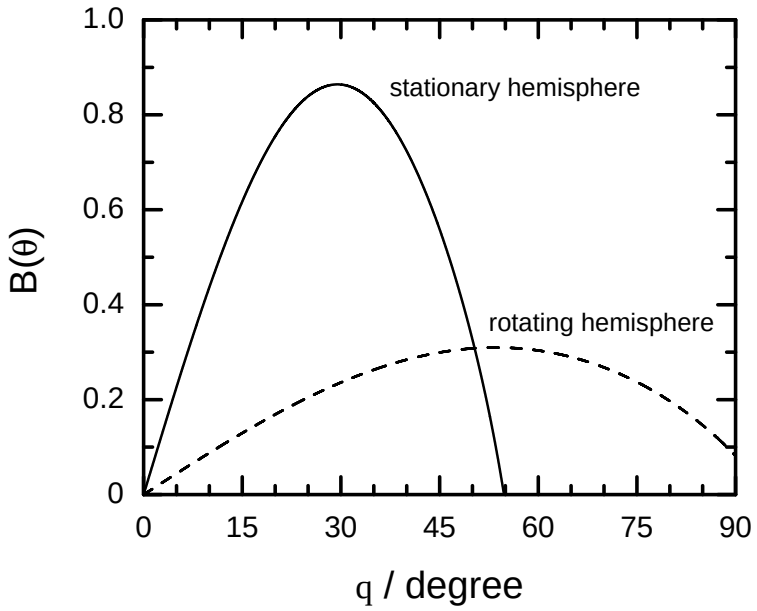

Figure 2-6: Calculated dimensionless surface shear stress as a function of angle θ. Solid lines represent the result for the stationary hemisphere under submerged jet impingement and dashed lines represent the result for the rotating hemisphere.

of the Navier-Stokes and the continuity equations. Numerical solution of the governing equations was developed by Dr. Gert Nelissen, Vrije Universiteit Brussel, Belgium.

2.6.1 Governing Equations

As shown in Figure 2-7, a two-dimensional cylindrical coordinate system was employed to describe the system. The r-coordinate corresponded to the horizontal axis, and z-coordinate was assumed in the vertical direction. In this representation, the third dimension, *i.e.*, θ-coordinate, was assumed to be around the vertical z-coordinate. The flow was symmetric in the θ-coordinate, therefore the θ velocity component and the derivative of quantities in the θ direction were substituted by zero in the governing equations. The mathematical development and numerical approach used in the present work are described by Nelissen *et al.*[42] The flow was assumed to be steady state, and the fluid was assumed to be incompressible. Thus,

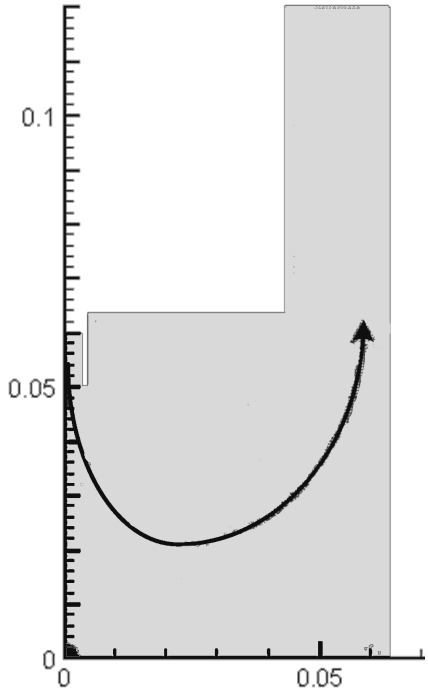

Figure 2-7: Schematic representation of the simulated flow geometry. The dimensions are given in units of m. The arrow represents the general direction of flow, and the cylindrical electrode is located at the origin.

conservation of momentum in r, and z-coordinates could be expressed by

$$\rho\left(v_r\frac{\partial v_r}{\partial r}+v_z\frac{\partial v_r}{\partial z}\right)=-\frac{\partial p}{\partial r}+\mu\left[\frac{\partial}{\partial r}\left(\frac{1}{r}\frac{\partial\left(rv_r\right)}{\partial r}\right)+\frac{\partial^2 v_r}{\partial z^2}\right] \tag{2-39}$$

and

$$\rho\left(v_r\frac{\partial v_z}{\partial r}+v_z\frac{\partial v_z}{\partial z}\right)=-\frac{\partial p}{\partial z}+\mu\left[\frac{1}{r}\frac{\partial}{\partial r}\left(r\frac{\partial v_z}{\partial r}\right)+\frac{\partial^2 v_z}{\partial z^2}\right] \tag{2-40}$$

where ρ is the fluid density, p is the pressure, μ is the molecular viscosity of the fluid. For the incompressible fluid, conservation of mass is represented by

$$\frac{1}{r}\frac{\partial\left(rv_r\right)}{\partial r}+\frac{\partial v_z}{\partial z}=0 \tag{2-41}$$

Under turbulent conditions, Reynolds averaged NavierStokes (RANS) equations were used.[42] The boundary conditions for equations (2-39), (2-40), and (2-41) were that no-slip and no-penetration conditions applied at solid surfaces, and that a uniform fluid velocity profile was imposed at the inlet to the system

(corresponding to the nozzle). In addition, a reference point for the pressure was located at the outlet of the system.

The boundary conditions for equations (2-39), (2-40), and (2-41) are:

1. The no slip boundary condition *i.e.*, $v_r = v_z = 0$ at the electrode surface.

2. Imposed fluid velocity profile from the inlet. In this case, fluid field was assumed to be emanating with a constant velocity across the nozzle.

3. A reference point for the pressure *i.e.*, $p = p_{ref} = 0$ was assumed to be located at the outlet of the system.

2.6.2 Numerical Method

The partial differential equations (2-39), (2-40), and (2-41) were solved with residual distribution method.[43] The discretization was done on the grids of triangles in the geometric domain of interest. The Lax-Wendroff[43] scheme was applied to the convection terms of the momentum balances. The viscous terms were treated in a standard finite element manner. The numerical scheme provided a second order accuracy. The resulting non-linear set of equations were solved by using the Newton-Raphson method, with explicit calculation of the jacobian matrices. An incomplete LU preconditions gmres was used to approximate the solution of the linear system. The grid in the boundary layer regime contained at least ten elements in the direction normal to the electrode.

2.6.3 Simulation Results

The calculated results presented here correspond to two different inlet flow rates. Fluid properties were assumed to be those of water at 25 °C. Simulations corresponding to an inlet Reynolds number of 1,100 are presented in Figure 2-8. The flow in the inlet region is laminar. The false color images indicate that the pressure near the electrode is large at the stagnation point ($\theta = 0$), decreases in the region

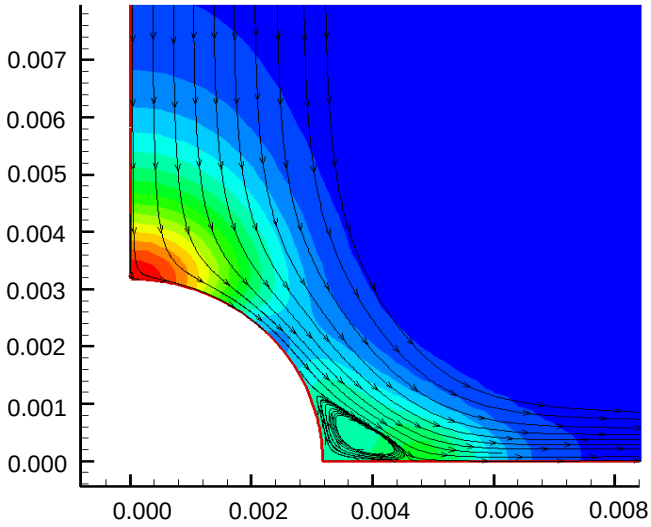

Figure 2-8: Fluid streamlines in the vicinity of the electrode for an inlet Reynolds number of 1,100. The color map indicate the pressure distribution. The radial dimension is given in units of m.

of ($\theta = \pi/4$), and increases near the electrode-insulator interface ($\theta = \pi/2$). The adverse pressure gradient seen for angles larger that $\theta = \pi/4$ induces a boundary layer separation, just as predicted by potential flow calculations. The fluid field shows a circulation zone starting at an angle of about 62° which is slightly larger than the value of 54.8° obtained by the boundary-layer hydrodynamic model.

The flow field for an inlet Reynolds number of 11,000 is presented in Figure 2-9. In this case, the inlet flow is turbulent. The results again show that a circulation zone is formed at an angle near 62°. Figure 2.9(b) provides an enlarged image of the recirculation zone shown near the electrode-insulator interface in Figure 2.9(a).

2.7 Summary

This chapter has presented two hydrodynamic models for fluid flow around a stationary submerged hemisphere under jet impingement. The first model was based upon semi-analytical solution of the momentum and mass conservation equation. The results of the calculation show a formation of boundary layer separation for the system. The point of boundary layer separation was predicted to occur at 54.8°. The second model numerically solved the momentum and the

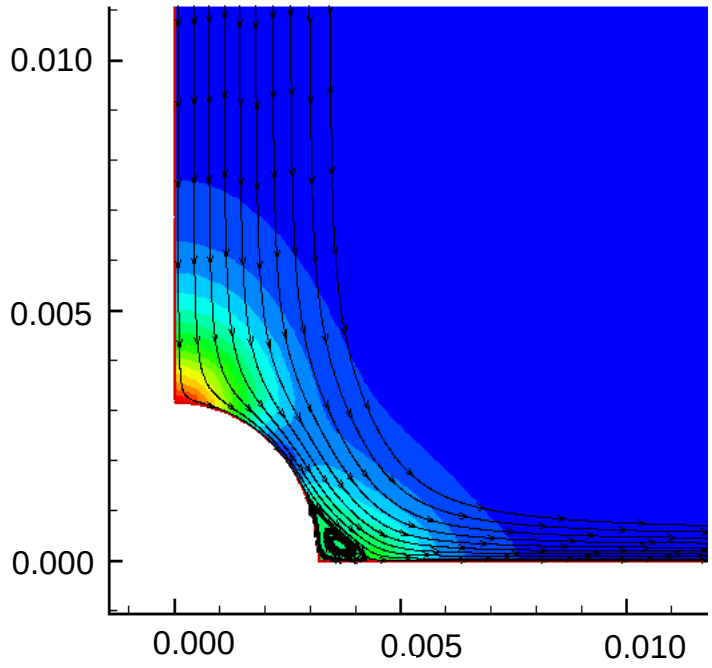

(a)

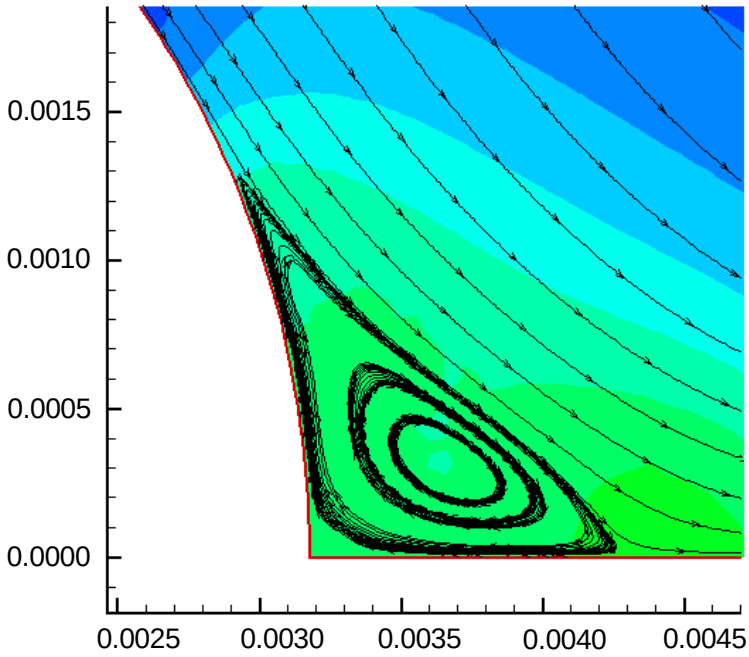

(b)

Figure 2-9: Fluid streamlines in the vicinity of the electrode for an inlet Reynolds number of 11,000. The color map indicate the pressure distribution. The radial dimension is given in units of m. Figure 2.9(b) provides an enlarged image of the recirculation shown in Figure 2.9(a).

continuity equations without invoking any approximations. This model also successfully show the formation of vortex in separated part of the boundary layer, and the point of boundary layer septation was predicted at 62°. The results of the hydrodynamic models are used in subsequent chapters.

CHAPTER 3
CONVECTIVE-DIFFUSION MODELS FOR A STATIONARY HEMISPHERICAL ELECTRODE UNDER SUBMERGED JET IMPINGEMENT

This chapter provides a detailed description of convective-diffusion processes taking place in the boundary layer of a hemispherical electrode under submerged jet impingement. A solution for convective-diffusion equation of the system is provided in this chapter. The obtained solution provide a framework for further investigation of impinging jet hemispherical electrode.

3.1 Governing Equations

Under the assumptions that the Peclet number is large and that the concentration of the reactant c_R is small with respect to the supporting electrolyte, the steady-state convective diffusion equation within the boundary layer can be written as

$$v_r \frac{\partial c_R}{\partial r} + \frac{v_\theta}{r_0} \frac{\partial c_R}{\partial \theta} = D_R \frac{\partial^2 c_R}{\partial r^2} \tag{3-1}$$

where v_r and v_θ are the radial and colatidute velocity components of fluid flow field with in the boundary layer. Their expressions have been obtained from the fluid mechanics development presented in Chapter 2. The followings assumptions were made in deriving equation (3-1):

1. the fluid flow in the boundary layer is laminar and normal derivative of all quantities are much larger compare to the tangential derivatives,

2. the diffusion of reactant c_R in the tangential direction direction is much smaller compare to the normal direction at the electrode surface, and

3. the thickness of the mass transfer boundary layer, δ_m, is infinitely small compare to the radius of the hemisphere.

It is important to note that equation (3-1) is only valid in the unseparated part of the momentum boundary layer at the electrode surface.

The objective here is the calculation of the mass-transfer-limited current distribution at the electrode surface; thus, the boundary conditions for equation (3-1) are given as

$$c_R|_{r=r_0,\theta} = c_0 \tag{3-2}$$

$$c_R|_{r=\infty,\theta} = c_\infty \tag{3-3}$$

and

$$c_R|_{r,\theta=0} = c_\infty \tag{3-4}$$

The concentration c_R can be expanded as a series function of θ, ξ, and $\mathrm{Sc}^{-\frac{1}{3}}$ as

$$\frac{c_R - c_\infty}{c_0 - c_\infty} = \sum_{i=1}^{n} \theta^{2i-2} \Phi_{1,2i-1}(\xi) + \mathrm{Sc}^{-\frac{1}{3}} \sum_{i=1}^{n} \theta^{2i-2} \Phi_{2,2i-1}(\xi) \tag{3-5}$$

such that the first term of the expansion provides the solution under the assumption that the Schmidt number Sc is infinitely large, and the second term provides a correction for a finite value of Sc.

The characteristic dimensionless distance for mass transfer can be defined to be

$$Z = \mathrm{Sc}^{1/3} \xi \tag{3-6}$$

which accounts for the difference in scale between the convection and mass transfer boundary layer thicknesses.

Fourteen coupled ordinary differential equations for $\Phi_{1,2i-1,1}$ and $\Phi_{2,2i-1}$ were obtained through following steps:

1. Substitution of v_r and v_θ in terms of a Taylor series dimensionless velocities $F(\theta,\xi)$ and $H(\theta,\xi)$ from equation (2-34) and (2-35) with $n=14$ into equation (3-1),

2. introduction of dimensionless concentration from equation and scaled distance Z from equation (3-5) and (3-6), respectively, and

3. collection of terms corresponding to θ^{2i} and $\theta^{2i}\mathrm{Sc}^{-1/3}$.

The derived equations can be written in general form as following:

$$\begin{aligned}\frac{d^2\,\Phi_{1,2i-1}(Z)}{d\,Z^2}-\frac{1}{2}H_1''(0)Z^2\frac{d\,\Phi_{1,2i-1}(Z)}{d\,Z}-2iF_i'(0)Z\Phi_{1,2i-1}(Z)\\ =Z^2\sum_{n=1}^{n=i}\frac{1}{2}H_{2n+1}''(0)\frac{d\,\Phi_{1,2i-1}(Z)}{d\,Z}\\ +Z\sum_{n=1}^{n=i-1}2nF_{2(i-n)+1}'(0)\Phi_{1,2n+1}(Z)\end{aligned}\tag{3-7}$$

and

$$\begin{aligned}\frac{d^2\,\Phi_{2,2i-1}(Z)}{d\,Z^2}-\frac{1}{2}H_1''(0)Z^2\frac{d\,\Phi_{2,2i-1}(Z)}{d\,Z}-2iF_i'(0)Z\Phi_{1,2i-1}(Z)\\ =Z^3\sum_{n=0}^{n=i}\frac{1}{2}H_{2n+1}'''(0)\frac{d\,\Phi_{2,2i-1}(Z)}{d\,Z}\\ +Z^2\sum_{n=0}^{n=i-1}(i-n)F_{2n+1}''(0)\Phi_{1,2(i-n)+1}(Z)\\ +Z^2\sum_{n=1}^{n=i}\frac{1}{2}H_{2n+1}''(0)\frac{d\,\Phi_{2,2(i-n)+1}(Z)}{d\,Z}\\ +Z\sum_{n=1}^{n=i-1}2(i-n)F_{2n+1}'(0)\Phi_{2,2(i-n)+1}(Z)\end{aligned}\tag{3-8}$$

where equation sets (3-7) and (3-8) represent 14 ordinary differential equations for $\Phi_{1,2i-1}$ and $\Phi_{2,2i-1}$, respectively.

The boundary conditions for $\Phi_{1,2i-1}$ and $\Phi_{2,2i-1}$ are

$$\Phi_{1,1} = 1.0 \tag{3-9}$$

$$\Phi_{1,2i-1} = 0.0$$

$$\Phi_{2,2i-1} = 0.0$$

at $Z = 0$, and

$$\Phi_{1,2i-1} = 0.0 \tag{3-10}$$

$$\Phi_{2,2i-1} = 0.0$$

at $Z = \infty$. The analytic solutions of $\Phi_{1,2i-1}$ and a numerical solutions of $\Phi_{1,2i-1}$ are provided in the next section.

3.2 Solution Method and Results

The equation set (3-7) corresponding to $\Phi_{1,2i-1}$ with boundary conditions (3-9) and (3-10) were solved analytically. For $i = 1$, the solution corresponds to the disk electrode under submerged jet impingement,[44] and it is given as

$$\Phi_{1,1}(Z) = 1.0 - 0.8500069 \int_0^Z \exp\left[-\frac{Z^3 H_1''(0)}{3}\right] dZ \tag{3-11}$$

For $i > 1$, the general solution of the equation set (3-7) is given by

$$\Phi_{1,2i-1}(Z) = \exp\left[-\frac{Z^3 H_1''(0)}{3}\right] \sum_{j=1}^{j=i-1} \left(\lambda_j Z^{3j-2}\right) \tag{3-12}$$

where values of λ_j were deduced by substitution of equation (3-12) into equation (3-7). The complete expressions of $\Phi_{1,2i-1}$ for $2 \leq i \leq 14$ are given in Appendix B.

The equations (3-8) for $1 \leq i \leq 14$ were solved numerically using tridiagonal BAND algorithm described by Newman.[39] The expressions involving $\Phi_{1,2i-1}$ in

Table 3.1: Calculated values for coefficients $\Phi'_{1,2i-1}(0)$ and $\Phi'_{2,2i-1}(0)$ used in equation (3-14) for mass-transfer-limited current distribution.

i	$\Phi'_{1,2i-1}(0)$	$\Phi'_{2,2i-1}(0)$
1	-0.8500077	0.0719099
2	0.5456994	-0.0850449
3	0.1954955	-0.0193952
4	0.4638516	-0.0203633
5	0.3719751	-0.0182829
6	0.3247121	-0.0172154
7	0.2949598	-0.0166429
8	0.2761729	-0.0164106
9	0.2647235	-0.0164366
10	0.2585353	-0.0166741
11	0.2563565	-0.0170954
12	0.2574086	-0.0176849
13	0.2612022	-0.0184347
14	0.2674345	-0.0194908

equations set (3-8) were substituted with their analytical expressions as provided in Appendix B. The numerical simulation were performed for different values of grid spacing H. The quantities of interest for mass-transfer-limited current are first derivatives of $\Phi_{1,2i-1}$ and $\Phi_{1,2i-1}$ with respect to Z at the electrode surface. In order to minimize the influence of finite-difference errors, the differential equations were approximated to the order of the square of the mesh-size, and the numerical values of $\Phi'_{2,2i-1}(0)$ were obtained by extrapolation to zero mesh size. Calculated values for $\Phi'_{1,2i-1}(0)$ and $\Phi'_{2,2i-1}(0)$ are provided in Table 3.1.

3.3 Mass Transfer Limited Current

The flux at the electrode surface is given by

$$N_R = - D_R \frac{\partial c_R}{\partial r}\bigg|_{r=r_0} \tag{3-13}$$

which can be evaluated in the form of a mass-transfer-limited current density in terms of the dimensionless variables introduced above as

$$i_{\lim}(\theta) = \frac{nF\left(c_\infty - c_0\right) D_R}{r_0} \mathrm{Sc}^{1/3} \mathrm{Re}^{1/2} \left[\sum_{i=1}^{n} \theta^{2i-2} \Phi'_{1,2i-1}(0) + \mathrm{Sc}^{-1/3} \left(\sum_{i=1}^{n} \theta^{2i-2} \Phi'_{2,2i-1}(0) \right) \right] \tag{3-14}$$

where the Reynolds number Re is defined to be

$$\mathrm{Re} = \frac{a r_0^2}{\nu} \tag{3-15}$$

Equation (3-14) can be expressed in terms of a characteristic number

$$N^* = -\frac{nF\left(c_\infty - c_0\right) D_R}{r_0} \mathrm{Sc}^{1/3} \mathrm{Re}^{1/2} \tag{3-16}$$

as

$$\frac{i_{\lim}(\theta)}{N^*} = \Psi(\theta) + \mathrm{Sc}^{-\frac{1}{3}} \Lambda(\theta) \tag{3-17}$$

where $\Psi(\theta)$ is the mass-transfer-limited current density for an infinite Schmidt number, and $\Lambda(\theta)$ is the correction to account for the finite value of the Schmidt number. Thus,

$$\Psi(\theta) = -\sum_{i=1}^{n} \theta^{2i-2} \Phi'_{1,2i-1}(0) \tag{3-18}$$

and

$$\Lambda(\theta) = -\sum_{i=1}^{n} \theta^{2i-2} \Phi'_{2,2i-1}(0) \tag{3-19}$$

The calculated values for $\Psi(\theta)$ and $\Lambda(\theta)$ are presented in Figures 3.1(a) and 3.1(b), respectively, as functions of colatitude angle θ.

The boundary-layer solution is valid only up to the point of boundary layer separation. The result obtained for the stationary hemispherical electrode is in stark contrast to that obtained by Barcia *et al.*[19] for the rotating hemispherical electrode, also shown in Figure 3-1, which does not show such a boundary layer separation. For the stationary electrode in Figure 3.1(a), the region of circulation is represented by a uniform extension of the value of Ψ at the point of separation.

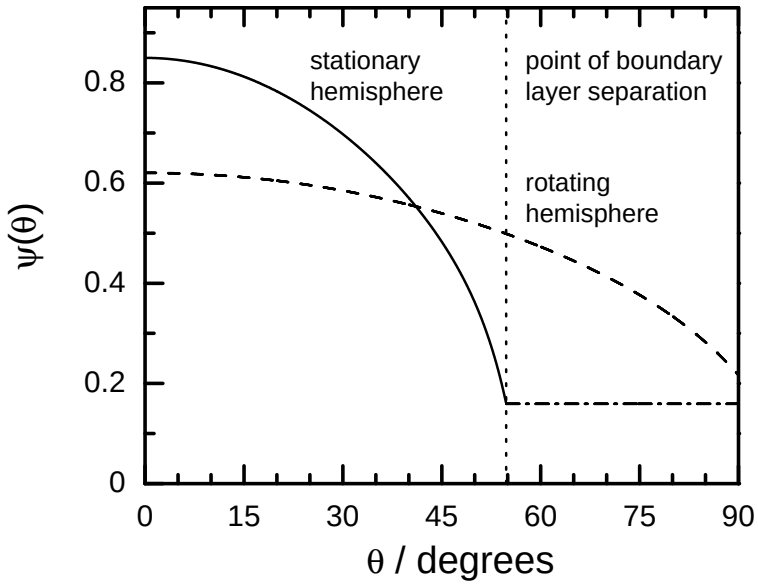

(a)

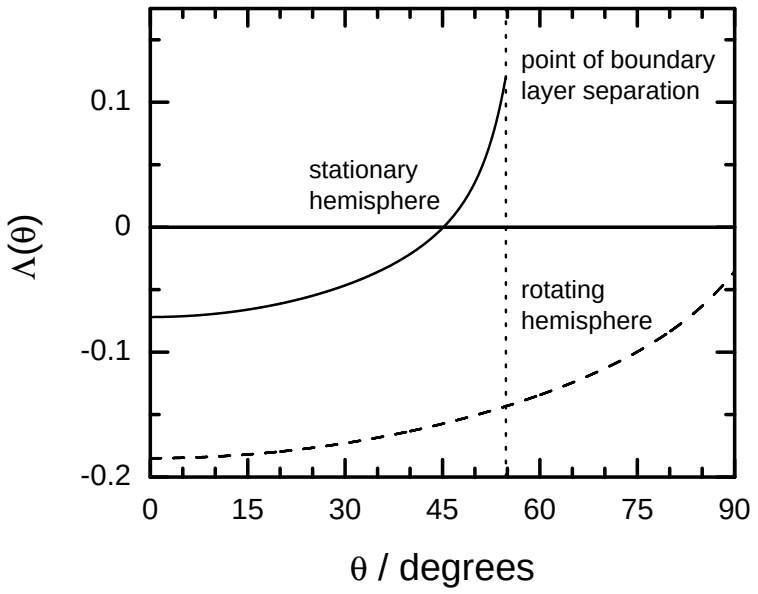

(b)

Figure 3-1: Calculated mass-transfer limited current density for a hemispherical electrode subjected to a submerged impinging jet. Solid lines represent results for the stationary electrode, and the dashed lines represent results for the rotating hemispherical electrode.a) Contribution to equation (3-17) for an infinite Schmidt number; b) Contribution to equation (3-17) providing correction for a finite Schmidt number.

Work is needed to provide a more correct estimation of the mass-transfer rate in this region. A preliminary approach could be to assume a uniform value for a mass-transfer coefficient k_{MT}. Thus, within the region of circulation, $i_{\lim}$ can be expressed as

$$i_{lim} = nFk_{MT}\left(c_{\infty} - c_0\right) \tag{3-20}$$

Integration of equations (3-14) and (3-20) over the electrode surface is required to obtain a value for the total current which is accessible from experimental measurement.

3.4 Numerical Simulations

The aforementioned model gives an expression of convective-diffusion processes up to the point of boundary-layer separation. Numerical solutions, however, were used to obtain a solution of convective-diffusion over the entire electrode surface. Numerical simulation of the governing equation was performed by Dr. Gert Nelissen, Vrije Universiteit Brussel, Belgium. The convective-diffusion model in the cylindrical coordinate system is given by

$$v_r\frac{\partial c_R}{\partial r} + v_z\frac{\partial c_R}{\partial z} = D_R\left[\frac{1}{r}\frac{\partial}{\partial r}\left(r\frac{\partial c_R}{\partial r}\right) + \frac{\partial^2 c_R}{\partial z^2}\right] \tag{3-21}$$

where v_r and v_z are the fluid velocity component calculated by the computational fluid dynamic model in the previous chapter, c_R is the concentration of reacting species, and D_R is the molecular diffusivity of the reacting species. Fluid flow was assumed to be laminar in the mass transfer boundary layer. The transport of the reactant due to electric field in equation (3-21) has been neglected by assuming the presence of excess supporting electrolyte. The system is assumed to operate under isothermal conditions. At the electrode surface, the boundary conditions for equation (3-21) were:

$$c_R = 0 \tag{3-22}$$

and in the bulk

$$c_R = c_\infty \tag{3-23}$$

Equation (3-21) was solved with boundary conditions (3-22) and (3-23) using numerical scheme presented in the previous chapter. To ensure positivity, the convection term in the convective-diffusion equation were discretized using the N-scheme.[45,42]Standard finite element discretization was applied to the diffusion term. In numerical simulations, the diameter of electrode and nozzle was fixed to be $1/4$ inch, and nozzle was assumed to be placed at 5.0 cm from the electrode. The physical properties of the electrolyte used in the simulations are listed in Table 3.2. The concentration distribution of reactant as a function of distance from the electrode surface is shown in Figure 3-2. Directly on the electrode surface the reactant concentration is zero, which is depicted by the blue line. The area represented by the red corresponds to the bulk reactant concentration. Above the electrode surface, the concentration distribution of reactant exhibit a very sharp gradient, shown in Figure 3-2 by marked change in color. However, at the point of separation (θ=62°), the color variation becomes wider signaling a drop in concentration gradient. This confirms that the mass-transfer is minimal at the point of boundary layer separation. The expression of mass-transfer-limited current is given by:

$$i_{lim} = nFD_R \frac{\partial c_R}{\partial r} \tag{3-24}$$

The limiting current density vector at the electrode surface was calculated using the simulation. The parameters used in simulations are given in Table 3.2. The results of simulations are presented in Figure 3-3. Simulation were done for two Reynolds number of fluid in the nozzle. At high Re, the current is higher. Current reaches a minimum at the point of boundary layer separation for both Re numbers. The current in the separated zone is higher than at the point of separation for both cases.

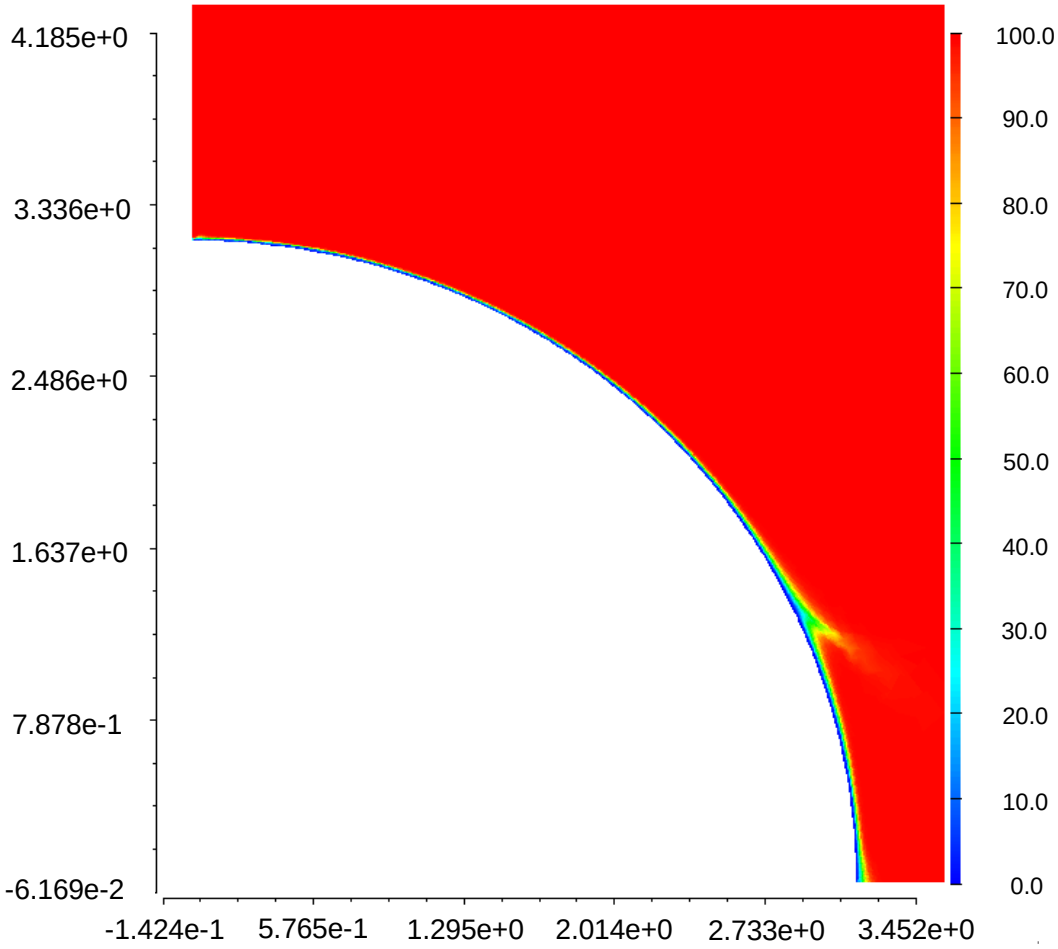

Figure 3-2: Reactant concentration distribution as a function of distance from electrode surface, obtained through numerical simulation of equation (3-21). The blue line corresponds to zero concentration on the electrode surface, whereas red corresponds to the bulk reactant concentration. The radial dimension is given in units of cm. These simulations were performed for $Re = 11300$ in the nozzle.

Table 3.2: Physical properties of the electrolyte used in the numerical solution of equation (3-21).

Property	Value
$\nu/\mathrm{m}^2\ \mathrm{sec}^{-1}$	1.0×10^{-6}
$D_R/\mathrm{m}^2\ \mathrm{sec}^{-1}$	7.0×10^{-10}
$c_\infty/\mathrm{mol\ m}^{-3}$	100.0

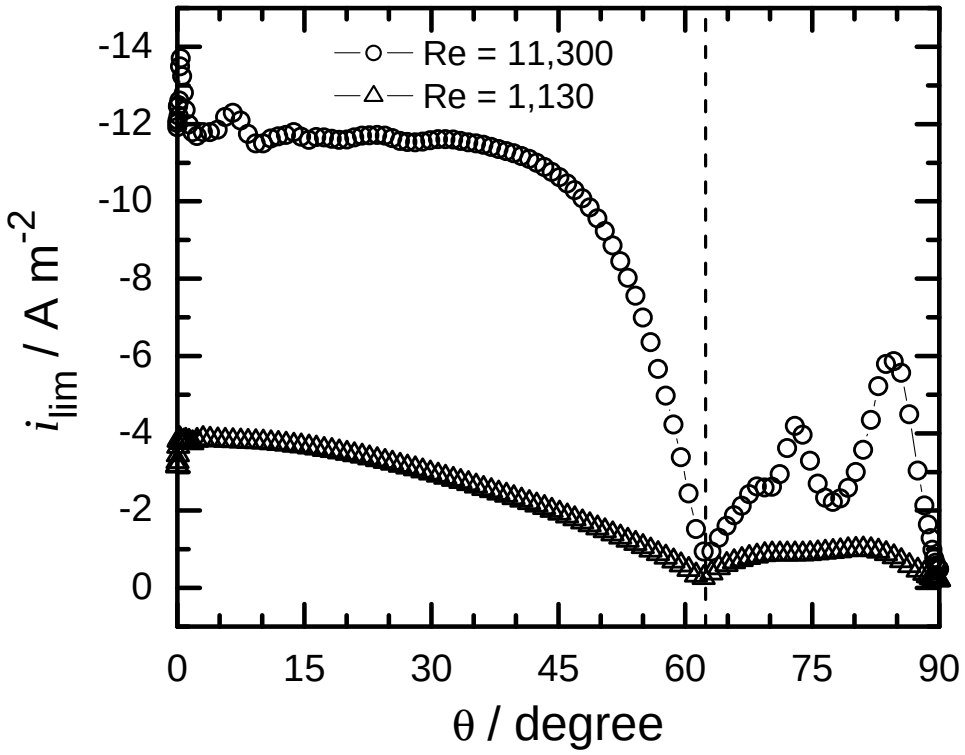

Figure 3-3: Calculated mass-transfer-limited current density for different Reynolds number at the inlet of the nozzle. The vertical dash line at 62° is the point of boundary layer separation. The physical properties of the electrolyte used in the simulations are listed in Table 3.2.

3.5 Conclusion

Steady state mass-transfer was obtained for the system. Two models were presented. The first model was based upon semi-analytical series expansion method. The models used the fluid velocity fields obtained in Chapter 2. The second model made use of a numerical scheme to solve the convective-diffusion equation. Both model predicted a finite value of mass-transfer-limited current at the point of boundary layer separation. The second model was able to calculate the mass-transfer in the separated region of the boundary. The mass-transfer is increased in the separated region with a minimum at the point of separation. This result is analogous to the heat-transfer in sphere, where heat-transfer is enhanced in the separated part of the boundary layer.[46] An implication of this calculation is that the current can be assumed to be constant in the region of boundary layer

separation. This approximation will be used in the calculation of the current distribution for the system in Chapter 5.

CHAPTER 4
HYDRODYNAMIC AND MASS-TRANSFER MODELS FOR A ROTATING HEMISPHERICAL ELECTRODE

The hemispherical electrode under jet impingement represents a modification to the rotating hemispherical electrode described in this work. The present work provides a review of previous hydrodynamic and the steady-state mass-transfer models of a rotating hemispherical electrode system. New calculation results are being presented alongside results of Bercia *et al.*[19] and subsequently compared. This study provides a correction to the published work.[19]

4.1 Schematic Illustration of the System

The rotating hemispherical electrode was first suggested by Chin[17] as an alternative to rotaing disk electrode for study of electrochemical systems. The advantage of the hemisphere over rotating disk is that the current distribution remains uniform even at large fraction of mass transfer limited current.[18] This uniformity of current can be exploited to study electrochemical processes at higher current density. A schematic of the system is presented in Figure 4-1.

In Figure 4-1, a hemispherical electrode is fixed in a insulating material with a no gap at the point of intersection with the insulating plane. The system is rotated

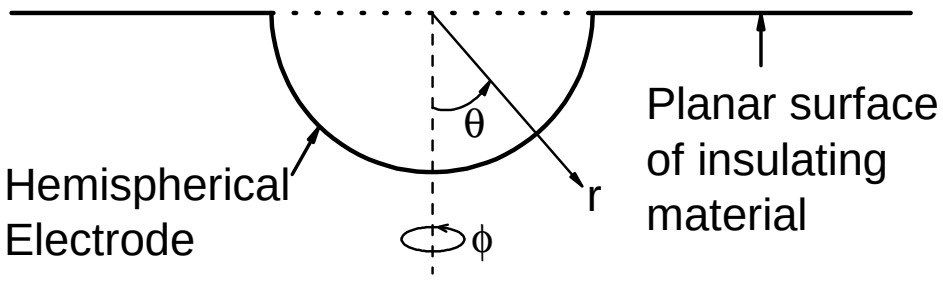

Figure 4-1: Schematics illustration of Rotating Hemispherical Electrode.

in the electrolytic solution in the azimuthal direction. The spherical polar coordinate system is used to describe the system, where r is the radially outward normal direction with origin at the center of hemisphere, θ is colatitude direction, and ϕ is the azimuthal direction; and v_r, v_θ, and v_ϕ are the components of fluid velocity field in r, θ, and ϕ direction, respectively.

4.2 Hydrodynamic Model

The hydrodynamic model of the rotating hemisphere has been addressed in literature by several workers.[19,17,47] It has been based on the hydrodynamic model of a rotating sphere in a quiescent fluid. Howarth[36] first introduced the problem of a rotating sphere in 1951. He provided a solution of the model equations using a polynomial series expansion for v_r, v_θ, and v_ϕ in terms of θ. His solution was limited to the first two terms in the expansion. He also suggested that the fluid flow near the equator can not be described by boundary layer equations. Nigam[48] suggested a different form of series expansion than that of Howarth.[36] He proposed that the velocity expansions in terms of trigonometric functions of θ for velocity components, and provided a solution for first three terms of v_r, v_θ, and v_ϕ. His calculations suggested that the boundary layer remains intact at the equator; thus, boundary layer equations adequately describe the flow near equator. Stewartson[49] stated that the fluid flow at equator is outward along the equatorial plane; therefore, boundary layer will break down near the equator. He suggested that the thickness of the region, where boundary layer assumptions fail, is within $O(\nu^{1/2})$ distance of the equator. Banks[50] improved the solution by solving for coefficients in the series expansion up to four terms. His series expansions were based upon Howarth's[36] model. Manohar,[51] on the other hand, solved the boundary layer equations using a finite difference technique. He reported a better convergence of solution than that of Howarth's[36] series method.

Chin[17,47] treated the hydrodynamics of the rotating hemispherical electrode (RHE), as described in Figure 4-1, like that of rotating spherical electrode. He used Howarth's method of series expansion for velocity components and limited it to four terms. More recently, Barcia and coworkers[19] extended the series expansion up to ten terms. Inclusion of additional terms was needed to obtain the accuracy needed for impedance calculations.

The next section revisits the hydrodynamic model of the RHE. This was motivated by the observation that the results provided by Barcia *et al.*[19] do not satisfy the continuity equation at the electrode surface. The results presented in this chapter provide a correction to the results of Barcia and coworkers.[19]

4.2.1 Governing Equations

The governing equations,[36] which describe the fluid motion within the boundary layer of RHE, are written as

$$\frac{1}{r_0}\frac{\partial v_\theta}{\partial \theta} + \frac{\partial v_r}{\partial r} + \frac{v_\theta}{r_0}\cot(\theta) = 0 \tag{4-1}$$

$$\frac{v_\theta}{r_0}\frac{\partial v_\theta}{\partial \theta} + v_r\frac{\partial v_\theta}{\partial r} - \frac{v_\phi^2}{r_0}\cot(\theta) = \nu\frac{\partial^2 v_\theta}{\partial r^2} \tag{4-2}$$

$$\frac{v_\theta}{r_0}\frac{\partial v_\phi}{\partial \theta} + v_r\frac{\partial v_\phi}{\partial r} + \frac{v_\theta v_\phi}{r_0}\cot(\theta) = \nu\frac{\partial^2 v_\phi}{\partial r^2} \tag{4-3}$$

where equation (4-1) is the continuity equation, and equations (4-2) and (4-3) are the momentum balances in θ and ϕ directions, respectively. The underlying assumption is that derivatives of quantities with respect to ϕ vanish and there is no imposed pressure gradient. The boundary conditions for equations (4-1)-(4-3) are

$$v_r = v_\theta = 0\ ,\ v_\phi = \omega r_0 \sin(\theta) \qquad \text{at} \qquad r = r_0 \tag{4-4}$$

and

$$v_\theta \to 0\ ,\ v_\phi \to 0 \qquad \text{at} \qquad r \to \infty \tag{4-5}$$

where r_0 is the radius of the electrode, and ω is its rotation speed. Dimensionless variables for r, v_r, v_θ, and v_ϕ can be given by

$$\xi = \sqrt{\frac{\omega}{\nu}}(r - r_0) \tag{4-6}$$

$$v_r = \sqrt{(\nu\omega)}H(\theta, \xi) \tag{4-7}$$

$$v_\theta = (r_0\omega)\, F(\theta, \xi) \tag{4-8}$$

and

$$v_\phi = (r_0\omega)\, G(\theta, \xi) \tag{4-9}$$

where dimesionless quantities $H(\theta, \xi)$,$F(\theta, \xi)$, and $G(\theta, \xi)$ are defined as polynomial series expansion with respect to θ such that

$$H(\theta, \xi) = \sum_{i=1}^{n} \theta^{2i-1} H_{2i-1}(\xi) \tag{4-10}$$

$$F(\theta, \xi) = \sum_{i=1}^{n} \theta^{2i-1} F_{2i-1}(\xi) \tag{4-11}$$

$$G(\theta, \xi) = \sum_{i=1}^{n} \theta^{2i-1} G_{2i-1}(\xi) \tag{4-12}$$

where n is the number of terms included in the expansion. Substitution of equations (4-6) to (4-12) into equations (4-1), (4-2), and (4-3) yields $3n$ ordinary differential equations for $H_{2i-1}(\xi)$, $F_{2i-1}(\xi)$, and $G_{2i-1}(\xi)$. The boundary conditions for the derived equations are

$$H_{2i-1}(0) = F_{2i-1}(0) = 0\ ,\ G_{2i-1}(0) = \frac{-1^{i+1}}{(2i-1)!} \tag{4-13}$$

at $\xi = 0$ and

$$F_{2i-1}(\infty) \to 0\ ,\ G_{2i-1}(\infty) \to 0 \tag{4-14}$$

The Taylor series expansion of $H(\theta, \xi)$ and $F(\theta, \xi)$ close to the electrode surface is given by:

$$H(\theta, \xi) = \frac{1}{2}\left[\sum_{i=1}^{i=n} \theta^{2i-1} H''_{2i-1}(0)\right]\xi^2 + \frac{1}{6}\left[\sum_{i=1}^{i=n} \theta^{2i-1} H'''_{2i-1}(0)\right]\xi^3 \tag{4-15}$$

and

$$F(\theta,\xi)=\left[\sum_{i=1}^{i=n}\theta^{2i-1}F'_{2i-1}(0)\right]\xi+\frac{1}{2}\left[\sum_{i=1}^{i=n}\theta^{2i-1}F''_{2i-1}(0)\right]\xi^2 \tag{4-16}$$

and the dimensionless shear stress at the electrode surface is given by:

$$B(\theta)=\sum_{i=1}^{i=n}\theta^{2i-1}F'_{2i-1}(0) \tag{4-17}$$

The dimensionless shear stress derived by Barcia *et al.*,[19] Chin,[47] and Manohar[51,52] are plotted in Figure 4-2. Barcia and coworkers[19] solution is presented by a solid line, whereas those of Chin[47] and Manohar[51,52] are presented by dashed and dotted lines, respectively. Newman[52] obtained an expression for dimensionless shear stress by fitting a polynomial in θ to the results of Manohar.[51] It is rewritten as

$$B(\theta)=0.51023\theta-0.1808819\theta^3-0.04408\sin^3(\theta) \tag{4-18}$$

Newman[52] considered Manohar's[51] solution to be more accurate than that of Chin[47] for large angle θ. As seen in Figure 4-2, the $B(\theta)$ presented by dotted line has the lowest value of the at large angles.

The objective of the hydrodynamics calculations is to estimate the values of $F'_{2i-1}(0)$ and $H''_{2i-1}(0)$. These coefficients are used directly in the steady-state mass transfer, current distribution, and convective diffusion impedance calculations. The values of $F''_{2i-1}(0)$ and $H'''_{2i-1}(0)$[53] are obtained by substituting boundary conditions. They are given by

$$F''_{2i-1}(0)=\frac{-1^i 2^{2i-2}}{(2i-1)!} \tag{4-19}$$

$$H'''_{2i-1}(0)=\begin{cases}2 & \text{if } i=1\\ 3\frac{-1^{i+1}2^{2i-3}}{(2i-2)!} & \text{if } i>1\end{cases} \tag{4-20}$$

The values of $F''_{2i-1}(0)$ and $H'''_{2i-1}(0)$ are determined from above equation, whereas, coefficient expressions $F'_{2i-1}(0)$ and $H''_{2i-1}(0)$ are obtained from the numerical solution of governing equations describing the boundary-layer hydrodynamic model.

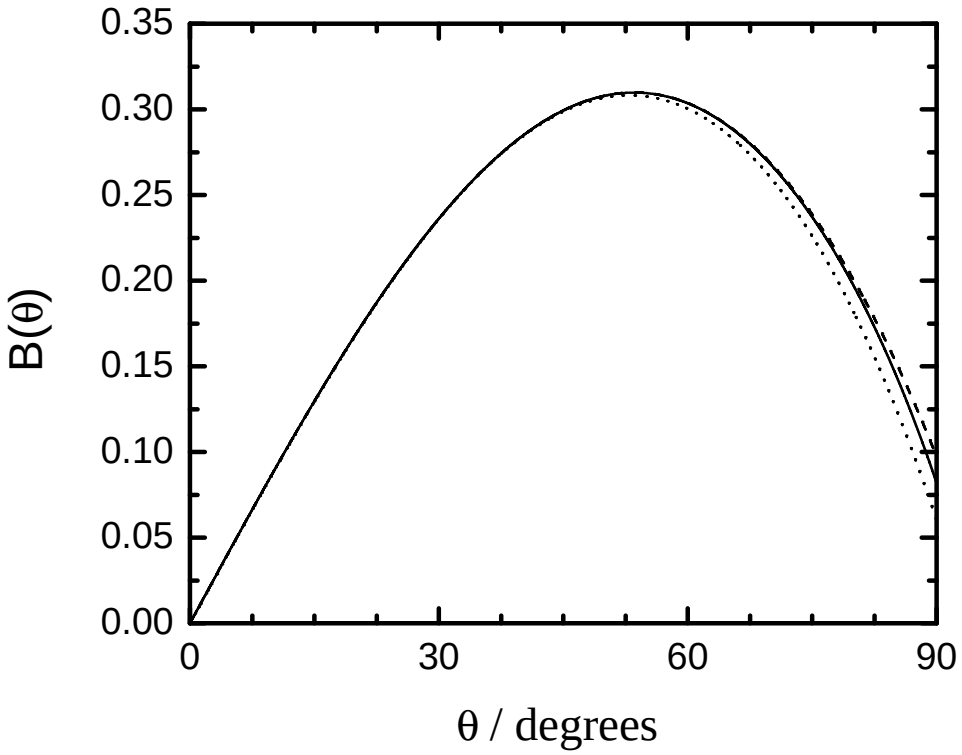

Figure 4-2: Shear Stress Distribution at the electrode surface. Solid line represent results of Barcia *et al.* , the dashed line represent the results of Chin , and the dotted line represent the result of Manohar.

4.2.2 Results

Barcia *et al.*[19] solved the ordinary differential equations for hydrodynamics with $n = 10$ using BAND[39,23] algorithm. They showed that their calculations were in agreement with that of Chin[17,47] for $n = 4$. However, it was found that the substitution of $F'_{2i-1}(0)$ in the continuity equations for $i > 4$ does not yield the reported values[19] of $\frac{1}{2}H''_{2i-1}(0)$. For example, the value of $\frac{1}{2}H''_{9}(0)$ is reported as 0.30978×10^{-3}, whereas continuity equation yields a value of -0.20763×10^{-3}. The error in the values of coefficients will have a larger implication in estimation of mass-transfer-limited current and convective-diffusion impedance. It is assumed in this work that the values of coefficients $F'_{2i-1}(0)$ reported Barcia *et al.*[19] are sufficiently accurate. The corresponding values of $\frac{1}{2}H''_{2i-1}(0)$ are calculated from continuity equations. They are tabulated in Table 4.1. In comparing the values of $\frac{1}{2}H''_{2i-1}(0)$ from Table 4.1, it is observed that the values differ for $n > 5$ than that of

Table 4.1: $F'_{2i-1}(0)$ and $H''_{2i-1}(0)$ coefficients in the series expansion of equations (4-16) and (4-15) for $H(\theta,\xi)$ and $F(\theta,\xi)$ at $\xi = 0$. The third column in the table lists the values reported by Barcia *et al.* and the fourth column lists the values calculated using the continuity equation.

i	$F'_{2i-1}(0)$	$\frac{1}{2}H''_{2i-1}(0)$ reported by Barcia *et al.*,[19]	$\frac{1}{2}H''_{2i-1}(0)$
1	0.51023	-0.51023	-0.51023
2	-0.22128	0.52761	0.52760
3	0.20711E-1	-0.93344E-1	-0.93344E-1
4	-0.18905E-2	0.90951E-2	0.90951E-2
5	-0.11499E-4	0.30978E-3	-0.20763E-3
6	-0.41534E-4	0.21299E-3	0.23024E-3
7	-0.11468E-4	0.70451E-4	0.71604E-4
8	-0.18727E-5	0.12325E-4	0.12434E-4
9	-0.89351E-6	0.75296E-5	0.75405E-5
10	-0.21900E-6	0.20009E-5	0.20020E-5

Barcia's *et al.*[19]

4.2.3 Fluid Flow at the Corner

The fluid motion of at the corner *i.e.*, at the intersection of hemispherical electrode and insulating plane, is discussed here. Existing literature has overlooked this detail. The problem has been ignored in the literature, however, there may be some compelling implication of this issue. For example, Stewartson[49] suggested that boundary layer equations are not valid within $O(\nu^{1/2})$ distance of the equator. This would mean that for aqueous electrolytes the distance would be $O(0.1\mathrm{cm})$, which represents a considerable portion of a $O(0.635\mathrm{cm})$ diameter electrode. On other hand, Nisançiöglu[18] suggested that the thickness of the region where boundary layer fails is of the order of $O\left(\frac{1}{\mathrm{Re}}\right)$ where Reynolds number Re is defined as

$$\mathrm{Re} = \frac{\omega r_0^2}{\nu} \tag{4-21}$$

Thus, the thickness of the region can be reduced by high rotation speed of the electrode. It is important to note that Nisançiöglu's[18] as well as Stewartson's[49] statements are for rotating spherical electrodes. Fluid motion in RHE will be more

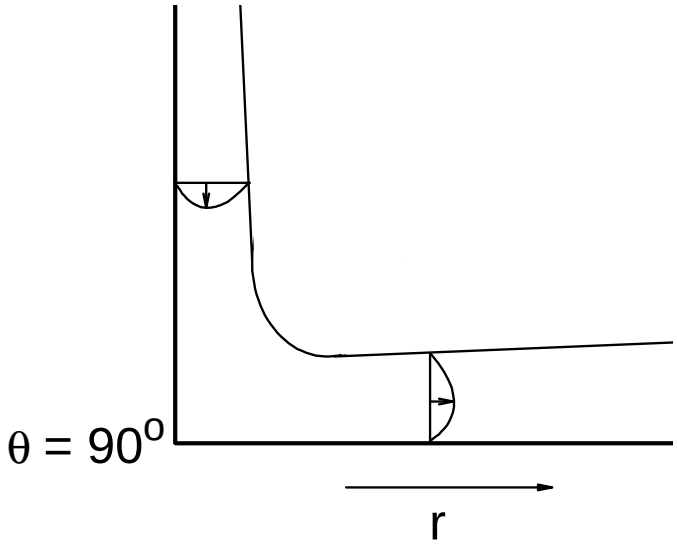

Figure 4-3: A two dimensional depiction of boundary layer at the intersection of electrode and insulating plane.

complicated than that that of rotating spherical electrode. A schematic representation of the fluid motion in the boundary layer near the corner is shown in Figure 4-3. As fluid moves along the boundary layer on the spherical surface of the electrode, it would encounter a 90.0° change in direction as it approaches the flat insulating plane where fluid will move along the plane in the outward r direction.

The bulk of aforementioned paragraph describes a rotating hemispherical electrode. However, for ease of operation, insulating plane can also rotate with the electrode. As a result, the fluid flow will be further accelerated along the insulating plane due to its rotation, causing the boundary layer at the corner to shrink. This problem requires further investigation, and it is suggested as future work.

4.3 Mass Transfer

The steady state convective-diffusion equation governing the mass transfer in the boundary layer can be written as

$$v_r \frac{\partial c_R}{\partial r} + \frac{v_\theta}{r_0} \frac{\partial c_R}{\partial \theta} = D_R \frac{\partial^2 c_R}{\partial r^2} \tag{4-22}$$

where c_R is the reacting species, v_r and v_θ are the radial and colatidute velocity components of fluid flow field with in the boundary layer, and D_R is the diffusivity

of the reacting species. The objective is to calculate the steady-state mass-transfer-limited current distribution at the electrode surface, utilizing the fluid velocity coefficients reported in this work. The boundary conditions for equation (4-22) are given as

$$c_R|_{r=r_0,\theta} = c_0 \tag{4-23}$$

$$c_R|_{r=\infty,\theta} = c_\infty \tag{4-24}$$

and

$$c_R|_{r,\theta=0} = c_\infty \tag{4-25}$$

As stated in Chapter 3, c_R can be expanded as a functions of θ, and ξ, and $\mathrm{Sc}^{-\frac{1}{3}}$ as :

$$\frac{c_R - c_\infty}{c_0 - c_\infty} = \sum_{i=1}^{n} \theta^{2i-2}\Phi_{1,2i-1}(\xi) + \mathrm{Sc}^{-\frac{1}{3}} \sum_{i=1}^{n} \theta^{2i-2}\Phi_{2,2i-1}(\xi) \tag{4-26}$$

such that the first term of the expansion provides the solution under the assumption that the Schmidt number(Sc) is infinitely large and the second term provides a correction for a finite value of Sc.

The characteristic dimensionless distance for mass transfer can be defined as

$$Z = \mathrm{Sc}^{1/3}\xi \tag{4-27}$$

which accounts for the difference in scale between the convection and mass transfer boundary layer thicknesses.

Ten coupled ordinary differential equations for $\Phi_{1,2i-1}$ and $\Phi_{2,2i-1}$ obtained by following steps:

1. Substitution of v_r and v_θ with dimensionless velocities $H(\theta,\xi)$ and $F(\theta,\xi)$ given by equations (4-15) and (4-16), respectively with $n = 10$.

2. Representing c_R with the dimensionless concentrations $\Phi_{1,2i-1}$ and $\Phi_{2,2i-1}$ given in equation (4-26).

Table 4.2: Calculated values for coefficients used in equation (4-29) for calculating mass-transfer-limited current distribution.

i	$\Phi'_{1,2i-1}(0)$	$\Phi'_{2,2i-1}(0)$
1	-0.62045	0.18490
2	0.12831	-0.43440E-1
3	0.34750E-2	-0.15360E-2
4	0.14694E-2	-0.55010E-3
5	0.35468E-3	-0.19855E-3
6	0.10783E-3	-0.56713E-4
7	0.34006E-4	-0.17257E-4
8	0.99642E-5	-0.60689E-5
9	0.32183E-5	-0.19643E-5
10	0.10249E-5	-0.66980E-6

3. Substitution of r with Z as given by equation (4-27).

4. The above three substitutions were made in equation (4-22). The terms corresponding to θ^{2i} and $\theta^{2i}\mathrm{Sc}^{-\frac{1}{3}}$ were collected to get the governing equations.

The obtained equations were solved using Newman's BAND[54] algorithm. The obtained results in the form of first derivatives of $\Phi_{1,2i-1}(Z)$ and $\Phi_{2,2i-1}(Z)$ at $Z = 0$ are tabulated in Table 4.2. The value of $\Phi'_{1,2i-1}(0)$ and $\Phi'_{2,2i-1}(0)$ are not in agreement with those calculated by Barcia *et al.*[19] for $i > 4$.

The concentration flux at the electrode surface is given by

$$N_R = - D_R \frac{\partial c_R}{\partial r}\bigg|_{r=r_0} \tag{4-28}$$

which can be evaluated in the form of a mass-transfer-limited current density in terms of the dimensionless variables introduced above as

$$i_{\lim}(\theta) = \frac{nF\,(c_\infty - c_0)\,D_R}{r_0}\mathrm{Sc}^{1/3}\mathrm{Re}^{1/2}\left[\sum_{i=1}^{n}\theta^{2i-2}\Phi'_{1,2i-1}(0) + \mathrm{Sc}^{-1/3}\left(\sum_{i=1}^{n}\theta^{2i-2}\Phi'_{2,2i-1}(0)\right)\right] \tag{4-29}$$

where the Reynolds number Re is defined to be

$$\mathrm{Re} = \frac{\omega r_0^2}{\nu} \tag{4-30}$$

Equation (4-29) can be expressed in terms of a characteristic number

$$N^* = -\frac{nF\left(c_\infty - c_0\right) D_R}{r_0}\mathrm{Sc}^{1/3}\mathrm{Re}^{1/2} \tag{4-31}$$

as

$$\frac{i_{\lim}(\theta)}{N^*} = \Psi(\theta) + \mathrm{Sc}^{-\frac{1}{3}}\Lambda(\theta) \tag{4-32}$$

where $\Psi(\theta)$ is the mass-transfer-limited current density for an infinite Schmidt number, and $\Lambda(\theta)$ is the correction to account for the finite value of the Schmidt number. Both $\Psi(\theta)$ and $\Lambda(\theta)$ are given by

$$\Psi(\theta) = -\sum_{i=1}^{n} \theta^{2i-2}\Phi'_{1,2i-1}(0) \tag{4-33}$$

and

$$\Lambda(\theta) = -\sum_{i=1}^{n} \theta^{2i-2}\Phi'_{2,2i-1}(0) \tag{4-34}$$

The calculated values for $\Psi(\theta)$ and $\Lambda(\theta)$ are presented in Figures 4.4(a) and 4.4(b), respectively, as functions of θ. The average of mass Transfer limited current is given by:

$$\frac{I_{\lim}}{N^*} = \int_0^{\frac{\pi}{2}} \Psi(\theta)\sin(\theta)d\theta + \mathrm{Sc}^{-\frac{1}{3}}\int_0^{\frac{\pi}{2}} \Lambda(\theta)\sin(\theta)d\theta \tag{4-35}$$

Upon integrating $\Psi(\theta)\sin(\theta)$ and $\Lambda(\theta)\sin(\theta)$ with respect θ, one obtains:

$$\frac{I_{\lim}}{N^*} = 0.45710\left(1 - 0.27896\mathrm{Sc}^{-\frac{1}{3}}\right) \tag{4-36}$$

whereas Barcia *et al.*,[19] reported $I_{\lim}$ as

$$\frac{I_{\lim}}{N^*} = 0.45636\left(1 - 0.28002\mathrm{Sc}^{-\frac{1}{3}}\right) \tag{4-37}$$

For $\mathrm{Sc} = 1000$, the relative error between the two expressions would be about 0.18%. A graph of relative error as a function of Sc number is presented in Figure 4-5. The relative error is minimum for infinite Sc number, and increase as value of Sc number is decreased.

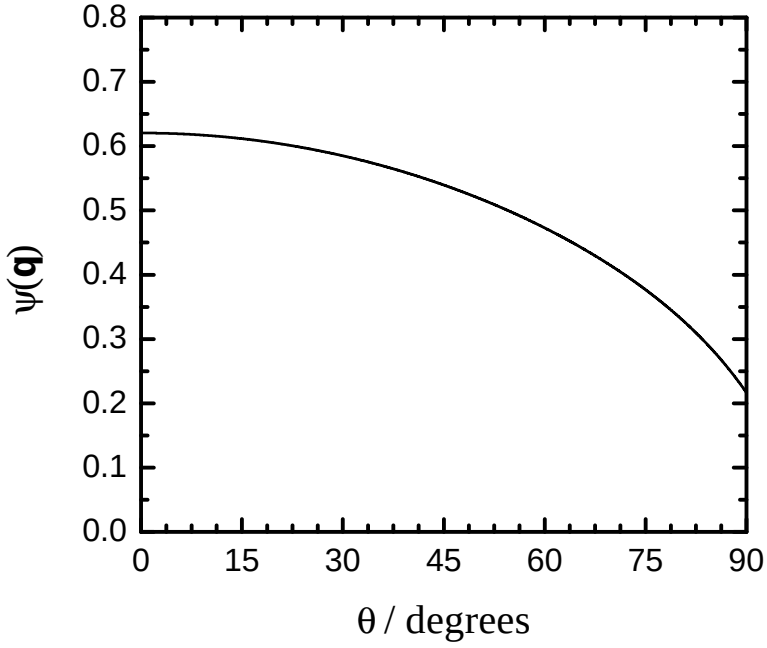

(a)

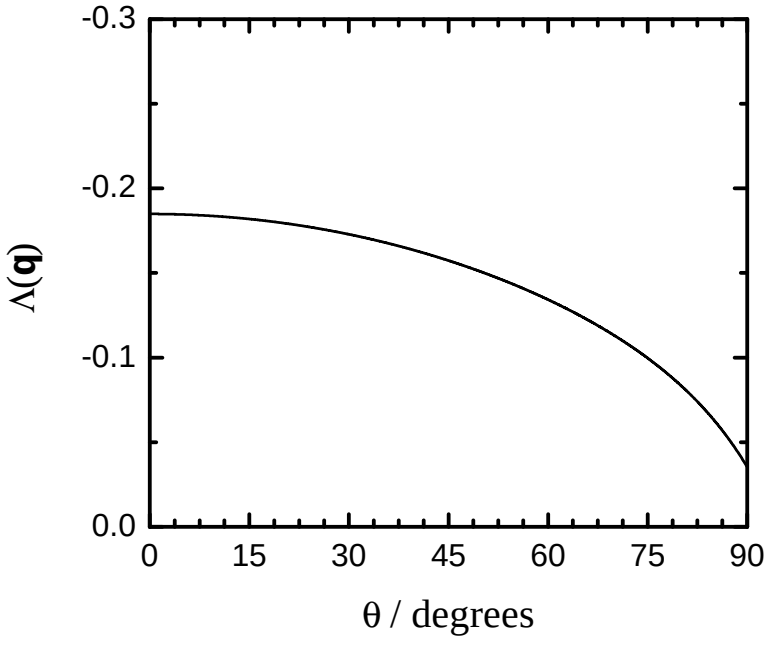

(b)

Figure 4-4: Calculated mass-transfer limited current density for a rotating hemispherical electrode. a) Contribution to equation (4-32) for an infinite Schmidt number; b) Contribution to equation (4-32) providing correction for a finite Schmidt number.

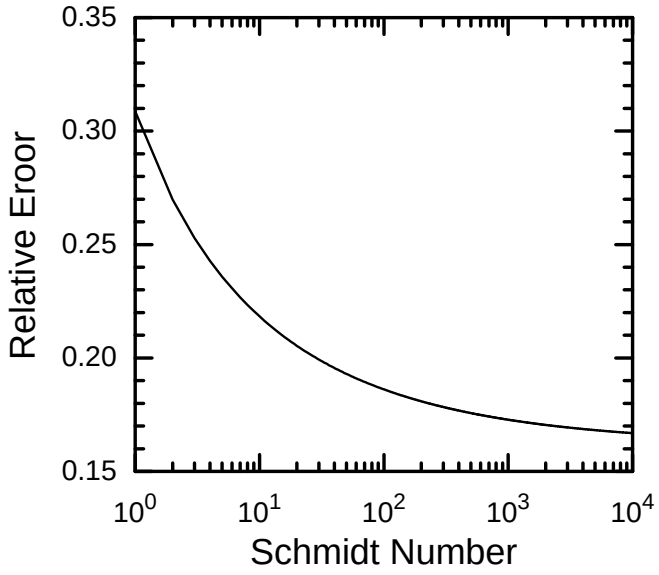

Figure 4-5: Relative error in mass-transfer-limited current given by expressions (4-36) and (4-37) as a function of Schmidt number.

4.4 Summary

Following Barcia and coworker,[19] the hydrodynamic and convective-diffusion models for a rotating hemispherical system was presented in this chapter. The second order radial velocity coefficients $H''_{2i-1}(0)$ were calculated such that residuals of the continuity equation at the electrode surface is equal to zero. The calculated velocity coefficients were then utilized to obtain an expression of mass-transfer limited current. The relative error in the mass-transfer-limited current presented in this chapter and to the one presented by Barcia and coworkers[19] is about 0.18% for a value of $\mathrm{Sc} = 1000$. An accurate development of convective-diffusion impedance can be achieved using the hydrodynamic model presented here.

CHAPTER 5
CURRENT AND POTENTIAL DISTRIBUTION AT AXISYMMETRIC ELECTRODES

In Chapters 2 and 3, hydrodynamic and convective diffusion models were developed for a stationary submerged hemispherical electrode under jet impingement. This chapter discusses the current and potential distribution of a stationary hemispherical electrode. The current distribution for a disk electrode was also calculated and compared to the hemispherical electrode results. The shear stress, obtained by the semi-analytical hydrodynamic model in Chapter 2, was used in the current distribution calculations for the stationary hemispherical electrode.

A generalized axisymmetric model for current distribution is developed in this chapter. The model can describe the current distribution for the disk and the hemispherical geometries. Calculations for a rotating hemisphere are also performed in this chapter. These calculations accounted for corrections in mass-transfer due to finite Schmidt number. The shear stress obtained in Chapter 4 was used in case of rotating hemispherical electrode system.

5.1 Introduction

Current distribution plays an essential role in electrochemical fabrication technologies and in interpretation of electrochemical processes.[55] Significant effort has been made on development of new rotating electrode designs to obtain the ideal balance between uniform current distributions, well-defined mass transfer, and ease of surface characterization.[56] The need to couple surface characterization with electrochemical measurements on uniform current distributions was addressed by Matlosz and coworkers*et al.*,[28] who used a removable disk electrode

inserted in a rotating hemispherical electrode. The flat disk was suitable for ex-situ surface analysis, and numerical simulations were used to identify conditions under which the influence of the flat surface on the current distribution could be neglected. Dinan *et al.*[30] proposed a recessed rotating disk electrode that would provide a uniform current distribution by compromising the uniform accessibility of the rotating disk.

The advantage of using a disk electrode under jet impingement is that, so long as the disk lies within the stagnation region of flow, an accurate solution is available for convective diffusion, and the current distribution is uniform under mass-transfer-limited conditions. The current and potential distribution on a disk electrode below the mass-transfer-limited current is not uniform,[5] and it has been shown that neglect of the nonuniform current distribution introduces error in estimation of kinetic parameters from steady-state measurements.[7–9] Similar errors are observed when impedance measurements are interpreted under the assumption of a uniform current distribution.[13,14]

Stationary electrodes are attractive because they can easily be adapted to use of in-situ observation or surface analysis techniques. The objective of this study was to understand the influence of fluid mechanics, convective-diffusion, and electric field below the mass-transfer-limited current for submerged stationary disk and hemispherical electrodes under jet impingement. The current distribution at the rotating hemispherical electrode was also explored. The calculations were accounted for the effect of finite Schmidt number on mass-transfer.

5.2 Development of Mathematical Model

A two-dimensional mathematical model describing current and potential distribution was developed for axisymmetric bodies in a curvilinear coordinate system. Examples of axisymmetric electrochemical systems are the disk and

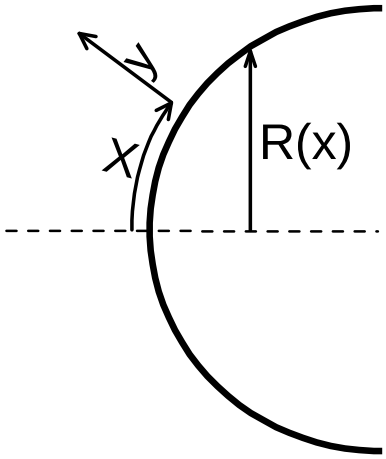

Figure 5-1: Schematics illustration of an axisymmetric body in a curvilinear coordinate system. The horizontal dash line represents the axis of symmetry, and the fluid field is assumed to be symmetric around this axis.

hemispherical electrodes with symmetric fluid flow field. A schematic representation of an axisymmetric system in curvilinear coordinates is illustrated in Figure 5-1. The geometry of the axisymmetric bodies can be described by x, y, and $R(x)$ where x is an arc length measured along a meridian section from point of stagnation , y is perpendicular to surface, and $R(x)$ is the radius of the section of the body perpendicular to its axis of symmetry. In this development, the fluid flow field is assumed to be symmetric with respect to the y axis at $x = 0$.

5.2.1 Hydrodynamics

The velocity components of the fluid field in the boundary layer are given by v_x and v_y. v_x is assumed to be known and is represented as

$$v_x = \beta(x)y \tag{5-1}$$

where $\beta(x)$ is the tangential shear stress, obtained by solving the Navier-Stokes equations along with the continuity equation. The continuity equation for incompressible fluid within the boundary layer of axisymmetric flow can be represented by

$$\frac{1}{R(x)}\frac{\partial(R(x)v_x)}{\partial x} + \frac{\partial v_y}{\partial y} = 0 \tag{5-2}$$

Substitution of v_x from equation (5-1) into equation (5-2) yields the following expression for v_y.

$$v_y = -\frac{1}{2}y^2 \frac{1}{R(x)} \frac{d\beta(x)R(x)}{dx} \tag{5-3}$$

Hence, v_x and v_y can be expressed in terms of tangential shear stress in curvilinear coordinates as presented by equations (5-1) and (5-3), respectively.

5.2.2 Mass Transfer

The convective diffusion equation in the curvilinear coordinate system within the boundary layer can be written as:

$$v_x \frac{\partial c_R}{\partial x} + v_y \frac{\partial c_R}{\partial y} = D_R \frac{\partial^2 c_R}{\partial x^2} \tag{5-4}$$

where c_R is the concentration of reacting species, and D_R is the diffusivity of the reacting species. Equation (5-4) is valid under the following assumptions.

1. The Peclet number is large and diffusion in the y direction can be neglected.
2. Concentration of the reactant c_R is small with respect to the supporting electrolyte. As a result, the migration of c_R due to the electric field is negligible.

The objective here is to solve equation (5-4) along with the following boundary conditions:

$$c_R = c_R(\mathrm{x}) \qquad \mathtt{at} \qquad y = 0 \tag{5-5}$$

and

$$c_R = c_\infty \qquad \mathtt{at} \qquad y \to \infty \tag{5-6}$$

where c_∞ is the bulk concentration of c_R. However, it is convenient to solve equation (5-4) using the Lighthill transformation[57] and then transforming the solution for boundary conditions (5-5) and (5-6). The boundary conditions for Lighthill transformations are given as

$$c_R = c_0 \qquad \mathtt{at} \qquad y = 0 \tag{5-7}$$

where c_0 is the uniform surface concentration of the reactant along the electrode surface,

$$c_R = c_\infty \qquad \texttt{at} \qquad y \to \infty \tag{5-8}$$

and

$$c_R = c_\infty \qquad \texttt{at} \qquad x = 0 \tag{5-9}$$

The solution of equation (5-4) using the Lighthill's transformation can be represented by

$$N(x) = \frac{D_R c_\infty \sqrt{R(x)\beta(x)}}{\Gamma\left(\frac{4}{3}\right)\left(9D_R \int_0^x R(x)\sqrt{R(x)\beta(x)}dx\right)^{1/3}} \tag{5-10}$$

where $N(x)$ is flux of the reactant to the electrode. The corresponding mass transfer limited current is given by

$$i(x) = \frac{nFD_R\left(c_\infty - c_0\right)}{(1-t_R)s_R\Gamma\left(\frac{4}{3}\right)} \frac{\sqrt{R(x)\beta(x)}}{\left(9D_R \int_0^x R(x)\sqrt{R(x)\beta(x)}dx\right)^{1/3}} \tag{5-11}$$

where F is the Faraday's constant, n is the number of electrons taking part in the reduction of reactant, t_R is the transference number of the species, and s_R is the stoichiometric coefficient of the reactant.

Duhamel's theorem[58] was used to transform equation (5-11) for nonuniform surface concentration given by equation (5-5) and bulk concentration condition given by equation (5-6). The resulting integral equation can be expressed as

$$i(x) = \frac{-nFD_R\sqrt{R(x)\beta(x)}}{(1-t_+)s_R\Gamma\left(\frac{4}{3}\right)} \left[\int_0^x \left.\frac{dc(x)}{dx}\right|_{x=x_0} \frac{dx_0}{\left(9D_R \int_0^x R(x)\sqrt{R(x)\beta(x)}dx\right)^{1/3}} + \frac{\left(c_R(x=0) - c_\infty\right)}{\left(9D_R \int_0^x R(x)\sqrt{R(x)\beta(x)}dx\right)^{1/3}}\right] \tag{5-12}$$

Equation (5-12) provides a solution of the mass transfer to the electrode under nonuniform surface concentration. This approach has several advantages, which will be elucidated later.

5.2.3 Electrode Kinetics

The current generated due to electrode-reactant charge transfer can be described empirically by the Butler-Volmer equation. This equation relates the surface overpotential η_s to the current by

$$i(x) = i_0 \left(\frac{c_R(x)}{c_\infty}\right)^\gamma \left[exp\left(\frac{\alpha_a z F \eta_s(x)}{RT}\right) - exp\left(-\frac{\alpha_c z F \eta_s(x)}{RT}\right)\right] \tag{5-13}$$

where i_0 is the exchange current density for the bulk concentration of the reactant, α_a and α_c are the anodic and cathodic charge transfer coefficients, respectively, R is the gas constant, T is the temperature of the system, and $Z = -z_+ z_- / (z_+ - z_-)$ for a binary salt, and $Z = -n$ for a reactant with excess supporting electrolyte. The term $\left(\frac{c_R(x)}{c_\infty}\right)^\gamma$ provides a correction to the exchange current density for surface concentration of the reactant, where the constant γ depends on the kinetic mechanism of the reaction.

5.2.4 Concentration Overpotential

The concentration gradient across the mass-transfer boundary layer leads to a concentration overpotential. A general form of concentration overpotential can be expressed as

$$\eta_c(x) = \frac{RT}{ZF}\left[\ln\left(\frac{c_R(x)}{c_\infty}\right) + t_R\left(1 - \frac{c_R(x)}{c_\infty}\right)\right] \tag{5-14}$$

where $\eta_c(x)$ is the concentration overpotential as a function of x. In the development of equation (5-14), the concentration variation is assumed to be linear within the diffusion layer. Furthermore, the conductivity variations of electrolyte are negligible.

5.2.5 Solution Potential in Outer Region

If there are no concentration variation and electrolyte is electrically neutral, the potential of the solutions in the diffuse part of the solution can be described by Laplace's equation

$$\nabla^2 \Phi = 0 \tag{5-15}$$

and the current flowing in the electrolyte solution is given by

$$i = -\kappa \nabla \Phi \tag{5-16}$$

where κ is the electrical conductivity of the electrolyte. Under steady state, the current calculated from equation (5-16) would balance the current from electrode kinetics and mass-transport. A solution of equation (5-14) for the disk and hemispherical geometries is discussed in the following sections.

Disk Electrode A disk electrode of radius r_0 embedded in infinitely large insulating plane is considered here. The potential far from the disk can be assumed to be equal to zero, *i.e.,*

$$\Phi = 0 \qquad \texttt{at} \qquad \mathrm{z}^2 + \mathrm{r}^2 \rightarrow \infty \tag{5-17}$$

where z and r are the axial and cylindrical coordinates, respectively. The current on the insulating plane is equal to zero, hence, equation (5-16) yields

$$\frac{\partial \Phi}{\partial z} = 0 \qquad \texttt{at} \qquad z = 0,\ r > r_0 \tag{5-18}$$

The solution of Laplace's equation satisfying above boundary conditions can be expressed in the rotational elliptical coordinate system. The coordinate system is defined as

$$z = r_0 \zeta \eta, \qquad r = r_0 \sqrt{(1+\zeta^2)\,(1-\eta^2)}$$

where ζ and η are the coordinate axes for the rotational elliptical system. The local potential of the solution potential in rotational elliptical coordinate system can be

expressed by

$$\Phi = \frac{RT}{ZF} \sum_{n=0}^{\infty} B_n P_{2n}(\eta)\, M_{2n}(\zeta) \tag{5-19}$$

In the absence of concentration variation, the potential Φ is related to current density i according to equation (5-16); hence, the current at the electrode can also be given by

$$i = -\kappa \left.\frac{\partial \Phi}{\partial z}\right|_{z=0} = -\frac{\kappa}{r_0 \eta} \left.\frac{\partial \Phi}{\partial \zeta}\right|_{\zeta=0} = -\frac{\kappa RT}{r_0 \eta ZF} \sum_{n=0}^{\infty} B_n P_{2n}(\eta)\, M'_{2n}(0) \tag{5-20}$$

The coefficient B_n are calculated by applying the orthogonality property of Legendre polynomials. Thus,

$$B_n = \frac{r_0 ZF}{\kappa M_{2n}{}'(0) RT} \int_0^1 i(\eta) P_{2n}(\eta) \eta d\eta \tag{5-21}$$

An explicit expression for local solution potential as a function of position is obtained by substitution of B_n into equation (5-19).

Hemispherical Electrode A hemispherical electrode of radius r_0 embedded in a infinitely insulating plane is considered here. Spherical polar coordinates adequately describe the system. The potential far away from the electrode can be assumed to be equal to zero. Thus, the potential boundary condition at $r \to \infty$ is given by

$$\Phi = 0 \tag{5-22}$$

The current at the insulating plane is equal to zero; hence

$$\frac{\partial \Phi}{\partial \theta} = 0 \qquad \texttt{at} \qquad \theta = \frac{\pi}{2} \tag{5-23}$$

The above condition will also be valid at $\theta = 0$ to satisfy the condition of symmetry.

The solution of Laplace's equation (5-15), subjected to boundary conditions (5-22) and (5-23), can be expressed as

$$\Phi = \frac{RT}{ZF} \sum_{n=0}^{\infty} B_n\, P_{2n}(\cos\theta) \left(\frac{r_0}{r}\right)^{2n+1} \tag{5-24}$$

Application of equation (5-16) relates the current at the electrode to the potential according to

$$i(\theta) = -\kappa \frac{\partial \Phi}{\partial r}\bigg|_{r=r_0} = \frac{\kappa r_0 ZF}{RT} \sum_{n=0}^{\infty} B_n \, P_{2n}(\cos\theta) \left(\frac{r_0}{r}\right)^{2n+1} \tag{5-25}$$

and the coefficient B_n are obtained by applying the orthogonality property of Legendre polynomials. Thus, the expression for B_n is given by

$$B_n = -\frac{ZF}{RT} \frac{(4n+1)}{(2n+1)} \int_0^{\frac{\pi}{2}} i(\theta) P_{2n}(\cos\theta) \sin\theta d\theta \tag{5-26}$$

An explicit expression for local solution potential as a function of position is obtained by substitution of B_n in equation (5-24).

5.2.6 Electrode Potential

The electrode potential V with respect to a reference electrode can be partitioned as

$$V - \Phi_{ref} = \eta_s + \eta_c + \Phi_0 \tag{5-27}$$

where Φ_{ref} is the potential of a reference electrode, Φ_0 is the solution potential near the electrode surface, η_s and η_c are the surface and concentration potentials, respectively. Under the assumption that the thickness of the diffuse layer is negligible, Φ_0 can be assumed to be the electrolyte solution potential along the electrode surface.

5.3 Dimensionless Quantities

The disk electrode can be easily described in cylindrical coordinates. The curvilinear coordinate relates to the cylindrical coordinate system through the following equations:

$$x = r, \qquad y = z, \qquad R(x) = r$$

where r and z are the cylindrical coordinate axes. The dimensionless shear stress $\beta(x)$ is given by

$$\beta(\mathtt{x}) = \beta(r) = c_h \frac{a_h^{3/2}}{\nu^{1/2}} r \tag{5-28}$$

where c_h is a constant, obtained by solving the Navier-Stokes and the Continuity equations for the disk electrode, and a_h is the hydrodynamic constant. For the rotating disk electrode, a_h is replaced by disk rotation speed, ω. The value of c_h is 0.51023 for a rotating disk electrode, and 0.36023 for a disk electrode under submerged jet impingement.

After substitution of above quantities in equation (5-12), an expression for current at the disk electrode is given as

$$i_{disk}(r) = \frac{-nFD\left(3c_h\right)^{1/3}}{(1-t_R)s_R\Gamma\left(\frac{4}{3}\right)}\left(\frac{\nu}{9D}\right)^{1/3}\sqrt{\frac{a_h}{\nu}}\left[r\int_0^r \left.\frac{dc(r)}{dr}\right|_{r=x}\frac{dr}{\left(r^3-x^3\right)^{1/3}} + \left(c_\infty - c_R(0)\right)\right] \tag{5-29}$$

A dimensionless current i^*_{disk}, along with a dimensionless concentration and parameter N are given by the following

$$i* = \frac{ir_0ZF}{\kappa RT} \tag{5-30}$$

$$C(\mathtt{x}) = \frac{c_R(\mathtt{x})}{c_\infty} \tag{5-31}$$

$$N = -\frac{nZF^2Dc_\infty}{RT\kappa(1-t_+)}\sqrt{\frac{r_0^2a_h}{\nu}}\left(\frac{\nu}{9D_R}\right)^{1/3} \tag{5-32}$$

where N is measure of the mass-transfer resistance to the ohmic resistance.

After substitution of above quantities into equation (5-29), the dimensionless current at the disk electrode can be written as

$$i^*_{disk}(r) = \frac{N\left(3c_h\right)^{1/3}}{\Gamma\left(\frac{4}{3}\right)}\left[r\int_0^r \left.\frac{dC}{dr}\right|_{r=x}\frac{dx}{\left(r^3-x^3\right)^{1/3}} + \left(C(0)-1\right)\right] \tag{5-33}$$

Equation (5-33) provides a convenient method to calculate the at the disk electrode surface by specifying parameter N and surface concentration distribution.

For the hemispherical electrode system, the curvilinear coordinates x, y, and $R(x)$ are related to the spherical-polar coordinates by

$$x = r\theta, \qquad y = r, \qquad R(x) = r_0 \sin\theta$$

and the corresponding shear stress $\beta(x)$ is expressed as

$$\beta(x) = \beta(\theta) = \frac{a_h^{3/2} r_0}{\nu^{1/2}} B(\theta) \tag{5-34}$$

An analytical expression of $B(\theta)$ for stationary hemispherical electrode under jet impingement has been obtained in Chapter 2. Similarly, $B(\theta)$ for the rotating hemispherical electrode has been derived in Chapter 4. After substitution of above coordinate relationships and dimensionless quantities i^*, C, and N into equation (5-12), an expression for dimensionless current is given by:

$$i^*_{hemisphere}(\theta) = \frac{N\sqrt{\sin\theta B(\theta)}}{\Gamma\left(\frac{4}{3}\right)} \left[\int_0^{\theta} \left.\frac{dC}{dx}\right|_{\theta=\theta_0} \frac{d\theta_0}{\left(\int_{\theta_0}^{\theta} \sin\theta \sqrt{\sin\theta B(\theta)}\, d\theta\right)^{1/3}} + \frac{(C(0)-1)}{\left(\int_0^{\theta} \sin\theta \sqrt{\sin\theta B(\theta)}\, d\theta\right)^{1/3}} \right] \tag{5-35}$$

Equation (5-35) provides a convenient way to calculate the current distribution for a given surface concentration distribution at the hemispherical electrode. Equations (5-33) and (5-35) can also used to calculate surface concentration distribution for a given current distribution at the electrode surface.

The dimensionless quantities J, E_s, E_c, and E are defined as:

$$J = \frac{i_0 r_0 ZF}{RT\kappa}, \qquad E_s = \frac{ZF\eta_s}{RT}, \qquad E_c = \frac{ZF\eta_c}{RT}, \qquad E = E_s + E_c$$

where J represents the ratio of ohmic resistance of electrolyte to kinetic resistance, E_s is the dimensionless surface overpotential, E_c is the dimensionless

concentration overpotential, and E is the total dimensionless overpotential. With the introduction of above mentioned dimensionless quantities, equation (5-14) for concentration overpotential and equation (5-13) for electrode kinetics can be as rewritten as

$$E_c(x) = E(x) - E_s(x) = \log(C(x)) + t_R(1 - C(x)) \tag{5-36}$$

and

$$i^*(x) = JC^{\gamma}\left[\exp\left(\alpha_a E_s\right) - \exp\left(-\alpha_c E_s\right)\right] \tag{5-37}$$

respectively. Equations (5-36) and (5-37) can be combined to eliminate the surface overpotential E_s. The resulting equation can be expressed as following

$$i^*(x) = J\left[C^{(\gamma-\alpha_a)}\exp\left(\alpha_a E - \alpha_a t_R\left(1-C\right)\right) - C^{(\gamma+\alpha_c)}\exp\left(-\alpha_c E + \alpha_c t_R\left(1-C\right)\right)\right] \tag{5-38}$$

Equation (5-38) provides a convenient way to calculate current distribution. Its usefulness will be elucidated in the subsequent section.

The dimensionless solution potential is defined as

$$\Phi^* = \frac{ZF\Phi}{RT} \tag{5-39}$$

Equation (5-19) can be recast using the dimensionless solution potential as

$$\Phi^* = \sum_{n=0}^{\infty} B_n P_{2n}\left(\eta\right) M_{2n}\left(\zeta\right) \tag{5-40}$$

where coefficients B_n are defined in terms of dimensionless current distribution i^*_{disk} as

$$B_n = \frac{1}{M_{2n}{}'(0)} \int_0^1 i^*_{disk}(\eta) P_{2n}(\eta)\eta d\eta \tag{5-41}$$

Similarly, dimensionless solution potential for hemispherical electrode can be expressed as

$$\Phi^* = \sum_{n=0}^{\infty} B_n\, P_{2n}(\cos\theta)\left(\frac{r_0}{r}\right)^{2n+1} \tag{5-42}$$

where coefficients B_n are defined in terms of dimensionless current distribution $i^*_{hemisphere}$ as

$$B_n = -\frac{4n+1}{2n+1}\int_0^{\frac{\pi}{2}} i^*_{hemisphere}(\theta)P_{2n}(\cos\theta)\sin\theta d\theta \tag{5-43}$$

and the dimensionless electrode potential V^* can be expressed by

$$V^* = E_s + E_c + \Phi^*_0 \tag{5-44}$$

The objective is to obtain the current profile below the mass-transfer-limited current. This involves a simultaneous solution of mass-transport, electrode kinetics, and calculation of electric field in the electrolyte. The dimensionless form of governing equations describing mass-transport, electrode kinetics, and solution potential provide a convenient way to calculate the current distribution. The dimensionless parameter J and N are the only variables present in the dimensionless form of the governing equations. Therefore, by altering J and N, a current distribution profile can be obtained for the disk and the hemispherical electrode.

5.4 Calculation Procedure

The Algorithm for calculating the current and potential distribution is outlined. The procedure presented is applicable for submerged electrode systems under jet impingement. The calculation procedure for disk electrode is presented first. Since the hydrodynamic model predicts the separation of boundary layer at the hemispherical electrode, a modified algorithm is presented in the subsequent subsection. The mathematical model was programmed using FORTRAN with double precision accuracy. The program listing is given in Appendix E.

5.4.1 Disk electrode

The following procedure calculated the current distribution at the disk electrode.

1. Values of J and N were assigned, and C was assumed to have a value between 0.0 and 1.0 at the center of the disk. Alternatively, values of electrode potential or current level can also be chosen. This adds an extra step in the calculation procedure, which iterates on the $C(0)$ at the center of the electrode.

2. The r/r_0 domain was discretized in irregularly spaced grid as outlined by Acrivos *et al.*[59]

3. The value of current at $r = 0$ was calculated by

$$i^*_{disk}(0) = -\frac{1.57886437117488\,(1 - C(0))\,N}{\Gamma\left(\frac{4}{3}\right)} \tag{5-45}$$

   This expression was derived by taking the limit of equation (5-33) at $r = 0$.

4. The values of surface overpotential E_s and concentration overpotential E_c were calculated at $r/r_0 = 0$ using equations (5-36) and (5-37), respectively.

5. As an initial guess, the values of E_s, E_c, and i^*_{disk} along each point at the electrode surface were assumed to be the same as at $r/r_0 = 0$. The values $C(r/r_0)$ were obtained from equation (5-35) using the method devised by Acrivos *et al.*[59]

6. The current distribution was calculated using equation (5-38) in the discretized domain.

7. The coefficients B_n for solution potential were calculated from equation (5-43). The number of terms in the summation were limited to 51. Additional terms in equation (5-43) did not improve the calculated solution potential.

8. The solution potential adjacent to the electrode surface was obtained by equation (5-42).

9. The value of the electrode potential at $r/r_0 = 0$ was obtained using equation (5-44).

10. A new overpotential distribution E was calculated using

$$E(r/r_0) = E(r/r_0) + \lambda(V^*(0) - \Phi^*(0) - E(r/r_0)) \tag{5-46}$$

where λ can have a value between 0 and 1. In this procedure, a value of 0.05 was chosen.

11. The relative percentage difference of coefficient B_0 was used as termination criterion. The B_0 represent the average dimensionless current at the electrode surface. If $(B_{0,new} - B_{0,old})/B_{0,old}$ was found to be less than 1.0^{-6}, calculation was terminated; otherwise, the calculation procedure was repeated starting from step 6 to 10.

12. The calculated current, potential, and concentration distribution were written to the file.

5.4.2 Hemispherical electrode

The algorithm for hemispherical electrode required modification due to boundary layer separation. At the point of separation, the value of $B(\theta)$ is zero. The method devised by Acrivos *et al.*[59] predicts that the current will also be zero at the point of separation. However, the numerical difficulty can be avoided by terminating the calculations just before the point of separation. The current distribution calculations were performed up to 54.4°, just before the point of boundary layer separation predicted to occur at 54.8° by the boundary layer theory. The following modified procedure was used to calculate the current distribution at the hemispherical electrode.

1. Values of J and N were assigned, and C was assumed to have a value between 0.0 and 1.0 at $\theta = 0$. Values of electrode potential or current level can also be chosen. This adds an extra step in the calculation procedure, which iterates on the $C(0)$ at $\theta = 0$.

2. The θ domain was discretized from 0° to 54.4° in an irregularly spaced grid as outlined by Acrivos *et al.*[59]

3. The value of current at $\theta = 0$ was calculated by

$$i^*_{hemisphere}(0) = -\frac{1.57886437117488\,(1 - C(0))\,N}{\Gamma\left(\frac{4}{3}\right)} \tag{5-47}$$

   This expression was derived by taking the limit of equation (5-35) at $\theta = 0$.

4. The values of surface overpotential E_s and concentration overpotential E_c were calculated at $\theta = 0$ using equations (5-36) and (5-37), respectively.

5. As an initial guess, the values of E_s, E_c, $i^*_{hemisphere}$ at each node was assumed to be same as at $\theta = 0$. The concentration distribution was obtained using equation (5-35) with the method devised by Acrivos *et al.*[59]

6. The current distribution was obtained using equation (5-38) in the discretized domain. The current beyond the point of boundary layer separation was assumed to be uniformly constant, and was assigned the obtained value at $\theta = 54.4^0$.

7. The coefficients B_n for solution potential were calculated using equation (5-43). The number of terms in the summation were limited to 51.

8. The solution potential adjacent to the electrode surface was obtained using equation (5-42).

9. The value of the electrode potential was obtained from equation (5-44) at $\theta = 0$.

10. A new overpotential distribution $E(\theta)$ was calculated using

$$E(\theta) = E(\theta) + \lambda(V^*(0) - \Phi^*(0) - E(\theta)) \tag{5-48}$$

where λ can have a value between 0 and 1. In this procedure, a value of 0.02 was selected.

11. The relative percentage difference of coefficient B_0 was used as termination criterion. The B_0 represent the average dimensionless current at the electrode surface. If $(B_{0,new} - B_{0,old})/B_{0,old}$ was found to be less than 1.0^{-6}, calculations was terminated, otherwise, the calculation procedure was repeated starting from step 6 to 10.

5.5 Current Distribution at Disk Electrode

The primary, secondary, and tertiary current distribution at the disk electrode are presented in this section. The simulation results for current distribution below the mass-transfer-limited current are discussed below.

5.5.1 Primary Distribution

If concentrations are uniform and the electrode reactions are fast, then E_s and E_c can be set equal to zero in the governing equations. As a result, the solution potential adjacent to the electrode will be equal to the electrode metal potential and will have a uniform value. This condition is satisfied by equation (5-40) for $n = 0$, and the resulting distribution is the primary current and potential distribution. The solution potential Φ^P is given by

$$\Phi^P = \Phi_0^P \left(1 - \frac{2}{\pi} \tan^{-1} \zeta\right) \tag{5-49}$$

where Φ_0^P is the solution potential at the electrode surface. The superscript P stands for primary distribution. The current distribution at the disk surface was evaluated from equation (5-20)

$$i = -\kappa \left.\frac{\partial \Phi^P}{\partial z}\right|_{z=0} = \frac{2\kappa\Phi_0^P}{\pi\sqrt{r_0^2 - r^2}} \tag{5-50}$$

the total current is

$$I = 2\pi \int_0^{r_0} irdr = 4\kappa r_0 \Phi_0^P \tag{5-51}$$

and the resistance is

$$R^P = \frac{\Phi_0^P}{I^P} = \frac{1}{4\kappa r_0} \tag{5-52}$$

For convenience, equation (5-50) is recast in terms of average current as

$$\frac{i}{i_{avg}} = \frac{0.5}{\sqrt{1 - \left(\frac{r}{r_0}\right)^2}} \tag{5-53}$$

where the average current is defined to be

$$i_{avg} = \frac{I}{\pi r_0^2} = \frac{4\kappa\Phi_0^P}{\pi r_0} \tag{5-54}$$

A graph of i/i_{avg} as a function of r/r_0 is presented in Figure 5-2. The current is fairly well behaved near the center of the electrode, but it approaches infinity at the edge of the electrode. As a result, the primary current distribution is highly non-uniform for the disk electrode.

5.5.2 Secondary Current Distribution

A secondary current distribution is a outcome of the balance between electrode kinetic rate and Ohm's law. For this case, the Laplace's equation for solution potential is solved with the Butler-Volmer equation for electrode kinetics, which acts as a boundary condition for the current at the electrode surface. The current given by Ohm's law is equated to the current generated at the electrode surface due to charge-transfer reactions. The secondary current distribution at the disk electrode

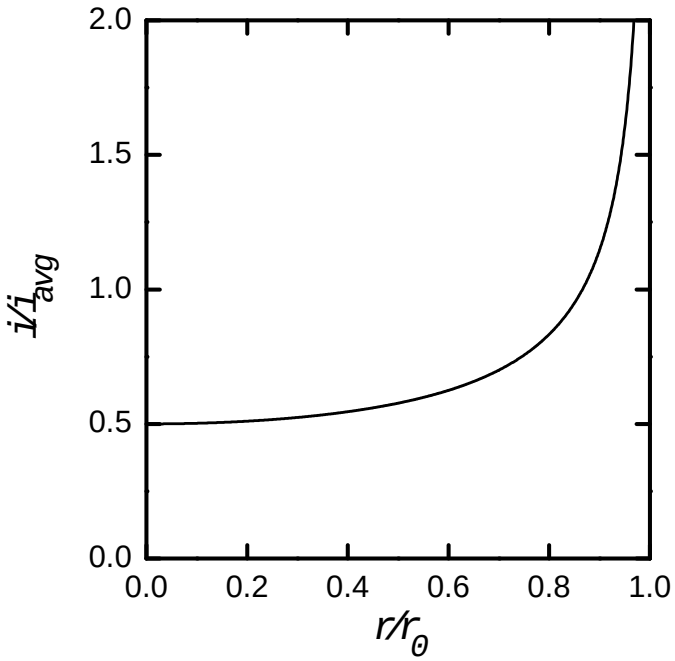

Figure 5-2: Primary current distribution at the disk electrode. The value of local current approaches to infinity as $r/r_0 \rightarrow 1$

has been discussed in detail by Newman.[23] The kinetics factor limits the value of current at the electrode edge. The final value of current distribution depends on the parameter J. Newman has shown that the current distribution becomes uniform at $J = 0.1$.

5.5.3 Tertiary Current Distribution

The current distribution below the mass-transfer-limited value was obtained at the disk electrode using the numerical algorithm presented in the previous section. The fluid mechanics coefficient c_h was used for the disk electrode under jet impingement. Numerical simulations were carried out for $J = 5$ and $N = 125$. The values of $C(0)$ were selected from 0.05 to 0.9. The values of α_a, α_c, γ, and t_R were kept fixed at 0.5. A plot of i/i_{lim} distribution is presented in Figure 5.3(a). The nonuniform behavior of the current can be seen as r/r_0 approaches 1.0. The current has a maximum value at $r/r_0 = 1$ for all $C(0)$ except at 0.5. For this condition, the maximum occurs before the periphery of the electrode. This observation is consistent with results reported by Durbha.[6] It can

be explained as following: As unreacted reactant material moves along the electro surface in the mass-transfer boundary layer, the concentration gradient, *i.e.*, $\partial C/\partial z$ builds up. This causes $\partial C/\partial z$ to be higher before the periphery. Therefore, a maximum in current is seen before $r/r_0 = 1$. The dimensionless concentration of the reactant at the electrode surface as a function of r/r_0 is presented in Figure 5.3(b). The dimensionless solution potential Φ_0^* is plotted in Figure 5.3(c). The solution potential distribution becomes uniform for $C(0)$ =0.9.

A parallel set of current distribution calculations for $C(0) =$ 0.4, 0.3, 0.2, 0.1, and 0.05 are presented in Figure 5.4(a). The corresponding concentration distribution is shown in Figure 5.4(b). The dimensionless solution potential along the electrode surface is presented in Figure 5.4(c).

The following expression was used to quantify the uniformity of current distribution

$$\Upsilon_{disk} = \sqrt{\frac{\int_0^{r_0} \left(\frac{i}{i_{r=0}} - 1\right)^2 r dr}{\int_0^{r_0} r dr}} \tag{5-55}$$

where Υ_{disk} represents the uniformity parameter for current distribution at the disk electrode. The quantity Υ_{disk} was calculated for the current distribution described in Figures 5-3 and 5-4. The obtained values are listed in Table 5.1. The value of Υ_{disk} is minimum for $C(0)$ equal to 0.05, and maximum for 0.7. The values of i_{avg}/i_{lim} and $i_{r=0}/i_{lim}$ are also given in Table 5.1. A graph of $1 - i_{r=0}/i_{lim}$ as a function of Υ_{disk} for different value of $C(0)$ is presented in Figure 5-5. This plot shows a monotonically increasing relationship between $1 - i_{r=0}/i_{lim}$ and Υ_{disk} up to $C(0) = 0.7$. The ratio i/i_{avg} as a function of r/r_0 for different values of $C(0)$ is presented in Figure 5-6. The current distribution is most uniform for $C(0) =$ 0.05 as seen in Figure 5-6, and the average current is about 98.9% of mass-transfer-limited current. The Υ_{disk} is 0.021 for $C(0) = 0.05$. This value of Υ_{disk} is chosen

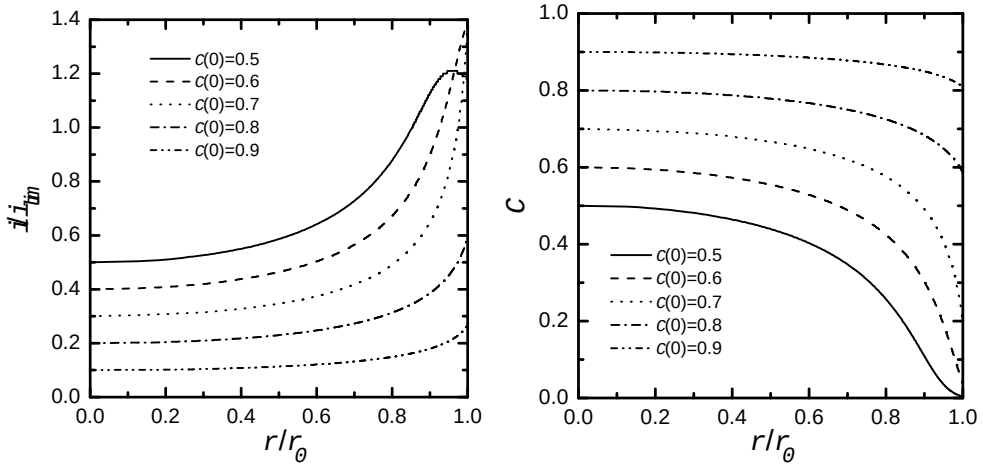

(a) (b)

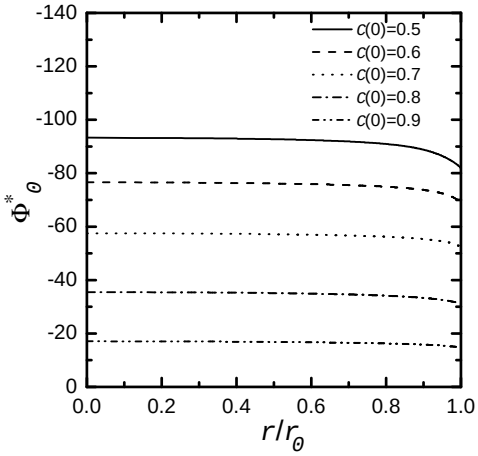

(c)

Figure 5-3: Calculated current, concentration, and solution potential distribution at the disk electrode. The simulations were done for $J = 5$, $N = 125$, and $C(0) =$ 0.5 to 0.9 in incremental steps of 0.1. a) i/i_{lim} as a function of r/r_0. b) Dimensionless concentration distribution as a function of r/r_0. c) Dimensionless solution potential at the electrode surface as a function of r/r_0.

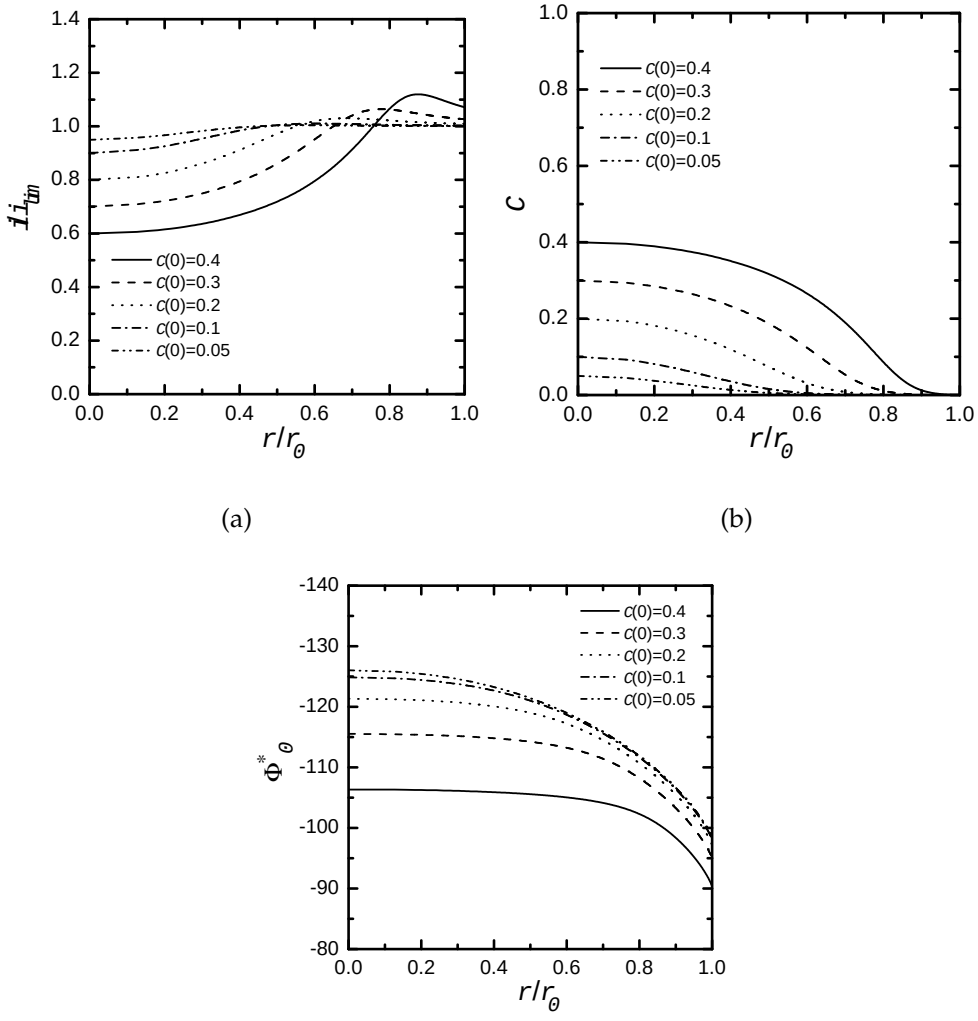

Figure 5-4: Calculated current, concentration, and solution potential distribution at the disk electrode. The simulations were done for $J = 5$, $N = 125$, and $C(0) =$ 0.4, 0.3, 0.2, 0.1, 0.05. a) i/i_{lim} as a function of r/r_0. b) Dimensionless concentration distribution as a function of r/r_0. c) Dimensionless solution potential at the electrode surface as a function of r/r_0.

Table 5.1: Calculated values for uniformity parameter Υ_{disk} (see equation (5-55)), i_{avg}/i_{lim}, and $i_{r=0}/i_{avg}$ for the current distributions presented in Figures 5-3 and 5-4. The values of J and N was 5 and 125, respectively.

$C(0)$	Υ_{disk}	i_{avg}/i_{lim}	$i_{r=0}/i_{avg}$
0.00	0.000	1.000	1.000
0.05	0.021	0.989	0.960
0.10	0.044	0.975	0.922
0.20	0.097	0.937	0.854
0.30	0.161	0.879	0.796
0.40	0.235	0.797	0.752
0.50	0.312	0.690	0.725
0.60	0.376	0.563	0.711
0.70	0.392	0.422	0.710
0.80	0.282	0.266	0.757
0.90	0.238	0.128	0.782

as condition of uniformity. Therefore, current distributions with Υ_{disk} <0.021 are uniform.

5.6 Current Distribution at Hemispherical Electrode

The primary, secondary, and tertiary current distribution at the stationary hemispherical electrode under submerged jet impingement are discussed in this section.

5.6.1 Primary Distribution

If no concentration variations exist in the system and reaction kinetics is not a limiting factor, the solution potential is a result of equation (5-24) equation for $n = 0$. It is given by

$$\Phi^P = \frac{\Phi_0^P r_0}{r} \tag{5-56}$$

and the current is given by

$$i = -\kappa \frac{\partial \Phi}{\partial r}\bigg|_{r=r_0} = \frac{\kappa \Phi_0^P}{r_0} \tag{5-57}$$

The total current to the hemisphere is expressed as

$$I = 2\pi\kappa r_0 \Phi_0^P \tag{5-58}$$

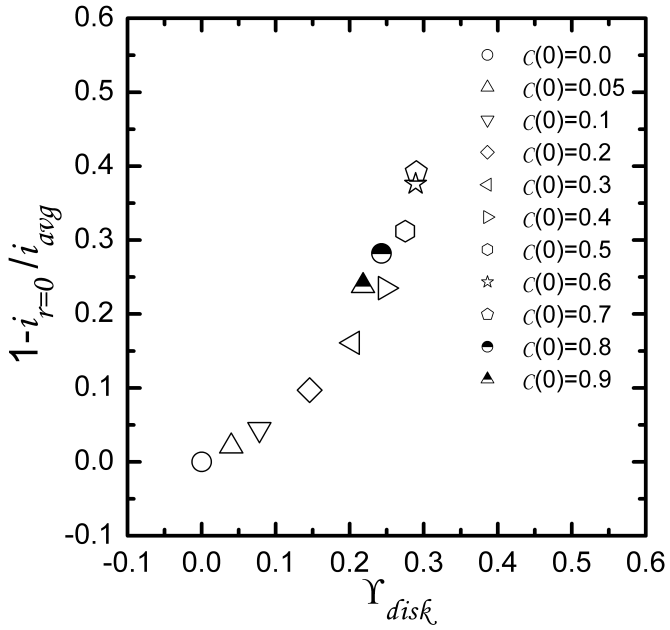

Figure 5-5: $1 - i_{r=0}/i_{avg}$ as a function Υ_{disk} for different values of $C(0)$.

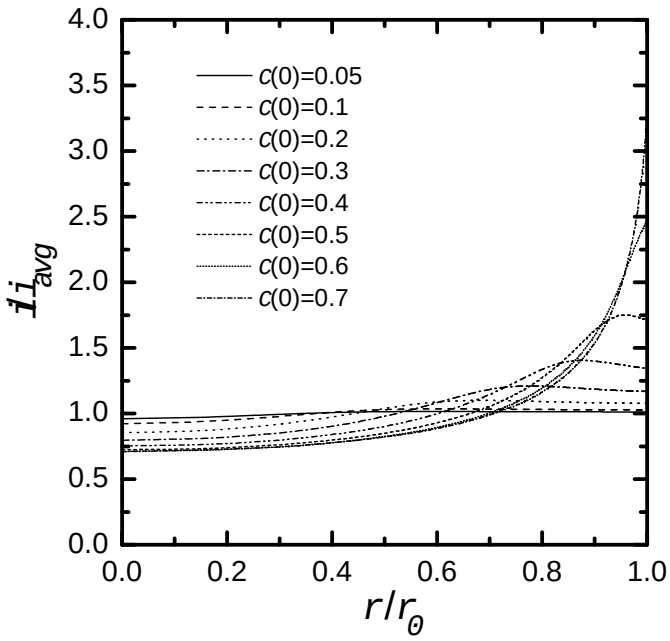

Figure 5-6: i/i_{avg} as a function r/r_0 for different values of $C(0)$.

Consequently, the resistance to the flow of current is

$$R_{sol}^{p} = \frac{\Phi_0^P}{I} = \frac{1}{2\pi\kappa r_0} \tag{5-59}$$

The R_{sol}^{p} provide a value of solution resistance to the current flow for the primary current distribution.

5.6.2 Secondary Distribution

When the rate of mass-transfer to the electrode is infinite, and slow electrode kinetics is taken into account, the resulting current calculation is called as secondary distribution. In the absence of mass-transfer resistance, the secondary current distribution in hemispherical geometry would yield a uniform current throughout the electrode surface. This can be easily deduced by solving the Butler-Volmer equation for the electrode kinetics with the Laplace's equation for the solution potential simultaneously.

5.6.3 Tertiary Distribution

The current distribution, dimensionless surface concentration, and solution potential below the mass-transfer limited conditions were obtained for the stationary hemispherical electrode under submerged jet impingement. Several simulations were carried out for various values J, N, and $C(0)$. The parameter $C(0)$ was varied between 0.5 and 0.9 in incremental steps of 0.1 for each value of J and N. The values of α_a, α_c, γ, and t_R were kept fixed at 0.5.

The calculated current distributions for four values of N (125, 50, 20, and 5), and $C(0) = 0.5$, 0.6, 0.7, 0.8, 0.9, and for a fixed value $J = 5$ are given in Figure 5.7(a). Comparison of Figures 5.7(a) to 5.7(d) show that the distribution of current becomes fairly uniform for the pole concentration of $C(0) = 0.9$. Simulation results in Figure 5.7(a) for $C(0) = 0.5$, 0.6, 0.7, and 0.8 display a maximum in current. The maximum is observed at the θ values between the pole and the point of boundary

layer separation. This feature of the current distribution starts to diminish as the value of N is changed to a lower quantity. Furthermore, the maximum in current disappears for $N = 5$ as shown in Figure 5.7(d).

The dimensionless concentration as a function of θ for parameters $J = 5$ and $N = 125$, 50, 20, and 5 are shown in Figure 5-8. The results correspond to the current distribution in Figure 5-7. The dimensionless solution potential along the electrode surface as a function of θ for $J = 5$ and $N = 125$, 50, 20, and 5 are presented in Figure 5-9.

The current distribution results for $N = 20$ and $J = 100$, 10, 1, and 0.1 are presented in Figures 5.10(a) to 5.10(d). The current distribution remains uniform for $C(0) = 0.9$ regardless of J values, as seen in Figure 5.10(d). Simulation results in Figure 5.10(a) for $C(0) = 0.5$, 0.6, 0.7, and 0.8, $J = 100$, and $N = 20$ display a maximum in current at the θ values between pole and point of boundary later separation. This feature of current distribution diminishes for $J = 10$, and $N = 20$ as shown in Figure 5.10(b), and remains unchanged as values of J are further decreased. The current distribution for parameters $N = 20$ and $J = 1\,, 0.1$ are shown in Figures 5.10(c) and 5.10(d), respectively.

The dimensionless concentration as a function θ for $N = 20$ and $J = 100$, 10, 1, and 0.1 are presented in Figure 5-11. The results in Figure 5-11 corresponds to the current distribution in Figure 5-10. The dimensionless solution potential along the electrode surface as a function θ for $N = 20$ and $J = 100$, 10, 1, and 0.1 are given in Figure 5-12.

The following expression was used to quantify the uniformity of current distribution:

$$\Upsilon_{hs} = \sqrt{\frac{\int_0^{\frac{\pi}{2}} \left(\frac{i(\theta)}{i(0)} - 1\right)^2 \sin\theta d\theta}{\int_0^{\frac{\pi}{2}} \sin\theta d\theta}} \tag{5-60}$$

where Υ_{hs} represents the parameter of uniformity for the current distribution at

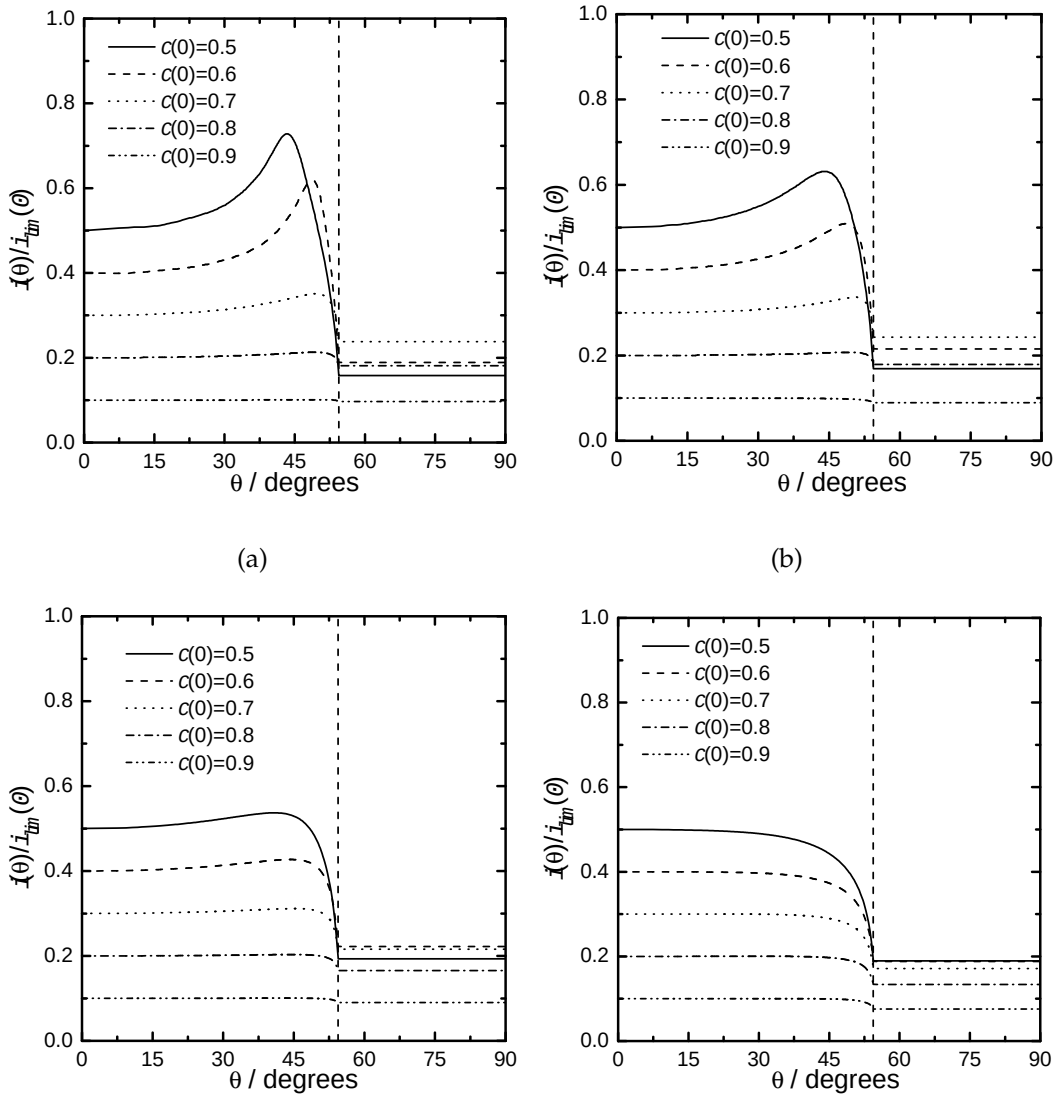

Figure 5-7: Calculated current distribution as a function θ at the stationary hemispherical electrode under submerged jet impingement. The simulation were done for different values of pole concentrations $C(0)$, and parameters J and N. The vertical dash line represent the point of boundary layer separation. (a) $N = 125$ and $J = 5$, (b) $N = 50$ and $J = 5$, (c) $N = 20$ and $J = 5$, and (d) $N = 5$ and $J = 5$.

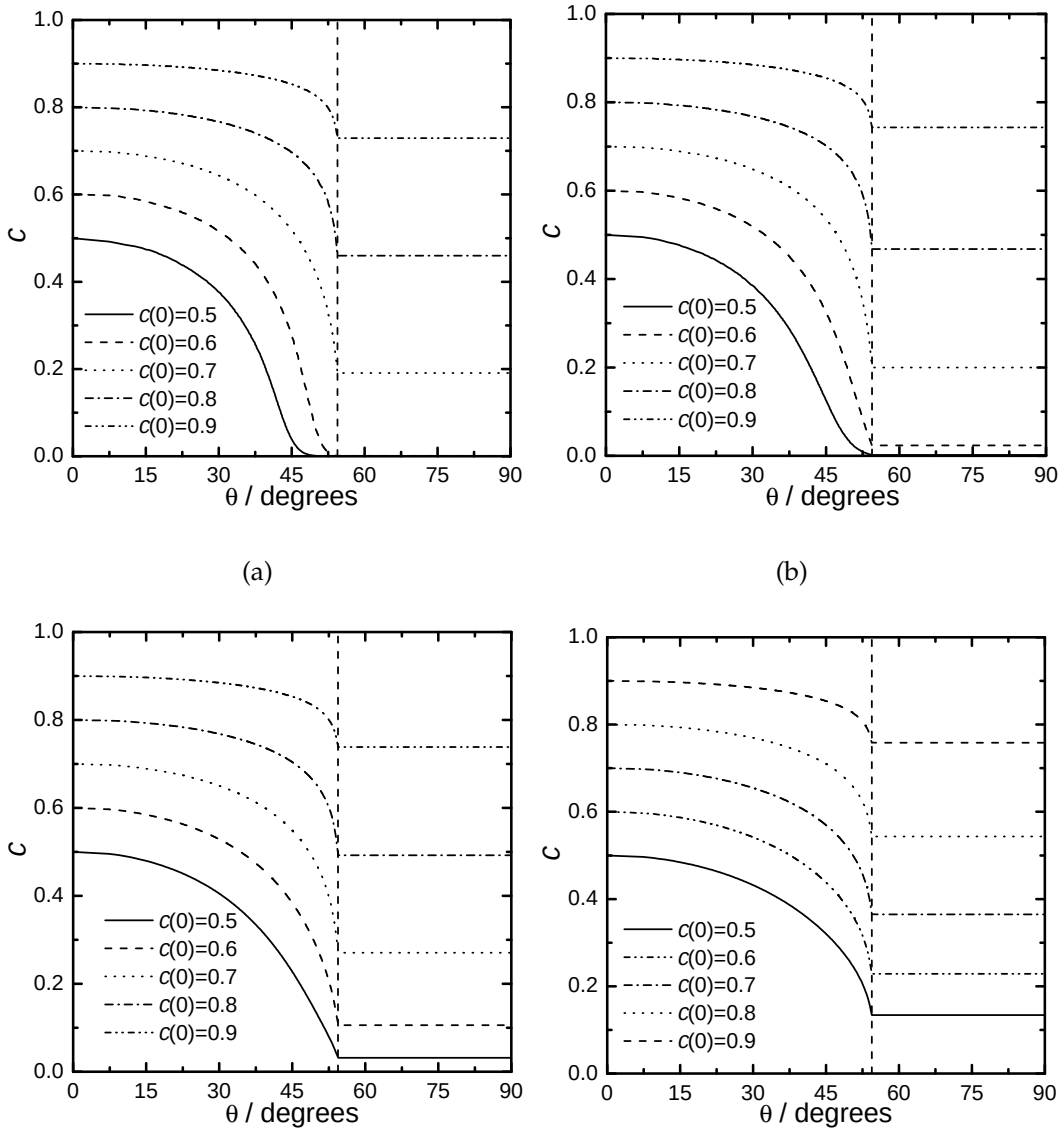

Figure 5-8: Calculated concentration profile corresponding to the current distribution presented in Figure 5-7 as a function θ at the stationary hemispherical electrode under submerged jet impingement. The simulation were done for different values of pole concentrations $C(0)$, and parameters J and N. The vertical dash line represent the point of boundary layer separation. (a) $N = 125$ and $J = 5$, (b) $N = 50$ and $J = 5$, (c) $N = 20$ and $J = 5$, and (d) $N = 5$ and $J = 5$.

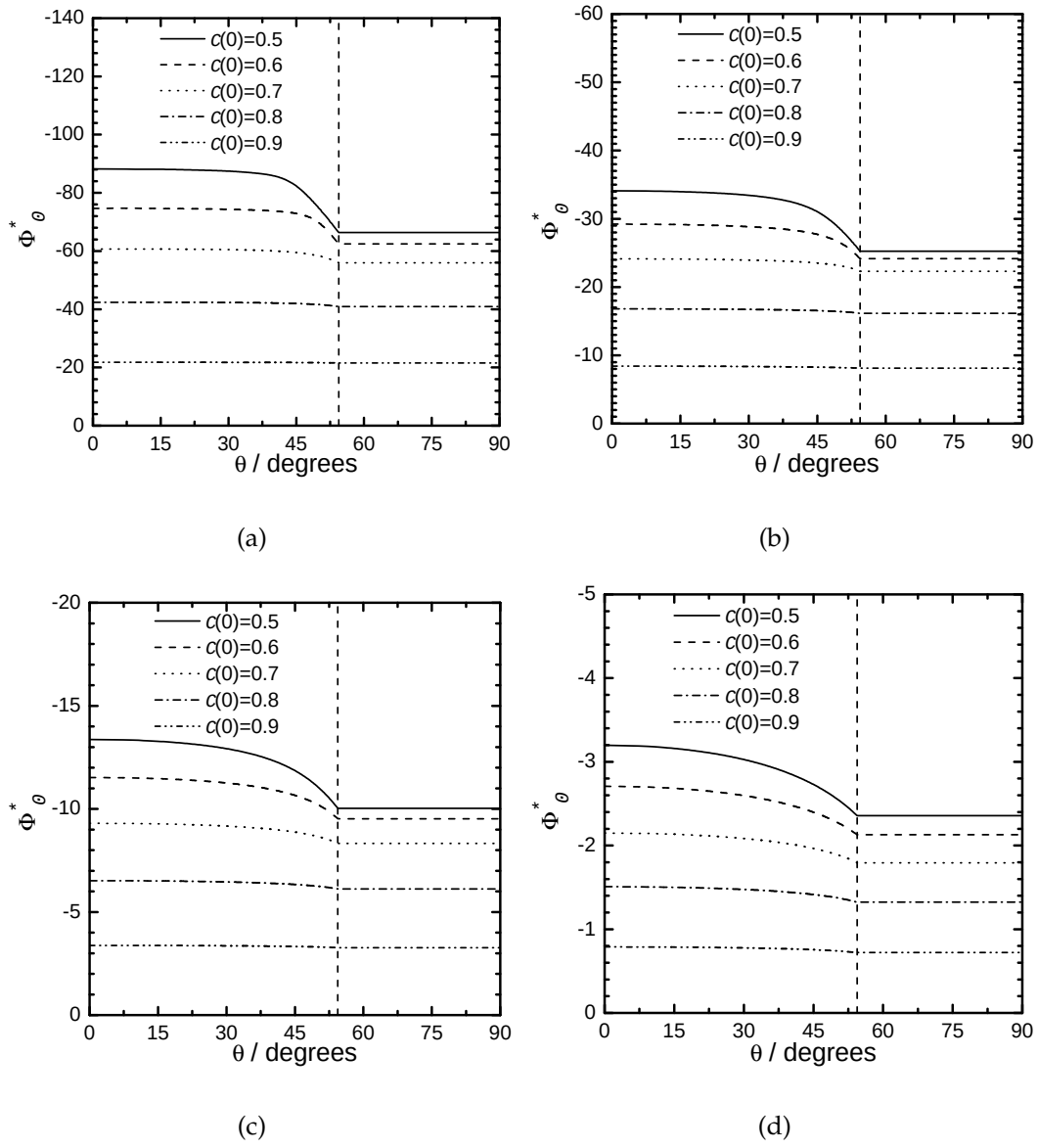

Figure 5-9: Calculated values of solution potential corresponding to the current distribution presented in Figure 5-7 as a function of θ at the stationary hemispherical electrode under submerged jet impingement. The simulation were done for different values of pole concentrations $C(0)$, and parameters J and N. The vertical dash line represent the point of boundary layer separation. (a) $N = 125$ and $J = 5$, (b) $N = 50$ and $J = 5$, (c) $N = 20$ and $J = 5$, and (d) $N = 5$ and $J = 5$.

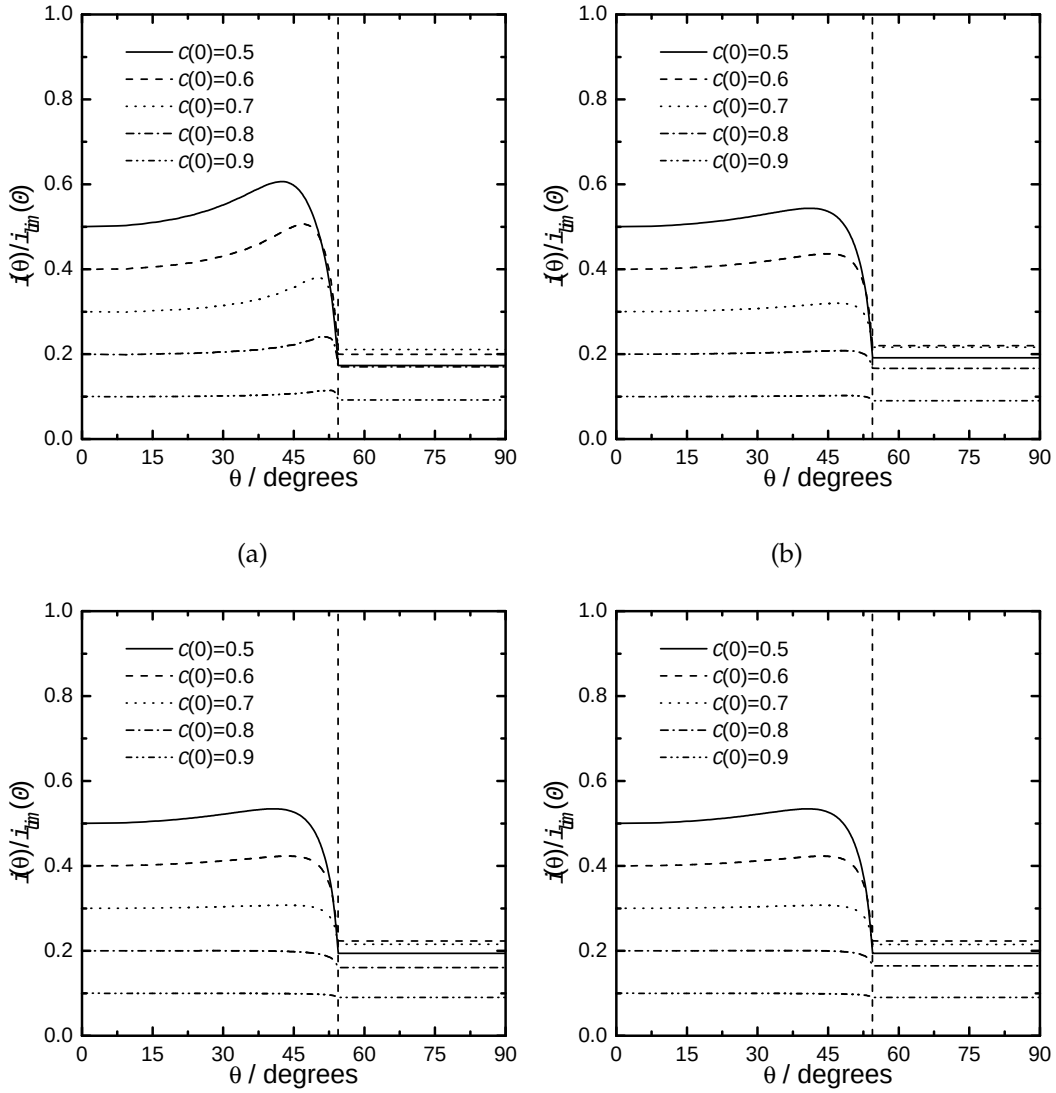

Figure 5-10: Calculated current distribution as a function of θ at the stationary hemispherical electrode under submerged jet impingement. The simulation were done for $N = 20$, and different values of pole concentrations $C(0)$ and parameters J. The vertical dash line represent the point of boundary layer separation. (a) $N = 20$ and $J = 100$, (b) $N = 20$ and $J = 10$, (c) $N = 20$ and $J = 1$, and (d) $N = 20$ and $J = 0.1$.

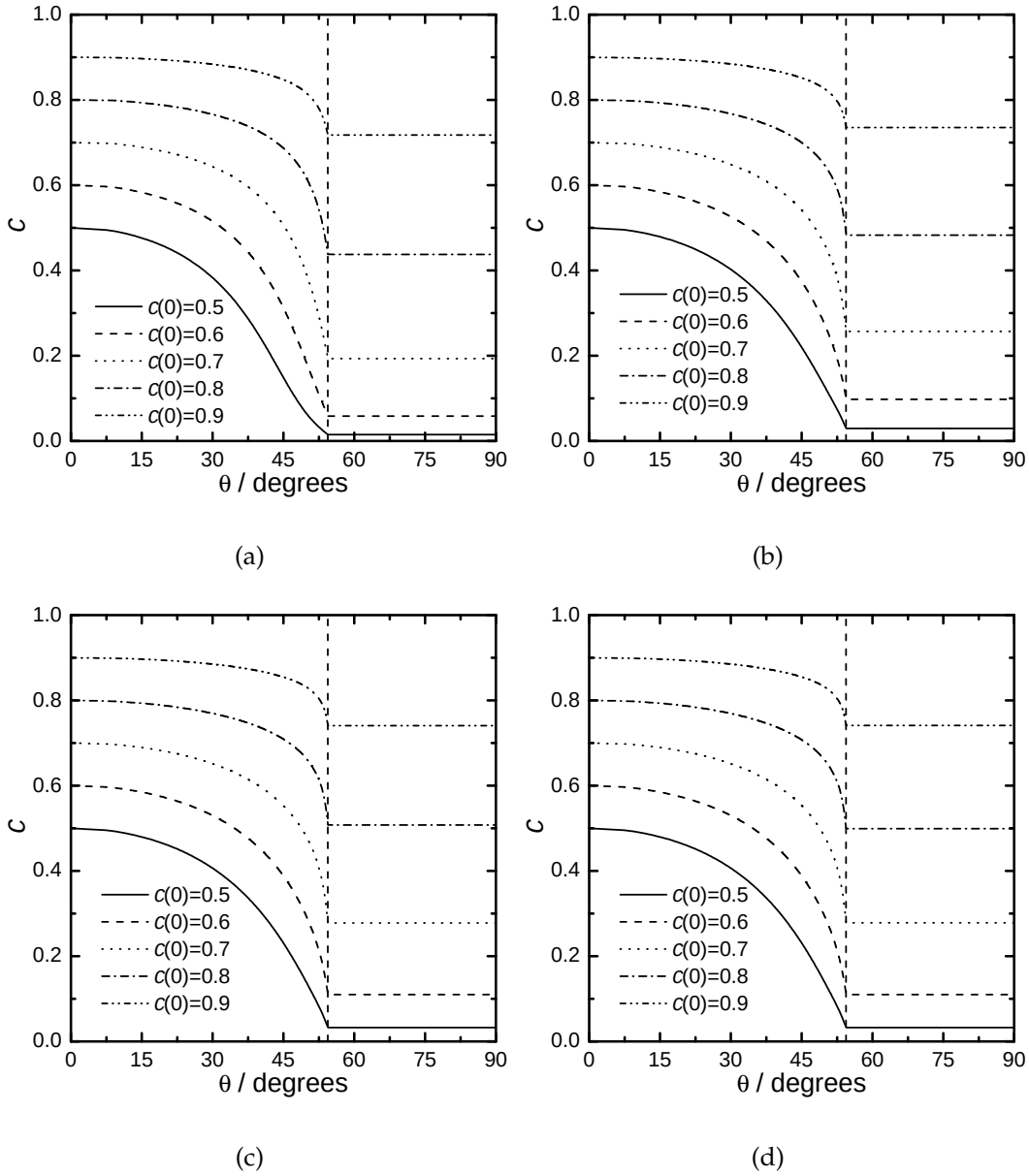

Figure 5-11: Calculated concentration profile corresponding to the current distribution presented in Figure 5-10 as a function of θ at the stationary hemispherical electrode under submerged jet impingement. The simulation were carried out for $N = 20$, and different values of pole concentrations $C(0)$ and parameters J. The vertical dash line represent the point of boundary layer separation. (a) $N = 20$ and $J = 100$, (b) $N = 20$ and $J = 10$, (c) $N = 20$ and $J = 1$, and (d) $N = 20$ and $J = 0.1$.

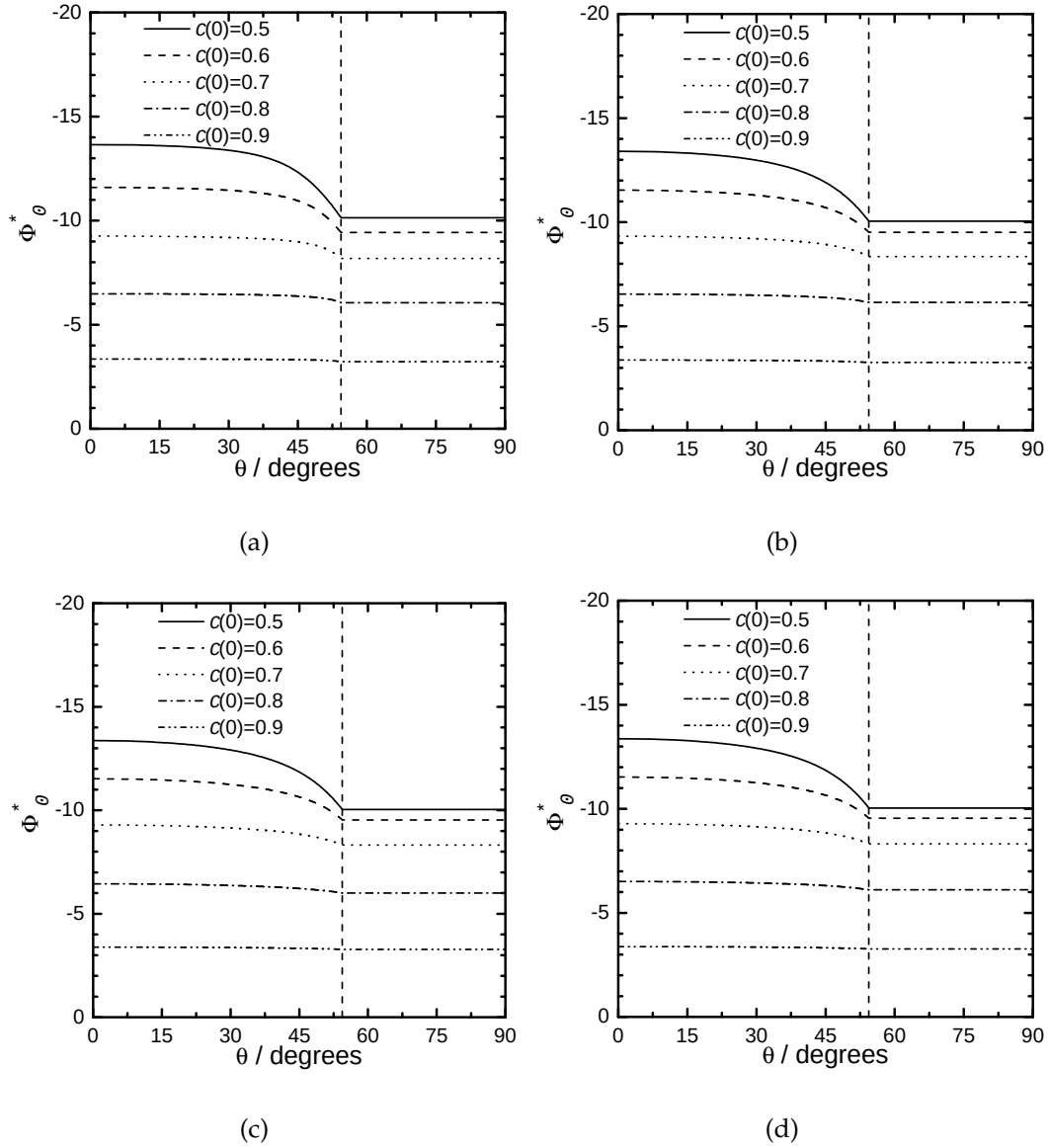

Figure 5-12: Calculated values of solution potential corresponding to the current distribution presented in Figure 5-10 as a function of θ at the stationary hemispherical electrode under submerged jet impingement. The simulation were carried out for $N = 20$, and different values of pole concentrations $C(0)$ and parameters J. The vertical dash line represent the point of boundary layer separation. (a) $N = 20$ and $J = 100$, (b) $N = 20$ and $J = 10$, (c) $N = 20$ and $J = 1$, and (d) $N = 20$ and $J = 0.1$.

Table 5.2: Values of uniformity parameter Υ_{hs} (see equation (5-60)) for for stationary The calculated values are for hemispherical electrode under jet impingement. the current distributions presented in Figure 5-7. Parameter J was fixed at 5.

Υ_{hs}				
$C(0)$	$N = 5$	$N = 20$	$N = 50$	$N = 125$
0.5	0.164	0.123	0.189	0.258
0.6	0.122	0.078	0.158	0.263
0.7	0.087	0.055	0.067	0.112
0.8	0.061	0.025	0.023	0.041
0.9	0.040	0.014	0.008	0.008

the hemispherical electrode. The quantity Υ_{hs} was calculated for the current distribution presented in Figures 5-7 and 5-10. The values of Υ_{hs} are provided in Table 5.2 for $J = 5$ and $N = 5$, 20, 50, and 125. It is observed that Υ_{hs} reaches a minimum for $C(0) = 0.9$ and a maximum at for $C(0) = 0.5$. For in between values of $C(0)$, the value of Υ_{hs} decreases monotonically for increasing $C(0)$. As seen in Figure 5-7, the current profiles display uniformity for all N and $C(0)$=0.9. The distribution starts to become nonuniform at $C(0)$=0.8, and non-uniformity increase for increasing $C(0)$. Using the condition of uniformity for the disk electrode, $\Upsilon_{disk} = 0.021$, $\Upsilon_{hs} = 0.02$ becomes the condition of uniform current distribution for the hemispherical electrode. By the application of the uniformity definition, the current distribution presented in Figure 5-7 is uniform for $C(0) = 0.9$ and $N =$ 20, 50, and 100.

The ratio $i_{avg}/(i_{lim})_{avg}$ represents the average current with respect to total mass-transfer-limited current at the electrode surface. The values of $i_{avg}/(i_{lim})_{avg}$ for $J = 5$ and $N = 5$, 20, 50 and 125 are given in Table 5.3. The average current level is about 25% of mass-transfer limited current for $C(0) = 0.9$. A one-to-one comparison of Table 5.2 and 5.3 shows that the current distribution become uniform at about 25% of mass-transfer-limited current.

Similarly, the calculated values of Υ_{hs} for $N = 20$ and $J = 0.1$, 1, 10 and 100 are

Table 5.3: Values of $i_{avg}/(i_{lim})_{avg}$ for stationary hemispherical electrode under jet impingement. The calculated values are for the current distributions presented in Figure 5-7. Parameter J was fixed at 5.

$i_{avg}/(i_{lim})_{avg}$				
$C(0)$	$N = 5$	$N = 20$	$N = 50$	$N = 125$
0.5	0.831	0.892	0.896	0.902
0.6	0.743	0.840	0.867	0.852
0.7	0.618	0.713	0.774	0.775
0.8	0.451	0.511	0.537	0.544
0.9	0.242	0.268	0.275	0.282

Table 5.4: Values of Υ_{hs} (see equation (5-60)) for stationary hemispherical electrode under jet impingement. The calculated values are for the current distributions presented in Figure 5-10. Parameter N was fixed at 20.

Υ_{hs}				
$C(0)$	$J = 0.1$	$J = 1$	$J = 10$	$J = 100$
0.5	0.121	0.121	0.126	0.173
0.6	0.075	0.075	0.085	0.165
0.7	0.043	0.043	0.052	0.142
0.8	0.028	0.035	0.031	0.101
0.9	0.021	0.019	0.017	0.067

given Table 5.4. The corresponding values of $i_{avg}/(i_{lim})_{avg}$ are listed in Table 5.5. As seen in Figure 5-10, the current distributions exhibit uniformity for $C(0) = 0.9$ for all values of J. However, the definition of uniformity indicates that the current profile is uniform for $J = 0.1$, 1, and 10.

Table 5.5: Values of $i_{avg}/(i_{lim})_{avg}$ for stationary hemispherical electrode under jet impingement. The calculated values are for the current distributions presented in Figure 5-10. Parameter N was fixed at 20.

$i_{avg}/(i_{lim})_{avg}$				
$C(0)$	$J = 0.1$	$J = 1$	$J = 10$	$J = 100$
0.5	0.892	0.892	0.892	0.894
0.6	0.837	0.839	0.842	0.843
0.7	0.708	0.709	0.719	0.736
0.8	0.507	0.499	0.516	0.535
0.9	0.267	0.267	0.269	0.277

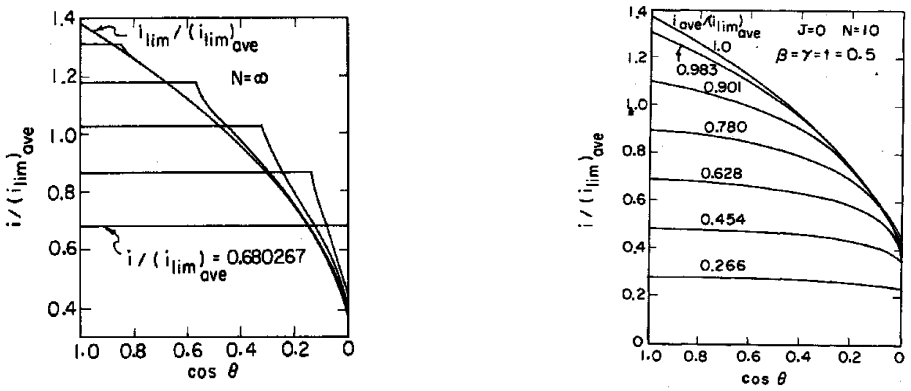

(a) (b)

Figure 5-13: Current distribution calculations presented in the paper by Nisançiöglu and Newman.(a) Figure 6 of the paper by Nisançiöglu *et al.* (b) Figure 2 of the paper by Nisançiöglu *et al.*

5.7 Current Distribution on the Rotating Hemispherical Electrode

Nisançiöglu and Newman[18] have addressed the issue of current distribution on a rotating spherical electrode. They reported that current distribution becomes uniform at about 68% of mass-transfer-limited current at the high rotation speed. The calculated current distribution by Nisançiöglu *et al.* is presented in Figure 5.13(b). In this figure, the value of N is infinite, and the current distribution in only controlled by the mass-transfer to the electrode. Another set of current distribution calculations by Nisançiöglu *et al.* are presented in Figure 5.13(b). These calculation were done for $J = 0$ and $N = 10$. As the value of total average current increases, the current distribution becomes more non uniform. As seen in Figure 5.13(b), the current distribution is most uniform at 26.6% of mass-transfer-limited current.

Nisançiöglu and Newman restricted their calculations for case of infinite Schmidt number. In the present work, current distribution calculations have been performed for finite Schmidt number. The governing equations, calculation algorithm, and results are presented next.

5.7.1 Governing Equations

The methodology suggested by Nisançiöglu[18] to formulate convective-diffusion in terms of a Schlichting integral[23] (see equation (5-35)) can not be applied to account for finite Sc number. However, a series solution for reactant concentration, which explicitly account for Sc number is more appropriate. This methodology is similar to the one presented in Chapter 3 (equation (3-5)), where dimensionless concentration was expanded in two terms. Following that, the dimensionless reactant concentration as a function θ and y can be expressed as

$$\frac{c_\infty - c_R}{c_\infty} = \left(\sum_{i=1}^{n} \theta^{2i-2} \Phi_{1,2i-1}(y) + \mathrm{Sc}^{-\frac{1}{3}} \sum_{i=1}^{n} \theta^{2i-2} \Phi_{2,2i-1}(y) \right) \tag{5-61}$$

where the first term on the right hand side provides the solution infinitely large Schmidt number Sc, and the second term provides a correction for a finite value of Sc. The corresponding dimensionless current at the electrode surface is given by

$$i^* = 9^{1/3} N \left(\sum_{i=1}^{n} \theta^{2i-2} \Phi'_{1,2i-1}(0) + \mathrm{Sc}^{-\frac{1}{3}} \sum_{i=1}^{n} \theta^{2i-2} \Phi'_{2,2i-1}(0) \right) \tag{5-62}$$

where prime denotes the first order derivative with respect y. The number of terms in the summations were limited to ten. After substitutions of dimensionless concentration in convective-diffusion equation, ten ordinary differential equations for $\Phi_{1,2i-1}$ and $\Phi_{2,2i-1}$ were derived. The obtained equations were solved using the BAND algorithm with appropriate boundary conditions, and their solution yielded the current distribution at the electrode surface. The governing equations for kinetics is represented by Butler-Volmer, whereas, the solutions potential is represented by Laplace's equation.

5.7.2 Numerical Procedure

An algorithm for calculating the current distribution, concentration distribution, and solution potential along the electrode surface is outlined below. The

algorithm was computationally intensive as twenty ordinary coupled differential equations were soled for each iteration.

1. Values of J and N were assigned, $C(0)$ was assumed to have a value between 0.0 and 1.0 at $\theta = 0$. Values of electrode potential or current level can also be chosen. This adds an extra step in the calculation procedure, which iterates on the $C(0)$ at the center of the electrode to reach the assigned value of the electrode potential or the specified current level.

2. As an initial guess, a monotonically decreasing positive concentration profile was assumed as shown below:

$$C(\theta) = C(0) - a * \theta^2 \tag{5-63}$$

   The small value of a was chosen so that $C(\theta)$ remains positive over entire electrode surface.

3. The θ domain was discretized from 0° to 90° in equally spaced grid.

4. An initial current distribution was obtained by solving the convective diffusion equations for $\Phi_{1,2i-1}$ and $\Phi_{2,2i-1}$. The differential equations were solved for different mesh sizes. The first derivatives of $\Phi_{1,2i-1}$ and $\Phi_{2,2i-1}$ were calculated by extrapolation to zero mesh size.

5. Values of surface overpotential E_s, and concentration overpotential E_c were obtained at each node in θ domain.

6. The solution potential adjacent to the electrode surface for the calculated current in the step 4 was determined.

7. A new overpotential distribution at each was $E(\theta)$ was calculated using the following expression:

$$E(\theta) = E(\theta) + \lambda(V^*(0) - \Phi^*(\theta) - E(\theta)) \tag{5-64}$$

where λ can have a value between 0 and 1. In this procedure, a small value of 0.02 was selected.

8. The surface concentration distribution using equation (5-38) by the Newton-Raphson[60] method was determined.

9. A polynomial in θ was fitted to the concentration profile obtained in the previous step. The functional form of the polynomial is given by

$$C(\theta) = 1 - \left(\sum_{i=1}^{10} \theta^{2i-2} \Phi_{1,2i-1}(0) \right) \tag{5-65}$$

where $\Phi_{1,2i-1}(0)$ are the coefficients of the polynomial at the electrode surface. The values of these coefficients act as boundary conditions for convective-diffusion equations for $\Phi_{1,2i-1}(r)$. It should noted that the regressed values of the coefficients $\Phi_{1,2i-1}(0)$ must be statistically significant. If the confidence intervals of $\Phi_{1,2i-1}(0)$ included zero, $\Phi_{1,2i-1}(0)$ were set to zero.

10. The current distribution was obtained by solving convective-diffusion equations for $\Phi_{1,2i-1}(r)$ and $\Phi_{2,2i-1}(r)$, and solution potential was calculated along the electrode surface for the obtained current distribution.

11. The relative percentage difference of coefficient B_0 was used as termination criterion. The B_0 represent the average dimensionless current at the electrode surface. If $(B_{0,new} - B_{0,old})/B_{0,old}$ was less than 1.0^{-6}, calculations were stopped, otherwise, the calculation procedure was repeated starting from step 5 to 10.

A FORTRAN implementation of the algorithm is presented in Appendix F.

5.7.3 Results

The current distribution was calculated for $J = 5$, and $N = 125$. The value of Schmidt number was fixed at 1000. The calculated results are presented in

Figure 5-14. The black colored lines in the Figure 5-14 corresponds to calculation with infinite Sc number, and grey colored lines corresponds to $\mathrm{Sc} = 1000$. The current distribution is presented in Figure 5.14(a) for different values of the pole concentrations $C(0)$. The Schmidt number correction lowers the value of current along the surface as shown in Figure 5.14(a). The corresponding dimensionless surface concentration distribution is presented in Figure 5.14(b). The concentration profile is slightly higher with Schmidt number correction. The dimensionless surface overpotential, and concentration overpotential are presented in Figures 5.14(c) and 5.14(d), respectively. The calculated dimensionless solution potential along the electrode surface for infinite Sc number is presented in Figure 5.15(a). The results with Sc correction are given in Figure 5.15(b).

These results show that the Sc number correction lowers the current along the electrode surface. The effect of Sc correction is more significant at higher current levels.

Values of Υ_{hs} are listed in Table 5.6. Uniformity parameter Υ_{hs} monotonically decreases for increasing values of $C(0)$. The condition of uniformity is achieved at $C(0) = 0.7$ for both simulation with Sc number correction and with $\mathrm{Sc} = \infty$. Values of $i_{avg}/(i_{lim})_{avg}$ are listed in Table 5.6. $i_{avg}/(i_{lim})_{avg}$ is about 0.4 for $C(0) = 0.7$, hence, current distribution at the rotating hemispherical electrode becomes uniform at about 40% of mass transfer limited current.

5.8 Summary

A generalized mathematical model for calculating current and potential distribution for both stationary disk and hemispherical electrodes under jet impingement was developed. For hemispherical electrode, the current distribution in the separated part of the boundary layer for hemispherical electrode was approximated with a uniform current. The current value at the point of separation was

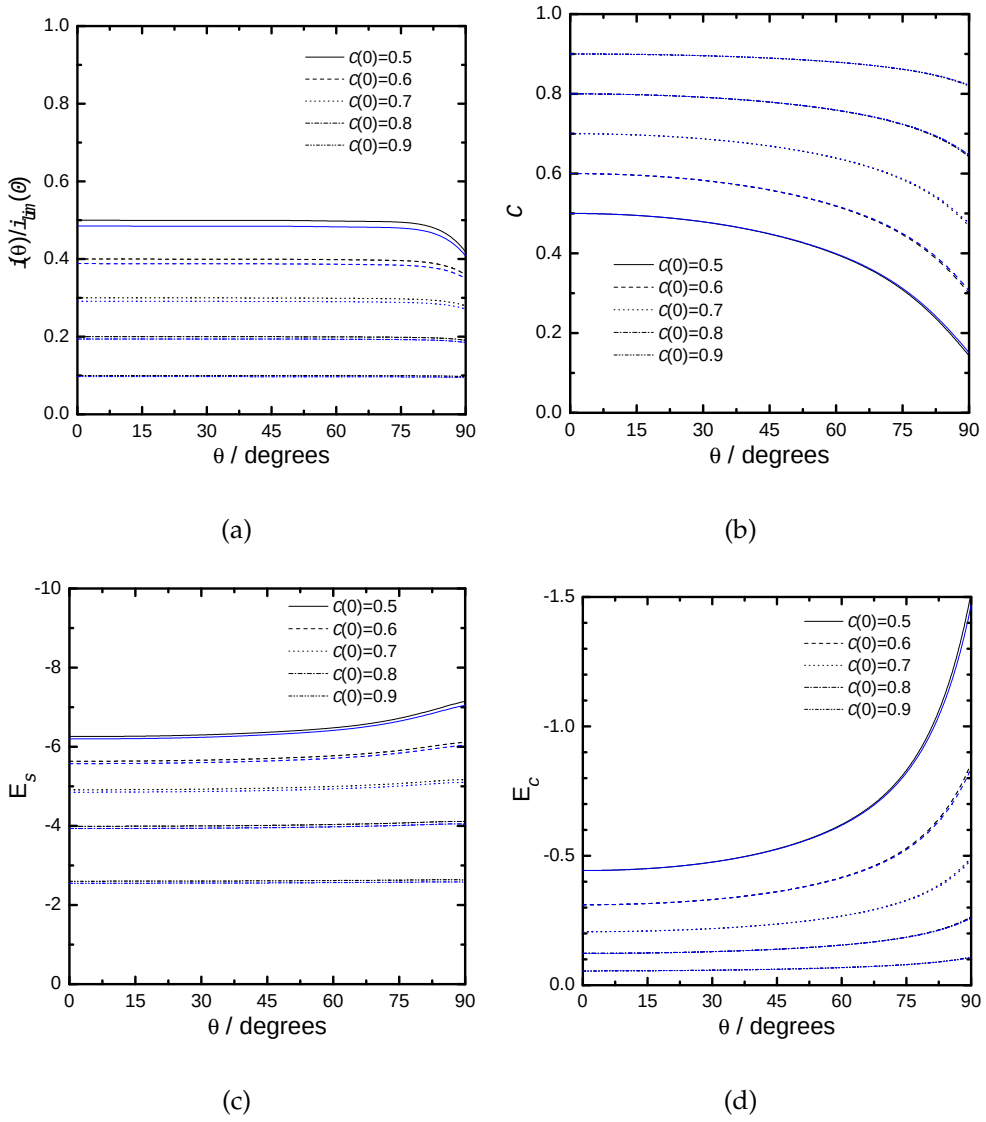

Figure 5-14: Calculated values of current distribution, concentration distribution, surface overpotential, and concentration overpotential as a function of θ at the rotating hemispherical electrode. The lines in black color corresponds to the calculations for infinite Schmidt number, and lines in blue color corresponds to calculated results with $\mathrm{Sc} = 1000.0$. These calculations were performed for $J = 5$ and $N = 125$. (a) Current distribution as a function of θ, (b) Dimensionless Concentration distribution as a function of θ, (c) Dimensionless surface overpotential as a function of θ, (d) Dimensionless concentration overpotential as a function of θ.

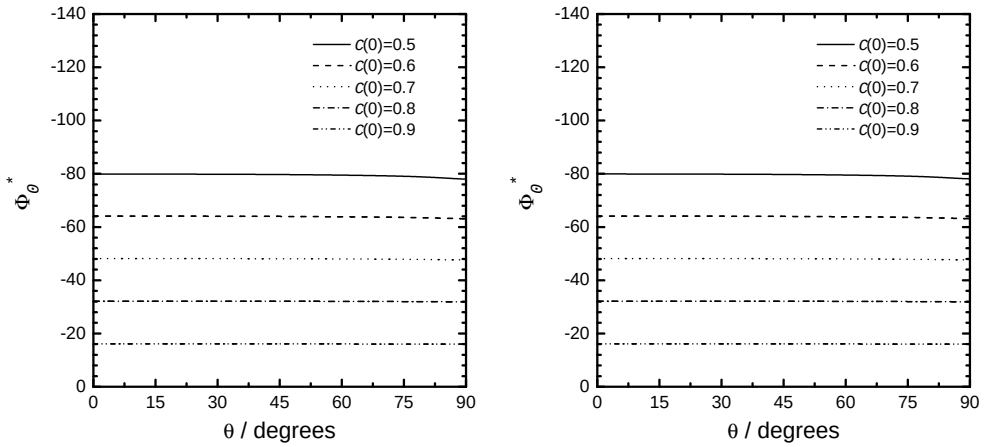

(a) (b)

Figure 5-15: Calculated dimensionless Solution potential along the electrode surface as a function of θ. The results corresponds to the current distributions given in Figure 5.14(a). (a) Dimensionless solution potential without Schmidt number correction, (b) Dimensionless solution potential with Schmidt number correction.

Table 5.6: Values of $i_{avg}/(i_{lim})_{avg}$ and Υ_{hs} for the rotating hemispherical electrode. The calculated values are for the current distributions presented in Figure 5.14(a). Parameters N and J was fixed at 125 and 5, respectively.

	$\mathrm{Sc} = \infty$		$\mathrm{Sc} = 1000$	
$C(0)$	Υ_{hs}	$i_{avg}/(i_{lim})_{avg}$	Υ_{hs}	$i_{avg}/(i_{lim})_{avg}$
0.5	0.035	0.668	0.035	0.667
0.6	0.023	0.537	0.023	0.536
0.7	0.016	0.404	0.016	0.403
0.8	0.011	0.271	0.012	0.270
0.9	0.007	0.135	0.007	0.135

assumed to be applicable in the separated part of the boundary layer. An iterative calculation algorithm was devised for solving the governing equations for current distribution. The results presented indicate that the current distribution becomes uniform at about 25% of mass-transfer limited current.

Likewise, another mathematical model was presented to estimate the effect of Sc number correction on the current distribution at the rotating hemispherical electrode. Again, the governing equations were solved with an iterative scheme. The results show that current distribution wields a significant effect in the presence of finite Sc number.

CHAPTER 6
VALIDATION OF THE MEASUREMENT MODEL CONCEPT

This chapter presents a comparative study of different forms of measurement models to estimate stochastic error contribution in the impedance and to asses consistency of the data with Kramers-Kronig relations. Voigt element, Constant phase element, and transfer function based impedance models were considered as the candidate measurement models. The development of regression procedure, key concepts, and estimation of stochastic errors with measurement models is presented in this chapter. A comparative Kramers-Kronig consistency checks of the impedance data were done with Voigt element and transfer function based measurement models.

6.1 Introduction

Interpretation of spectroscopy data is facilitated by a quantitative analysis of the measurement error structure.[61] Knowledge of the error structure has been shown to allow enhanced interpretation of light scattering measurements in terms of particle size distribution and particle classification.[62,63] The error analysis approach has been successful for light spectroscopy measurements because the short time required for such measurements minimizes nonstationary contributions to replicated spectra. In addition, optical measurements generally satisfy the Kramers-Kronig[64,65] relations, thus allowing extension of the measurable range of spectra.[63]

In contrast, the stochastic contribution to the error structure of electrochemical impedance spectroscopy measurements cannot be obtained directly from replicated measurements because the inherently non-stationary character of electrochemical systems introduces a non-negligible time-varying bias contribution to

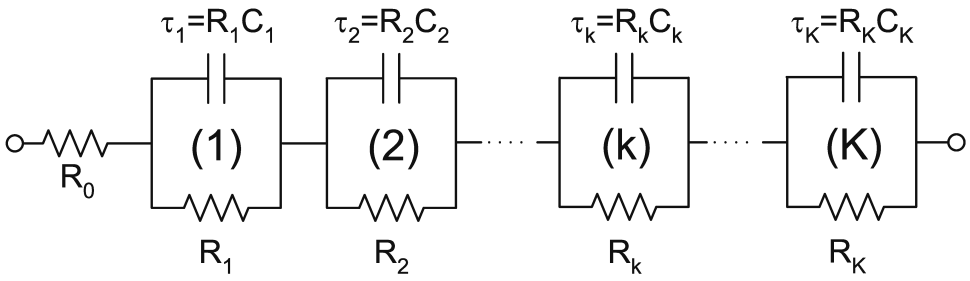

Figure 6-1: A schematic representation of a Voigt element measurement model.

the error.[66] In addition, the comparatively long time required for impedance measurements frequently introduces non-stationary contributions to impedance spectra which violate the Kramers-Kronig relations.

Agarwal *et al.*[31–33]have introduced a measurement model as a means to identify the error structure of imperfectly replicated impedance data. Agarwal *et al.* proposed that a generalized Voigt model could be used to filter the replication errors of impedance data in order to distinguish between stochastic or random errors and deterministic errors caused, for example, by systematic changes in system properties. The measurement model proposed by Agarwal *et al.*[31] was composed of Voigt elements in series with a solution resistance, as shown in Figure 6-1, *i.e.*,

$$Z = R_0 + \sum_{k=1}^{K} \frac{R_k}{1 + j\omega\tau_k} \tag{6-1}$$

With a sufficient number of parameters, the Voigt model was able to provide a statistically significant fit to a broad variety of impedance spectra.[31]

As the measurement model was chosen to be consistent with the Kramers-Kronig relations, Agarwal *et al.*[31–33] showed that it could also be used to allow a check of consistency of data without explicit integration of the Kramers-Kronig relations. A unique feature of the approach was that the weighting strategy made use of the measured stochastic error structure; thus the evaluation of consistency was conducted within the context of an overall error analysis. The concept of using circuit models to check for consistency of data was described much earlier

by Brachman and Macdonald[67,68] and later by Boukamp and Macdonald[69] and by Boukamp.[70] These approaches, however, did not include a comprehensive error analysis.

The concept proposed by Agarwal *et al.*[31] was that the measurement model consists of a superposition of line-shapes which can be arbitrarily chosen subject to the constraints that the parameter estimates were statistically significant and that the model satisfied the Kramers-Kronig relations. Therefore, other transfer function models can be considered. For example, equation (6-1) can be generalized to allow Constant-Phase-Element behavior, *i.e.*,

$$Z = R_0 + \sum_{k=1}^{N} \frac{R_k}{1 + (j\omega)^{1-\alpha_k}\tau_k} \tag{6-2}$$

This measurement model is Kramers-Kronig consistent provided α_k lies between zero and one.[71]

Pauwels *et al.*[34] have proposed that a transfer function formulation

$$Z = \frac{\sum_{k=0}^{M} b_k \left((j\omega)^n\right)^k}{\sum_{m=0}^{P} a_m \left((j\omega)^n\right)^m} \tag{6-3}$$

that may be a more parsimonious model for certain classes of impedance measurements. Pauwels *et al.*[34] noted in particular that, for $n = 1/2$, equation (6-3) yields a frequency dependence that may be particularly useful for modeling data influenced by diffusion processes. If $n = 1$, equation (6-3) shows a frequency behavior similar to that of a Voigt model (equation (6-1)).

The introduction of new measurement models introduces the potential to evaluate some of the key assumptions of the measurement model approach. The objective of the present work was to ascertain that the stochastic error structure obtained using the measurement model paradigm is independent of the form of measurement model used. The second objective was to assess the suitability of the different measurement models for assessing consistency of data with the Kramers-Kronig relations.

6.2 Definition of Errors

The errors in an impedance measurement can be expressed in terms of the difference between the observed value $Z(\omega)$ and a model value $\widehat{Z}(\omega)$ as

$$\begin{aligned}\varepsilon_{\text{res}}(\omega) &= Z(\omega) - \widehat{Z}(\omega) \\ &= \varepsilon_{\text{fit}}(\omega) + \varepsilon_{\text{bias}}(\omega) + \varepsilon_{\text{stoch}}(\omega)\end{aligned} \tag{6-4}$$

where ε_{res} represents the residual error, $\varepsilon_{\text{fit}}(\omega)$ is the systematic error that can be attributed to inadequacies of the model, $\varepsilon_{\text{bias}}(\omega)$ represents the systematic experimental bias error that cannot be attributed to model inadequacies, and $\varepsilon_{\text{stoch}}(\omega)$ is the stochastic error with expectation $\mathbb{E}\left\{\varepsilon_{\text{stoch}}(\omega)\right\} = 0$.

A distinction is drawn, following Agarwal *et al.*,[31–33] between stochastic errors that are randomly distributed about a mean value of zero, errors caused by the lack of fit of a model, and experimental bias errors that are propagated through the model. The experimental bias errors, assumed to be those that cause lack of consistency with the Kramers-Kronig relations,[72,65,64] may be caused by nonstationarity or by instrumental artifacts. The problem of interpretation of impedance data is therefore defined as consisting of two parts: one of identification of experimental errors, which includes assessment of consistency with the Kramers-Kronig relations, and one of fitting, which entails model identification, selection of weighting strategies, and examination of residual errors. The error analysis provides information that can be incorporated into regression of process models.

6.3 Equivalence of Measurement Models

The three measurement models differ with each other in terms of their parameters. However, under certain conditions a parametric equivalence can be established between the models. For example, Constant-Phase-Element(CPE) is a generalized form of Voigt element; hence, for $\alpha_k = 0$, CPE measurement model is same

as Voigt model. A similar equivalence can be formed between Constant-Phase-Element based and transfer function based measurement models. For $N = M = P$ and $\alpha = n = 0.5$ in the equation (6-2) and (6-3), following relationships between the parameters of both measurement models can be deduced:

$$
\begin{aligned}
a_0 &= 1 \\
a_1 &= \sum_{i=1}^{n} \tau_i \\
a_2 &= \sum_{i=1}^{N} \sum_{j=1}^{N} \tau_i \tau_j (i \neq j) \\
a_3 &= \sum_{i=1}^{N} \sum_{j=1}^{N} \sum_{k=1}^{N} \tau_i \tau_j \tau_k (i \neq j \neq k) \\
&\vdots \\
b_0 &= \sum_{i=1}^{N} R_i \\
b_1 &= R_0 a_1 + \sum_{i=1}^{N} \sum_{j=1}^{N} R_i \tau_j (i \neq j) \\
b_2 &= R_0 a_2 + \sum_{i=1}^{N} \sum_{j=1}^{N} \sum_{k=1}^{N} R_i \tau_j \tau_k (i \neq j \neq k) \\
b_3 &= R_0 a_3 + \sum_{i=1}^{N} \sum_{j=1}^{N} \sum_{k=1}^{N} \sum_{l=1}^{N} R_i \tau_j \tau_k \tau_l (i \neq j \neq k \neq l) \\
&\vdots
\end{aligned}
$$

This analysis has been limited to $N = 3$. The above relationships show that the transfer function based measurement model parameters can be expressed in terms of constant-phase-element measurement model. Thus, the transfer function based measurement model is a special case of Constant-Phase-element based measurement model.

6.4 Kramers-Kronig Relations

Electrochemical impedance measurements are conducted under the following general assumptions[73] about the system

1. **Linear**: The system is linear around the steady state at which perturbation signals are applied. As a result, the impedance is independent of magnitude of perturbation and response.

2. **Stable**: The steady-state position of the system does not drift with time, and response of the applied perturbations remain bounded.

3. **Causal**: The response of the system is only due to the perturbations applied *i.e.,* the response can not precede the applied input perturbation signal.

The Kramers-Kronig transforms provide the mathematical equalities, by which the above conditions can be tested for a collected data set. The transforms can be written as following:

$$Z_r(\omega) - Z_r(\infty) = \left(\frac{2}{\pi}\right) \int_0^\infty \frac{xZ_j(x) - \omega Z_j(\omega)}{x^2 - \omega^2} dx \tag{6-5}$$

or

$$Z_r(\omega) - Z_r(0) = \left(\frac{2\omega}{\pi}\right) \int_0^\infty \left[\left(\frac{\omega}{x}\right) Z_j(x) - \omega Z_j(\omega)\right] \frac{1}{x^2 - \omega^2} dx \tag{6-6}$$

and

$$Z_j(\omega) = -\left(\frac{2\omega}{\pi}\right) \int_0^\infty \frac{Z_r(x) - \omega Z_r(\omega)}{x^2 - \omega^2} dx \tag{6-7}$$

where Z_r, Z_j are the real and imaginary part of the impedance, respectively, and ω is the frequency of measurement, and x is the integration variable. Relations given by equations (6-5) and (6-6) are for predicting real part of impedance using imaginary part. If the high frequency asymptote is known, equation (6-5) is applicable, and if zero frequency asymptote of real part is known, equation (6-6) is

a suitable transform to use. Similarly, imagery part of the impedance can be predicted with equation (6-7). Thus, for given a real part of a impedance spectrum, the imaginary part can be predicted and vice versa. These relationships can also be used to check the consistency of the spectrum with aforementioned assumptions about the system. However, a straightforward applications of the transforms is not feasible due to limited frequency range of EIS experiments. By applying the measurement models which are consistent with the transforms, the assumptions can be validated for the electrochemical system under study.

6.5 Complex Nonlinear Least-square Regression

The parameters of the measurement model, for given EIS data, are calculated using regression. Since regression involves a nonlinear model with real and imaginary part to a data set with complex numbers, the method is known as Complex Nonlinear Least-Square (CNLS) regression. To show the key concepts of the regression procedure, the Voigt element measurement model is considered. The model impedance $\hat{Z}(\omega)$ can be written as

$$\hat{Z}(\omega) = \hat{Z}_r(\omega) + j\hat{Z}_j(\omega) \tag{6-8}$$

where $\hat{Z}_r(\omega)$ and $\hat{Z}_j(\omega)$ are the real and complex parts of $\hat{Z}(\omega)$, respectively. $\hat{Z}_r(\omega)$ and $\hat{Z}_j(\omega)$ can be expressed in terms of R_0, R_1, $\tau_1, \ldots$, R_k, τ_k as following:

$$\hat{Z}_r(\omega) = R_0 + \sum_{i=1}^{k} \frac{R_i}{(1+\tau_i^2\omega^2)} \tag{6-9}$$

and

$$\hat{Z}_j(\omega) = \sum_{i=1}^{k} -\frac{R_i\tau_i\omega}{(1+\tau_i^2\omega^2)} \tag{6-10}$$

R_0, R_1, $R_1, \ldots$, R_k, and τ_k can be determined by CNLS regression. This method (CNLS) was first developed by Sheppard *et al.*[74,75] who applied CNLS to permittivity measurements. Macdonald *et al.*[76] were the first to apply CNLS to EIS data.

The residual sum of squares for CNLS is written as

$$SSE(\theta) = \sum_{i=1}^{n} \frac{(Z_{ri} - \hat{Z}_{ri}(\theta))^2}{\sigma_{ri}^2} + \sum_{i=1}^{n} \frac{(Z_{ji} - \hat{Z}_{ji}(\theta))^2}{\sigma_{ji}^2} \tag{6-11}$$

where

$$\theta = \begin{bmatrix} R_0 \\ R_1 \\ \tau_1 \\ \vdots \\ R_k \\ \tau_k \end{bmatrix}$$

n is the number of data points, Z_{ri} and Z_{ji} are the real and imaginary part of the measured impedance at the i^{th} frequency and σ_{ri}^2 and σ_{ji}^2 are the variances of the real and imaginary part of the measurement, respectively at the i^{th} frequency. The objective is to calculate the parameter set θ such that $SSE(\theta)$ is globally minimized. For the sake of convenience, $SSE(\theta)$ can be rewritten as

$$SSE(\theta) = \sum_{i=1}^{2n} \frac{(Z_i - \hat{Z}_i(\theta))^2}{\sigma_i^2} \tag{6-12}$$

where $Z_i = Z_{ri}$, $\hat{Z}_i = \hat{Z}_{ri}$ and $\sigma_i^2 = \sigma_{ri}^2$ if $i \leq n$ and $Z_i = Z_{ji}$, $\hat{Z}_i = \hat{Z}_{ji}$ and $\sigma_i^2 = \sigma_{ji}^2$ if $i > n$. Minimization of $SSE(\theta)$ requires that the derivatives of $SSE(\theta)$ with respect to different parameters should be equal to zero. This condition gives

$$\frac{\partial SSE(\theta)}{\partial R_0} = \frac{\partial SSE(\theta)}{\partial R_1} = \frac{\partial SSE(\theta)}{\partial \tau_1} = \cdots = \frac{\partial SSE(\theta)}{\partial \tau_k} = 0 \tag{6-13}$$

The partial derivatives of $SSE(\theta)$ with respect to different parameters are written

as:

$$\begin{aligned}
\frac{\partial SSE(\theta)}{\partial R_0} &= \sum_{i=1}^{2n} \frac{(Z_i - \hat{Z}_i)}{\sigma_i^2} \frac{\partial \hat{Z}_i}{\partial Z_0} \\
\frac{\partial SSE(\theta)}{\partial R_1} &= \sum_{i=1}^{2n} \frac{(Z_i - \hat{Z}_i)}{\sigma_i^2} \frac{\partial \hat{Z}_i}{\partial R_1} \\
\frac{\partial SSE(\theta)}{\partial \tau_1} &= \sum_{i=1}^{2n} \frac{(Z_i - \hat{Z}_i)}{\sigma_i^2} \frac{\partial \hat{Z}_i}{\partial \tau_1} \\
&\vdots \\
\frac{\partial SSE(\theta)}{\partial \tau_k} &= \sum_{i=1}^{2n} \frac{(Z_i - \hat{Z}_i)}{\sigma_i^2} \frac{\partial \hat{Z}_i}{\partial \tau_k}
\end{aligned} \tag{6-14}$$

The above set of equations (6-14) are rewritten in the matrix form. Matrix algebra, then, facilitates ease of solving equations (6-14) simultaneously.

$$\begin{bmatrix}
\frac{1}{\sigma_1}\frac{\partial \hat{Z}_1}{\partial R_0} & \frac{1}{\sigma_2}\frac{\partial \hat{Z}_2}{\partial R_0} & \cdots & \frac{1}{\sigma_{2n}}\frac{\partial \hat{Z}_{2n}}{\partial R_0} \\
\frac{1}{\sigma_1}\frac{\partial \hat{Z}_1}{\partial R_1} & \frac{1}{\sigma_2}\frac{\partial \hat{Z}_2}{\partial R_1} & \cdots & \frac{1}{\sigma_{2n}}\frac{\partial \hat{Z}_{2n}}{\partial R_1} \\
\frac{1}{\sigma_1}\frac{\partial \hat{Z}_1}{\partial \tau_1} & \frac{1}{\sigma_2}\frac{\partial \hat{Z}_2}{\partial \tau_1} & \cdots & \frac{1}{\sigma_{2n}}\frac{\partial \hat{Z}_{2n}}{\partial \tau_1} \\
\vdots & & & \\
\frac{1}{\sigma_1}\frac{\partial \hat{Z}_1}{\partial R_k} & \frac{1}{\sigma_2}\frac{\partial \hat{Z}_2}{\partial R_k} & \cdots & \frac{1}{\sigma_{2n}}\frac{\partial \hat{Z}_{2n}}{\partial R_k} \\
\frac{1}{\sigma_1}\frac{\partial \hat{Z}_1}{\partial \tau_k} & \frac{1}{\sigma_2}\frac{\partial \hat{Z}_2}{\partial \tau_k} & \cdots & \frac{1}{\sigma_{2n}}\frac{\partial \hat{Z}_{2n}}{\partial \tau_k}
\end{bmatrix}
\begin{bmatrix}
\frac{(Z_1 - \hat{Z}_1)}{\sigma_1} \\
\frac{(Z_2 - \hat{Z}_2)}{\sigma_2} \\
\frac{(Z_3 - \hat{Z}_3)}{\sigma_3} \\
\vdots \\
\frac{(Z_{2n-1} - \hat{Z}_{2n-1})}{\sigma_{2n-1}} \\
\frac{(Z_{2n} - \hat{Z}_{2n})}{\sigma_{2n}}
\end{bmatrix} = 0 \tag{6-15}$$

In equation (6-15), $\hat{Z}_i$ is further expanded using a Taylor series expansion about the parameter set θ. Second and higher order terms are dropped from the expansion. This gives

$$\begin{aligned}
\hat{Z}_i &= \hat{Z}_i(\theta) + \frac{\partial \hat{Z}_i}{\partial R_0}(R_{0,new} - Z_0) + \frac{\partial \hat{Z}_i}{\partial R_1}(R_{1,new} - \Delta_1) + \frac{\partial \hat{Z}_i}{\partial \tau_1}(\tau_{1,new} - \tau_1) + \cdots \\
&+ \frac{\partial \hat{Z}_i}{\partial R_k}(R_{k,new} - R_k) + \frac{\partial \hat{Z}_i}{\partial \tau_k}(\tau_{k,new} - \tau_k)
\end{aligned} \tag{6-16}$$

Substitution of $\hat{Z}_i$ in equation (6-15) for i=1,…, 2n gives

$$\begin{bmatrix} \frac{1}{\sigma_1}\frac{\partial \hat{Z}_1}{\partial R_0} & \frac{1}{\sigma_2}\frac{\partial \hat{Z}_2}{\partial R_0} & \cdots & \frac{1}{\sigma_{2n}}\frac{\partial \hat{Z}_{2n}}{\partial R_0} \\ \frac{1}{\sigma_1}\frac{\partial \hat{Z}_1}{\partial R_1} & \frac{1}{\sigma_2}\frac{\partial \hat{Z}_2}{\partial R_1} & \cdots & \frac{1}{\sigma_{2n}}\frac{\partial \hat{Z}_{2n}}{\partial R_1} \\ \frac{1}{\sigma_1}\frac{\partial \hat{Z}_1}{\partial \tau_1} & \frac{1}{\sigma_2}\frac{\partial \hat{Z}_2}{\partial \tau_1} & \cdots & \frac{1}{\sigma_{2n}}\frac{\partial \hat{Z}_{2n}}{\partial \tau_1} \\ \vdots & & & \\ \frac{1}{\sigma_1}\frac{\partial \hat{Z}_1}{\partial R_k} & \frac{1}{\sigma_2}\frac{\partial \hat{Z}_2}{\partial R_k} & \cdots & \frac{1}{\sigma_{2n}}\frac{\partial \hat{Z}_{2n}}{\partial \Delta_k} \\ \frac{1}{\sigma_1}\frac{\partial \hat{Z}_1}{\partial \tau_k} & \frac{1}{\sigma_2}\frac{\partial \hat{Z}_2}{\partial \tau_k} & \cdots & \frac{1}{\sigma_{2n}}\frac{\partial \hat{Z}_{2n}}{\partial \tau_k} \end{bmatrix} \begin{bmatrix} \begin{bmatrix} \frac{(Z_1-\hat{Z}_1(\theta))}{\sigma_1} \\ \frac{(Z_2-\hat{Z}_2(\theta))}{\sigma_2} \\ \frac{(Z_3-\hat{Z}_3(\theta))}{\sigma_3} \\ \vdots \\ \frac{(Z_{2n-1}-\hat{Z}_{2n-1}(\theta))}{\sigma_{2n-1}} \\ \frac{(Z_{2n}-\hat{Z}_{2n}(\theta))}{\sigma_{2n}} \end{bmatrix} \end{bmatrix} -$$

$$\begin{bmatrix} \frac{1}{\sigma_1}\frac{\partial \hat{Z}_1}{\partial R_0} & \frac{1}{\sigma_1}\frac{\partial \hat{Z}_1}{\partial R_1} & \frac{1}{\sigma_1}\frac{\partial \hat{Z}_1}{\partial \tau_1} & \cdots & \frac{1}{\sigma_1}\frac{\partial \hat{Z}_1}{\partial R_k} & \frac{1}{\sigma_1}\frac{\partial \hat{Z}_1}{\partial \tau_k} \\ \frac{1}{\sigma_2}\frac{\partial \hat{Z}_2}{\partial R_0} & \frac{1}{\sigma_2}\frac{\partial \hat{Z}_2}{\partial R_1} & \frac{1}{\sigma_2}\frac{\partial \hat{Z}_2}{\partial \tau_1} & \cdots & \frac{1}{\sigma_2}\frac{\partial \hat{Z}_2}{\partial R_k} & \frac{1}{\sigma_2}\frac{\partial \hat{Z}_2}{\partial \tau_k} \\ \frac{1}{\sigma_3}\frac{\partial \hat{Z}_3}{\partial R_0} & \frac{1}{\sigma_3}\frac{\partial \hat{Z}_3}{\partial R_1} & \frac{1}{\sigma_3}\frac{\partial \hat{Z}_3}{\partial \tau_1} & \cdots & \frac{1}{\sigma_3}\frac{\partial \hat{Z}_3}{\partial R_k} & \frac{1}{\sigma_3}\frac{\partial \hat{Z}_3}{\partial \tau_k} \\ \vdots & & & & & \\ \frac{1}{\sigma_{2n}}\frac{\partial \hat{Z}_{2n}}{\partial R_0} & \frac{1}{\sigma_{2n}}\frac{\partial \hat{Z}_{2n}}{\partial R_1} & \frac{1}{\sigma_{2n}}\frac{\partial \hat{Z}_{2n}}{\partial \tau_1} & \cdots & \frac{1}{\sigma_{2n}}\frac{\partial \hat{Z}_{2n}}{\partial R_k} & \frac{1}{\sigma_{2n}}\frac{\partial \hat{Z}_{2n}}{\partial \tau_k} \end{bmatrix} \begin{bmatrix} \begin{bmatrix} (R_{0,new} - Z_0) \\ (R_{1,new} - R_1) \\ (\tau_{1,new} - \tau_1) \\ (R_{2,new} - R_2) \\ \vdots \\ (\tau_{k,new} - \tau_k) \end{bmatrix} \end{bmatrix} = 0 \tag{6-17}$$

Let

$$A = \begin{bmatrix} \frac{1}{\sigma_1}\frac{\partial \hat{Z}_1}{\partial R_0} & \frac{1}{\sigma_1}\frac{\partial \hat{Z}_1}{\partial R_1} & \frac{1}{\sigma_1}\frac{\partial \hat{Z}_1}{\partial \tau_1} & \cdots & \frac{1}{\sigma_1}\frac{\partial \hat{Z}_1}{\partial R_k} & \frac{1}{\sigma_1}\frac{\partial \hat{Z}_1}{\partial \tau_k} \\ \frac{1}{\sigma_2}\frac{\partial \hat{Z}_2}{\partial R_0} & \frac{1}{\sigma_2}\frac{\partial \hat{Z}_2}{\partial R_1} & \frac{1}{\sigma_2}\frac{\partial \hat{Z}_2}{\partial \tau_1} & \cdots & \frac{1}{\sigma_2}\frac{\partial \hat{Z}_2}{\partial R_k} & \frac{1}{\sigma_2}\frac{\partial \hat{Z}_2}{\partial \tau_k} \\ \frac{1}{\sigma_3}\frac{\partial \hat{Z}_3}{\partial R_0} & \frac{1}{\sigma_3}\frac{\partial \hat{Z}_3}{\partial R_1} & \frac{1}{\sigma_3}\frac{\partial \hat{Z}_3}{\partial \tau_1} & \cdots & \frac{1}{\sigma_3}\frac{\partial \hat{Z}_3}{\partial R_k} & \frac{1}{\sigma_3}\frac{\partial \hat{Z}_3}{\partial \tau_k} \\ \vdots & & & & & \\ \frac{1}{\sigma_{2n}}\frac{\partial \hat{Z}_{2n}}{\partial R_0} & \frac{1}{\sigma_{2n}}\frac{\partial \hat{Z}_{2n}}{\partial R_1} & \frac{1}{\sigma_{2n}}\frac{\partial \hat{Z}_{2n}}{\partial \tau_1} & \cdots & \frac{1}{\sigma_{2n}}\frac{\partial \hat{Z}_{2n}}{\partial R_k} & \frac{1}{\sigma_{2n}}\frac{\partial \hat{Z}_{2n}}{\partial \tau_k} \end{bmatrix} \tag{6-18}$$

and

$$err(\theta) = \begin{bmatrix} \frac{(Z_1-\hat{Z}_1(\theta))}{\sigma_1} \\ \frac{(Z_2-\hat{Z}_2(\theta))}{\sigma_2} \\ \frac{(Z_3-\hat{Z}_3(\theta))}{\sigma_3} \\ \vdots \\ \frac{(Z_{2n-1}-\hat{Z}_{2n-1}(\theta))}{\sigma_{2n-1}} \\ \frac{(Z_{2n}-\hat{Z}_{2n}(\theta))}{\sigma_{2n}} \end{bmatrix} \tag{6-19}$$

A and $err(\theta)$ are substituted in equation (6-17). This gives

$$A^T \left[err(\theta) - A \left[\theta_{new} - \theta\right]\right] = 0 \tag{6-20}$$

Rearrangement of the equation (6-20) for θ_{new} yields

$$\theta_{new} = \theta + (A^T A)^{-1} A^T err(\theta) \tag{6-21}$$

A successive solution of above equation provide a parameter vector θ_{new}, where residual sum of square $SSE(\theta_new)$ is minimum.

6.5.1 Solution Method

Estimation of θ was obtained by the Levenberg–Marquardt method.[77,78] The method interpolates between Gradient method[79] and Steepest decent method.[79] The Hessian matrix $H(\theta)$ used in steepest decent matrix is equal to $A^T A$. Marquard[80] suggested an alternative computation scheme to ensure that inverse of the Hessian matrix always exists and $H^{-1}(\theta)$ is a positive definite. He proposed that $H(\theta)$ should be defined as:

$$H(\theta) = \left[A^T(\theta) A(\theta) + \lambda I\right] \tag{6-22}$$

where λ is a positive number. After substitution of $H(\theta)$ in equation (6-20) in place of $A^T A$ yields

$$\theta_{new} = \theta + H^{-1}(\theta) A^T(\theta) err(\theta) \tag{6-23}$$

The calculation of θ, which minimizes $SSE(\theta)$, involves the repeated calculation of $H(\theta)$ and θ_{new} using equation (6-22) and (6-23). The steps followed in the calculation of parameter set θ were:

1. The initial value of parameter set θ was chosen.

2. $A(\theta)$, $err(\theta)$ and $A^T(\theta) A(\theta)$ were calculated.

3. A value of $\lambda = \lambda_{low}$ was selected, and $H(\theta)$ was calculated using equation (6-22).

4. A value of θ_{new} was gotten by equation (6-23) and $SSE(\theta)$ was calculated.

5. If $SSE(\theta_{new}) < SSE(\theta)$, the value of θ was assigned to be θ_{new}, and λ was updated to $\lambda \times \lambda_{low}$. A check was applied for the convergence criterion. If convergence criterion was satisfactorily met, the calculations were stopped, otherwise, a new $H(\theta)$ was calculated using equation (6-22). The calculations were again repeated starting from step 4.

6. If $SSE(\theta_{new}) > SSE(\theta)$, the value λ was set to $\lambda \times \lambda_{high}$, $H(\theta)$ was calculated using equation (6-22). The calculations were again repeated starting from step 4.

The values of λ_{low} and λ_{high} can be arbitrarily chosen. Suggested values of λ_{low} and λ_{high} are 1.0×10^{-3} and 1.0×10^{3}, respectively.

6.5.2 Convergence Criterion

There convergence criteria were used for Levenberg–Marquardt method. These criteria were tested in the step 5 of the calculation procedure. They were tested in the order listed below.

1. If the relative error in $SSE(\theta)$ *i.e.*, $\frac{(SSE(\theta_{new})-SSE(\theta))}{(1.0\times10^{-20}+SSE(\theta))}$ was found less than prescribed value, the second convergence criterion was tested. 1.0×10^{-20} was added in the denominator to avoid a numerical singularity when $SSE(\theta)$ =0.0

2. The second convergence criterion is the relative error in the parameter set *i.e.*, If $\frac{(\theta_{new}-\theta)}{(1.0\times10^{-20}+\theta)}$ is less than prescribed value, calculations were stopped.

3. If the number of iterations exceeded the maximum allocated number, calculations were stopped.

6.5.3 Weighting Strategy

Weighting is an essential component of nonlinear regression, because the effect of noisy data on parameter estimation can be reduced by assigning them less weight. A sound weighting strategy yields a better estimate of parameter set θ with smaller confidence interval. In the first application of CNSL to EIS data, Macdonald and Garber[76] used the unity weighting *i.e.*, $\sigma_r = \sigma_j = 1$. They also suggested that standard deviation of measurement X can be written as

$$\sigma_x = a\,|X|^n \tag{6-24}$$

where a is a proportionality constant and the exponent n satisfies $1 \geq n \geq -4$. The authors tested the above weighting scheme for different values of n and found that confidence intervals of parameter set were smallest when $-\frac{1}{2} \leq n \leq -1$.

Several other weighting strategies have been proposed after Macdonald *et al.*[76] Zoltowski[81–83] suggested a modulus weighting scheme. He proposed that

$$\sigma_r(\omega) = \sigma_j(\omega) = a\,|Z(\omega)| \tag{6-25}$$

where a is a proportionality constant. He argued that the modulus weighting scheme is appropriate when errors in real and imaginary impedance are correlated. Boukamp[84] supported the idea of Zoltowski and used modulus weighting scheme in his calculations. The idea of modulus weighting was refuted by Macdonald and Potter.[85] They stated that errors in real and imaginary part of the impedance are correlated by the measuring apparatus. They suggested the proportional weighting scheme (PWT). In PWT, the standard deviations of real and imaginary part were assumed to be proportional to the magnitude of the measurement of that component. Two other weighting strategies, which could be reduced to proportional weighting scheme, were also suggested by Macdonald and Potter. The first was called VWT and it's form is described in equation (6-24). The second

was termed as CWT. It can be written as

$$\sigma_k^X = 1 + B_w \left|X_k\right|^n \tag{6-26}$$

where B_w is a proportionality constant. For $B_w = 0$, equation (6-26) yields unity weighting. For large B_w and $n = 1$, it converges to proportional weighting. Another weighting scheme was termed as residual iteration weighting(RWT[85]) in which each term in the objective function is weighted by the residual error between model prediction and observed value at k^{th} frequency at last iteration.

Agarwal *et al.*[32] took a different approach for the estimation of standard deviation. They carried out several repeated measurement for stationary and pseudo-stationary systems(A pseudo stationary system does not change much over a scan but it may change considerably over a long period of time.). They observed that the standard deviations of real and imaginary parts are functions of frequency, and their magnitudes are same for a given frequency. They proposed that

$$\sigma_r = \sigma_j = \sigma = \alpha \left|Z_j\right| + \beta \left|Z_r\right| + \gamma \frac{\left|Z\right|^2}{R_m} \tag{6-27}$$

where Z_r and Z_j are the real and imaginary part of impedance Z and α, β, γ and R_m are constants which are determined experimentally. A modification to equation (6-27) was suggested by Orazem *et al.*[86] to include an additional parameter. The modified error structure model was suggested as

$$\sigma_r = \sigma_j = \sigma = \alpha \left|Z_j\right| + \beta \left|Z_r\right| + \gamma \frac{\left|Z\right|^2}{R_m} + \delta \tag{6-28}$$

where δ is the additional parameter. Later, Orazem *et al.*,[87] refined the error structure based upon further experimental observation. Their refined model was proposed as

$$\sigma_r = \sigma_j = \sigma = \alpha \left|Z_j\right| + \beta \left|Z_r - R_\infty\right| + \gamma \frac{\left|Z\right|^2}{R_m} + \delta \tag{6-29}$$

where R_∞ is the additional constant. Equation (6-29)is applicable for systems where electrolyte resistance are much higher to the impedance of system. Durbha

et al.[88] gave an analytic proof for the equality of variance for real and imaginary part of the impedance.

6.5.4 Computer Program Implementation

A FORTRAN code was written to implement the regression of the measurement models. The software package titled Algorithm 717[89] was downloaded from Netlib Repository located at Oak Ridge National Laboratory. A usage summary of the software can be found in a report by Gay.[90] The software comprises of several subroutines. The main subroutine of the software is called DGLGB. The input to the subroutine consists of data set, the functional form the measurement model, parameter's lower and upper bound, and gradients of the input measurement model with respect to its parameters. The output from the code contains regressed model parameters, the variance-covariance matrix, and the level of convergence. A graphical interface called MMToolBox of the FORTRAN code was developed in-house using VISUAL BASIC.

6.5.5 Confidence Interval

The performance of the weighting strategy can be seen through the estimated parameter value and their confidence interval. If the confidence interval *i.e.*, parameter value$\pm 2\sigma$ does not contain zero, it can be said with 95.4% probability that the estimated parameter is not equal to zero. The variance for i^{th} parameter is given by

$$\sigma^2_{(i_{th}parameter)} = \alpha_{ii} s^2$$

where α_{ii} is i^{th} diagonal element of the matrix $A^T A$ and $s^2 = \frac{SSE(\theta)}{(2N-2k-1)}$ for k Voigt elements. This method of calculating confidence interval is still a matter of research. Since the measurement model was linearised around parameter set θ, the above calculation procedure gives the confidence intervals for linearised model parameter set.

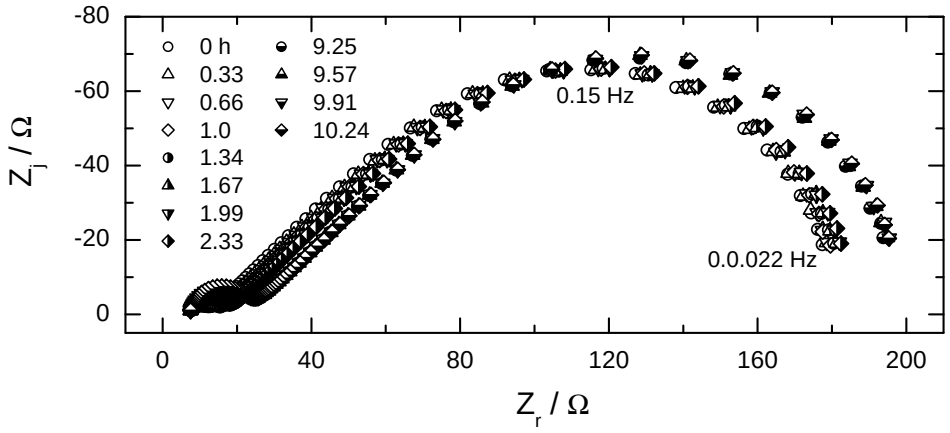

Figure 6-2: Impedance spectra obtained for the reduction of ferricyanide on a platinum rotating disk electrode.

6.6 Method

The use of measurement models for analysis of errors requires replicate measurement of the impedance response using the same measurement frequencies for each replicate. The discussion here is centered on a series of impedance measurements reported by Orazem *et al.*[15] for reduction of ferricyanide on a platinum disk rotating at 120 rpm. The electrolyte consisted of 0.01 M $K_3Fe(CN)_6$ and 0.01 M $K_4Fe(CN)_6$ in 1 M KCl. The temperature was controlled at 25.0±0.1 °C. The measurements were conducted under potentiostatic regulation. For the experiments described here, the potential was set at a value for which the current measured was 1/4 of the mass-transfer-limited current. A subset of the impedance results, consisting of the first four scans collected, the second four scans and the final four scans, are presented in Figure 6-2. The sequence of measurements indicates that there was a substantial change from one measurement to another. This lack of reproducibility, in itself, raises the question of whether each individual measurement was corrupted by nonstationary phenomena. The issue of whether an individual measurement was corrupted by nonstationary phenomena is addressed in a subsequent section by evaluation of consistency with the Kramers-Kronig relations.

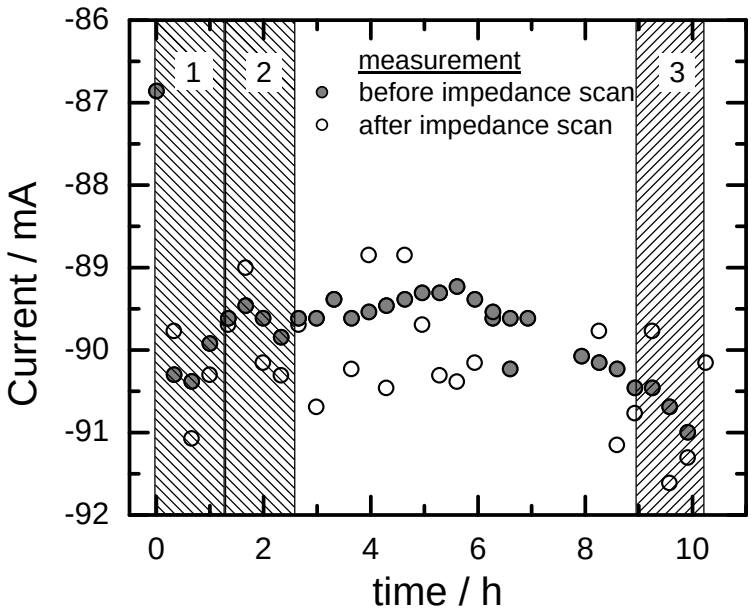

Figure 6-3: Current measurements before and after the impedance scans shown in Figure 6-2. The data sets singled out for error analysis are highlighted.

The current measured before and after each scan is reported in Figure 6-3. The significant shift in measured current before and after the first scan taken suggests that the first measurement may have been influenced by changes in system properties. The DC current values do not shed light on subsequent measurements.

6.7 Results

The subsets selected for interpretation by the Voigt and transfer-function measurement models are indicated in Figure 6-3. Each of three sets were treated as replicated measurements. The objective of this selection was to determine the influence of the nonstationarity evident in the first scan on the error structure obtained through the measurement model approach. The subsequent sets of four are not replicated in the sense that there are systematic differences between the scans, but each scan will be found to satisfy the Kramers-Kronig relations.

6.7.1 Evaluation of Stochastic Errors

To eliminate the contribution of the drift from scan to scan, the Voigt and transfer-function measurement models were regressed to each scan using the max-

imum number of parameters that could be resolved from the data. This value was determined by calculating the confidence interval for each parameter using the assumption that the regression could be linearized about the trial solution. Under these conditions, the standard deviations for parameter estimates could be determined using the standard equations for linear regression. For the determination of error structure, modulus weighting was employed. In the subsequent evaluation of consistency with the Kramers-Kronig relations, the weighting was based on the error structure determined in this step.

Following Agarwal *et al.*,[32] the variance of real and imaginary residual errors can be obtained as a function of frequency, *i.e.*,

$$\sigma^2_{Z_r}(\omega) = \frac{1}{N-1}\sum_{k=1}^{N}\left(\varepsilon_{\mathrm{res},Z_r,k}(\omega) - \overline{\varepsilon}_{\mathrm{res},Z_r}(\omega)\right)^2 \tag{6-30}$$

where N is the number of replicates, $\varepsilon_{\mathrm{res},Z_r,k}$ represents the residual error at frequency ω for scan k, obtained from its unique model, and $\overline{\varepsilon}_{\mathrm{res},Z_r}$ represents the mean value for the residual errors at frequency ω. A similar expression is used for the imaginary part of the impedance. Equation (6-30) can provide a good estimate for the variance of stochastic errors under the following set of assumptions:

1. The model parameters account for the drift from one scan to another.

2. The frequency-dependent systematic errors associated with the lack of fit are unchanged from one scan to another. This assumption is justified only if the same number of statistically significant parameters are used for each scan and if the same features are evident in the successive impedance scans.

3. The systematic errors associated with instrument artifacts are unchanged from one scan to another. This assumption is justified under the conditions that Assumption (2) is justified.

4. The systematic error associated with nonstationary behavior is unchanged from one scan to another.

The objective of the present work was to examine the validity of assumption (1) by seeing whether the error structure obtained is dependent on the measurement model used. A finding that the error structure depends on the model used would undermine the very premise on which the measurement model approach is based.

After assumption (1), assumption (4) represents the the most serious restriction to the measurement model approach for estimation of error structure. It can be anticipated that the influence of nonstationarity may be largest for the first of a sequence of impedance measurements. Under conditions that the data sets do not satisfy the Kramers-Kronig relations, the measurement model approach may overestimate the standard deviation of stochastic errors. The incorrect error structure may bias the regression used to check consistency with the Kramers-Kronig relations. This difficulty can be addressed in an iterative approach in which the data identified as being inconsistent with the Kramers-Kronig relations are removed from the data set used to obtain the stochastic error structure estimate. In any case, the estimate obtained using the measurement model approach will be more accurate than would be obtained by direct calculation of the standard deviation. Thus, the variance of the real and imaginary residual errors provides a good estimate for the frequency-dependent variance of the stochastic noise in the measurement.

The deviation of individual spectra from the mean value for data set #1, the first four spectra, is presented in Figure 6.4(a) and 6.4(b) for real and imaginary parts of the impedance, respectively. Direct calculation of the standard deviation for data set #1 clearly includes a significant contribution from systematic changes between spectra, and, thus, significantly overestimates the standard deviation of stochastic errors.

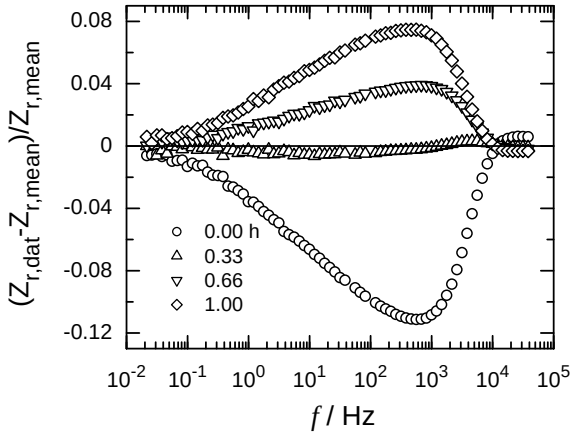

(a)

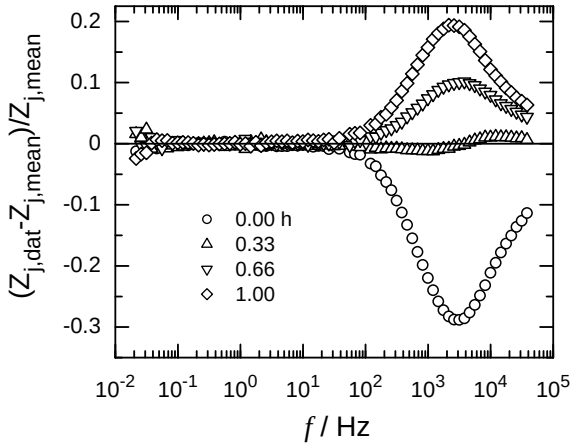

(b)

Figure 6-4: Relative departures from the mean value for the first four spectra given in Figure 6-2: a) real part and b) imaginary part of the impedance.

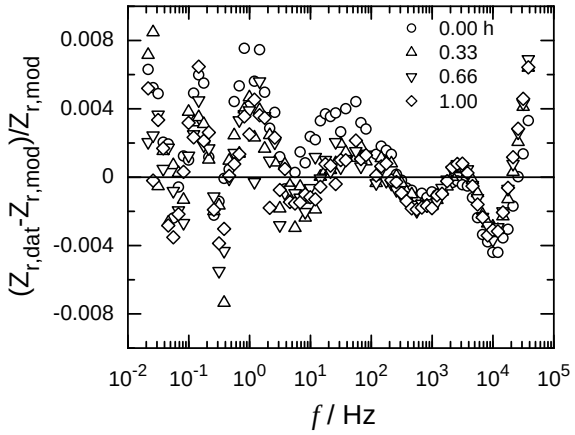

(a)

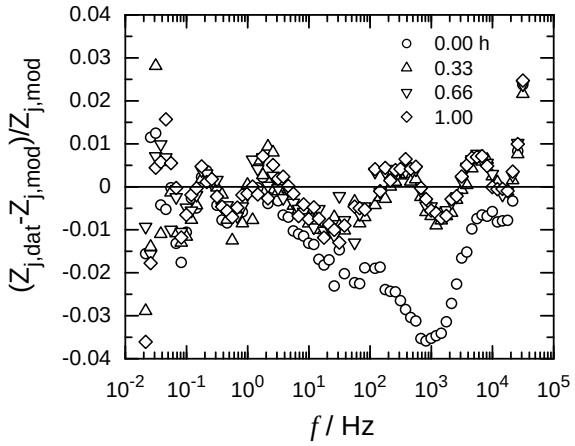

(b)

Figure 6-5: Residual errors for the fit of a transfer-function measurement model, equation (6-3), to the impedance data presented in Figure 6-2: a) real part and b) imaginary part of the impedance.

The transfer-function measurement model was regressed to each of the four spectra which comprise Date Set #1 using the maximum number of parameters that could be obtained with 95.4% confidence intervals that did not include zero. The model required 11 parameters. The relative residual errors for these regressions are presented in Figure 6.5(a) and 6.5(b), respectively, for real and imaginary parts of the impedance. The residual errors were smaller than 0.8 percent for the real part of the impedance and smaller than 3 percent for the imaginary part. The results presented in Figure 6.5(b) show that the relative residual errors

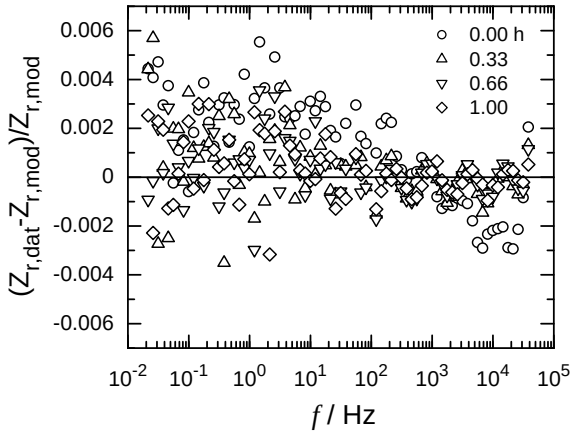

(a)

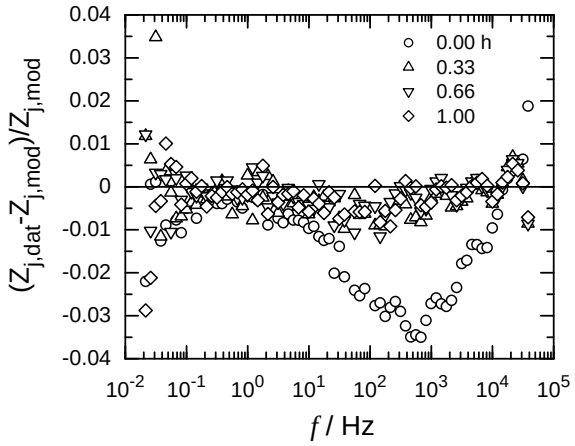

(b)

Figure 6-6: Residual errors for the fit of a Voigt measurement model, equation (6-1), to the impedance data presented in Figure 6-2: a) real part and b) imaginary part of the impedance.

for the imaginary impedance of the first spectrum measured do not overlay the residual errors for subsequent spectra. These results suggest that the first measurement was subject to bias errors that were not evident in subsequent spectra.

The Voigt measurement model was applied as well to each of the four spectra that comprise Set #1. Ten Voigt elements, or 21 parameters were used. The resulting relative residual errors are presented in Figures 6.6(a) and 6.6(b) for real and imaginary parts of the impedance, respectively. The residual errors were comparable to those shown in Figure 6-5. The residual errors were smaller than 0.6 percent

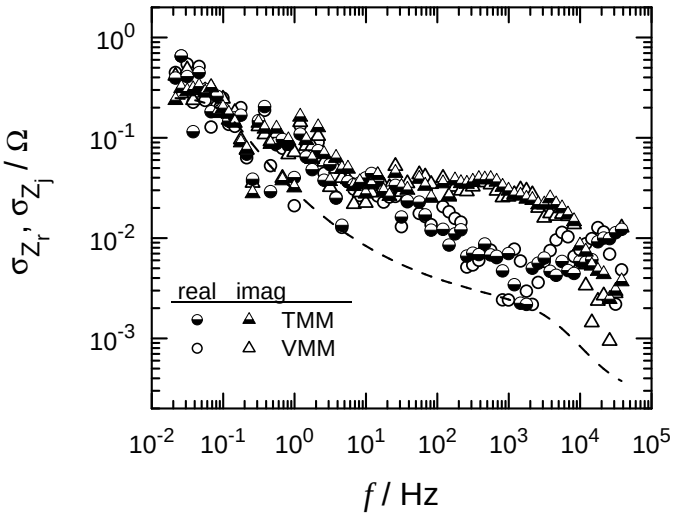

Figure 6-7: Standard Deviations for the data presented in Figure 6-2, obtained from the residual errors presented in Figures 6-5 and 6-6. The dashed line represents the results obtained for the Kramers-Kronig -consistent data in set 2 and3.

for the real part of the impedance and smaller than 3 percent for the imaginary part. In agreement with Figure 6.5(b), the results presented in Figure 6.6(b) show that the relative residual errors for the imaginary impedance of the first spectrum measured do not overlay the residual errors for subsequent spectra.

The standard deviation of the stochastic part of the measurements was estimated by calculating the standard deviations of the residual errors presented in Figures 6-5 and 6-6. The results, presented in Figure 6-7, show that the error structure obtained using the transfer-function and Voigt measurement models are in full agreement. The standard deviations for real and imaginary parts of the impedance are equal at low frequencies, but at higher frequencies, the standard deviation for the imaginary part is much larger than that seen for the real part of the impedance. The observed inequality of standard deviations is in conflict with the observation that the variance of stochastic errors of real and imaginary parts of the impedance are equal when obtained using instrumentation based on Fourier analysis.[91–93] Thus, it is likely that bias errors not filtered by the measurement

model strategy contributed to the error structure. This suggestion is supported by the observation that the errors are larger than the errors represented by the dashed line that were estimated from subsequent, more stationary, sets of data. The principal result shown in Figure 6-7 is that, in spite of the difficulties caused by unfiltered bias errors, the error structure obtained using the two measurement models are in full agreement at all frequencies.

A parallel treatment was made for the second four spectra which comprise Set #2. As shown in Figure 6-8, significant systematic differences are seen, even though each scan might be assumed to be more stationary than those in Set #1. The relative residual errors, shown in Figure 6-9 for the transfer-function measurement model and in Figure 6-10 for the Voigt measurement model, are now closely grouped for each of the spectra analyzed. The trending shown in Figures 6-9 and 6-10 indicate that the measurement models do not describe completely the physics of the experimental system. The standard deviation of the residual errors obtained using the transfer-function and Voigt measurement models, as shown in Figure 6.11(a), are in agreement. The error structure obtained for Set #3 and presented plotted in Figure 6.11(b) shows a similar agreement between results obtained using the transfer-function and the Voigt measurement models. The arbitrary choice of measurement model does not change the characteristics of the estimated stochastic error structure. This work serves to validate the foundation of the measurement model approach for error analysis of non-replicated measurements.

6.7.2 Evaluation of Bias Errors

In principle, since the Voigt measurement model is itself consistent with the Kramers-Kronig relations, the ability to fit this model to within the noise level of the measurement should indicate that the data are consistent. A refined ap-

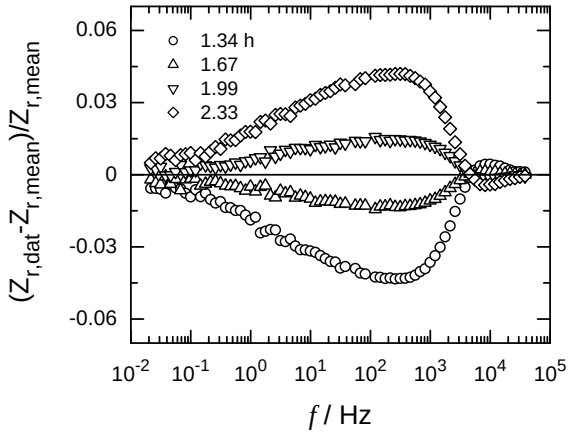

(a)

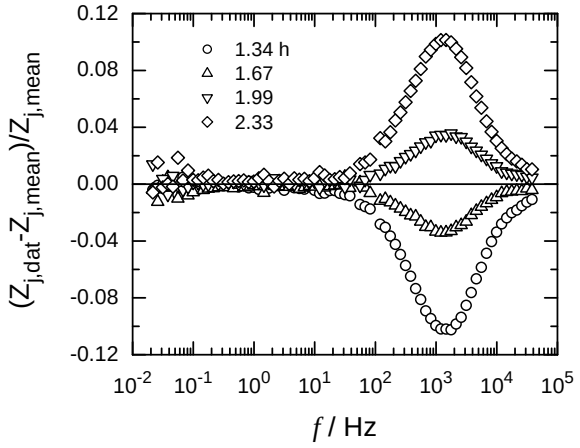

(b)

Figure 6-8: Relative departures from the mean value for the second four spectra given in Figure 6-2: a) real part and b) imaginary part of the impedance.

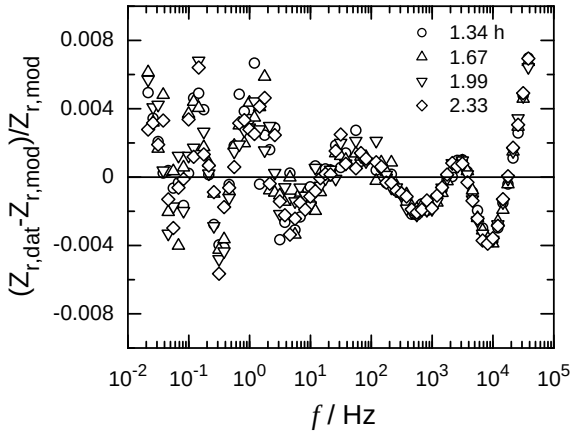

(a)

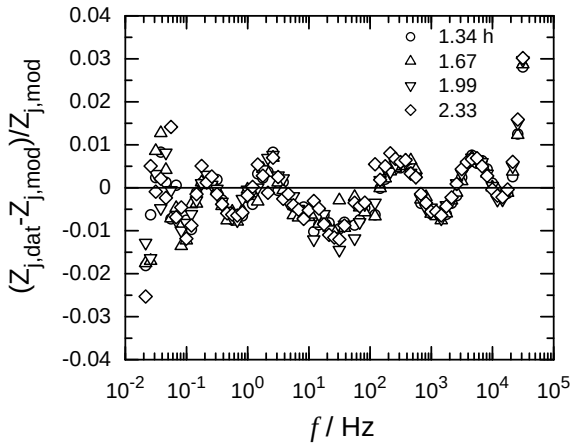

(b)

Figure 6-9: Residual errors for the fit of a transfer-function measurement model, equation (6-3), to the impedance data presented in Figure 6-2: a) real part and b) imaginary part of the impedance.

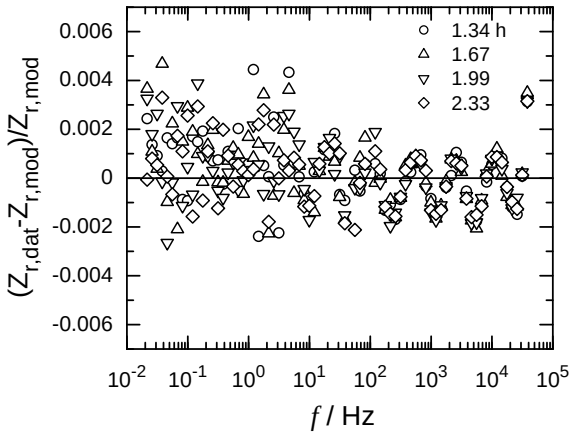

(a)

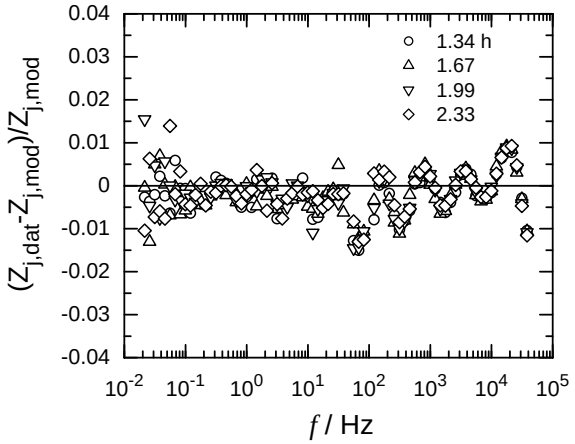

(b)

Figure 6-10: Residual errors for the fit of a Voigt measurement model, equation (6-1), to the impedance data presented in Figure 6-2: a) real part and b) imaginary part of the impedance.

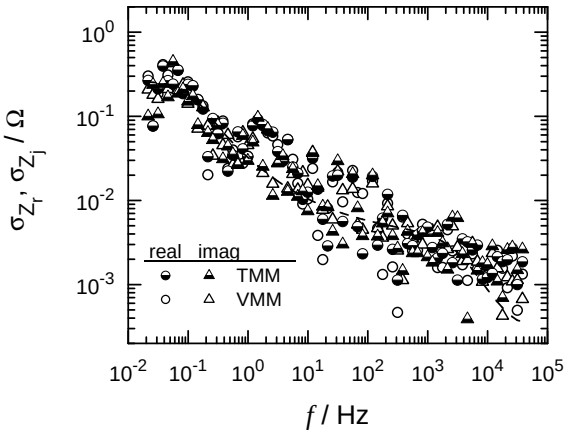

(a)

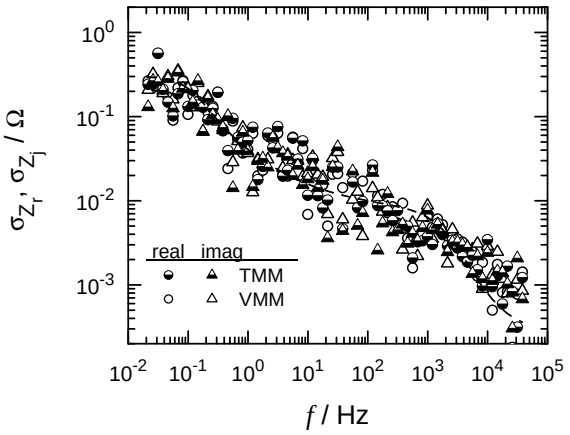

(b)

Figure 6-11: Standard Deviations for the data presented in Figure 6-2: a) results obtained from the residual errors presented in Figures 6-9 and 6-10, and b) results obtained from the residual errors for Data set 3. The dashed line represents the results obtained for the Kramers-Kronig -consistent data in set 2 and 3.

proach was developed to resolve the ambiguity that exists when the model does not provide a good fit to the data. The lack of fit of the model could be due to causes other than inconsistency with the Kramers-Kronig relations. For example, the number of frequencies measured might be insufficient to allow regression with a sufficient number of Voigt parameters, the noise level of the measurement might be too large to allow regression with a sufficient number of Voigt parameters, or the initial guesses for the non-linear regression could be poorly chosen.

While in principle a complex fit of the measurement model could be used to assess the consistency of impedance data, sequential regression to either the real or the imaginary provides greater sensitivity to lack of consistency. The optimal approach is to fit the model to the component that contains the greatest amount of information. Our work suggests that imaginary part of the impedance is much more sensitive to contributions of minor line shapes than is the real part of the impedance. Typically, more Voigt lineshapes can be resolved when fitting to the imaginary part of the impedance than can be resolved when fitting to the real part. The solution resistance cannot be obtained by fitting the measurement model to the imaginary part of the impedance. The solution resistance is treated as an arbitrarily adjustable parameter when fitting to the imaginary part of the impedance.

The application of measurement models to assess consistency with the Kramers-Kronig relations is demonstrated for the first scan shown in Figure 6-2. A measurement model was fit to the imaginary part of the spectrum using the experimentally determined error structure to weight the regression. The number of Voigt elements was increased until the maximum number of statistically significant parameters was obtained. The fit to the imaginary part is shown in Figure 6.12(a), where dotted lines represent the $\pm 2\sigma$ bound for the stochastic error structure determined in the previous section. The corresponding prediction of the real

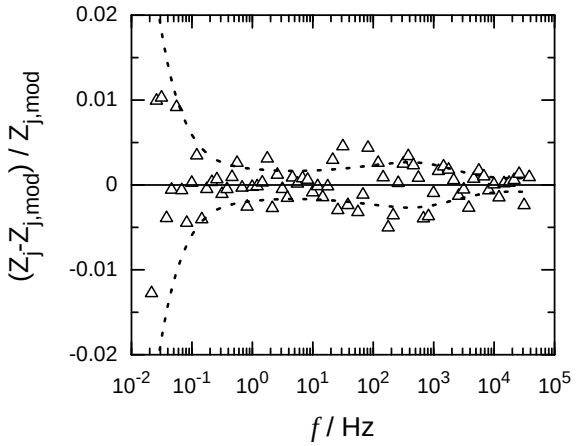

(a)

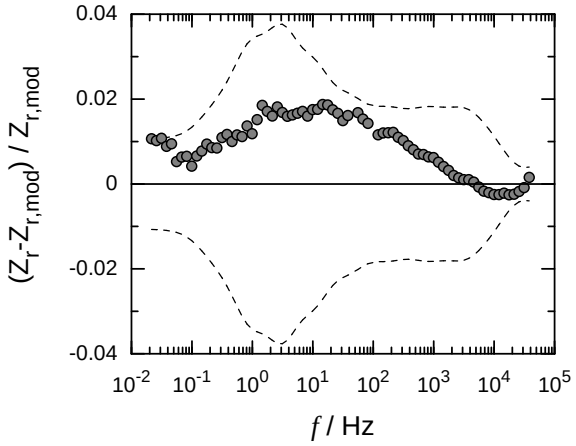

(b)

Figure 6-12: Residual errors for the fit of a Voigt measurement model to the imaginary part of the first impedance spectrum presented in Figure 6-2. a) fit to the imaginary part, where dashed lines represent the $\pm 2\sigma$ bound for the stochastic error structure determined in the previous section; b) prediction of the real part where dashed lines represent the 95.4% confidence interval for the model obtained by Monte Carlo simulation using the calculated confidence intervals for the estimated parameters.

part is given in Figure 6.12(b) where dashed lines represent the 95.4% confidence interval for the model obtained by Monte Carlo simulation using the calculated confidence intervals for the estimated parameters. The systematic departure of the real part from its expected value evident in Figure 6.12(b) is symptomatic of inconsistency with the Kramers-Kronig relations; however, only a few data points at low frequency fell outside the confidence interval for the model. Regression to the reduced data set provides an increase in the number of parameters that could be resolved, confirming the determination that the data was corrupted by non-stationary phenomena. Application of the Voigt measurement model to all other spectra revealed that the data were consistent with the Kramers-Kronig relations at all frequencies.

A similar analysis was performed for the same data set using the transfer-function measurement model. The fit to the imaginary part is shown in Figure 6.13(a), where dotted lines represent the $\pm 2\sigma$ bound for the stochastic error structure determined in the previous section. The significant trending apparent in Figure 6.13(a) reflects the smaller number of parameters that could be resolved. The corresponding prediction of the real part is given in Figure 6.13(b) where dashed lines represent the 95.4% confidence interval for the model obtained by Monte Carlo simulation using the calculated confidence intervals for the estimated parameters. The confidence interval shown in Figure 6.13(b) for the transfer-function measurement model was much larger than that estimated for the Voigt measurement model and shown in Figure 6.12(b). Thus, the regression procedure could not be used to justify eliminating data based on failure to conform to the Kramers-Kronig relations.

An appreciation for the differences between the Voigt and transfer-function measurement models can be obtained by examination of the model parameters

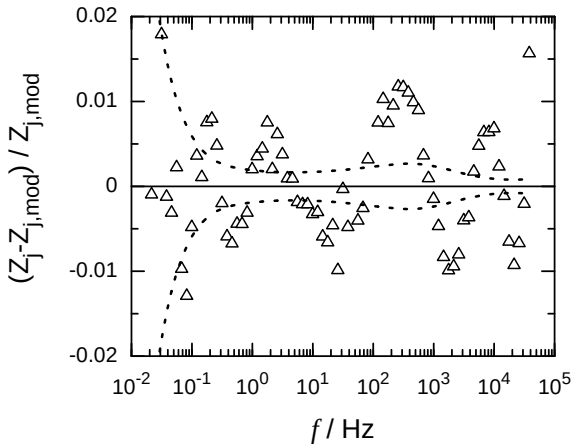

(a)

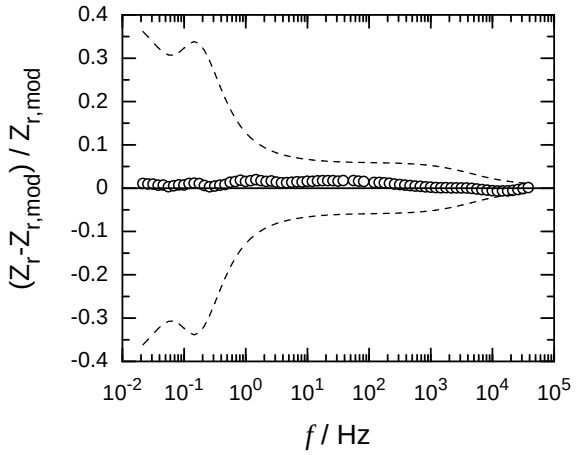

(b)

Figure 6-13: Residual errors for the fit of a transfer-function measurement model to the imaginary part of the first impedance spectrum presented in Figure 6-2. a) fit to the imaginary part, where dashed lines represent the $\pm 2\sigma$ bound for the stochastic error structure determined in the previous section; b) prediction of the real part where dashed lines represent the 95.4% confidence interval for the model obtained by Monte Carlo simulation using the calculated confidence intervals for the estimated parameters.

Table 6.1: Model parameters for the fit of a Voigt measurement model to impedance scans #1, #5, and #25 presented in Figure 6-3.

Variable	Spectrum #1	Spectrum #5	Spectrum #25
τ_1 / 10^{-6}s	2.74 ± 0.16	2.65 ± 0.14	1.62 ± 0.29
R_1 / Ω	0.5640 ± 0.0056	0.5526 ± 0.0051	0.610 ± 0.058
τ_2 / 10^{-5}s	1.837 ± 0.055	1.93 ± 0.10	5.96 ± 0.13
R_2/ Ω	1.9056 ± 0.0912	1.35 ± 0.16	8.23 ± 0.44
τ_3 / 10^{-5}s	4.82 ± 1.87	15.93 ± 0.96	1.23 ± 0.08
R_3/ Ω	2.28 ± 0.07	1.89 ± 0.08	0.496 ± 0.018
τ_4 / 10^{-5}s	21.24 ± 0.12	4.63 ± 0.12	61.28 ± 3.95
R_4/ Ω	1.35 ± 0.037	5.69 ± 0.09	2.56 ± 0.08
τ_5 / 10^{-4}s	9.71 ± 0.56	7.62 ± 0.39	1.283 ± 0.055
R_5/ Ω	1.880 ± 0.066	1.962 ± 0.053	6.46 ± 0.38
τ_6 / 10^{-3}s	4.08 ± 0.24	3.65 ± 0.17	2.90 ± 0.21
R_6/ Ω	3.23 ± 0.14	3.31 ± 0.11	3.27 ± 0.14
τ_7 / 10^{-2}s	1.59 ± 0.11	1.538 ± 0.073	1.247 ± 0.075
R_7/ Ω	5.85 ± 0.23	6.20 ± 0.20	6.06 ± 0.21
τ_8 / 10^{-2}s	5.78 ± 0.42	6.36 ± 0.33	5.18 ± 0.27
R_8/ Ω	10.31 ± 0.49	12.06 ± 0.52	11.6 ± 0.4
τ_9 / s	0.2029 ± 0.0092	0.221 ± 0.010	0.1955 ± 0.0070
R_9/ Ω	20.38 ± 0.52	19.26 ± 0.48	20.77 ± 0.41
τ_{10} / s	1.120 ± 0.007	1.127 ± 0.007	1.142 ± 0.006
R_{10}/Ω	123.5 ± 0.50	123.22 ± 0.52	131.01 ± 0.41
R_e/Ω	7.57 (fixed)	7.57 (fixed)	6.9857 (fixed)

and associated standard deviations. The standard deviations were calculated under the assumption that the nonlinear regression could be linearized about the trial solution. Thus, the standard equations could be used for calculation of the standard deviation of parameter estimates.[60]

The Voigt measurement model parameters obtained by regression to the imaginary part of the impedance are presented in Table 6.1 along with the standard deviations. The electrolyte resistance was assumed to be a constant in the regression as the model for the imaginary part of the impedance is independent of solution resistance. The structure of the Voigt model is such that the Voigt elements have their most significant contribution near its characteristic frequency. Thus, the

Table 6.2: Model parameters for the fit of a Transfer function measurement model to the impedance scan #1,#5, and #25 presented in Figure 6-3.

Variable	Spectrum #1	Spectrum #5	Spectrum #25
b_0 / $10^6\ \Omega$	4.5521 ± 0.6943	3.2792 ± 0.8019	5.9425 ± 1.9083
b_1 / $10^6\ \Omega s^{1/2}$	3.4334 ± 0.8660	2.4170 ± 0.9536	6.1223 ± 2.7290
b_2 / $10^6\ \Omega s$	3.9612 ± 0.1323	2.7820 ± 0.1719	2.9781 ± 0.6399
b_3 / $10^5\ \Omega s^{3/2}$	3.8834 ± 0.0945	3.3097 ± 0.0556	2.5932 ± 0.0385
b_4 / $10^2\ \Omega s^2$	10.575 ± 0.1556	6.5448 ± 0.0976	4.9186 ± 0.1359
b_5 / $\Omega s^{3/2}$	6.9962 (fixed)	6.9962 (fixed)	6.9962 (fixed)
a_0 / 10^4	2.5301 ± 0.4343	1.7860 ± 0.4858	3.2725 ± 1.1080
a_1 / $10^4 s^{1/2}$	2.1278 ± 0.2252	1.4323 ± 0.2487	1.7834 ± 0.5899
a_2 / $10^4 s$	3.5138 ± 0.8719	2.4923 ± 0.9571	6.1119 ± 2.5412
a_3 / $10^4 s^{3/2}$	3.1355 ± 0.0719	2.0817 ± 0.0297	1.1696 ± 0.0139
a_4 / s^2	104.29 ± 3.1515	48.016 ± 2.0385	24.122 ± 2.0288
a_5 / $s^{3/2}$	1.0 (fixed)	1.0 (fixed)	1.0 (fixed)

confidence interval at low frequencies is influenced most by the confidence intervals of the Voigt elements with the largest time constants. The results shown in Table 6.1 indicate that the confidence intervals for parameter estimates were very tight for the Voigt elements 9 and 10, which had the largest time constants. Similar results were seen for the 5th and 25th impedance scans made, for which the Kramers-Kronig relations were found to be satisfied.

The corresponding parameter estimates for the transfer-function measurement model are presented in Table 6.2. Parameters a_5 and b_5 were constants within the regression. The dominant terms in the model at the low-frequency limit are b_0 and a_0, which have large confidence intervals. The standard deviation represented a large portion of the parameter value; thus, the confidence interval for the model at low frequencies was large. The confidence interval at high frequencies is dominated by the higher order terms, which have a much tighter confidence interval. The smaller confidence interval at high frequency, evident in Figure 6.13(b), suggests that the transfer-function measurement model may be more sensitive to

high-frequency Kramers-Kronig inconsistencies that could arise from instrument artifacts.

6.8 Conclusions

The development of different forms of measurement models for impedance has allowed examination of key assumptions on which the use of such models to assess error structure are based. The stochastic error structures obtained using the transfer-function and Voigt measurement models were identical, even when non-stationary phenomena caused some of the data to be inconsistent with the Kramers-Kronig relations.

As reported in the literature,[34] the transfer-function measurement model could provide an adequate fit to impedance data with a smaller number of parameters than was obtained using the Voigt measurement model. The suitability of the measurement model for assessment of consistency with the Kramers-Kronig relations, however, was found to be more sensitive to the confidence interval for the parameter estimates than to the number of parameters in the model. A tighter confidence interval was obtained for Voigt measurement model, which made the Voigt measurement model a more sensitive tool for identification of inconsistencies with the Kramers-Kronig relations.

The development of different forms of measurement models for impedance has allowed examination of key assumptions on which the use of such models to assess error structure are based. The stochastic error structures obtained using the transfer-function and Voigt measurement models were identical. The suitability of the measurement model for assessment of consistency with the Kramers-Kronig relations, however, was found to be more sensitive to the confidence interval for the parameter estimates than to the number of parameters in the model.

CHAPTER 7
ELECTROCHEMICAL MEASUREMENTS OF OXYGEN REDUCTION AT NICKEL ELECTRODE

This chapter presents the experimental investigation of oxygen reduction reaction on commercially pure nickel. Nickel is known to have excellent corrosion resistance in neutral and alkaline salt solutions.[94] The composition of commercially pure nickel, also known as Nickel 270, electrode is listed in Table 7.1. The calculations in Chapter 5 show that current distribution should become uniform at about 25% of the mass- transfer limited current on a hemispherical electrode; whereas, it remains non-uniform even for a lower percentage value of total transport-limited current on a disk electrode in submerged impinging jet system. The objective of this study is to understand the difference in response of Electrochemical impedance spectroscopy (EIS) experiments at the disk and hemispherical electrode geometry in submerged impinging jet system for oxygen reduction reaction, thereby, delineating the effect of electrode geometry and current distribution by EIS experiments.

Table 7.1: Chemical composition of Nickel 270

Element	percentage composition
Carbon	0.006
Si	0.001
Cu	0.001
Ti	0.001
Zr	0.001
Ni	99.99

7.1 Reaction Mechanism of Oxygen Reduction

The reduction of oxygen is an important reaction in electrochemical systems dealing with corrosion of metals in aqueous and open environments.[95,96] It is also a source of energy generation in polymer electrolyte based fuel-cell[97] as well solid oxide fuel cell.[98] The mechanism of this important reaction is a source of debate in literature. In neutral aqueous electrolyte solutions, the oxygen reduction reactions is assumed to follow mainly two parallel reaction paths.[96] The first reaction path can be represented as:

$$\mathrm{O_2} + 2\mathrm{H_2O} + 4\mathrm{e^-} \rightarrow 4\mathrm{OH^-} \tag{7-1}$$

where one mole of $\mathrm{O_2}$ is reduced to four moles of $\mathrm{OH^-}$ ions by combining with two moles of water. This path is known as the four electron reaction path.

A parallel competing reaction mechanism also occurs simultaneously. It can be represented in two steps as following:

$$\mathrm{O_2} + 2\mathrm{H_2O} + 2\mathrm{e^-} \rightarrow 2\mathrm{H_2O_2} + 2\mathrm{OH^-} \tag{7-2}$$

where one mole of $\mathrm{O_2}$ is first reduced to two moles of $\mathrm{H_2O_2}$ and one mole $\mathrm{OH^-}$. This reaction is followed by:

$$2\mathrm{H_2O_2} + 4\mathrm{e^-} \rightarrow 4\mathrm{OH^-} \tag{7-3}$$

where hydrogen peroxide is further reduced to $\mathrm{OH^-}$ ions.

The evidence of secondary reaction paths described above has been widely reported in the literature. There exists a large body of experimental work in literature on the reaction mechanism of oxygen reduction. Most of the experimental work has been reported on a Rotating-Ring disk electrode (RRDE) system,[99] which consists of a disk electrode and a ring electrode. The ring electrode encircles the disk electrode, and thw electrodes are separated by insulating material. The reaction products formed at the disk electrode electrode are carried to the ring by

convection, where they can be detected by applying an appropriated potential to the ring. King *et al.*[100] studied the oxygen reduction reaction on copper in a neutral NaCl electrolyte solution using the RRDE. They concluded that oxygen is reduced via a series of pathways where hydrogen peroxide is involved as an adsorbed species. However, the formation of peroxide is dependent upon electronic state of the electrode potential. At high electronic states, *i.e.,* more cathodic electrode potentials, less peroxide will be produced. A similar study was conducted by Jovancicevic *et al.*[101] on iron electrode. They considered five possible mechanisms for this reaction. They concluded that $\mathrm{O_2}$ reduction proceeds via four-electron pathway with little $\mathrm{H_2O_2}$ as an intermediate on the bare iron.

Anastasijevic *et al.*[102–104]presented a mathematical approach to account for the number of electron transfers based upon experimental results. In their first paper,[104] they analyzed the experimental results of $\mathrm{O_2}$ reduction on a gold electrode. The mathematical model was mainly developed for a rotating disk electrode. Their analysis suggested that four electron steps dominate at higher cathodic potential; however, at low cathodic potentials, the model suggested that the two electron step is predominant. In subsequent papers,[102,103] a very general kinetic model of $\mathrm{O_2}$ reduction was presented for the RRDE. In this model, all electrochemical reactions were accounted as at most one-electron exchange processes. Their calculation results concluded that up to 90% of current is produced by four-electron step and the $\mathrm{H_2O_2}$ step accounted for 2-4%. The remaining flux was assumed to be due to the intermediate.

Hsueh *et al.*[105] studied the effect of electrolyte pH on oxygen reduction via $\mathrm{H_2O_2}$ formation. They concluded that a majority $(80-97\%)$of the reduction take place via four-electron reduction path, and the amount of $\mathrm{H_2O_2}$ produced is independent of the electrolyte pH. More recently, Vukmirovic *et al.*[106] studied the oxygen

reduction reaction on copper in a $0.1\mathrm{M}\mathrm{Na_2SO_4}$ electrolyte solution as a function of pH. Their experimental results suggested that the four-electron mechanism is predominant on copper in the alkaline medium over entire pH range.

Some work has been reported for $\mathrm{O_2}$ reduction on nickel electrode. Most notable, Shumilova *et al.*[107] studied the oxygen reduction reaction on nickel electrode in alkaline medium. They concluded that oxygen reduction via the intermediate hydrogen peroxide formation to that of oxygen reduction directly to hydroxyl ion depends on the surface state of the nickel electrode and its potential. In a subsequent study, Batotgky *et al.*[108] tried to quantify the reaction rate and quantity produced.

In the present work, it is assumed that the oxygen reduction occurs via four electron step. To the author's knowledge, this is the first time the EIS of the $\mathrm{O_2}$ reaction reaction is being reported.

7.2 Experimental

A disk electrode and a hemispherical electrode of $\frac{1}{4}$ inch diameter, embedded in nonconducting Acrylic, were made with a Nickel 270 rod. The disk electrode was mechanically polished with 2400 silicon carbide sand paper and 1200 grid emory cloth. An alumina slurry (polishing powder 0.05 $\mu\mathrm{m}$ in deionized water) was used during the mechanical polishing with emory cloth. Then, the electrode was was subjected to ultrasound cleaning in a 1:1 solution of deionized water and ethyl alcohol. The hemispherical electrode was mechanically polished by a convex cavity of emory cloth with alumina powder polishing slurry. It was also subjected to ultrasound cleaning before experiments.

The electrolyte solution of 0.1 M NaCl was made with purified water and sodium chloride salt. The water was purified with a BarnStead E-pure system. The purification process yielded the water with electrical resistivity greater than

16 MΩcm. The sodium chloride salt was procured from Fisher Scientific, Inc.

A schematic of the experimental setup is shown in Figure 7-1. The system consisted of the impinging jet electrochemical cell, electrolyte solution reservoir, centrifugal pump, piping, value, temperature controller, pH meter and peripherals. The piping, connections and solution reservoir were made of propylene. A cooling coil made of glass was submerged in the reservoir to maintain the desired temperature of electrolyte in the reservoir. The coolant temperature was controlled by a Fisher Scientific Isotemp Refrigerated Model 910. The temperature of the electrolyte was controlled at 25°±0.1°C. Temperature control is very important in aqueous electrochemistry, as transport properties of various species exhibit a very strong dependence on the temperature of the electrolyte. The pH of the solution was monitored by a Fisher Scientific model Accumet pH Meter 915. The electrolyte in the reservoir was bubbled with air to saturate it with oxygen . Air was first passed through a CO_2 scrubber to remove the carbon dioxide from air. The purified air was then bubbled for about thirty minutes before start of each experiment. The flow system pumped electrolyte solution, via a centrifugal pump powered by a VARIAC power supply.The fluid velocity in the jet was controlled by VARIAC output and use of a bypass line. The flow in the bypass line was controlled by a throttle valve. The fluid flow rate in the impinging jet was adjusted between 0.2 gallon/minute to 3.0 gallon/minute.

The electrochemical cell, presented schematically in Figure 7.2(a), consisted of a submerged axisymmetric jet, a counter electrode, a working electrode with holder, a port for reference electrode, and one window to monitor the sample *in situ* . The counter electrode was inserted into the cell through the top plate. It was made of platinum foil with dimensions of ca. 40.0 mm×40.0 mm. The impinging jet was centered over the sample. Important call dimensions are shown in Figure 7.2(b).

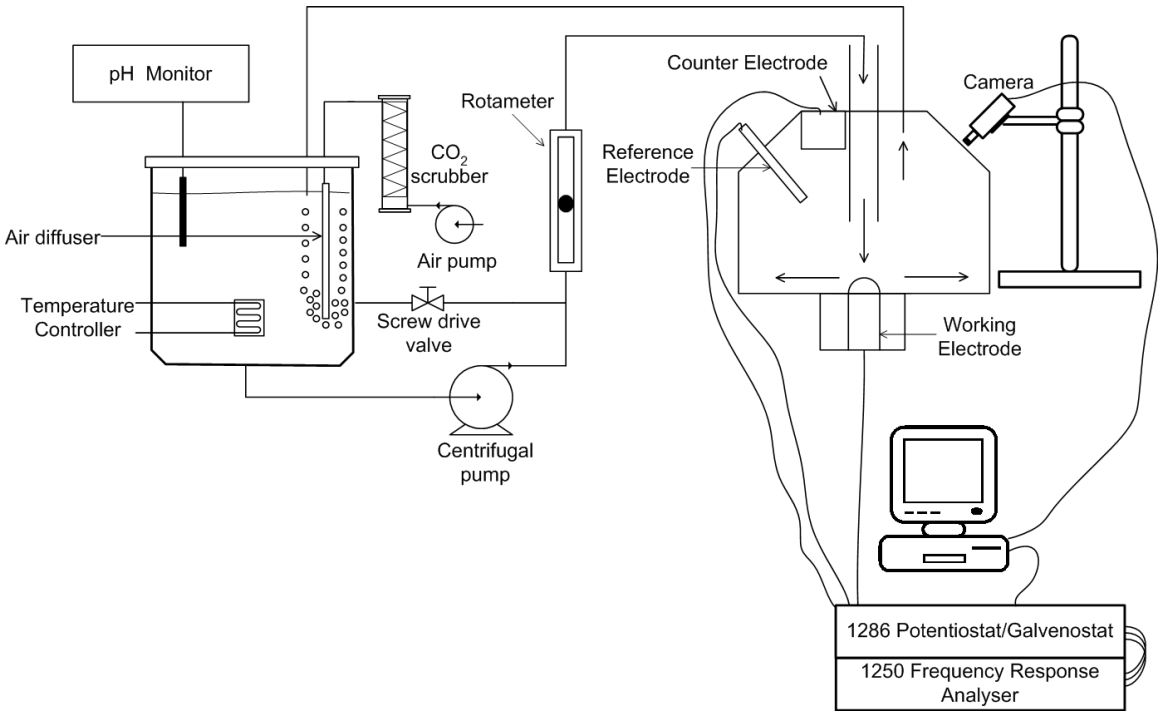

Figure 7-1: Experimental setup used for the study of oxygen reduction reaction.

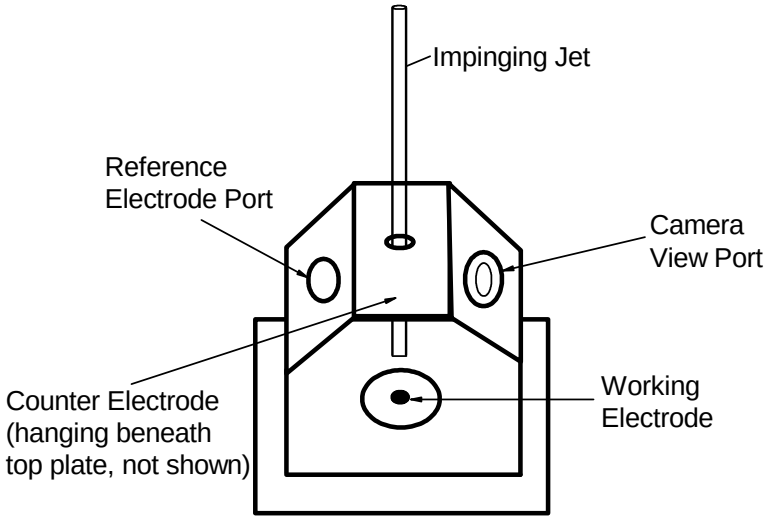

(a)

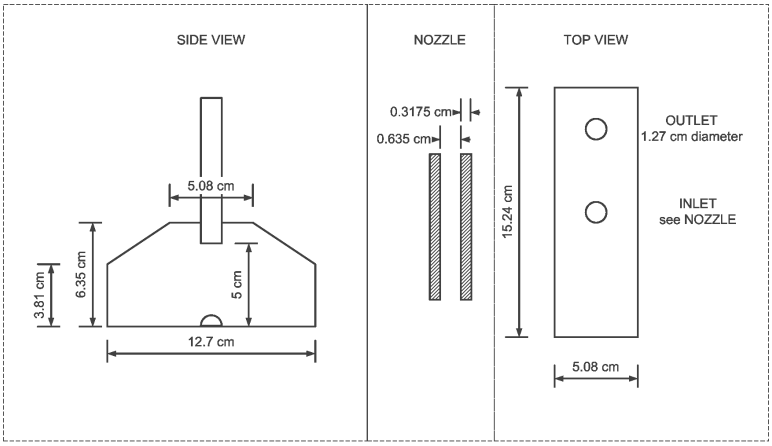

(b)

Figure 7-2: Schematic diagram of impinging jet electrochemical cell. a) Layout of the cell with its component. b) Important cell dimensions.

Table 7.2: Properties of oxygen saturated 0.1 M NaCl at $25^{o}\mathrm{C}$.

Property	0.1 M NaCl
pH	6.99
$\kappa_{\infty}/\mathrm{ohm}^{-1}\ \mathrm{cm}^{-1}$	0.011
$\nu/\mathrm{cm}^2\ \mathrm{sec}^{-1}$	1.01×10^{-2}
$D_{O_2}/\mathrm{cm}^2\ \mathrm{sec}^{-1}$	1.93×10^{-5}
$C_{bO_2}/\mathrm{mol}\ \mathrm{cm}^{-3}$	2.25×10^{-7}

The potential and current in the cell were controlled and measured by Solatran 1286 potentiostat/galvenostat. A frequency response analyzer Solatran 1250 (FRA) was used to apply a perturbation signal and then measure the corresponding impedance of the system. FRA was connected in series to the potentiostat. Both the potentiostat and FRA were connected to a computer via a GPIB (IEEE 488.2) controller card. The control commands were sent to the potentiostat and FRA, and data was collected by a software developed in-house utilizing Labview,[109] a graphical interfacing software. A saturated calomel electrode (SCE) was used as a reference electrode. All potentials are reported with respect to the saturated calomel electrode.

Polarization experiments were carried out on both disk and hemispherical electrode. The electrode potential was varied from a cathodic potential to a more positive potential. Before the start of a polarization run, the electrode was polarized at -1.2 V for three minutes. This process provides cathodic cleaning of the electrode surface, thus eliminating any oxide layer formed at the open circuit potential.

Impedance experiments were conducted in potentiostatic mode. A perturbation signal of 10 mV was applied on top of the bias potential. The frequency range was chosen to be 65K Hz to 0.5 Hz with ten logarthimcally spaced points per decade for the disk electrode and 65K Hz to 1.0 Hz for the hemispherical electrode. A large autointegration (1% closure error) option of frequency response analyzer was used, and the channel for integration was that corresponding to current.

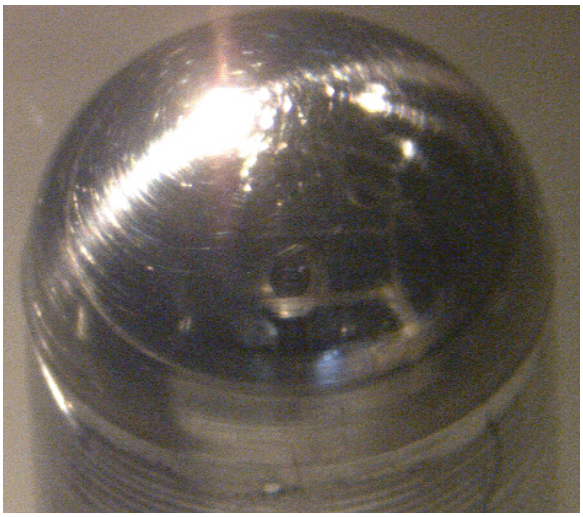

Figure 7-3: Image of the hemispherical electrode during the polarization measurement of oxygen reduction reaction.

7.3 Polarization Measurements

Polarization curves for disk electrode and hemispherical electrode were collected at three different jet velocities. The electrode potential was scanned in anodic direction starting with initial potential of -1.2 V to final value of 0.2 V. It was varied in steps of 2 mV. The resulting current was measured after a delay of two seconds. Polarization curves for disk electrode are presented in Figure 7-4. Polarization curves for the hemispherical electrode are presented in Figure 7-5. The transport limited diffusion current was observed between potential range of -0.8 V to -1.15 V. It is observed in Figures 7-4 and 7-4 that the diffusion-limited current varies slightly with potential. This is attributed to hydrogen evolution reaction.[95] A middle point of the diffusion-limited range was chosen as mass-transfer-limited current for different experimental conditions. Values of the diffusion-limited current at the disk electrode are plotted as a function of square root of average fluid velocity in the jet. This is presented in Figure 7-6. A linear fit to data points yields a straight line passing through origin with a slope of 0.66664 ± 0.01973. A similar plot depicting mass transfer limited current as a function of square root of the average jet velocity for hemispherical electrode is presented in Figure 7-7. A linear

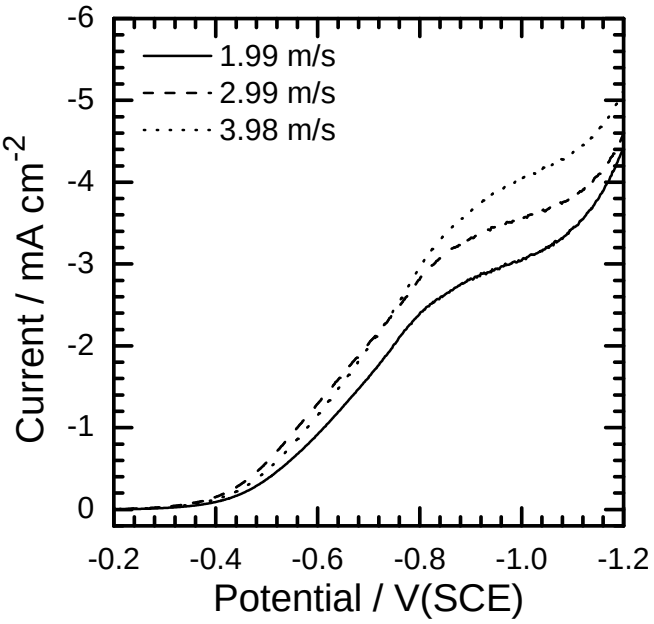

Figure 7-4: Polarization curve for the oxygen reduction reaction collected at the disk electrode. The solid line corresponds to average fluid jet velocity of 1.99 m/s, dash line corresponds to 2.99 m/s, and dotted line corresponds to 3.98 m/s.

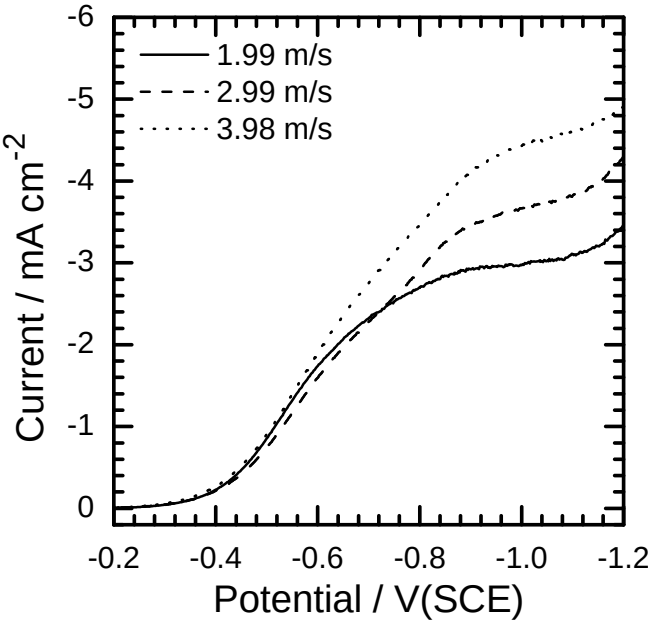

Figure 7-5: Polarization curve for the oxygen reduction reaction collected at the hemispherical electrode. The solid line corresponds to average fluid jet velocity of 1.99 m/s, dash line corresponds to 2.99 m/s, and dotted line corresponds to 3.98 m/s.

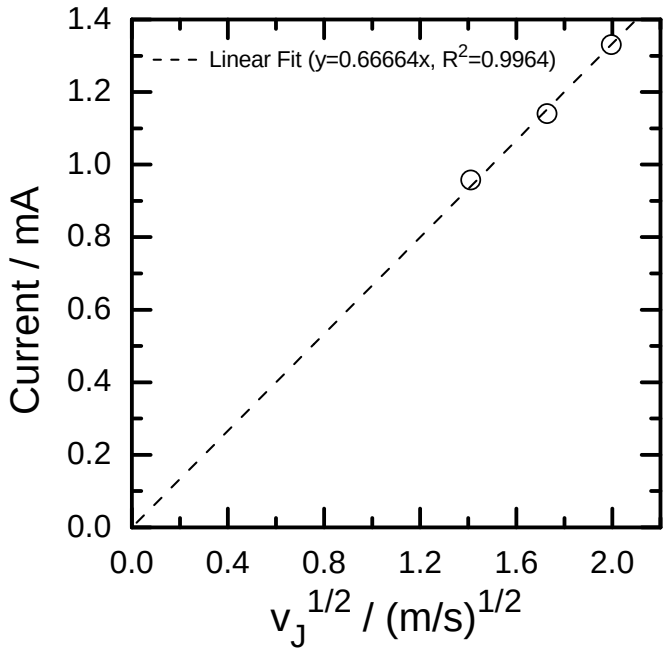

Figure 7-6: Diffusion limited current for oxygen reduction in 0.1 M NaCl as a function of square root of the jet velocity for Ni 270 disk electrode. The dashed line is a linear fit to the data points.

fit yields a slope of 1.40536 ± 0.04216. No visual change at the electrode surface was observed during the course of experiments. The electrode surface was monitored with a video camera, and images were collected every thirty seconds. A representative image is illustrated in Figure 7-3.

A Pourbaix diagram,[110] of nickel in sodium chloride is presented in Figure 7-8. These calculations were performed using CorrosionAnalyzer 1.3 software developed by OLI Systems, Inc. The vertical dashed line in this figure corresponds to a pH of oxygen saturated 0.1 M sodium chloride electrolyte. The species and reactions considered in generating Figure 7-8 are listed in Table 7.3. For these calculations, the activity of nickel ions was assumed to be 1×10^{-6} M. This value was also used by Pourbaix.[110] The pourbaix diagram indicates that nickel should remain immune at cathodic potentials in the sodium chloride electrolyte solution.

The value of the hydrodynamic constant for each experimental condition was calculated from the mass-transfer limited current for both disk and hemispherical

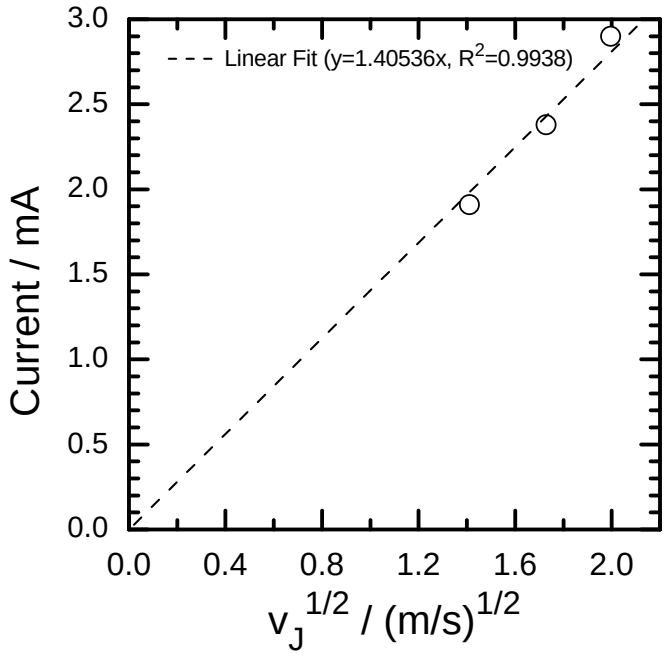

Figure 7-7: Diffusion limited current for oxygen reduction in 0.1 M NaCl as a function of square root of the jet velocity for Ni 270 hemispherical electrode. The dashed line is a linear fit to the data points.

Table 7.3: Species considered in calculation of the Pourbaix diagram presented as Figure 7-8.

Aqueous Phase	**Solid Phase**	**Vapor Phase**
Water	Nickel	Water
Chloride ion(-1)	Nickel(II) chloride dihydrate	Hydrogen
Hydrogen	Nickel(II) chloride hexahydrate	Hydrogen chloride
Hydrogen chloride	Nickel(II) chloride tetrahydrate	Nitrogen
Hydrogen ion(+1)	Nickel(II) hydroxide	Oxygen
Hydroxide ion(-1)	Nickel(II) oxide	
Nickel ion(+2)	Nickel(III) hydroxide	
Nickel ion(+3)	Nickel(IV) oxide	
Nickel(II) hydroxide	Sodium chloride	
Nickel(II) monochloride ion(+1)	Sodium hydroxide	
Nickel(II) monohydroxide ion (+1)	Sodium hydroxide monohydrate	
Nickel(II) trihydroxide ion(-1)	Trinickel tetraoxide	
Nitrogen		
Oxygen		
Sodium ion(+1)		

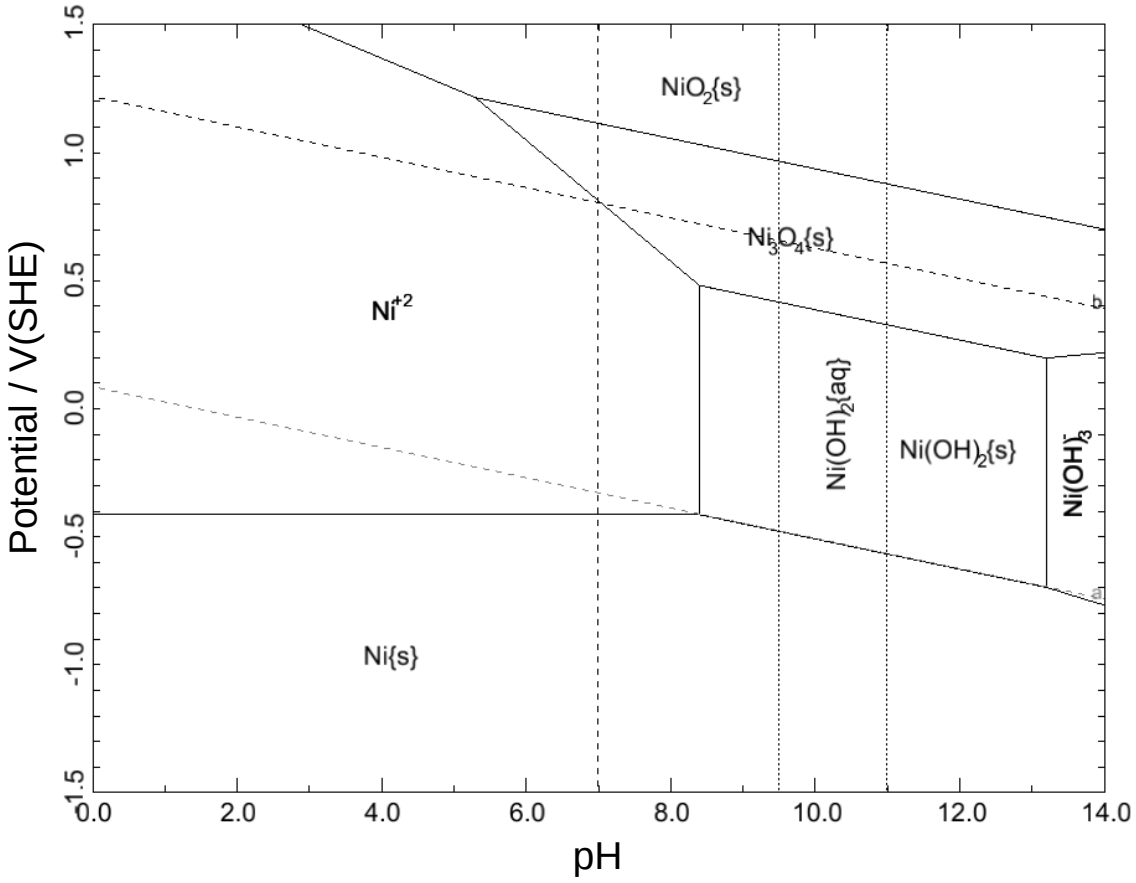

Figure 7-8: The potential-pH diagram of nickel in oxygen saturated sodium chloride solution. The potential is reported with respect to standard hydrogen electrode(SHE). The vertical dash line corresponds to pH of 0.1 M sodium chloride solution. This diagram was generated by computer software CorrosionAnalyzer 1.3 Revision 1.3.33. OLI Systems, Inc. The activity of nickel ions was assumed to be 1.0×10^{-6}M.

Table 7.4: Computed values of hydrodynamic constant a for the disk electrode.

Jet Valocity, v_J (m/s)	Diffusion limited current,i_{lim} (amp)	Hydrodynamics Constant, a (1/s)
1.99	0.957×10^{-3}	699.62
2.99	1.140×10^{-3}	992.77
3.98	1.331×10^{-3}	1351.27

Table 7.5: Calculated values of hydrodynamics constant a for the hemispherical electrode.

Jet Valocity, v_J (m/s)	Diffusion limited current,i_{lim} (amp)	Hydrodynamics Constant, a (1/s)
1.99	1.91×10^{-3}	4109.10
2.99	2.38×10^{-3}	6380.12
3.98	2.90×10^{-3}	9472.75

electrodes. The mass-transfer-limited current is given by

$$I_{lim} = 0.85\pi r_0^2 nFC_{bO_2}\sqrt{a\nu}\mathrm{Sc}^{-2/3} \tag{7-4}$$

for the disk electrode,[111] and

$$I_{lim} = 0.35 \times 2\pi r_0^2 nFC_{bO_2}\sqrt{a\nu}\mathrm{Sc}^{-2/3} \tag{7-5}$$

for hemispherical electrode. In deriving equation (7-5), it was assumed that current in the separated part of the boundary layer is same as at the point of boundary-layer separation. The point of separation occur at an angle of 54.8° as derived in Chapter 2.

The calculated values of hydrodynamic constants for the disk electrode are presented in Table 7.4, and the values for the hemispherical electrode are listed in Table 7.5. It is evident from Tables 7.4 and 7.5 that the hydrodynamics constants are six times higher for the hemispherical electrode than for the disk electrode.

7.4 Impedance Measurements

Impedance measurements were performed for this system at different jet velocity and bias potential. For each jet velocity, two potential points were chosen from

Table 7.6: Experimental conditions for impedance scan of oxygen reduction at disk and hemispherical electrode

Jet Velocity (m/s)	Current level (i/i_{lim})	Bias Potential (Disk Electrode)	Bias Potential (Hemispherical Electrode)
1.99	1/4	-0.535 V	-0.525 V
1.99	1/2	-0.650 V	-0.665 V
2.99	1/4	-0.540 V	-0.570 V
2.99	1/2	-0.635 V	-0.665 V
3.98	1/4	-0.535 V	-0.570 V
3.98	1/2	-0.665 V	-0.730 V

polarization curves presented in previous section. The two potential points corresponded to half and quarter of mass-transfer-limited current, respectively. The experimental condition for all impedance measurements at the disk and hemispherical electrode are listed in Table 7.6.

Complex plane plots of first impedance spectrum at the disk electrode for different jet velocities and bias potentials are presented in Figure 7-9. The first twelve data points were deleted from each spectrum. These data points showed a clear presence of instrument artifacts at high frequency. As seen in Figure 7-9, the impedance value changes as jet velocity is increased. Impedances were higher at lower values of bias potential. Nyquist plots of the first impedance scan at the hemispherical electrode for different jet velocities and bias potential are presented in Figure 7-10. In this case , the first twelve data points were also deleted from each spectrum at high-frequency end. To show temporal variation of impedance, complex plane, and real and imaginary as a function of frequency of impedance spectra obtained at jet velocity of 1.99 m/s and bias potential of -0.54 V are presented in Figure 7-11.

7.5 Measurement Model Analysis

Measurement model analysis was performed to estimate the stochastic contribution of error in impedance. The consistency of impedance with the Kramers-

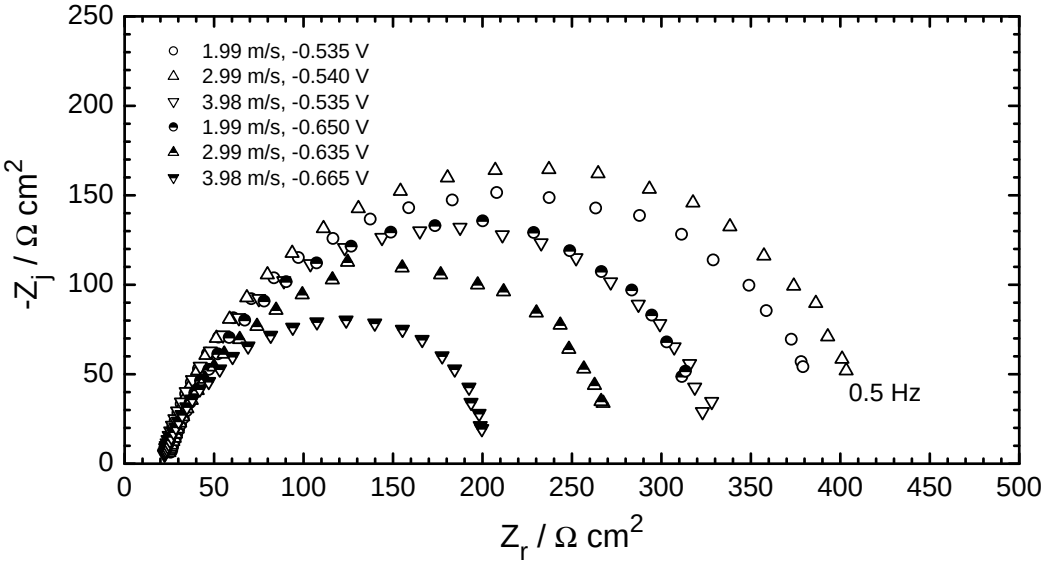

Figure 7-9: First impedance scan collected during the study of oxygen reduction at the disk electrode under submerged jet impingement. The impedance spectrum were collected for different jet velocities and bias potential.

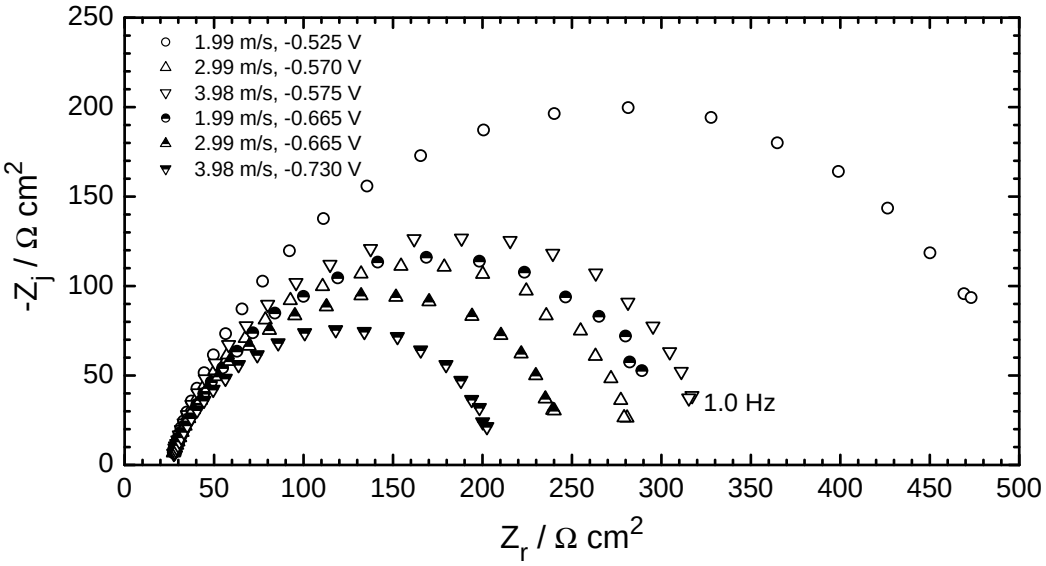

Figure 7-10: First impedance scan collected during the study of oxygen reduction at the hemispherical electrode under submerged jet impingement. The impedance spectrum were collected for different jet velocities and bias potential.

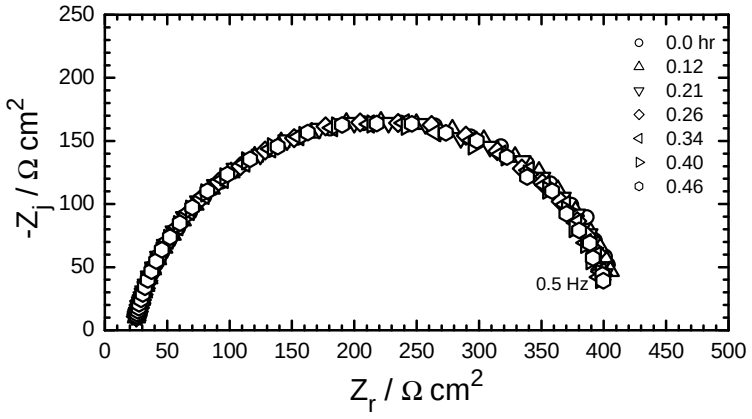

(a)

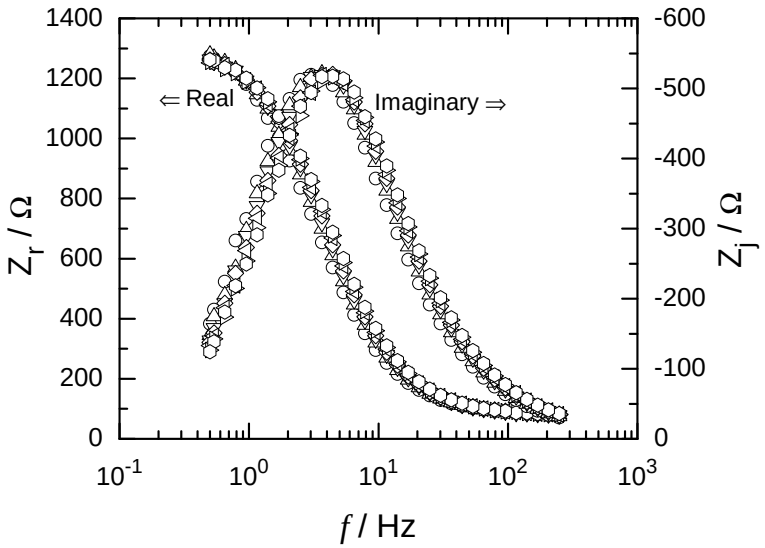

(b)

Figure 7-11: Collected impedance spectrum for jet velocity of 2.99m/s and bias potential of -0.540 V. a) Complex plane plot; Real and imaginary impedance are normalized with surface area; b) Real and imaginary impedance as a function of frequency.

Kronig consistency relations was checked to determine the inconsistent portion of impedance spectra at each experimental condition.

7.5.1 Determination of Stochastic Error Structure

The stochastic error structure of the impedance measurements were obtained using measurement model approach. The Voigt-element-based measurement model was selected, and modulus weighting was used in regression of the measurement model. A maximum possible number of statistically significant Voigt elements were regressed to the impedance spectra at each experimental condition. The calculation procedure was as described in Chapter 6. The variance of the stochastic error was estimated for all data sets at each experimental condition. The results of the calculation are described below.

For impedance data presented in Figure 7-9 by open symbols, four Voigt element measurement model were regressed to each data set. These data correspond to lower value of the bias potential (quarter of mass-transfer limited current). Some impedance spectra were not used for the calculation, as it was found that the noise level in the data was higher, and regression was able to resolve fewer Voigt elements. The estimated error structure is presented in Figure 7.12(a). At higher value of bias potential, which correspond to half of diffusion-limited current, only three statistically significant Voigt elements could be resolved from regression for each data set. The resulting error structure for this case is presented in Figure 7.12(b).

A parallel treatment was applied to impedance data set collected on the hemispherical electrode. A four Voigt element measurement model was regressed to data sets collected at different jet velocities and bias potentials corresponding to a quarter of mass-transfer-limited current. Standard deviations of stochastic error for real and imaginary parts are presented in Figure 7.13(a). A similar procedure

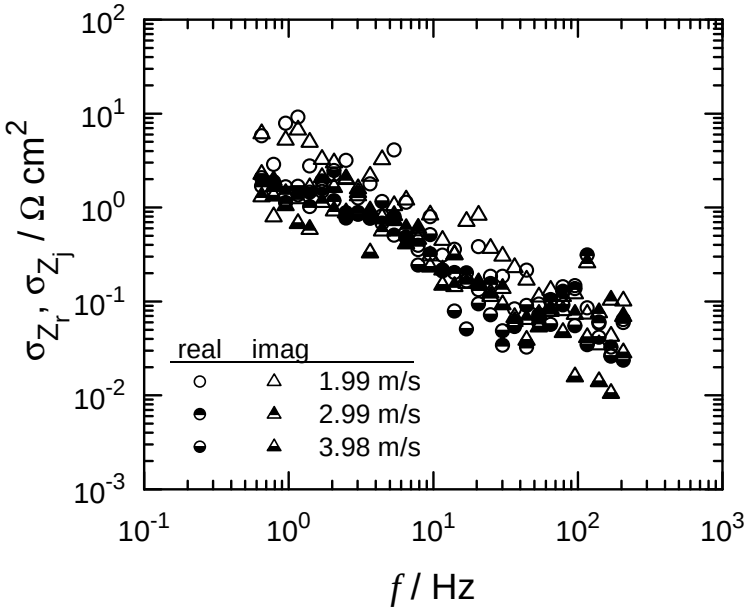

(a)

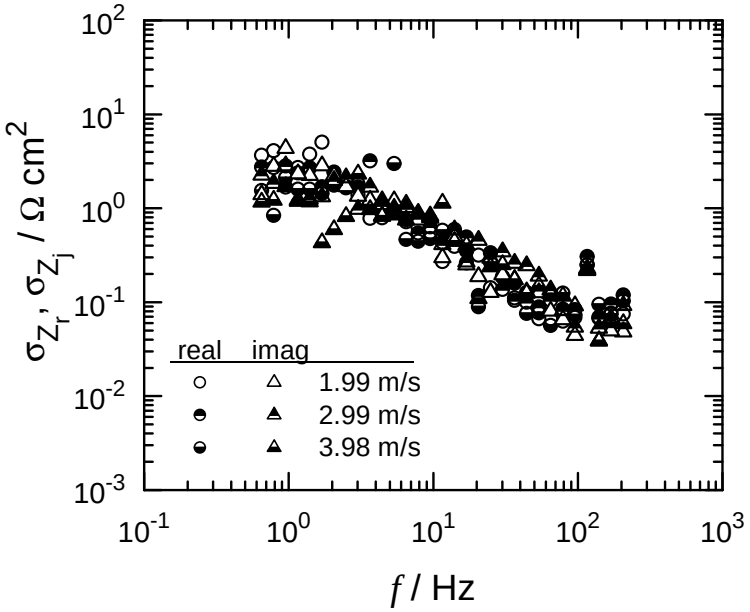

(b)

Figure 7-12: Standard Deviations of stochastic errors for the impedance data collected on disk electrode. A representative first scan of the analyzed data is presented in Figure 7-9. The results are presented for different jet velocities and applied bias potentials. a) Values of bias potentials was selected to provide the average current level at about quarter of mass-transfer-limited current; b) Values of bias potentials was selected to provide the average current level at about half of mass-transfer-limited current.

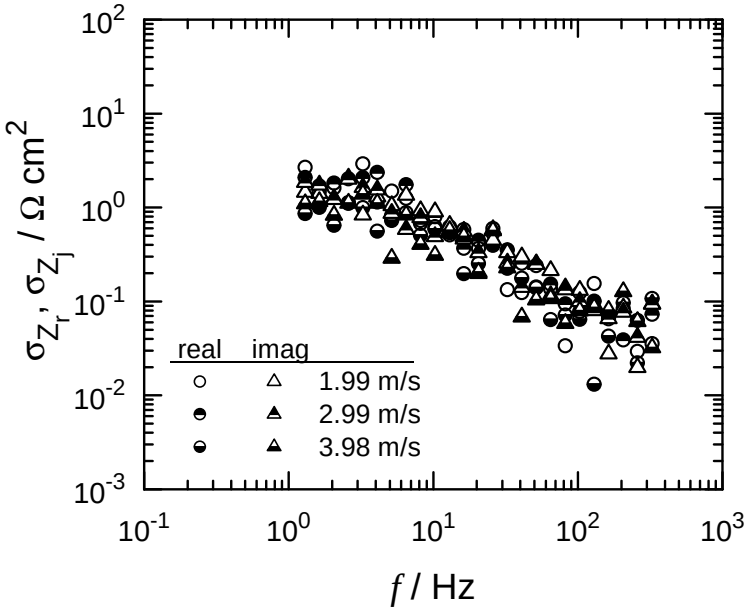

(a)

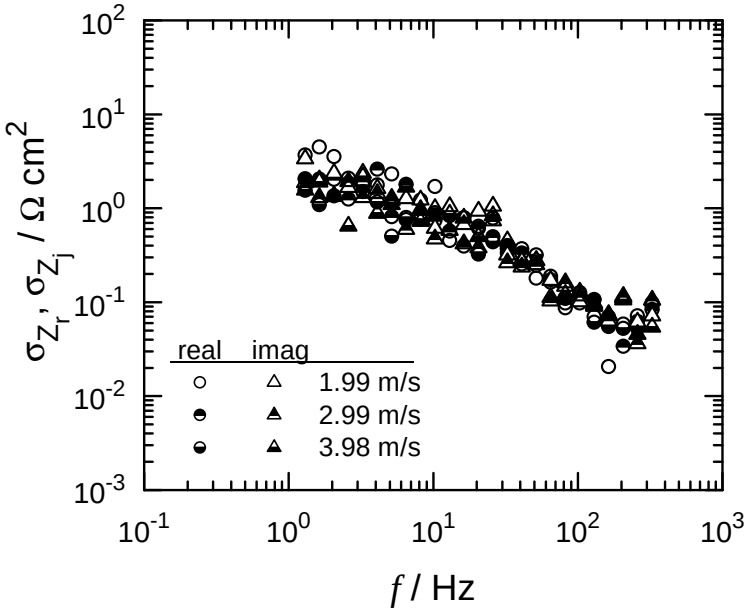

(b)

Figure 7-13: Standard Deviations of stochastic errors for the impedance data collected on disk electrode. A representative first scan of the analyzed data is presented Figure 7-10. The results are presented for different jet velocities and applied bias potentials. a) Values of bias potentials was selected to provide the average current level at about quarter of mass-transfer-limited current; b) Values of bias potentials was selected to provide the average current level at about half of mass-transfer-limited current.

Table 7.7: Model parameters of error structure for different experimental conditions on disk electrode.

Jet Velocity, Bias Potential (m/s, V)	γ	δ
1.99, -0.535	1.035×10^{-5}	0.146
2.99, -0.540	0.301×10^{-5}	0.193
3.98, -0.535	0.518×10^{-5}	0.052
1.99, -0.650	1.099×10^{-5}	0.173
2.99, -0.635	1.115×10^{-5}	0.274
3.98, -0.665	1.322×10^{-5}	0.283

Table 7.8: Model parameters of error structure for different experimental conditions on hemispherical electrode.

Jet Velocity, Bias Potential (m/s, V)	γ	δ
1.99, -0.525	0.637×10^{-5}	0.112
2.99, -0.570	1.656×10^{-5}	0.063
3.98, -0.575	0.637×10^{-5}	0.112
1.99, -0.665	2.253×10^{-5}	0.069
2.99, -0.665	1.853×10^{-5}	0.079
3.98, -0.730	0.656×10^{-5}	0.083

was followed for impedance spectra at higher bias potentials. Only three Voigt elements could be resolved with regression of data. The estimated standard deviation of stochastic errors is presented in Figure 7.13(b). The standard deviations of error are on the same order in Figures 7.13(a) and 7.13(b)

A generalized error-structure model could not be obtained for all the experimental conditions. Different error-structure models were developed for each experimental condition according to equation (6-28). The term R_m was assigned at a value of 100.0 as this value of current measuring resistor was used for all experimental conditions. Only γ, and δ could be obtained from the error-structure model because the confidence interval for α and β included zero. The results of the linear model regression are presented in Table 7.7 for the disk electrode. The error-structure model parameters at the hemispherical electrode are

given in Table 7.8.

7.5.2 Kramers-Kronig Consistency Check

Kramers-Kronig transforms relate the real part of the impedance data to the imaginary part. The consistency check ensures that electrochemical system was linear, causal,stable, and stationary during the experiments.

Error structure weighting was used in regression of impedance spectrum to check for Kramers-Kronig transforms. This strategy assigns less weight to noisy data and more weight to good data. The consistency checks were performed for fist spectrum of each data set. The procedure was followed as outlined in Chapter 6. Some representative results are presented here.

Disk Electrode. The Voigt measurement model was regressed to the imaginary part of first impedance scan collected at 1.99 meter/sec jet velocity and -0.535 V bias potential (quarter of mass-transfer limited current). This data set is represented by open circles in Figure 7-9. The regression yielded four statistically significant line shapes. Voigt element parameters are listed in the second column of Table 7.9. Normalized residual errors for the imaginary part are presented in Figure 7.14(a) where dotted lines represent the $\pm 2\sigma$ bound for the stochastic error structure determined in the previous section. The corresponding prediction of the real part is given in Figure 7.14(b) where dashed lines represent the 95.4% confidence interval for the model obtained by Monte Carlo simulation using the calculated confidence intervals for the estimated parameters. The value of the solution resistance was fixed at 63.28 Ω in the calculation. This data set was found to be consistent with Kramers-Kronig relation. A parallel treatment was performed for first impedance scan collected at 1.99 meter/sec jet velocity and -0.650 V bias potential (half of mass-transfer-limited current). The data set is represented by open triangles in Figure 7-9. In this case, only three statistically significant line

Table 7.9: Model parameters for the fit of a Voigt measurement model to imaginary part of first impedance scans at disk electrode. The jet velocity for this set of experiments was at 1.99 meter/sec.

Variable	Spectrum # 1 (-0.530 V)	Spectrum # 1 (-0.650 V)
τ_1 / 10^{-4}s	4.70 ± 1.48	–
R_1 / Ω	14.56 ± 1.86	–
τ_2 / 10^{-3}s	4.73 ± 0.71	1.14 ± 0.26
R_2/ Ω	42.87 ± 7.81	14.51 ± 1.64
τ_3 / 10^{-2}s	2.15 ± 0.15	0.96 ± 0.12
R_3/ Ω	430.04 ± 38.86	63.08 ± 7.28
τ_4 / 10^{-2}s	5.82 ± 0.22	6.82 ± 0.21
R_4/ Ω	664.52 ± 43.54	830.65 ± 13.14
R_e/Ω	63.28 (fixed)	75.81 (fixed)

shapes could be resolved by regression. The Voigt element parameters obtained are given in the third column of Table 7.9. Normalized residual errors for imaginary parts are presented in Figure 7.15(a). Again, the corresponding prediction of the real part is given in Figure 7.15(b).

Hemispherical Electrode. A similar treatment was applied to the impedance data collected at the hemispherical electrode. The results of the consistency test are presented for a jet fluid velocity of 3.98 meter/sec. The measurement model was regressed to the imaginary part of first impedance scan collected at -0.57 V bias potential (quarter of mass-transfer-limited current). This data set is represented by half filled circles in Figure 7-10. In this case, four statistically significant line shapes were obtained by regression to the imaginary part of the spectrum. The obtained Voigt model parameters are listed in the second column of Table 7.10. The results of the regression are presented in Figure 7-16. Normalized residual errors for the imaginary part are shown in Figure 7.16(a). The corresponding prediction of the real part is given in Figure 7.16(b). The value of solution resistance for this calculation was fixed at 39.52 Ω. A parallel treatment was applied to the first impedance scan collected at -0.73 V bias potential (half of mass-transfer-limited current). The

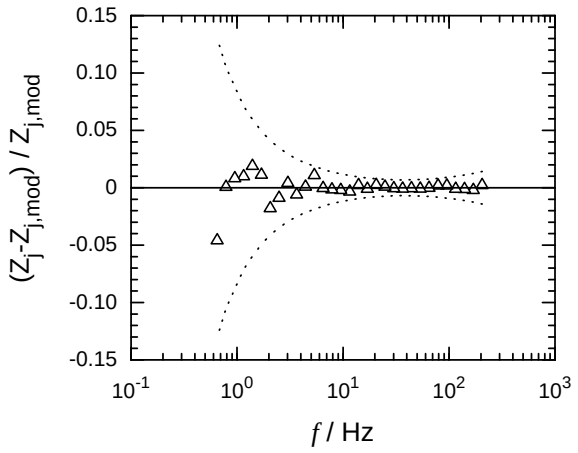

(a)

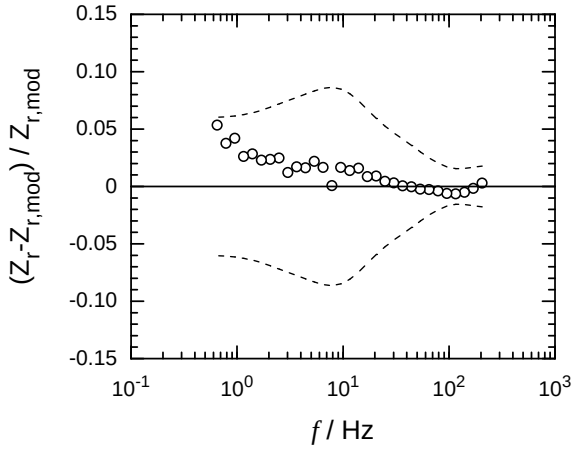

(b)

Figure 7-14: Residual errors for the fit of a Voigt measurement model to the imaginary part of the impedance spectrum presented in Figure 7-9 by open circles. a) fit to the imaginary part, where dashed lines represent the $\pm 2\sigma$ bound for the stochastic error structure determined in the previous section; b) prediction of the real part where dashed lines represent the 95.4% confidence interval for the model obtained by Monte Carlo simulation using the calculated confidence intervals for the estimated parameters.

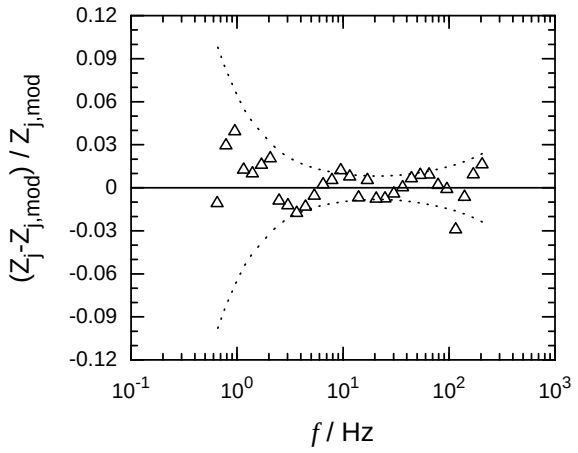

(a)

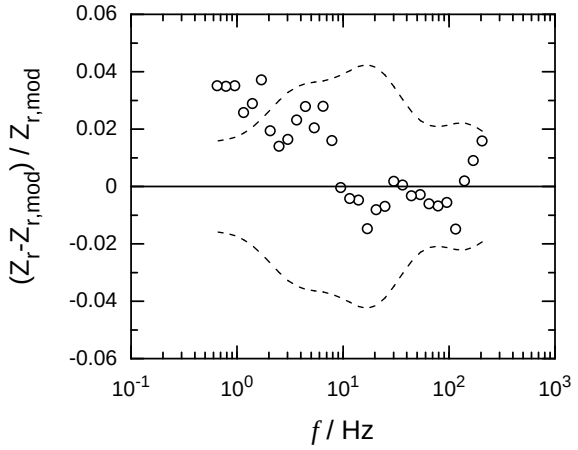

(b)

Figure 7-15: Residual errors for the fit of a Voigt measurement model to the imaginary part of the impedance spectrum presented in Figure 7-9 by half filled circles. a) fit to the imaginary part, where dashed lines represent the $\pm 2\sigma$ bound for the stochastic error structure determined in the previous section; b) prediction of the real part where dashed lines represent the 95.4% confidence interval for the model obtained by Monte Carlo simulation using the calculated confidence intervals for the estimated parameters.

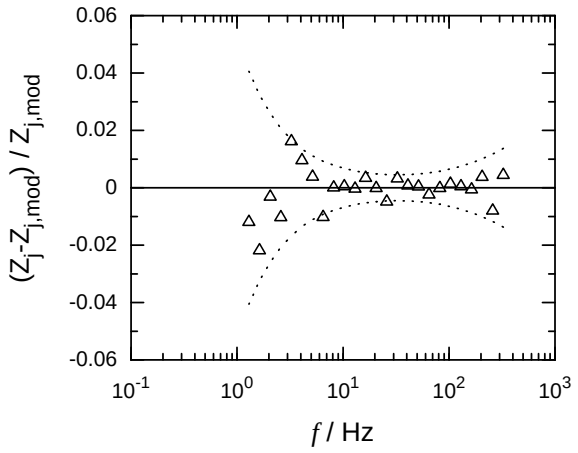

(a)

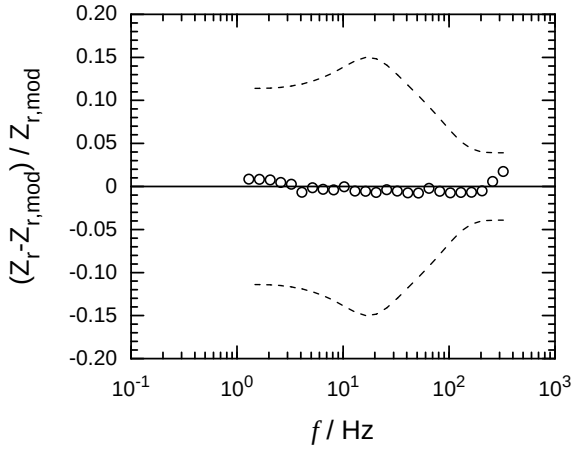

(b)

Figure 7-16: Residual errors for the fit of a Voigt measurement model to the imaginary part of the impedance spectrum presented in Figure 7-10 by open traingles. a) fit to the imaginary part, where dashed lines represent the $\pm 2\sigma$ bound for the stochastic error structure determined in the previous section; b) prediction of the real part where dashed lines represent the 95.4% confidence interval for the model obtained by Monte Carlo simulation using the calculated confidence intervals for the estimated parameters.

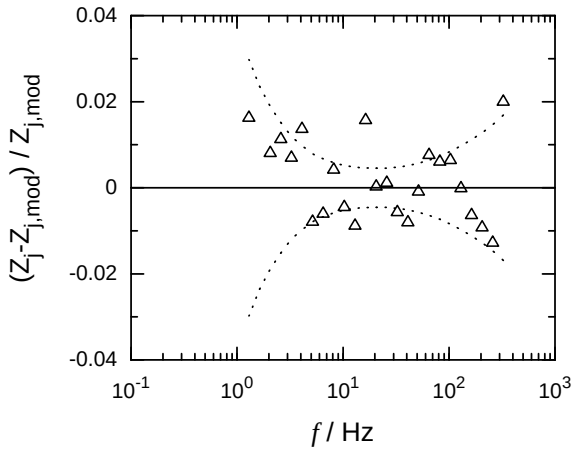

(a)

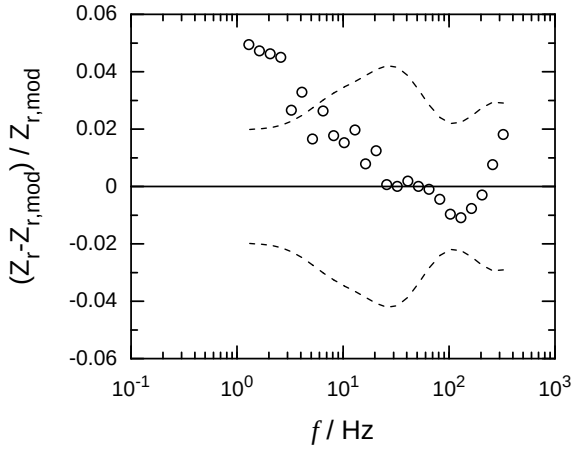

(b)

Figure 7-17: Residual errors for the fit of a Voigt measurement model to the imaginary part of the first impedance spectrum presented in Figure 7-10 by inverted half filled triangles. a) fit to the imaginary part, where dashed lines represent the $\pm 2\sigma$ bound for the stochastic error structure determined in the previous section; b) prediction of the real part where dashed lines represent the 95.4% confidence interval for the model obtained by Monte Carlo simulation using the calculated confidence intervals for the estimated parameters.

Table 7.10: Model parameters for the fit of a Voigt measurement model to imaginary part of first impedance scans at hemispherical electrode. The jet velocity for this set of experiments was at 3.98 meter/sec.

Variable	Spectrum # 1 (-0.570 V)	Spectrum # 1 (-0.730 V)
τ_1 / 10^{-4}s	4.99 ± 1.60	5.88 ± 1.78
R_1 / Ω	9.96 ± 1.28	9.16 ± 0.84
τ_2 / 10^{-3}s	3.27 ± 1.05	5.81 ± 0.72
R_2/ Ω	23.94 ± 9.92	35.40 ± 4.12
τ_3 / 10^{-2}s	1.21 ± 0.26	–
R_3/ Ω	135.91 ± 35.76	–
τ_4 / 10^{-2}s	3.05 ± 0.22	2.75 ± 0.08
R_4/ Ω	296.43 ± 43.12	225.22 ± 4.36
R_e/Ω	39.52 (fixed)	39.52 (fixed)

data set is represented by half filled inverted triangles in Figure 7-10. A three Voigt element measurement model was regressed to imaginary part of the data set with error structure weighting. The values of regressed Voigt element parameters are listed in Table 7.10. Normalized residual errors for imaginary parts are presented in Figure 7.17(a). The regression of measurement model provides fitting errors of the order of stochastic error of the measurements. The corresponding prediction of the real part is given in Figure 7.17(b). A systematic departure of the real part of data set at low frequency is evident in Figure 7.17(b). A total of six data points lie outside the prediction band starting at the frequency of 4.1 Hz to 1 Hz. This is in agreement with the observation that the measuring instrument, Solartron FRA 1250, recorded an error code[112] 82 at these data point. The error code 82 is an indication that the auto integration of measured the current was not successful in the allotted time.

7.6 Process Model

Interpretation of impedance in the complex plane diagrams (Figures 7-9 and 7-10) suggests that a constant phase element based empirical process model could

describe the system.The transfer function for this equivalent circuit is given by:

$$Z(\omega) = R_{sol} + \frac{R_{ct}}{1 + \tau(j\omega)^{1-\alpha}} \tag{7-6}$$

where R_{sol} is the solution resistance, R_{ct} is the charge transfer resistance, ω is frequency in radians, and α is distribution parameter.

This equivalent circuit process model was developed after followings phenomena were observed in the collected impedance spectrum of both the disk and the hemispherical electrode.

1. Complex plane plots do not distinctly show the mass-transfer diffusion impedance characteristics, and

2. impedance in complex plane show the characteristics of depressed semi circles.

Under the aforementioned observations about impedance, a constant phase element based process model could describe the impedance of the system. It was further assumed that the oxygen reduction occur via four electron process described by equation (7-1). A CPE element[113–116] is known to describe the distribution of the reaction rate at the electrode surface. It is hypothesized that the CPE parameters can be related to the current distribution. Orazem and coworkers[117] established a relationship between parameters α of CPE elements to voigt elements. The authors concluded that larger the value of α, the more time constants can be resolved from impedance. Hence, α represents degree of nonuniformity in reaction rate at the electrode surface.

The process model described in equation (7-6) was regressed to the Kramers-Kronig consistent part of each impedance spectrum. The error-structure weighting was used in regression. The models of error-structure for each the experimental conditions are given in Table 7.7 and 7.8. A regression result is presented in Figure

Table 7.11: Estimated model parameters of a CPE equivalent circuit model to impedance data collected at the disk electrode. Reported parameters values are average of seven replicate spectrum collected at an experimental condition.

Experimental Conditions (Jet Velocity (m/s), Bias Potential)	R_{sol}/Ω	R_{ct}/Ω	$\tau/10^{-2}$s	α
1.99 , −0.535 V	68.0	1223.9	6.56	0.1215
2.99 , −0.540 V	73.1	1251.8	5.92	0.1164
3.98 , −0.540 V	66.5	994.1	5.21	0.1161
1.99 , −0.650 V	74.9	1064.3	10.04	0.1502
2.99 , −0.635 V	72.9	814.2	6.53	0.1631

Table 7.12: Estimated model parameters of a CPE equivalent circuit model to impedance data collected at the hemispherical electrode. Reported parameters values are average of seven replicate spectrum collected at an experimental condition.

Experimental Conditions (Jet Velocity (m/s), Bias Potential)	R_{sol}/Ω	R_{ct}/Ω	$\tau/10^{-2}$s	α
1.99 , −0.535 V	41.2	754.8	4.71	0.1339
2.99 , −0.540 V	41.2	399.4	3.31	0.1438
3.98 , −0.540 V	41.5	475.2	3.16	0.1281

7-18 for the first spectrum collected at a jet velocity of 2.99 m/s and bias potential of -0.540 V. A fit to impedance in data is presented in Figure 7.18(a). The corresponding values of real and imaginary residual errors are presented in Figure 7.18(b). For few experimental conditions, the CPE process model could not be regressed successfully. This was due to fact that the consistency check eliminated a majority of data point and a meaningful regression was not possible for reduced date set. CPE parameters values, obtained from regression of impeance data set at the disk electrode, are given in Table 7.11. The reported values of parameters are the average of seven replicate spectra collected at each experimental condition. The results of regression for impedance data set at hemispherical electrode are given in Table 7.12.

The values of α for the disk electrode in Table 7.11 suggests that current dis-

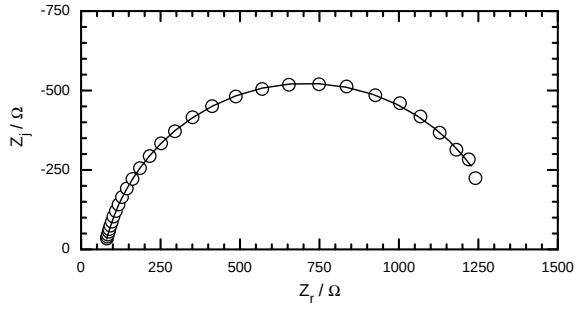

(a)

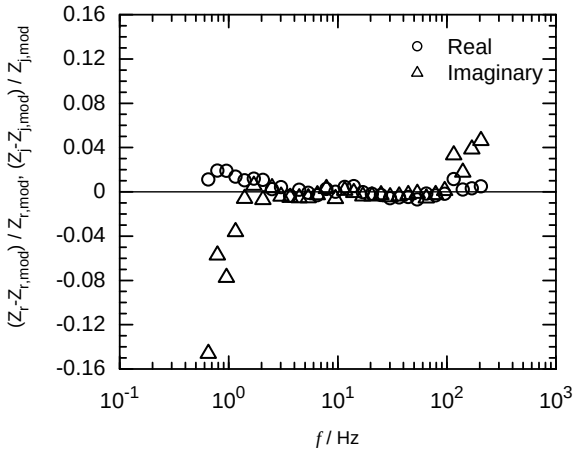

(b)

Figure 7-18: A CPE equivalent circuit model fit to the impedance data collect at the jet velocity of 2.99 m/s. The bias potential was set at -0.540 V. a) Colpmex plane plot of the fit to the data; b) Real and imaginary residual errors as a function of frequency.

tribution is more uniform at lower value of bias potential as compared to higher values. However, no such conclusion can be drawn about hemispherical electrode because α values could not be obtained for the impedance data collected at higher bias potential. A comparison α for the disk and the hemisphere suggests that current distribution is more uniform at disk electrode for same level of bias potential.

7.7 Summary

This chapter has presented results of electrochemical measurements of oxygen reduction reaction at both disk and hemispherical electrodes. The analysis of impedance data suggest that the current distribution if more uniform at disk electrode than at hemispherical electrode. This is quite contrary to the calculations results in Chapter 5. However, the results of the analysis could be debated because process model was limited by its assumptions.

CHAPTER 8
ELECTROCHEMICAL MEASUREMENTS OF FERRICYANIDE REDUCTION AT NICKEL ELECTRODE

This chapter presents an experimental study of reduction of ferricyanide at the nickel electrode in the electrolyte made of sodium hydroxide, potassium ferrocyanide, and potassium ferricyanide. Electrochemical Impedance experiments were conducted on both the disk and hemispherical electrode geometry under submerged jet impingement. Polarization and impedance measurements were conducted in order to explore the differences associated with the disk and hemispherical electrode geometries. Impedance data was graphically analyzed and electorate surface was characterized with Energy Dispersive Spectroscopy. The results and analysis of the impedance experiments are presented in this chapter.

8.1 Introduction

Reduction of ferricyanide is a one-electron charge transfer reaction. The stochiometry of this redox system can be represented as:

$$\mathrm{Fe(CN)_6^{3-}} + \mathrm{e^-} \rightarrow \mathrm{Fe(CN)_6^{4-}} \tag{8-1}$$

where ferricyanide ion ($\mathrm{Fe(CN)_6^{3-}}$) is reduced to ferrocyanide ion ($\mathrm{Fe(CN)_6^{4-}}$) by combining with one electron.

Historically, this system has been thought to be relatively simple to understand due to following reasons.

1. The electro transfer reaction is kinetically fast. This property of the system causes the kinetic and mass-transfer effects to be distinctly observed during impedance experiments.[118]

Table 8.1: Electrolyte properties used in experiments.

Supporting Electrolyte	1 M NaOH	0.1 M NaOH
T /°C	25	25
$r = \frac{c_{\mathrm{OH^-}}}{(c_{\mathrm{Na^+}}+c_{\mathrm{K^+}})}$	0.97	0.740
pH	13.87	12.83
$\kappa_\infty/\mathrm{ohm}^{-1}\mathrm{cm}^{-1}$	0.17418	0.02516
$\nu/\mathrm{cm}^2\mathrm{sec}^{-1}$	1.089×10^{-2}	0.912×10^{-2}

2. The effect of the supporting electrolyte on migration is quantified, and presence of excess supporting electrolyte concentration diminishes the effect of ohmic contribution.[23]

The objective of this study is to understand the difference in impedance response at disk and hemispherical electrode geometry.

8.2 Experimental Method

The experimental setup was the same as described in Chapter 7 for study of oxygen reduction studies. The electrolyte consisted of 17 MΩcm deionized water, 0.005 M $\mathrm{K_3Fe(CN)_6}$ (potassium ferricyanide), and 0.005 M $\mathrm{K_4Fe(CN)_6}$ (potassium ferrocyanide). Sodium hydroxide NaOH was used as the supporting electrolyte at concentrations of either 1 or 0.1 M. The corresponding electrolyte properties are given in Table 8.1.

The value of $r = c_{\mathrm{OH^-}}/(c_{\mathrm{Na^+}} + c_{\mathrm{K^+}})$ indicates the extent to which migration influences mass transfer. For the reduction of ferricyanide, migration acts to reduce the mass-transfer-limited current density, but the effect is small.[54] The mass-transfer-limited current density for $r = 0.952$ is roughly equal to 98 percent of the diffusion-limited current density. For $r = 0.995$, the influence of migration is suppressed completely.[119,120]

The disk electrode electrode and hemispherical electrodes were polished before use, with the final polishing stage consisting of 0.05 μm alumina slurry on a 1200 grid emery cloth. For the hemispherical electrode, the emery cloth was held

Table 8.2: Calculated values of solution resistance for primary current distribution, R_{sol}^{P}, using electrical conductivities of electrolyte listed in table 8.1

Supporting Electrolyte	1 M NaOH	0.1 M NaOH
R_{sol}^{p}/Ω(Disk Electrode)	2.30	15.7
R_{sol}^{p}/ΩHemispherical Electrode	1.44	9.96

in a concave cavity to avoid deformation of the electrode shape. The electrodes were cleaned for 15 minutes in an ultrasonic bath in a 1:1 mixture of deionized water and ethyl alcohol. Argon was bubbled in electrolyte reservoir to reduce the concentration of dissolved oxygen.

Electrochemical measurements were conducted with a Solartron 1286 potentiostat and a Solartron 1250 frequency response analyzer. Impedance measurements were conducted under potential modulation.

8.3 Experimental Results

The experimental results served to verify the influence of boundary layer separation. These results and discussion are presented in the following sections.

8.3.1 Steady-State Measurement

A polarization curve is presented in Figure 8-1 for the disk electrode in 1 M NaOH supporting electrolyte. The potential of the electrode is reported with respect to the saturated calomel electrode (SCE). The electrode potential was varied in steps of 2 mV, and current measurement was made after a two seconds initial delay. The polarization curve in Figure 8-1 is similar to the one reported by Durbha.[118] A mass-transfer-limited plateau was not clearly defined, and the mass transfer limited current was assumed to be at the current at a potential of -0.3 V(SCE). The electrode potential corresponding to an average current equal to one quarter of the mass-transfer-limited current was determined to be +0.195 V(SCE).

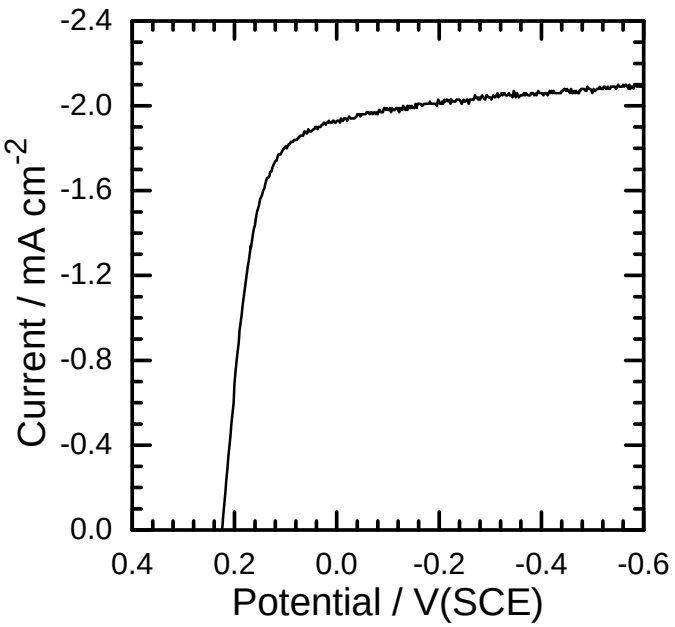

Figure 8-1: Polarization curve of nickel disk electrode in the solution of 1.0 M NaOH, 0.005 M $\mathrm{K_3Fe(CN)_6}$ and $\mathrm{K_4Fe(CN)_6}$. The average fluid velocity in the jet was 1.99 meter/second.

8.3.2 Impedance Measurement

Impedance measurements were conducted under potentiostatic modulation with a potential selected to provide an average current such that $i_{\mathrm{avg}} = (i_{\mathrm{lim}})_{\mathrm{avg}}/4$. Impedance data collected on the disk electrode in 1 M NaOH supporting electrolyte are presented in Figure 8-2. The frequency range for impedance measurement was 65 kHz to 0.1 Hz with frequencies logarithmically spaced at ten points per decade. The first twelve (high-frequency) data points were found to be corrupted by instrumental artifacts and were deleted from each measurement. Corresponding impedance data for the hemispherical electrode are shown in Figure 8-3.

The impedance data differ significantly from the spectra reported in the literature for reduction of ferricyanide on nickel electrodes. For both the disk and hemispherical geometries, the impedance increased with immersion time. A secondary lower frequency feature was seen that was attributed to oxygen reduction. Evidently, the experimental flow loop system could not be purged adequately of

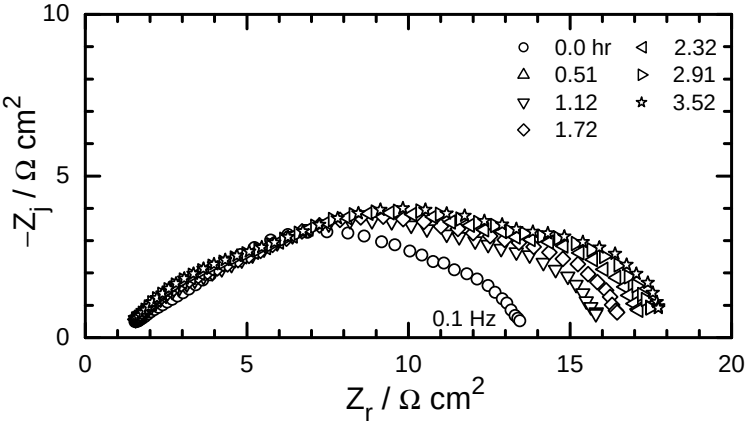

Figure 8-2: Impedance spectra obtained for the reduction of ferricyanide on a nickel disk electrode under submerged jet impingement. The average fluid velocity in the jet was set at 1.99 meter/second and a bias potential of +0.195 V was applied to the electrode. The electrolyte for this set of experiments consisted of 1.0 M $NaOH$, 0.005 M $K_3Fe(CN)_6$ and $K_4Fe(CN)_6$.

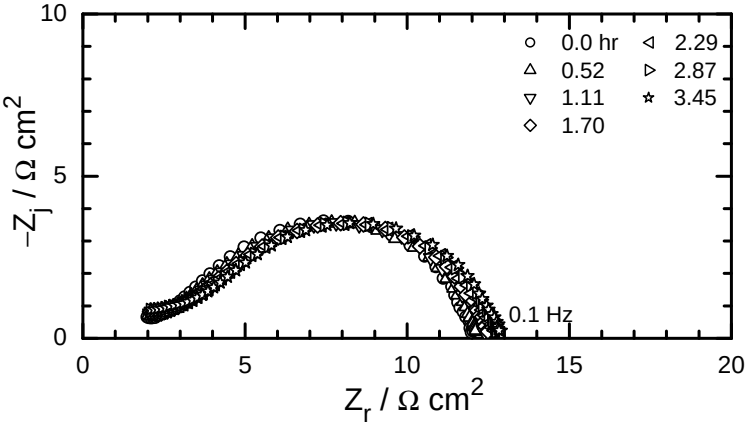

Figure 8-3: Collected Impedance spectra for the reduction of ferricyanide on a nickel hemispherical electrode under submerged jet impingement. The average fluid velocity in the jet was set at 1.99 meter/second and a bias potential of +0.195 V was applied to the electrode. The electrolyte for this set of experiments consisted of 1.0 M $NaOH$, 0.005 M $K_3Fe(CN)_6$ and $K_4Fe(CN)_6$.

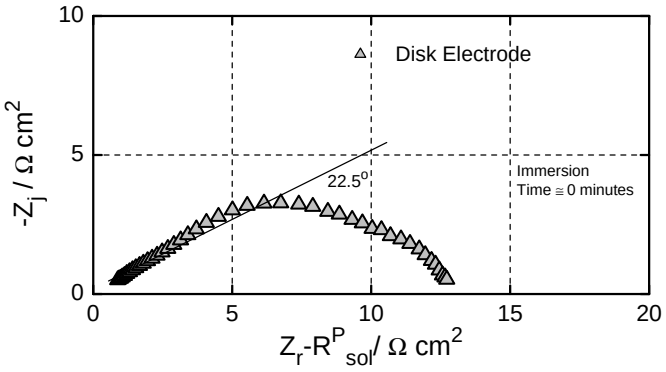

(a)

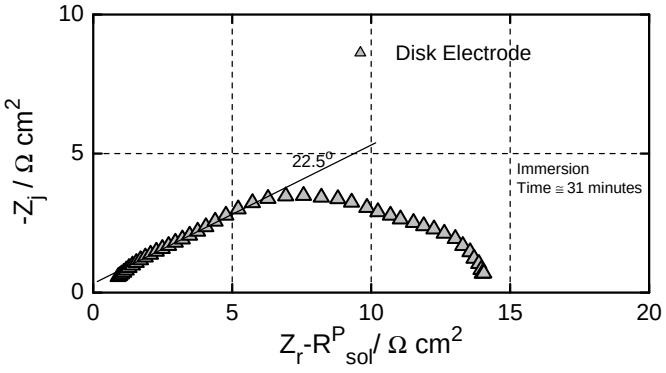

(b)

Figure 8-4: Complex-plane plots of impedance obtained on the disk electrode. a) $t = 60$ s; and b) $t = 1,860$ s.

dissolved oxygen. It is known that the ferricyanide reduction is influenced by both poisoning and surface blocking,[15] but, in previous experiments, the high-frequency asymptote yielded a slope of 45° for the complex-plane plot of the impedance.

In the present work, the slope of the complex-plane plot of impedance data presented in Figures 8-2 and 8-3 for the disk and hemispherical electrode, respectively, differ at high frequencies from the expected value of 45°. As shown in Figure 8.4(a), the slope of the complex-plane plot in the high frequency region is initially slightly larger than 22.5°. As seen in Figure 8.4(b), after a period of about 30 minutes, the slope approaches value of 22.5°. These results are consistent with the formation of a porous electrode.[121,122] The temporal evolution shown in

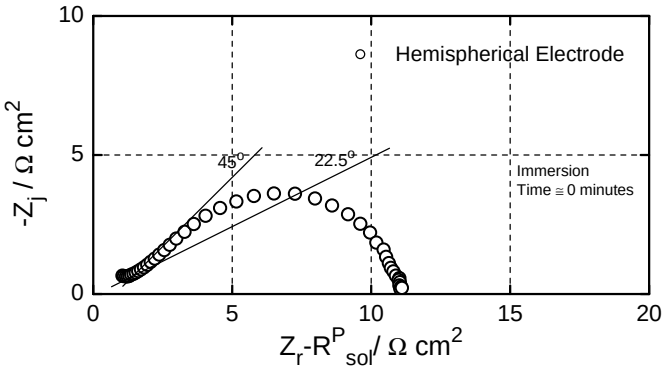

(a)

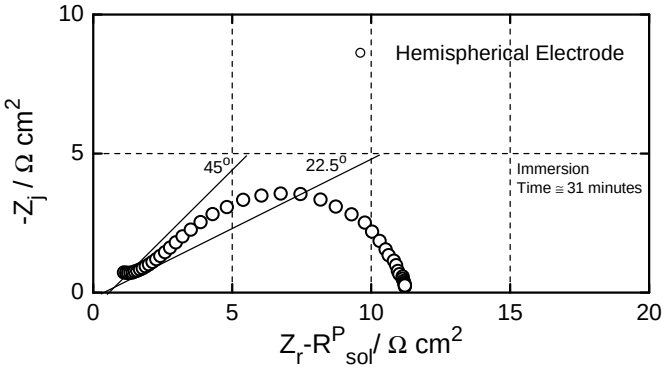

(b)

Figure 8-5: Complex-plane plots of impedance obtained on the hemispherical electrode. a) $t = 60$ s; and b) $t = 1,860$ s.

Figure 8-4 suggests that the porous film forms rapidly and behaves as a porous electrode rather than as a passive diffusion barrier.

The behavior on the hemispherical electrode differed from that on the disk. As seen in Figure 8.5(a) the slope of the first impedance scan for hemispherical electrode presented is near the expected value of 45°. After 30 minutes, as seen in Figure 8.5(b), the slope of the high-frequency region lies between 22.5° and 45°. Even after an immersion of over 3 hours, the slope never approached the value of 22.5° seen for the disk electrode. The results obtained for the hemispherical electrode suggest that the electrode surface may have been partially covered by a porous electrode; whereas, in contrast, the porous electrode covered the disk completely.

Table 8.3: Model of obtained error structure for impedance spectra on disk and hemispherical electrode.

System	γ	δ
Disk Electrode	4.17×10^{-5}	-3.47×10^{-4}
Hemispherical Electrode	11.88×10^{-5}	-9.56×10^{-4}

8.4 Measurement Model Analysis

Measurement model analysis was performed to determine the stochastic component of error in impedance measurement. Kramers-Kronig consistency check was also performed to determine the uncorrupted part of the data set from bias errors and instrumental artifacts.

8.4.1 Determination of Error Structure

The Voigt measurement model was used to determine the stochastic noise level in the impedance data. Each impedance spectrum collected at the disk electrode was regressed to seven voigt element measurement model. Modulus weighting was used in regression. The variance of stochastic error was calculated using procedure described in chapter 6. Results of the analysis are presented in Figure 8-6. A similar analysis was performed for impedance measurements at the hemispherical electrode. In this case, six voigt element measurement model was regressed to each spectrum. The resulting stochastic errors for the real and imaginary components of impedance is shown in Figure 8-7. A model for error structure was developed using equation (6-28). A universal model could not be obtained, as the model did not provide a good fit to both data set presented in Figures 8-6 and 8-7. An individual error structure model was developed from estimated stochastic errors at the disk and the hemispherical electrode. Only γ and δ could be extracted from data because values of α and β included zero in their confidence intervals. Solid lines in Figures 8-6 and 8-7 represent the error-structure model. The model parameters are tabulated in Table 8.3.

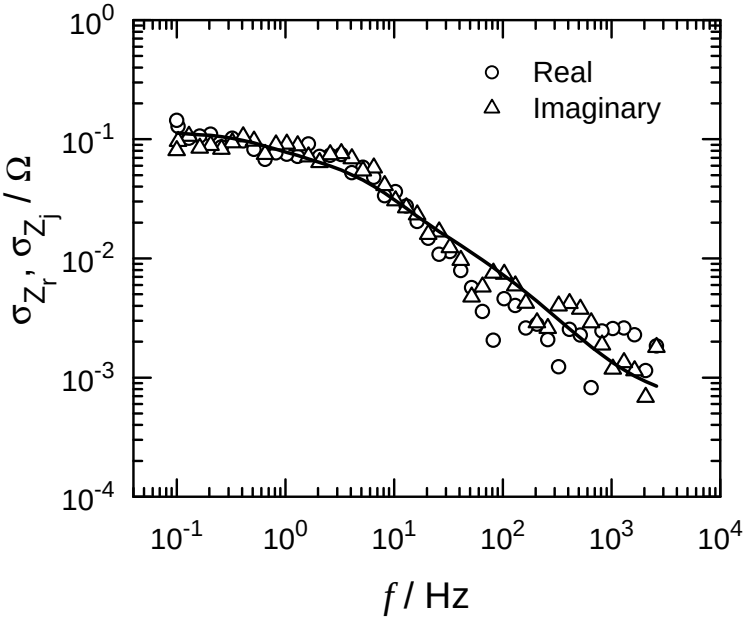

Figure 8-6: Standard Deviations for the data presented in Figure 8-2. The solid line represents the fit to the error structure.

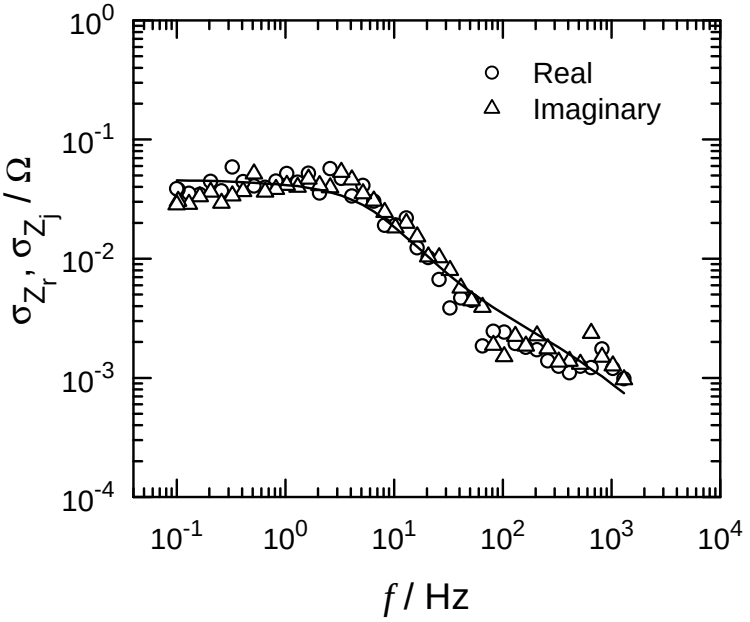

Figure 8-7: Standard Deviations for the data presented in Figure 8-3. The solid line represents the fit to the error structure.

8.4.2 Kramers-Kronig Consistency Check

The Kramers-Kronig consistency check were performed for the first impedance scan presented in Figures 8-2 and 8-3. The procedure was followed as outlined in chapter 6. The error structure model for stochastic component of errors were used as weights in the regression.

A voigt measurement model was regressed to the imaginary part of first impedance scan collected at 1.99 meter/sec jet velocity and quarter (195.0 mV bias potential) of mass transfer limited at the disk electrode. This impedance spectrum is represented by circles in Figure 8-2. In this case, seven statistically significant line shapes were obtained by regression of the measurement model. Voigt element model parameters are listed in in second column of Table 8.4. The results of the regression are shown in Figure 8-8. Normalized residual errors for imaginary part are presented in Figure 8.8(a) where dotted lines represent the $\pm 2\sigma$ bound for the stochastic error structure determined in the previous section. The corresponding prediction of the real part is given in Figure 8.8(b) where dashed lines represent the 95.4% confidence interval for the model obtained by Monte Carlo simulation using the calculated confidence intervals for the estimated parameters. The value of solution resistance was fixed at 1.7Ω. The impedance spectrum was found to be consistent with Kramers-Kronig transforms.

A parallel treatment was performed for the first impedance scan collected at hemispherical electrode. Measurement model was regressed to imaginary part of the first impedance scan. In this case, only six statistically significant line shapes could be obtained. Voigt model parameters are given in the third column of Table 8.4. The results of the regression are shown in Figure 8-9. Normalized residual errors for imaginary part are presented in Figure 8.9(a) where dotted lines represent the $\pm 2\sigma$ bound for the stochastic error structure determined in the previous

Table 8.4: Model parameters for the fit of a Voigt measurement model to imaginary part of first impedance scans at disk and hemispherical electrode

Variable	Spectrum # 1 (Disk Electrode)	Spectrum # 1 (Hemispherical Electrode)
τ_1 / 10^{-5}s	3.49 ± 0.34	3.585 ± 1.148
R_1 / Ω	2.146 ± 0.072	1.892 ± 0.236
τ_2 / 10^{-4}s	3.096 ± 0.292	3.439 ± 0.476
R_2/ Ω	1.968 ± 0.238	0.925 ± 0.376
τ_3 / 10^{-3}s	1.066 ± 0.216	1.671 ± 0.342
R_3/ Ω	2.563 ± 0.418	1.343 ± 0.118
τ_4 / 10^{-3}s	3.519 ± 0.78	8.676 ± 3.214
R_4/ Ω	3.485 ± 0.388	3.346 ± 1.764
τ_5 / 10^{-2}s	1.705 ± 0.192	2.613 ± 0.516
R_5/ Ω	13.75 ± 1.51	8.857 ± 1.648
τ_6 / 10^{-2}s	5.938 ± 1.718	21.61 ± 17.86
R_6/ Ω	7.566 ± 1.31	0.97 ± 0.58
τ_7 / 10^{-1}s	2.887 ± 0.444	–
R_7/ Ω	7.06 ± 1.12	–
R_e/Ω	3.1936 (fixed)	1.446 (fixed)

section. The corresponding prediction of the real part is given in Figure 8.9(b) where dashed lines represent the 95.4% confidence interval for the model obtained by Monte Carlo simulation using the calculated confidence intervals for the estimated parameters. The value of the solution resistance for this calculation was fixed at 2.34Ω. Normalized real residual errors lie between 95.4% confidence band, which indicates that the spectrum is consistent with Kramers-Kronig relations.

8.5 Surface Analysis for Disk Electrode

Optical micrographs of the disk electrode are presented in Figure 8-10. As seen in Figure 8.10(a), the disk electrode is completely covered with deposit. To show that contrast between metal surface and deposits, the film was removed from one side of the disk electrode by rubbing with sand paper. The resulting image is presented in Figure 8.10(b). The optical images support the conclusion that a deposit is formed on the disk electrode.

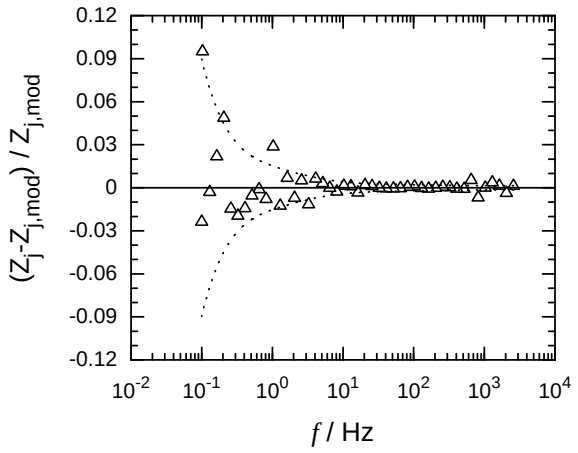

(a)

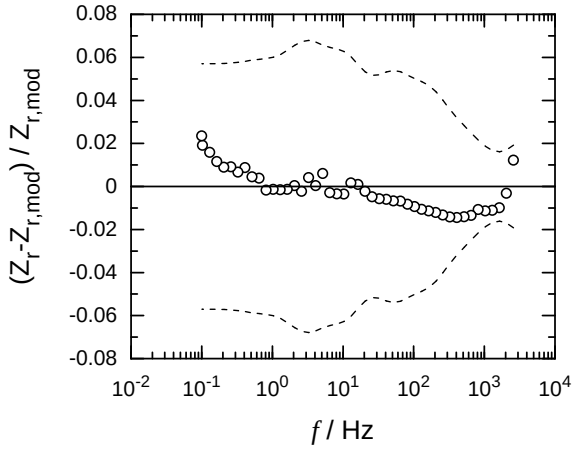

(b)

Figure 8-8: Residual errors for the fit of a Voigt measurement model to the imaginary part of the first impedance spectrum presented in Figure 8-2. a) fit to the imaginary part, where dashed lines represent the $\pm 2\sigma$ bound for the stochastic error structure determined in the previous section; b) prediction of the real part where dashed lines represent the 95.4% confidence interval for the model obtained by Monte Carlo simulation using the calculated confidence intervals for the estimated parameters.

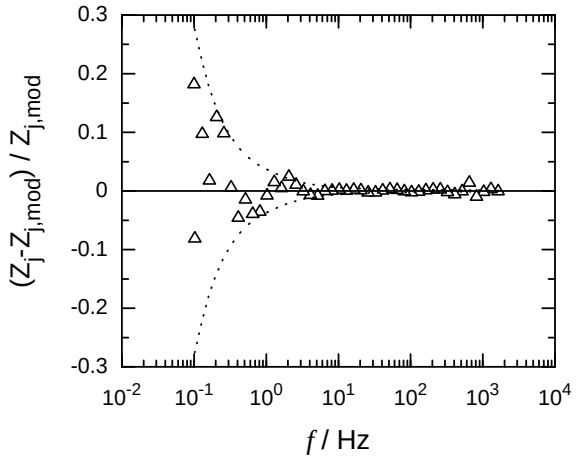

(a)

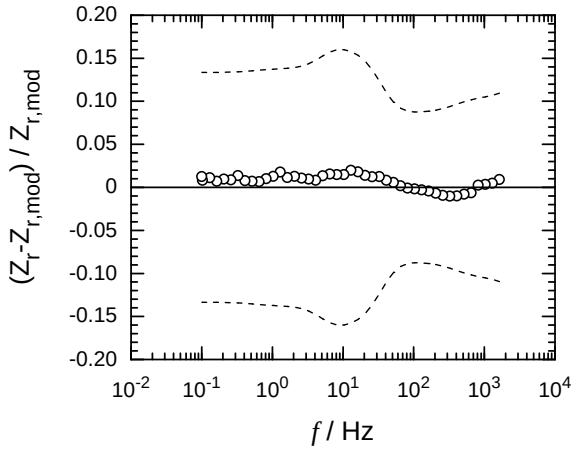

(b)

Figure 8-9: Residual errors for the fit of a Voigt measurement model to the imaginary part of the first impedance spectrum presented in Figure 8-3. a) fit to the imaginary part, where dashed lines represent the $\pm 2\sigma$ bound for the stochastic error structure determined in the previous section; b) prediction of the real part where dashed lines represent the 95.4% confidence interval for the model obtained by Monte Carlo simulation using the calculated confidence intervals for the estimated parameters.

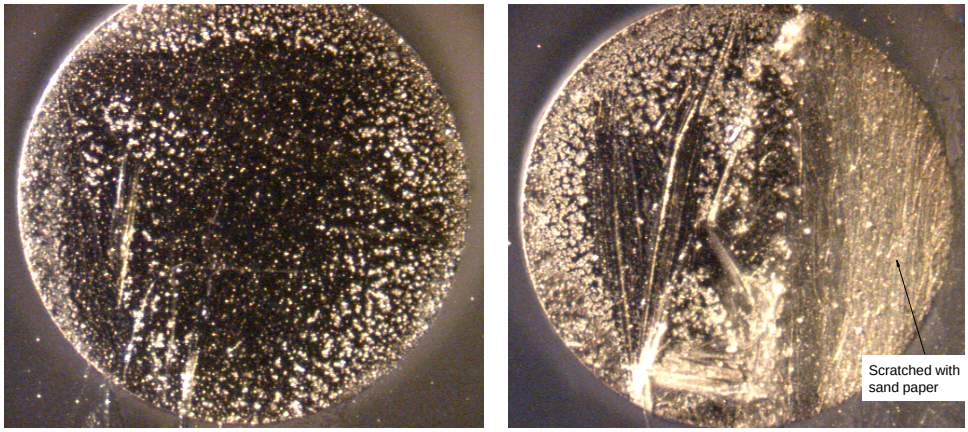

(a) (b)

Figure 8-10: Top view of the disk electrode after impedance experiments. a) Undisturbed image of electrode. b) Image obtained after the right side of disk electrode was cleaned with sand paper to highlight the contrast between metal surface and deposits.

A scanning electron microscopic image of surface deposits is presented in Figure 8-11. The image, taken with a JSM-6400 Scanning Microscope, shows that the deposits are in the form of clusters of crystals. The elemental composition of surface deposits was deduced with Energy Dispersive Spectroscopy (EDS), also carried out with JSM-6400. The energy of the electron beam was varied between 0.0 and 65.0 kVolts. The results of analysis are presented in Figure 8-12, where peaks in the spectrum corresponds to different elements. The EDS analysis revealed the presence of carbon, oxygen, potassium, iron, nickel, and sodium. Similar analysis conducted on the polished metal revealed the presence of nickel. The ratios obtained for elemental species are inconclusive due to the possible influence of the substrate and evaporated salts, but the presence of iron and nickel is consistent with the results of the thermodynamic analysis.

8.6 Optical Micrographs of the Hemispherical Electrode

A series of optical images of the the hemispherical electrode after impedance experiments in the electrolyte supported by 1.0 M NaOH are presented in Figure 8-13. A top view of the electrode, presented in Figure 8.13(a), reveals that

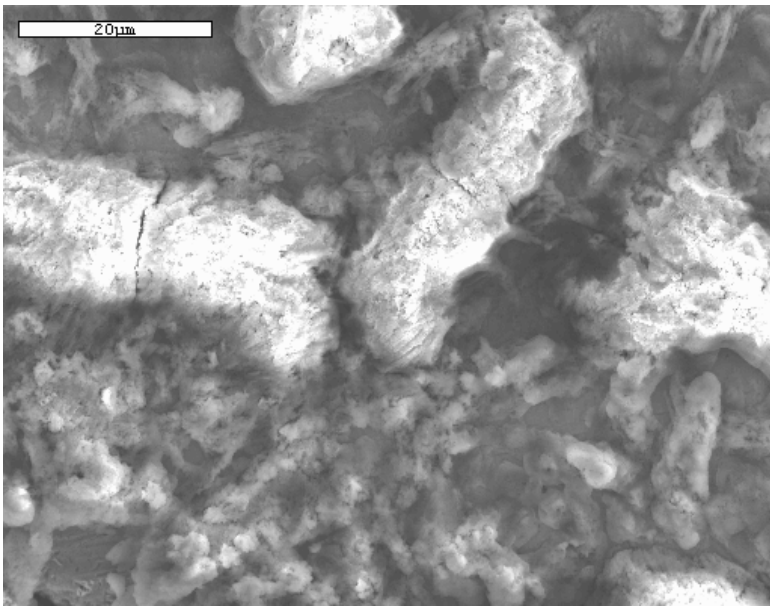

Figure 8-11: Scanning Electron spectroscopy of of a disk electrode after immersion in the electrolyte supported by 1.0 M NaOH.

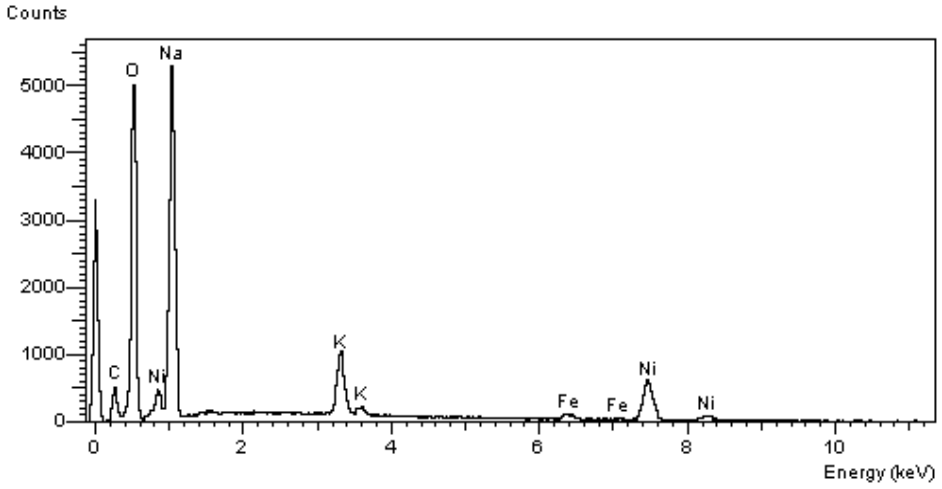

Figure 8-12: Energy Dispersive Spectroscopy (EDS) analysis of a disk electrode after immersion in the electrolyte supported by 1.0 M NaOH.

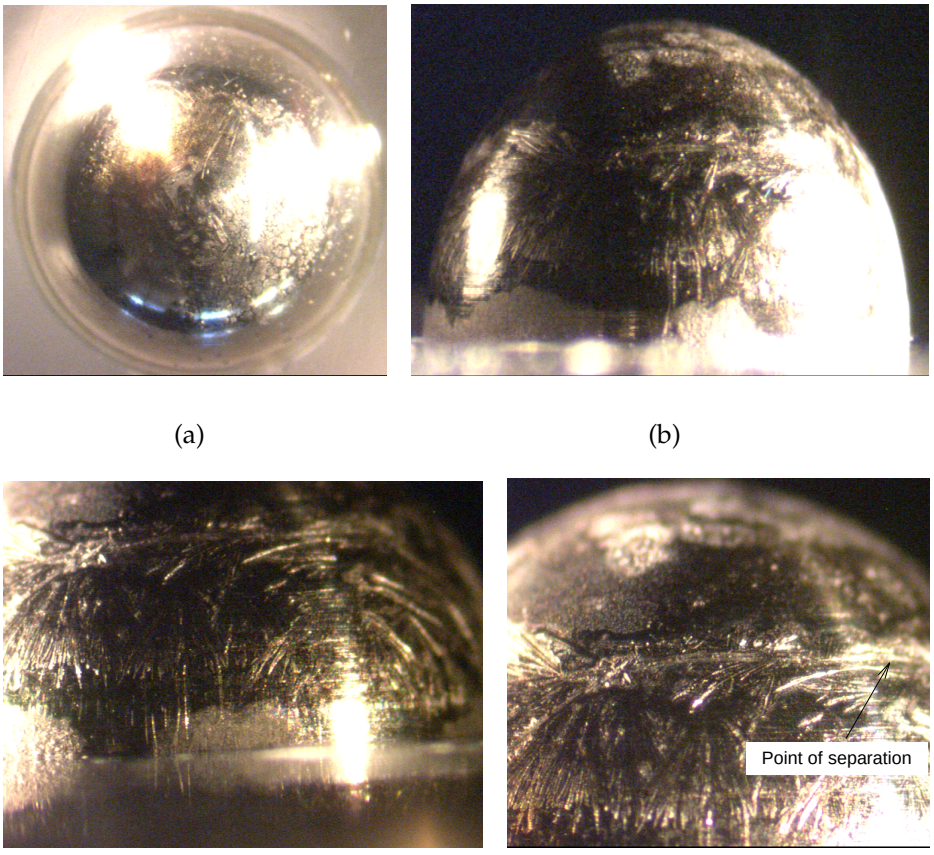

(a) (b)

(c) (d)

Figure 8-13: Images of hemispherical electrode after impedance experiments.

the electrode was only partially covered with surface deposits. The morphology of the deposit is much smoother than the granular morphology of the deposit on the disk electrode. A side view of the electrode is presented in Figure 8.13(b). In this image also, one can see that the hemispherical electrode was only partially covered, confirming the image presented in Figure 8.13(a). An enlarged image of lower portion of the electrode is presented in Figure 8.13(c). This image emphasizes the absence of coverage of the lower part of the electrode. Some tendrils of deposit can be seen, but, in contrast to the observations near the pole of the hemisphere, the surface near the insulating plane was not uniformly covered. A line of demarcation between the covered and the clean areas of the electrode is evident in Figure 8.13(d). The position at which the surface changes from complete coverage to mostly uncovered is located at an angle of 55° from the pole.

After these images were taken, the hemispherical electrode was rinsed with deionized water. The resulting image is presented in Figure 8-14. In agreement with the Pourbaix diagram, the surface layer is unstable in water of neutral pH, and the resulting electrode surface is completely clean without surface deposits. It can be inferred from this treatment that the deposits forming the porous layer are water soluble and that the electrode returned to its original mirror-like surface. The uneven formation of deposits on the hemispherical electrode cannot be attributed to a nonuniform current distribution because the average current density was sufficiently small as to allow a uniform current distribution. The demarkation at an angle of 55° between zones of even deposition and mostly uncovered surface suggests that the higher fluid velocities and shear forces in the recirculation zone either inhibited deposition or removed the deposit. The angle of 55° is quite close to the value of 54.8° predicted by semi-analytical hydrodynamic model to be the point of boundary layer separation.[123] These observations provide experimental

Figure 8-14: Side view of the hemispherical electrode after washing it with deionized water.

verification of the boundary-layer calculations.[123]

8.7 Thermodynamic Analysis

The hypothesis that the impedance response is influenced by formation of a porous layer is supported by thermodynamic calculations performed using CorrosionAnalyzer 1.3 software developed by OLI Systems, Inc.[124,125] The species and reactions considered in generating Figure 8-15 are listed in Table 8.5. For these calculations, the activity of nickel ions was assumed to be 1×10^{-6} M. This value was also used by Pourbaix.[110] Use of a smaller value will generally reduce the regions of stability for solid films. Activity coefficient corrections were used based on the public library used in the software.

Impedance spectra were collected at a bias potential of 0.195 V (SCE), which corresponds to 0.4 Volts with respect to the standard hydrogen reference electrode. For the electrolyte with 1.0 M $NaOH$, 0.005 M $K_3Fe(CN)_6$ and $K_4Fe(CN)_6$, the Pourbaix diagram suggests that di-iron nickel tetraoxide ($NiFe_2O_4$) would be stable under the conditions of the experiment. At lower values of pH, no solid phase will exist in equilibrium with nickel. Calculations performed assuming the absence of dissolved oxygen showed that the di-iron nickel tetraoxide ($NiFe_2O_4$) was not

stable and that no oxide layer should exist on the nickel. This latter result conforms to the experimental conditions reported in the literature.

To test the conclusion that the $NiFe_2O_4$ solid phase should be unstable at lower values of pH, experiments were conducted with a reduced 0.1 M concentration of NaOH. Again, some data points at the high frequency end were found to be corrupted by instrument artifacts and were deleted from the spectra. An impedance spectrum, obtained after five hours of immersion, is presented in Figure 8-16. Even after an immersion time of five hours in the electrolyte, the high-frequency portion of the impedance showed a slope of 45° as expected for a planar electrode. Visual examination of the electrode after experiments did not show any change in surface characteristics. Thus, observation through impedance spectroscopy of a porous electrode structure for an electrolyte supported with 1.0 M NaOH is in agreement with thermodynamic predictions of a $NiFe_2O_4$ layer; and the absence of porous electrode behavior for an electrolyte supported with 0.1 M NaOH is also in agreement with thermodynamic predictions.

8.8 Discussion

The boundary layer separation at the stationary hemispherical electrode was predicted by the semi-analytical hydrodynamic model and computational fluid mechanical simulation of the hydrodynamic equations. The experimental evidence of the phenomena was found in study of ferricyanide reduction at the nickel hemispherical electrode in the electrolyte consisting of 1 M NaOH with dissolved oxygen. The point of separation from these three observations are listed in Table 8.6.

The formation of porous layer for the ferricyanide reduction was unexpected. The presence of the layer was evident in impedance measurements, which was confirmed by the micrographs of both electrode surfaces after the experiments.

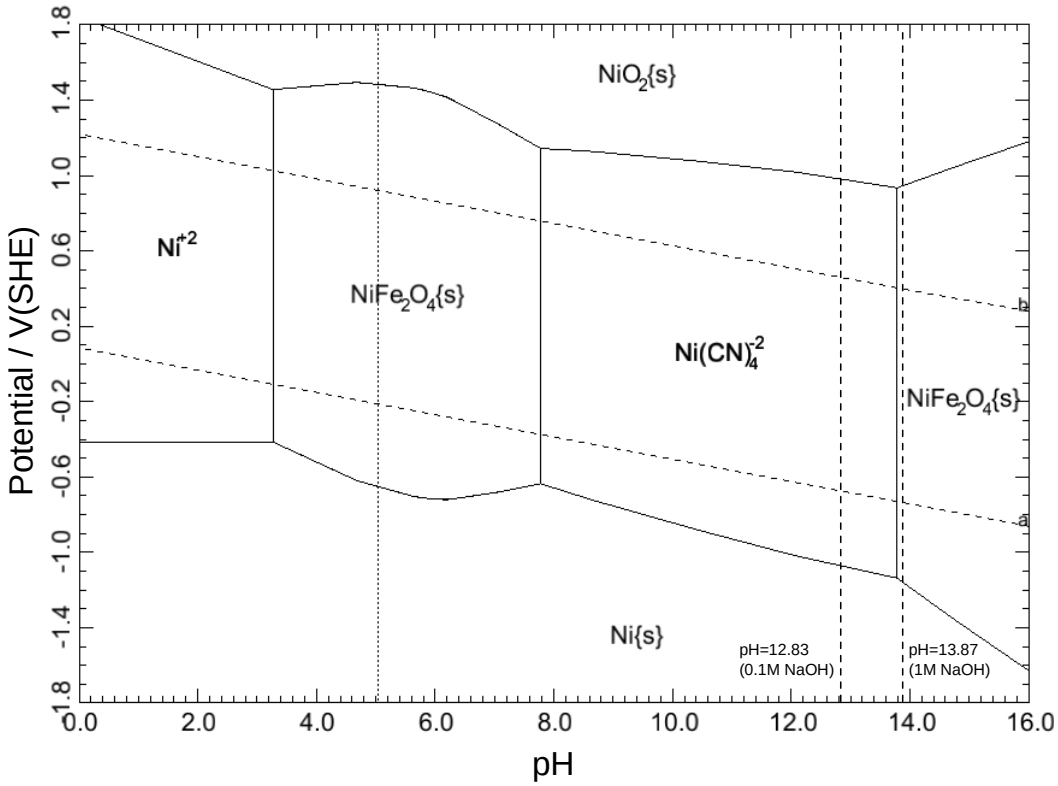

Figure 8-15: The potential-pH diagram for nickel in water containing sodium hydroxide, potassium ferricyanide, potassium ferrocyanide, and dissolved oxygen. The potential is reported with respect to standard hydrogen electrode(SHE). The vertical dashed lines represent the pH of electrolyte solution used in the present study. The line on the left corresponds to a solution containing 0.1 M NaOH, 0.005 M $\mathrm{K_3Fe(CN)_6}$ and $\mathrm{K_4Fe(CN)_6}$, and the line on the right corresponds to 1.0 M NaOH, 0.005 M $\mathrm{K_3Fe(CN)_6}$ and $\mathrm{K_4Fe(CN)_6}$. This diagram was generated using CorrosionAnalyzer 1.3 Revision 1.3.33 by OLI Systems, Inc. The activity of nickel ions was assumed to be 1×10^{-6} M.

Table 8.5: Species considered in calculation of the Pourbaix diagram presented as Figure 8-15.

Aqueous Phase	**Solid Phase**	**Vapor Phase**
Chloride ion(-1)	0.947-Iron oxide	Hydrocyanic acid
Cyanide ion(-1)	Diiron nickel tetraoxide	Hydrogen
Dihydrogen ferrocyanide ion(-2)	Iron	Hydrogen chloride
Diiron(III) dihydroxide ion(+4)	Iron (III) chloride	Nitrogen
Hydrocyanic acid	Iron(II) chloride	Oxygen
Hydrogen	Iron(II) chloride dihydrate	Water
Hydrogen chloride	Iron(II) chloride hexahydrate	
Hydrogen ferrocyanide(II) ion(-3)	Iron(II) chloride tetrahydrate	
Hydrogen ion(+1)	Iron(II) hydroxide	
Hydroxide ion(-1)	Iron(II) oxide	
Iron (III) chloride	Iron(III) chloride 2.5 hydrate	
Iron ion(+2)	Iron(III) chloride dihydrate	
Iron ion(+3)	Iron(III) chloride hexahydrate	
Iron(II) chloride	Iron(III) hexacyanoferrate(II)	
Iron(II) hexacyanide ion(-4)	Iron(III) hydroxide	
Iron(II) hydroxide	Iron(III) oxide	
Iron(II) monochloride ion(+1)	Iron(III) oxide hydroxide	
Iron(II) monohydroxide ion(+1)	Nickel	
Iron(II) tetrahydroxide ion(-2)	Nickel(II) chloride dihydrate	
Iron(II) trihydroxide ion(-1)	Nickel(II) chloride hexahydrate	
Iron(III) dichloride ion(+1)	Nickel(II) chloride tetrahydrate	
Iron(III) dihydroxide ion(+1)	Nickel(II) hydroxide	
Iron(III) hexacyanide ion(-3)	Nickel(II) oxide	
Iron(III) hydroxide	Nickel(II) tetracyanonickel	
Iron(III) monochloride ion(+2)	Nickel(III) hydroxide	
Iron(III) monohydroxide ion(+2)	Nickel(IV) oxide	
Iron(III) tetrachloride ion(-1)	Potassium chloride	
Iron(III) tetrahydroxide ion(-1)	Potassium cyanide	
Iron(VI) tetraoxide ion(-2)	Potassium ferricyanide(III)	
Nickel ion(+2)	Potassium ferrocyanide(II)	
Nickel ion(+3)	Potassium ferrocyanide(II) trihydrate	
Nickel(II) hydroxide	Potassium hydroxide	
Nickel(II) monochloride ion(+1)	Potassium hydroxide dihydrate	
Nickel(II) monohydroxide ion (+1)	Potassium hydroxide monohydrate	
Nickel(II) tetracyanide ion(-2)	Sodium chloride	
Nickel(II) trihydroxide ion(-1)	Sodium cyanide	
Nitrogen	Sodium cyanide dihydrate	
Oxygen	Sodium hydroxide	
Potassium chloride	Sodium hydroxide monohydrate	
Potassium ferricyanide(III) ion(-2)	Sodium iron(III) dioxide	
Potassium ferrocyanide(II) ion(-3)	Triiron tetraoxide	
Potassium ion(+1)	Trinickel tetraoxide	
Sodium ion(+1)		
Water		

Table 8.6: The boundary layer point of separation at the stationary hemispherical electrode.

Phenomena	Separation Point (in degrees)
boundary-layer hydrodynamic model	54.8
Computational fluid mechanic simulation	62.0
Reduction of ferricyanide	55 ± 2

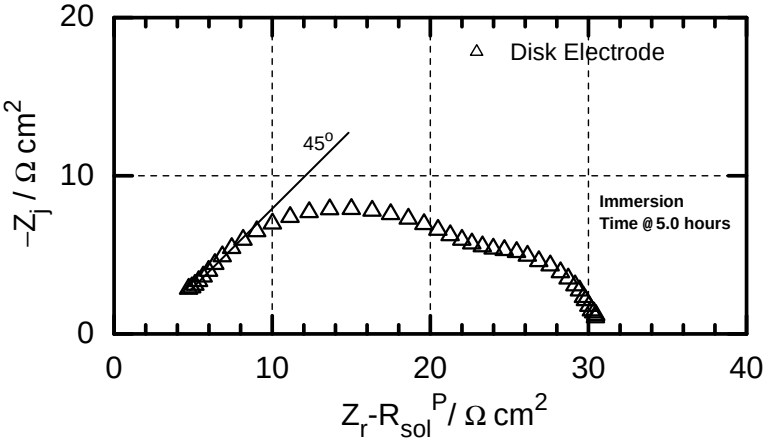

Figure 8-16: Collected Impedance spectrum for the reduction of ferricyanide on a nickel disk electrode under submerged jet impingement. The average fluid velocity in the jet was set at 1.99 meter/second and a bias potential of +0.195 V was applied to the electrode. The electrolyte for this experiment consisted of 0.1 M $NaOH$, 0.005 M $K_3Fe(CN)_6$ and $K_4Fe(CN)_6$. The represented impedance spectrum was collected after 5 hours of immersion of the electrode in the electrolyte.

From the micrographs of hemispheres, the angle of separation was found to be about 55.0 degrees with variation of $\pm$ 2 degrees. The energy dispersive spectroscopy analysis indicated of composition of the porous layer, which was determined to be di-iron nickel tetraoxide ($NiFe_2O_4$) from the equilibrium thermodynamic analysis in terms of Pourbaix diagram.

More work need to be done to validate the chemical composition of the porous layer. A study of the system in the rotating disk and hemispherical electrode is needed to further understand the response of impedance.

8.9 Conclusions

The numerical simulations and the observation of nonuniform deposition on the hemispherical electrode confirm the presence of boundary-layer separation

on the stationary hemispherical electrode under a submerged impinging jet. The stationary hemispherical electrode is therefore inappropriate for kinetic studies of electrochemical reactions in which deposition is expected.

A deposit was formed on the nickel when 1.0 M $NaOH$ was used as the supporting electrolyte and when dissolved oxygen was present. This film was observed in electron and optical micrographs. A Pourbaix analysis indicated that di-iron nickel tetraoxide ($NiFe_2O_4$) is thermodynamically stable under these conditions. EDS analysis of the electrodes revealed Ni, Fe, and O were present on the nickel electrode after the film was deposited, but that only Ni was seen on the electrode before the experiment. Impedance measurements show that the layer behaves, not as an inert barrier to mass transfer, but as a porous electrode. As a test of the Pourbaix analysis, experiments were conducted at a lower pH at which $NiFe_2O_4$ was predicted to be unstable. No film was observed in optical micrographs, and the impedance response was that of a clean surface.

CHAPTER 9
CONCLUSIONS

The quest for an stationary electrode system with uniform current distribution was explored in this work. To this task, stationary hemispherical electrode under submerged jet impingement was suggested as a candidate electrode geometry. The hydrodynamic model developed using boundary-layer theory predicted a separation of boundary layer. The angle of separation was predicted to occur at 54.8°. The computational fluid dynamics (CFD) model , developed at Vrije Universiteit Brussel, Belgium, predicted the separation point at 62.0°. The convective-diffusion solution for mass-transfer-limited-current showed a nonuniform distribution at the electrode surface. The CFD solution of convective-diffusion predicted a minimum in mass-transfer-limited current at the point of boundary layer separation. The CFD solution displayed an enhancement in mass-transfer in the separated part of boundary layer.

The calculations of current and potential distribution below the limiting conditions showed that the current distribution should become uniform at about 25% of total mass-transfer limited current. These calculations were performed under the assumption that current distribution is uniform beyond the point of separation. The current and potential distribution calculations for rotating hemispherical electrode were also performed. These simulations accounted for correction in mass-transfer due to finite Sc number. The resulting distribution of current depicted the effect of Sc number correction at the different levels of average current.

A systematic study was undertaken to evaluate the measurement model approach for assessing the error structure of impedance measurements. Transfer

function and Voigt-element based measurement model were applied to estimate stochastic errors for the impedance measurements collected at the rotating disk electrode of ferricyanide reduction. The estimated error structure was found to be independent of choice of measurement model. Furthermore, the same data set was also analyzed for Kramers-Kronig consistency check using the two measurement models. The confidence intervals of parameters for two measurement model were found to be significantly different. Voigt-element measurement model yielded a tighter confidence interval for model parameters. As a result, Kramers-Kronig consistency check was more sensitive for Voigt-element based measurement model.

An experimental study of oxygen reduction was explored at the nickel disk and hemispherical electrodes. Repeated electrochemical impedance measurements were collected. A constant-phase-element based equivalent circuit model was regressed to the Kramers-Kronig consistent impedance data. The regressed parameters showed that the current distribution is more uniform at the disk electrode than at the hemispherical electrode for the same level of average current.

Impedance spectra collected at the disk electrode for ferricyanide reduction revealed the behavior of a porous electrode. The interpretation of impedance data at the hemispherical electrode showed a behavior of partially covered surface. This feature of electrode surface was corroborated with optical micrographs of the electrode after experiments, equilibrium thermodynamic analysis, and energy dispersive spectroscopy. It is surmised that the vortex in the separated part of the boundary layer partially removed the deposits formed at the the electrode surface.

Based upon this work, It can be stated that the stationary hemispherical electrode under submerged jet impingement is not a suitable candidate for electroanalytical experiments.

CHAPTER 10
SUGGESTED FUTURE RESEARCH

The conclusion of this work has led to the fact that boundary layer separation inhibits the use of stationary hemispherical electrode for future convective-diffusion impedance model development. An interesting study would be to develop a semi-analytical model for fluid flow in the separated part of the boundary layer. The model then can be incorporated into the solution of convective diffusion and current distribution calculations.

The present work suggests that the rotating hemispherical electrode is the best candidate for high current electrochemical impedance experiments. The hydrodynamic model developed for rotating hemispherical electrode in this work should be used to develop an accurate model for convective-diffusion impedance. The rotating hemispherical electrode can be used in conjunction with a stationary disk electrode under jet impingement, where electrode surface can be monitored *in situ.* The observations from stationary electrode can be correlated with the model for impedance at the rotating hemispherical electrode.

APPENDIX A
HYDRODYNAMIC EQUATIONS IN SERIES EXPANSION

This appendix presents the hydrodynamic governing equations for variable $H_{2i-1}(\xi)$ and $F_{2i-1}(\xi)$ introduced in section 2.4 of Chapter 2.

A.1 Ordinary Differential Equations for $H_{2i-1}(\xi)$ and $F_{2i-1}(\xi)$

The governing equations for $H_3(\xi)$ and $F_3(\xi)$ are given by

$$F_1(\xi)F_3(\xi) - H_3(\xi)\frac{\partial F_1}{\partial \xi} - H_1(\xi)\frac{\partial F_3}{\partial \xi} = -\frac{8}{3} + \frac{1}{2}\frac{\partial^2 F_3(\xi)}{\partial \xi^2} \tag{A-1}$$

and

$$2F_3(\xi) - \frac{1}{6}F_1(\xi) = 2\frac{\partial H_3(\xi)}{\partial \xi} \tag{A-2}$$

where equations (A-1) and (A-2) represents the momentum and continuity equations, respectively.

The governing equations for $H_5(\xi)$ and $F_5(\xi)$ are given by

$$\frac{1}{4}\left[6F_1(\xi)F_5(\xi) + 3F_3^2(\xi)\right] - H_1(\xi)\frac{\partial F_5(\xi)}{\partial \xi} - H_3(\xi)\frac{\partial F_3(\xi)}{\partial \xi} - H_5(\xi)\frac{\partial F_1(\xi)}{\partial \xi} = \frac{32}{15} + \frac{1}{2}\frac{\partial^2 F_5(\xi)}{\partial \xi^2} \tag{A-3}$$

and

$$3F_5(\xi) - \frac{1}{6}F_3(\xi) - \frac{1}{90}F_1(\xi) = 2\frac{\partial H_5(\xi)}{\partial \xi} \tag{A-4}$$

where equations (A-3) and (A-4) represents the momentum and continuity equations, respectively.

The governing equations for $H_7(\xi)$ and $F_7(\xi)$ are given by

$$[2F_1(\xi)F_7(\xi) + 2F_3(\xi)F_5(\xi)] - H_1(\xi)\frac{\partial F_7(\xi)}{\partial \xi} - H_3(\xi)\frac{\partial F_5(\xi)}{\partial \xi} - H_5(\xi)\frac{\partial F_3(\xi)}{\partial \xi} - H_7(\xi)\frac{\partial F_1(\xi)}{\partial \xi} = -\frac{256}{315} + \frac{1}{2}\frac{\partial^2 F_7(\xi)}{\partial \xi^2} \tag{A-5}$$

and

$$4F_7(\xi) - \frac{1}{6}F_5(\xi) - \frac{1}{90}F_3(\xi) - \frac{1}{945}F_1(\xi) = 2\frac{\partial H_7(\xi)}{\partial \xi} \tag{A-6}$$

where equations (A-5) and (A-6) represents the momentum and continuity equations, respectively, for $H_5(\xi)$ and $F_5(\xi)$.

The governing equations for $H_9(\xi)$ and $F_9(\xi)$ are given by

$$\begin{aligned}\frac{1}{4}\left[10F_1(\xi)F_9(\xi) + 10F_3(\xi)F_7(\xi) + 5F_5^2(\xi)\right] - H_1(\xi)\frac{\partial F_9(\xi)}{\partial \xi} \\ -H_3(\xi)\frac{\partial F_7(\xi)}{\partial \xi} - H_5(\xi)\frac{\partial F_5(\xi)}{\partial \xi} - H_7(\xi)\frac{\partial F_3(\xi)}{\partial \xi} \\ -H_9(\xi)\frac{\partial F_1(\xi)}{\partial \xi} = \frac{4^8}{9!} + \frac{1}{2}\frac{\partial^2 F_9(\xi)}{\partial \xi^2}\end{aligned} \tag{A-7}$$

and

$$5F_9(\xi) - \frac{1}{6}F_7(\xi) - \frac{1}{90}F_5(\xi) - \frac{1}{945}F_3(\xi) - \frac{1}{9450}F_1(\xi) = 2\frac{\partial H_9(\xi)}{\partial \xi} \tag{A-8}$$

where equations (A-7) and (A-8) represents the momentum and continuity equations, respectively.

The governing equations for $H_{11}(\xi)$ and $F_{11}(\xi)$ are given by

$$\begin{aligned}\left[3F_1(\xi)F_{11}(\xi) + 3F_3(\xi)F_9(\xi) + 3F_5(\xi)F_7(\xi)\right] - H_1(\xi)\frac{\partial F_{11}(\xi)}{\partial \xi} \\ -H_3(\xi)\frac{\partial F_9(\xi)}{\partial \xi} - H_5(\xi)\frac{\partial F_7(\xi)}{\partial \xi} - H_7(\xi)\frac{\partial F_5(\xi)}{\partial \xi} - H_9(\xi)\frac{\partial F_3(\xi)}{\partial \xi} \\ -H_{11}(\xi)\frac{\partial F_1(\xi)}{\partial \xi} = -\frac{4^{10}}{11!} + \frac{1}{2}\frac{\partial^2 F_{11}(\xi)}{\partial \xi^2}\end{aligned} \tag{A-9}$$

and

$$\begin{aligned}6F_{11}(\xi) - \frac{1}{6}F_9(\xi) - \frac{1}{90}F_7(\xi) - \frac{1}{945}F_5(\xi) \\ -\frac{1}{9450}F_3(\xi) - \frac{1}{93555}F_1(\xi) = 2\frac{\partial H_{11}(\xi)}{\partial \xi}\end{aligned} \tag{A-10}$$

where equations (A-9) and (A-10) represents the momentum and continuity equations, respectively.

The governing equations for $H_{13}(\xi)$ and $F_{13}(\xi)$ are given by

$$\begin{aligned}\frac{1}{4}\left[14F_1(\xi)F_{13}(\xi)+14F_3(\xi)F_{11}(\xi)+14F_5(\xi)F_9(\xi)+7F_7^2(\xi)\right]\\ -H_1(\xi)\frac{\partial F_{13}(\xi)}{\partial\xi}-H_3(\xi)\frac{\partial F_{11}(\xi)}{\partial\xi}-H_5(\xi)\frac{\partial F_9(\xi)}{\partial\xi}-H_7(\xi)\frac{\partial F_7(\xi)}{\partial\xi}\\ -H_9(\xi)\frac{\partial F_5(\xi)}{\partial\xi}-H_{11}(\xi)\frac{\partial F_3(\xi)}{\partial\xi}-H_{13}(\xi)\frac{\partial F_1(\xi)}{\partial\xi}=\frac{4^{12}}{13!}+\frac{1}{2}\frac{\partial^2F_{13}(\xi)}{\partial\xi^2}\end{aligned}\tag{A-11}$$

and

$$\begin{aligned}7F_{13}(\xi)-\frac{1}{6}F_{11}(\xi)-\frac{1}{90}F_9(\xi)-\frac{1}{945}F_7(\xi)\\ -\frac{1}{9450}F_5(\xi)-\frac{1}{93555}F_3(\xi)-\frac{691}{638512875}F_1(\xi)=2\frac{\partial H_{13}(\xi)}{\partial\xi}\end{aligned}\tag{A-12}$$

where equations (A-11) and (A-12) represents the momentum and continuity equations, respectively. The governing equations for $H_{15}(\xi)$ and $F_{15}(\xi)$ are given by

$$\begin{aligned}\left[4F_1(\xi)F_{15}(\xi)+4F_3(\xi)F_{13}(\xi)+4F_5(\xi)F_{11}(\xi)+4F_7(\xi)F_9(\xi)\right]\\ -H_1(\xi)\frac{\partial F_{15}(\xi)}{\partial\xi}-H_3(\xi)\frac{\partial F_{13}(\xi)}{\partial\xi}-H_5(\xi)\frac{\partial F_{11}(\xi)}{\partial\xi}-H_7(\xi)\frac{\partial F_9(\xi)}{\partial\xi}\\ -H_9(\xi)\frac{\partial F_7(\xi)}{\partial\xi}-H_{11}(\xi)\frac{\partial F_5(\xi)}{\partial\xi}-H_{13}(\xi)\frac{\partial F_3(\xi)}{\partial\xi}-H_{15}(\xi)\frac{\partial F_1(\xi)}{\partial\xi}\\ =-\frac{4^{14}}{15!}+\frac{1}{2}\frac{\partial^2F_{15}(\xi)}{\partial\xi^2}\end{aligned}\tag{A-13}$$

and

$$\begin{aligned}8F_{15}(\xi)-\frac{1}{6}F_{13}(\xi)-\frac{1}{90}F_{11}(\xi)-\frac{1}{945}F_9(\xi)-\frac{1}{9450}F_7(\xi)\\ -\frac{1}{93555}F_5(\xi)-\frac{691}{638512875}F_3(\xi)-\frac{2}{18243225}F_1(\xi)=2\frac{\partial H_{15}(\xi)}{\partial\xi}\end{aligned}\tag{A-14}$$

where equations (A-13) and (A-14) represents the momentum and continuity equations, respectively. The governing equations for $H_{17}(\xi)$ and $F_{17}(\xi)$ are given by

$$\begin{aligned}\frac{1}{4}\left[18F_1(\xi)F_{17}(\xi)+18F_3(\xi)F_{15}(\xi)+18F_5(\xi)F_{13}(\xi)+18F_7(\xi)F_{11}(\xi)\right.\\ \left.+9F_9^2(\xi)\right]-H_1(\xi)\frac{\partial F_{17}(\xi)}{\partial\xi}-H_3(\xi)\frac{\partial F_{15}(\xi)}{\partial\xi}-H_5(\xi)\frac{\partial F_{13}(\xi)}{\partial\xi}\\ -H_7(\xi)\frac{\partial F_{11}(\xi)}{\partial\xi}-H_9(\xi)\frac{\partial F_9(\xi)}{\partial\xi}-H_{11}(\xi)\frac{\partial F_7(\xi)}{\partial\xi}-H_{13}(\xi)\frac{\partial F_5(\xi)}{\partial\xi}\\ -H_{15}(\xi)\frac{\partial F_3(\xi)}{\partial\xi}-H_{17}(\xi)\frac{\partial F_1(\xi)}{\partial\xi}=\frac{4^{16}}{17!}+\frac{1}{2}\frac{\partial^2F_{17}(\xi)}{\partial\xi^2}\end{aligned}\tag{A-15}$$

and

$$9F_{17}(\xi) - \frac{1}{6}F_{15}(\xi) - \frac{1}{90}F_{13}(\xi) - \frac{1}{945}F_{11}(\xi) - \frac{1}{9450}F_9(\xi) - \frac{1}{93555}F_7(\xi) - \frac{691}{638512875}F_5(\xi) - \frac{2}{18243225}F_3(\xi) - \frac{3617}{325641566250}F_1(\xi) = 2\frac{\partial H_{17}(\xi)}{\partial \xi} \quad \text{(A-16)}$$

where equations (A-15) and (A-16) represents the momentum and continuity equations, respectively. The governing equations for $H_{19}(\xi)$ and $F_{19}(\xi)$ are given by

$$\begin{aligned}[5F_1(\xi)F_{19}(\xi) + 5F_3(\xi)F_{17}(\xi) + 5F_5(\xi)F_{15}(\xi) + 5F_7(\xi)F_{13}(\xi) \\ +5F_9(\xi)F_{11}(\xi)] - H_1(\xi)\frac{\partial F_{19}(\xi)}{\partial \xi} - H_3(\xi)\frac{\partial F_{17}(\xi)}{\partial \xi} - H_5(\xi)\frac{\partial F_{15}(\xi)}{\partial \xi} \\ -H_7(\xi)\frac{\partial F_{13}(\xi)}{\partial \xi} - H_9(\xi)\frac{\partial F_{11}(\xi)}{\partial \xi} - H_{11}(\xi)\frac{\partial F_9(\xi)}{\partial \xi} - H_{13}(\xi)\frac{\partial F_7(\xi)}{\partial \xi} \\ -H_{15}(\xi)\frac{\partial F_5(\xi)}{\partial \xi} - H_{17}(\xi)\frac{\partial F_3(\xi)}{\partial \xi} - H_{19}(\xi)\frac{\partial F_1(\xi)}{\partial \xi} \\ = -\frac{4^{18}}{19!} + \frac{1}{2}\frac{\partial^2 F_{19}(\xi)}{\partial \xi^2}\end{aligned} \quad \text{(A-17)}$$

and

$$\begin{aligned}10F_{19}(\xi) - \frac{1}{6}F_{17}(\xi) - \frac{1}{90}F_{15}(\xi) - \frac{1}{945}F_{13}(\xi) - \frac{1}{9450}F_{11}(\xi) - \frac{1}{93555}F_9(\xi) \\ -\frac{691}{638512875}F_7(\xi) - \frac{2}{18243225}F_5(\xi) - \frac{3617}{325641566250}F_3(\xi) \\ -\frac{43867}{38979295480125}F_1(\xi) = 2\frac{\partial H_{19}(\xi)}{\partial \xi}\end{aligned} \quad \text{(A-18)}$$

where equations (A-17) and (A-18) represents the momentum and continuity equations, respectively.

The governing equations for $H_{21}(\xi)$ and $F_{21}(\xi)$ are given by

$$\begin{aligned}\frac{1}{4}[22F_1(\xi)F_{21}(\xi) + 22F_3(\xi)F_{19}(\xi) + 22F_5(\xi)F_{17}(\xi) + 22F_7(\xi)F_{15}(\xi) \\ +22F_9(\xi)F_{13}(\xi) + 11F_{11}^2(\xi)] - H_1(\xi)\frac{\partial F_{21}(\xi)}{\partial \xi} - H_3(\xi)\frac{\partial F_{19}(\xi)}{\partial \xi} \\ -H_5(\xi)\frac{\partial F_{17}(\xi)}{\partial \xi} - H_7(\xi)\frac{\partial F_{15}(\xi)}{\partial \xi} - H_9(\xi)\frac{\partial F_{13}(\xi)}{\partial \xi} - H_{11}(\xi)\frac{\partial F_{11}(\xi)}{\partial \xi} \\ -H_{13}(\xi)\frac{\partial F_9(\xi)}{\partial \xi} - H_{15}(\xi)\frac{\partial F_7(\xi)}{\partial \xi} - H_{17}(\xi)\frac{\partial F_5(\xi)}{\partial \xi} - H_{19}(\xi)\frac{\partial F_3(\xi)}{\partial \xi} \\ -H_{21}(\xi)\frac{\partial F_1(\xi)}{\partial \xi} = \frac{4^{20}}{21!} + \frac{1}{2}\frac{\partial^2 F_{21}(\xi)}{\partial \xi^2}\end{aligned} \quad \text{(A-19)}$$

and

$$11F_{21}(\xi) - \frac{1}{6}F_{19}(\xi) - \frac{1}{90}F_{17}(\xi) - \frac{1}{945}F_{15}(\xi) - \frac{1}{9450}F_{13}(\xi) - \frac{1}{93555}F_{11}(\xi) - \frac{691}{638512875}F_9(\xi) - \frac{2}{18243225}F_7(\xi) - \frac{3617}{325641566250}F_5(\xi) - \frac{43867}{38979295480125}F_3(\xi) - \frac{174611}{1531329465290625}F_1(\xi) = 2\frac{\partial H_{21}(\xi)}{\partial \xi} \quad \text{(A-20)}$$

where equations (A-19) and (A-20) represents the momentum and continuity equations, respectively. The governing equations for $H_{23}(\xi)$ and $F_{23}(\xi)$ are given by

$$[6F_1(\xi)F_{23}(\xi) + 6F_3(\xi)F_{21}(\xi) + 6F_5(\xi)F_{19}(\xi) + 6F_7(\xi)F_{17}(\xi) + 6F_9(\xi)F_{15}(\xi) + 6F_{11}(\xi)F_{13}(\xi)] - H_1(\xi)\frac{\partial F_{23}(\xi)}{\partial \xi} - H_3(\xi)\frac{\partial F_{21}(\xi)}{\partial \xi} - H_5(\xi)\frac{\partial F_{19}(\xi)}{\partial \xi} - H_7(\xi)\frac{\partial F_{17}(\xi)}{\partial \xi} - H_9(\xi)\frac{\partial F_{15}(\xi)}{\partial \xi} - H_{11}(\xi)\frac{\partial F_{13}(\xi)}{\partial \xi} - H_{13}(\xi)\frac{\partial F_{11}(\xi)}{\partial \xi} - H_{15}(\xi)\frac{\partial F_9(\xi)}{\partial \xi} - H_{17}(\xi)\frac{\partial F_7(\xi)}{\partial \xi} - H_{19}(\xi)\frac{\partial F_5(\xi)}{\partial \xi} - H_{21}(\xi)\frac{\partial F_3(\xi)}{\partial \xi} - H_{23}(\xi)\frac{\partial F_1(\xi)}{\partial \xi} = \frac{4^{22}}{23!} + \frac{1}{2}\frac{\partial^2 F_{23}(\xi)}{\partial \xi^2} \quad \text{(A-21)}$$

and

$$12F_{23}(\xi) - \frac{1}{6}F_{21}(\xi) - \frac{1}{90}F_{19}(\xi) - \frac{1}{945}F_{17}(\xi) - \frac{1}{9450}F_{15}(\xi) - \frac{1}{93555}F_{13}(\xi)\% - \frac{691}{638512875}F_{11}(\xi) - \frac{2}{18243225}F_9(\xi) - \frac{3617}{325641566250}F_7(\xi) - \frac{43867}{38979295480125}F_5(\xi) - \frac{174611}{1531329465290625}F_3(\xi) - \frac{155366}{13447856940643125}F_1(\xi) = 2\frac{\partial H_{23}(\xi)}{\partial \xi} \quad \text{(A-22)}$$

where equations (A-21) and (A-22) represents the momentum and continuity equa-

tions, respectively. The governing equations for $H_{25}(\xi)$ and $F_{25}(\xi)$ are given by

$$\begin{aligned}
&\frac{1}{4}\left[26F_1(\xi)F_{25}(\xi)+26F_3(\xi)F_{23}(\xi)+26F_5(\xi)F_{21}(\xi)+26F_7(\xi)F_{19}(\xi)\right.\\
&\left.+26F_9(\xi)F_{17}(\xi)+26F_{11}(\xi)F_{15}(\xi)+13F_{13}^2(\xi)\right]-H_1(\xi)\frac{\partial F_{25}(\xi)}{\partial\xi}\\
&-H_3(\xi)\frac{\partial F_{23}(\xi)}{\partial\xi}-H_5(\xi)\frac{\partial F_{21}(\xi)}{\partial\xi}-H_7(\xi)\frac{\partial F_{19}(\xi)}{\partial\xi}-H_9(\xi)\frac{\partial F_{17}(\xi)}{\partial\xi}\\
&-H_{11}(\xi)\frac{\partial F_{15}(\xi)}{\partial\xi}-H_{13}(\xi)\frac{\partial F_{13}(\xi)}{\partial\xi}-H_{15}(\xi)\frac{\partial F_{11}(\xi)}{\partial\xi}-H_{17}(\xi)\frac{\partial F_9(\xi)}{\partial\xi}\\
&-H_{19}(\xi)\frac{\partial F_7(\xi)}{\partial\xi}-H_{21}(\xi)\frac{\partial F_5(\xi)}{\partial\xi}-H_{23}(\xi)\frac{\partial F_3(\xi)}{\partial\xi}-H_{25}(\xi)\frac{\partial F_1(\xi)}{\partial\xi}\\
&=\frac{4^{24}}{25!}+\frac{1}{2}\frac{\partial^2F_{25}(\xi)}{\partial\xi^2}
\end{aligned}\tag{A-23}$$

and

$$\begin{aligned}
&13F_{25}(\xi)-\frac{1}{6}F_{23}(\xi)-\frac{1}{90}F_{21}(\xi)-\frac{1}{945}F_{19}(\xi)-\frac{1}{9450}F_{17}(\xi)\\
&-\frac{1}{93555}F_{15}(\xi)-\frac{691}{638512875}F_{13}(\xi)-\frac{2}{18243225}F_{11}(\xi)\\
&-\frac{3617}{325641566250}F_9(\xi)-\frac{43867}{38979295480125}F_7(\xi)\\
&-\frac{174611}{1531329465290625}F_5(\xi)-\frac{155366}{13447856940643125}F_3(\xi)\\
&-\frac{236364091}{201919571963756521875}F_1(\xi)=2\frac{\partial H_{25}(\xi)}{\partial\xi}
\end{aligned}\tag{A-24}$$

where equations (A-23) and (A-24) represents the momentum and continuity equations, respectively. The governing equations for $H_{27}(\xi)$ and $F_{27}(\xi)$ are given by

$$\begin{aligned}
&\left[7F_1(\xi)F_{27}(\xi)+7F_3(\xi)F_{25}(\xi)+7F_5(\xi)F_{23}(\xi)+7F_7(\xi)F_{21}(\xi)\right)\\
&+7F_9(\xi)F_{19}(\xi)+7F_{11}(\xi)F_{17}(\xi)+7F_{13}(\xi)F_{15}(\xi)]-H_1(\xi)\frac{\partial F_{27}(\xi)}{\partial\xi}\\
&-H_3(\xi)\frac{\partial F_{25}(\xi)}{\partial\xi}-H_5(\xi)\frac{\partial F_{23}(\xi)}{\partial\xi}-H_7(\xi)\frac{\partial F_{21}(\xi)}{\partial\xi}-H_9(\xi)\frac{\partial F_{19}(\xi)}{\partial\xi}\\
&-H_{11}(\xi)\frac{\partial F_{17}(\xi)}{\partial\xi}-H_{13}(\xi)\frac{\partial F_{15}(\xi)}{\partial\xi}-H_{15}(\xi)\frac{\partial F_{13}(\xi)}{\partial\xi}-H_{17}(\xi)\frac{\partial F_{11}(\xi)}{\partial\xi}\\
&-H_{19}(\xi)\frac{\partial F_9(\xi)}{\partial\xi}-H_{21}(\xi)\frac{\partial F_7(\xi)}{\partial\xi}-H_{23}(\xi)\frac{\partial F_8(\xi)}{\partial\xi}-H_{25}(\xi)\frac{\partial F_3(\xi)}{\partial\xi}\\
&-H_{27}(\xi)\frac{\partial F_1(\xi)}{\partial\xi}=\frac{4^{26}}{27!}+\frac{1}{2}\frac{\partial^2F_{27}(\xi)}{\partial\xi^2}
\end{aligned}\tag{A-25}$$

and

$$14F_{27}(\xi) - \frac{1}{6}F_{25}(\xi) - \frac{1}{90}F_{23}(\xi) - \frac{1}{945}F_{21}(\xi) - \frac{1}{9450}F_{19}(\xi) - \frac{1}{93555}F_{17}(\xi) - \frac{691}{638512875}F_{15}(\xi) - \frac{2}{18243225}F_{13}(\xi) - \frac{3617}{325641566250}F_{11}(\xi)) - \frac{43867}{38979295480125}F_9(\xi) - \frac{174611}{1531329465290625}F_7(\xi) - \frac{155366}{1344785694064 3125}F_5(\xi) - \frac{236364091}{201919571963756521875}F_3(\xi) - \frac{1315862}{11094481976030578125}F_1(\xi) = 2\frac{\partial H_{27}(\xi)}{\partial \xi} \quad \text{(A-26)}$$

where equations (A-25) and (A-26) represents the momentum and continuity equations, respectively.

A.2 Solutions of $H_{2i-1}(\xi)$ and $F_{2i-1}(\xi)$

The obtained solution profiles of $H_{2i-1}(\xi)$ and $F_{2i-1}(\xi)$ are presented in this section. $H_1(\xi)$ and $F_1(\xi)$ as a function of ξ are presented in Figure A.1(a), and $H_3(\xi)$ and $F_3(\xi)$ are shown in Figure A.1(b). Values of $H_3(\xi)$ and $F_3(\xi)$ have opposite signs compared to $H_1(\xi)$ and $F_1(\xi)$. Profiles of $H_5(\xi)$ and $F_5(\xi)$ are drawn in Figure A.1(c). Similarly, $H_7(\xi)$ and $F_7(\xi)$ are given in Figure A.1(d). As seen in Figure A-1, the magnitude of $H_5(\xi)$, $F_5(\xi)$, $H_7(\xi)$, and $F_7(\xi)$ is smaller compare to that of $H_1(\xi)$ and $F_1(\xi)$. This is attributed to the forcing term in the differential equation of $H_5(\xi)$, $F_5(\xi)$, $H_7(\xi)$, and $F_7(\xi)$ (see equations (A-3),(A-4), (A-5), and (A-6)) and their far field boundary condition at $\xi = \infty$.

The obtained solutions of $H_9(\xi)$ and $F_9(\xi)$ as a function of ξ is presented in Figure A.2(a). Profiles of $H_{11}(\xi)$ and $F_{11}(\xi)$ are displayed in Figure A.2(b). $H_{13}(\xi)$ and $F_{13}(\xi)$ are drawn in Figure A.2(c), and $H_{15}(\xi)$ and $F_{15}(\xi)$ are presented in Figure A.2(d). $F_9(\xi)$ and $F_{11}(\xi)$ shown oscillations close to the electrode surface whereas oscillations in $F_{13}(\xi)$ and $F_{15}(\xi)$ are damped down. The magnitudes and the signs of $H_9(\xi)$, $F_9(\xi)$, $H_{11}(\xi)$, $F_{11}(\xi)$,$H_{13}(\xi)$, $F_{13}(\xi)$,$H_{15}(\xi)$, and $F_{15}(\xi)$ are same in Figure A-2.

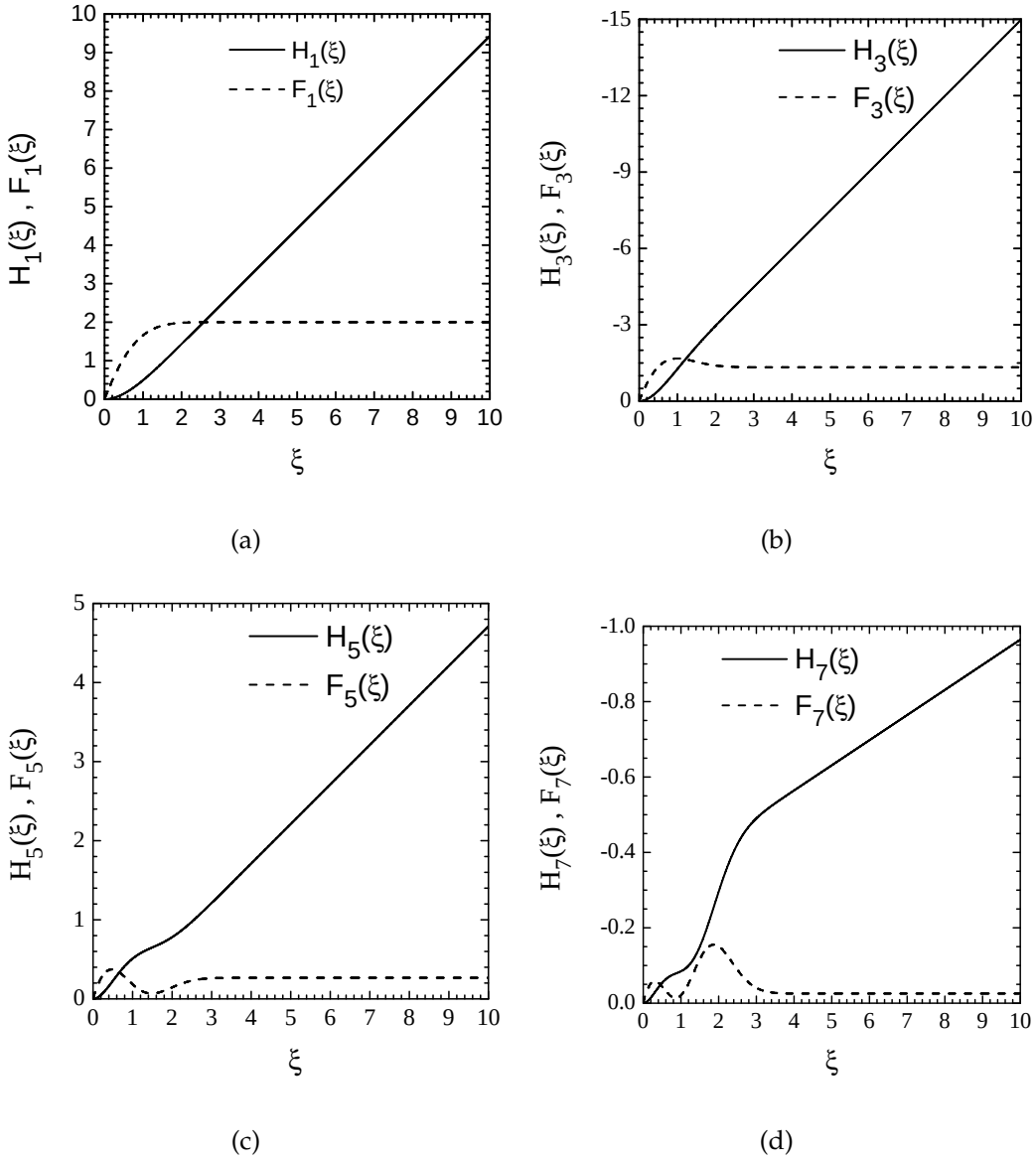

Figure A-1: Calculated profiles of dimensionless radial and colatitude functions in the expansion of (2-24) and (2-25). (a) $H_1(\xi)$ and $F_1(\xi)$ as a function ξ, (b) $H_3(\xi)$ and $F_3(\xi)$ as a function ξ, (c) $H_5(\xi)$ and $F_5(\xi)$ as a function ξ, and (d) $H_7(\xi)$ and $F_7(\xi)$ as a function ξ.

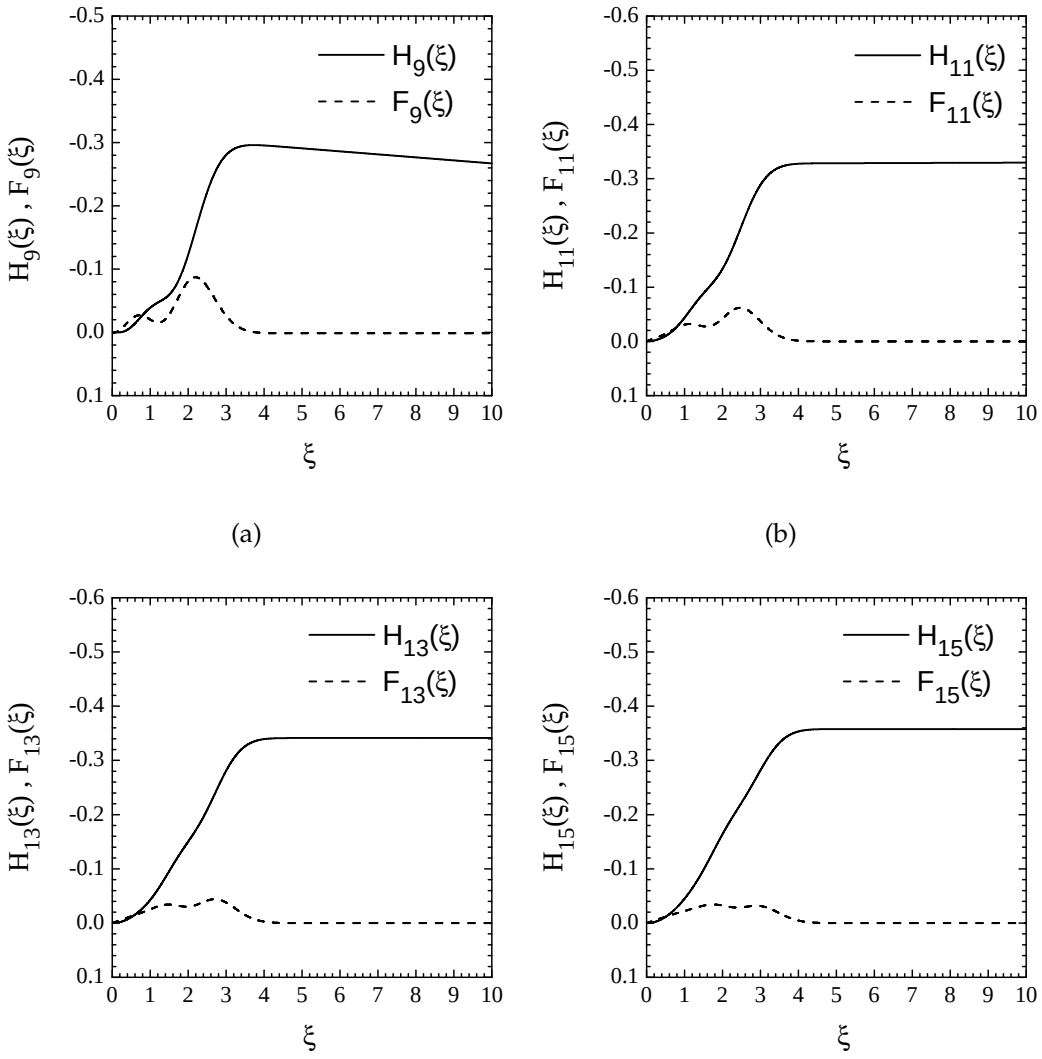

Figure A-2: Calculated profiles of dimensionless radial and colatitude functions in the expansion of (2-24) and (2-25). (a) $H_9(\xi)$ and $F_9(\xi)$ as a function of ξ, (b) $H_{11}(\xi)$ and $F_{11}(\xi)$ as a function of ξ, (c) $H_{13}(\xi)$ and $F_{13}(\xi)$ as a function of ξ, and (d) $H_{15}(\xi)$ and $F_{15}(\xi)$ as a function of ξ.

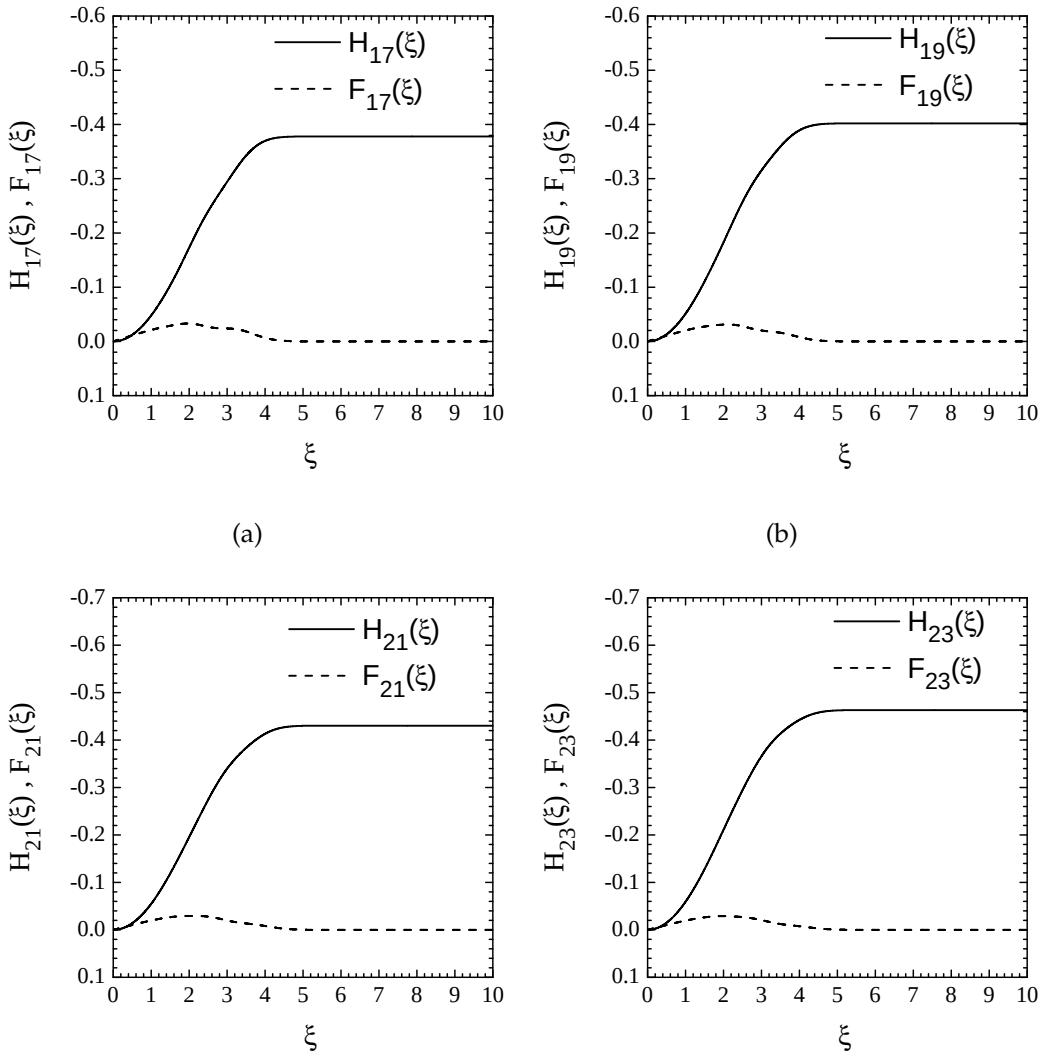

Figure A-3: Calculated profiles of dimensionless radial and colatitude in the expansion of (2-24) and (2-25). (a) $H_{17}(\xi)$ and $F_{17}(\xi)$ as a function of ξ, (b) $H_{19}(\xi)$ and $F_{19}(\xi)$ as a function of ξ, (c) $H_{21}(\xi)$ and $F_{21}(\xi)$ as a function of ξ, and (d) $H_{23}(\xi)$ and $F_{23}(\xi)$ as a function of ξ.

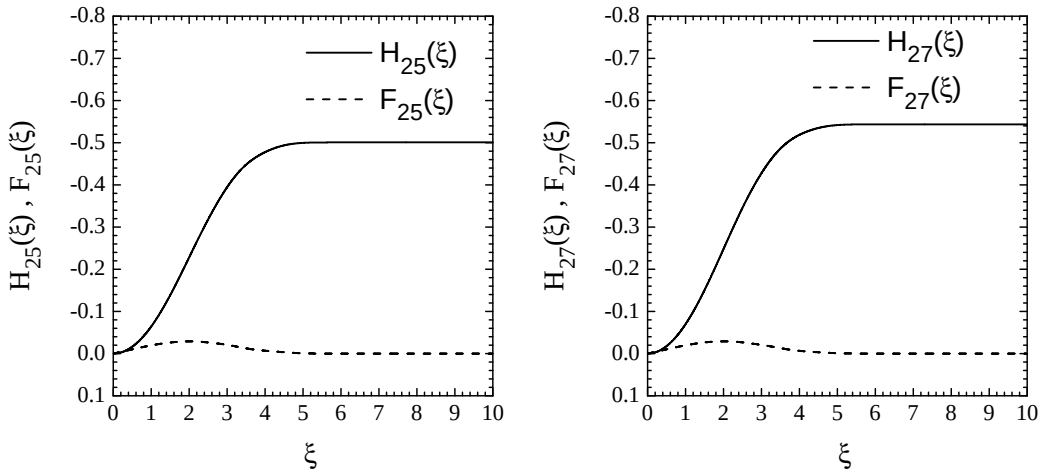

(a) (b)

Figure A-4: Calculated profiles of dimensionless radial and colatitude in the expansion of (2-24) and (2-25). (a) $H_{25}(\xi)$ and $F_{25}(\xi)$ as a function of ξ, (b) $H_{27}(\xi)$ and $F_{27}(\xi)$ as a function of ξ

The calculated solutions of $H_{17}(\xi)$ and $F_{17}(\xi)$ as a function of ξ is presented in Figure A.3(a). Similarly, $H_{19}(\xi)$ and $F_{19}(\xi)$ are given in Figure A.3(b). $H_{21}(\xi)$ and $F_{21}(\xi)$ are drawn in Figure A.3(c), and $H_{23}(\xi)$ and $F_{23}(\xi)$ are presented in Figure A.3(d).

The calculated solutions of $H_{25}(\xi)$ and $F_{25}(\xi)$ as a function of ξ is presented in Figure A.4(a). Profiles of $H_{27}(\xi)$ and $F_{27}(\xi)$ are plotted in Figure A.4(b).

A.3 Extrapolation of Finite Difference Values for $F'_{2i-1}(0)$

Values of $F'_{2i-1}(\xi)$ at ξ=0 were obtained by extrapolating them to zero mesh size. The calculation method has been given in detail in section 2.4.1 of Chapter 2.

$F'_{2i-1}(0)$ as function of H^2 for $1 \leq i \leq 4$ are given in Figure A-5. $F'_{2i-1}(0)$ as function of H^2 for $5 \leq i \leq 8$ are provided in Figure A-5. $F'_{2i-1}(0)$ as function of H^2 for $9 \leq i \leq 12$ are displayed in Figure A-5. $F'_{2i-1}(0)$ as function of H^2 for $i = 13$, and 14 are shown in Figure A-5. In the aforementioned figures, a straight line was regressed to the data set. The fit to the data by a solid line is also given in figures.

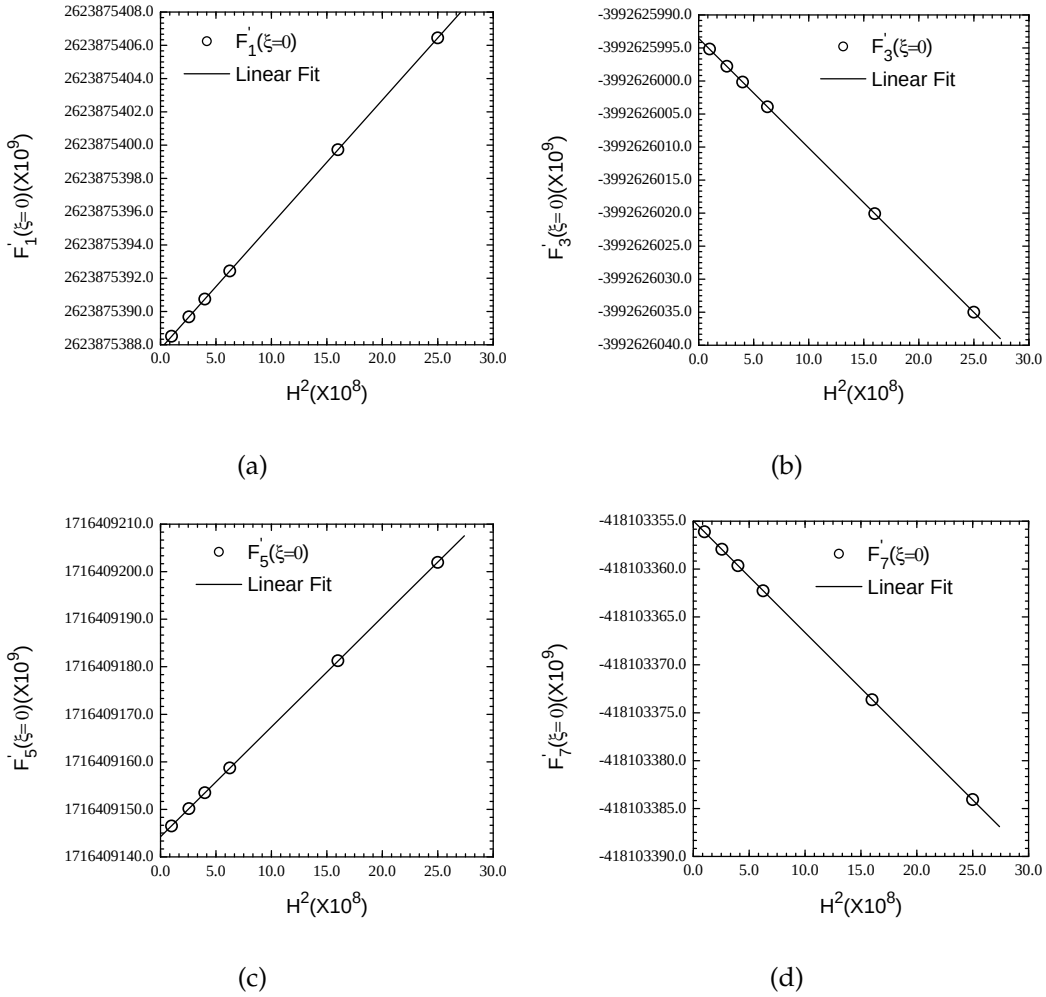

Figure A-5: First derivative of dimensionless colatitude velocity coefficients $F_{2i-1}(\xi)$ at ξ =0 for different grid spacing. (a) $F_1^{'}(0)$ as a function of H^2 , (b) $F_3^{'}(0)$ as a function of H^2, (c) $F_5^{'}(0)$ as a function of H^2, and (d) $F_7^{'}(0)$ as a function of H^2.

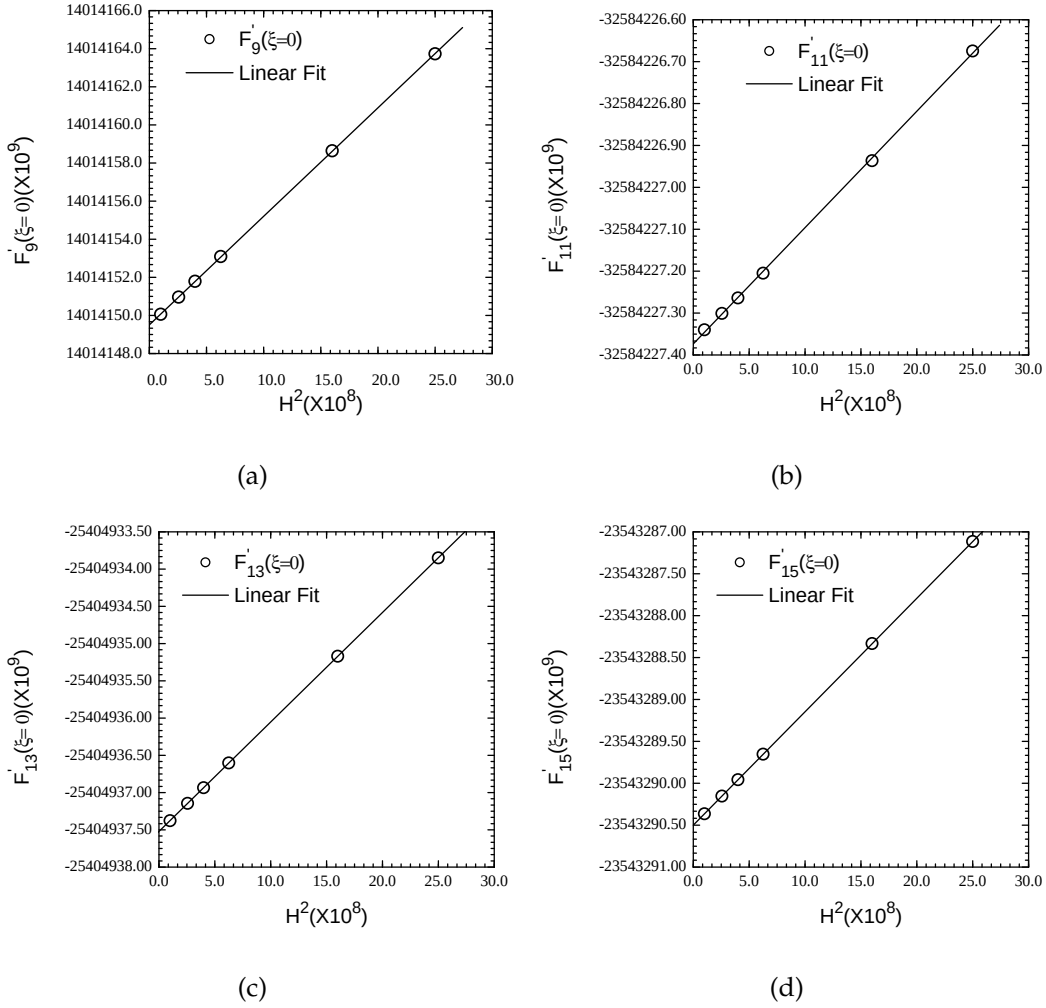

Figure A-6: First derivative of dimensionless colatitude velocity coefficients $F_{2i-1}(\xi)$ at ξ =0 for different grid spacing. (a) $F_9^{'}(0)$ as a function of H^2 , (b) $F_{11}^{'}(0)$ as a function of H^2, (c) $F_{13}^{'}(0)$ as a function of H^2, and (d) $F_{15}^{'}(0)$ as a function of H^2.

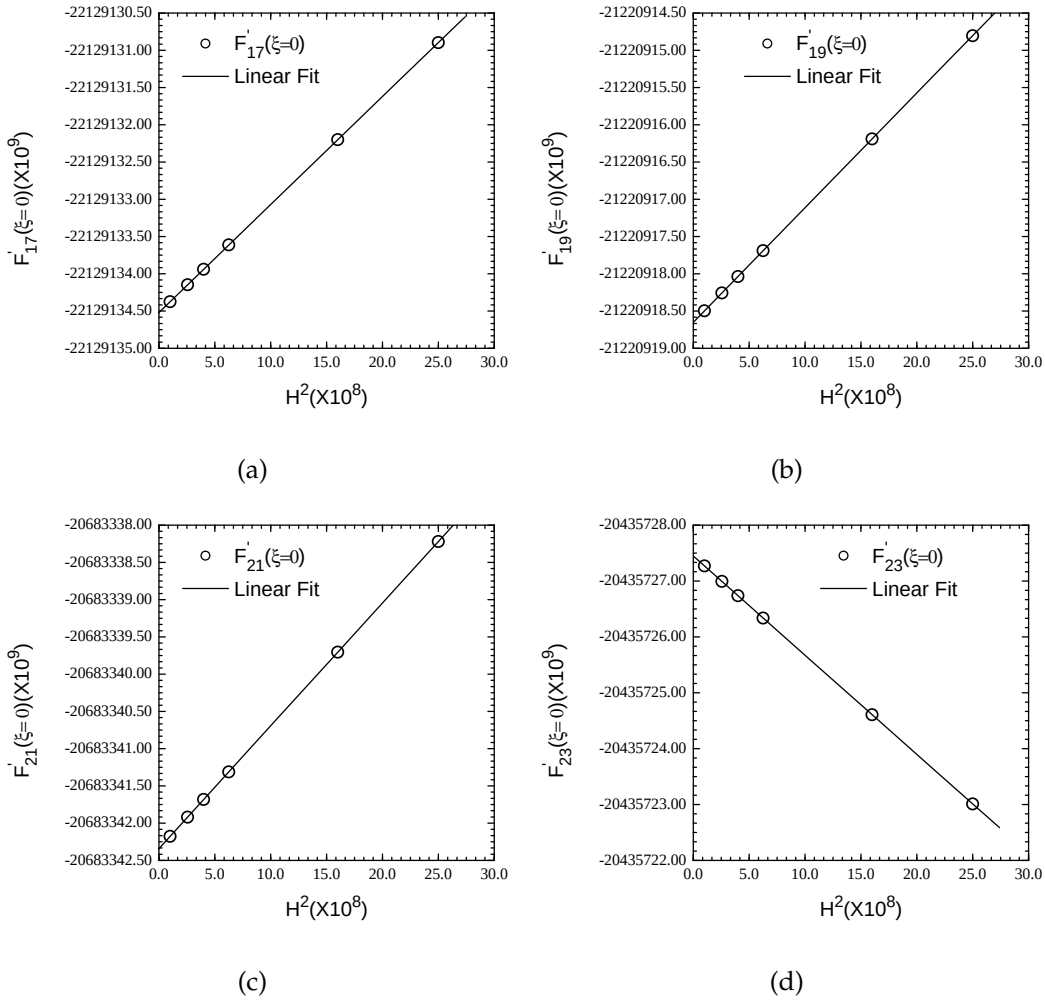

Figure A-7: First derivative of dimensionless colatitude velocity coefficients $F_{2i-1}(\xi)$ at ξ =0 for different grid spacing. (a) $F'_{17}(0)$ as a function of H^2 , (b) $F'_{19}(0)$ as a function of H^2, (c) $F'_{21}0)$ as a function of H^2, and (d) $F'_{23}(0)$ as a function of H^2.

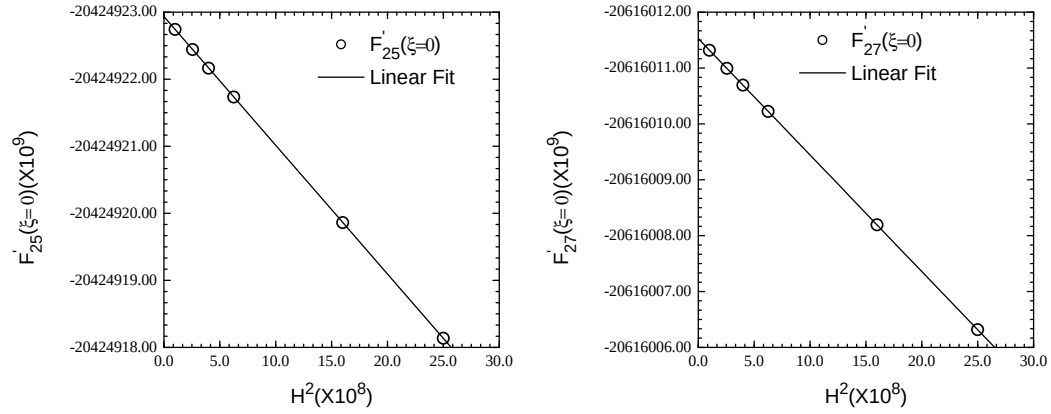

(a) (b)

Figure A-8: First derivative of dimensionless colatitude velocity coefficients $F_{2i-1}(\xi)$ at ξ =0 for different grid spacing. (a) $F'_{25}(0)$ as a function of H^2 , (b) $F'_{27}(0)$ as a function of H^2

APPENDIX B
SOLUTION OF CONVECTIVE-DIFFUSION EQUATION FOR INFINITE SCHMIDT NUMBER

A solution of equation set (3-7) mentioned in Chapter 3 were obtained analytically. The resulting solutions of $\Phi_{1,2i-1}(Z)$ for $2 \leq i \leq 14$ are given by below.

$$\Phi_{1,3}(Z) = 0.5456995862847621Z \exp\left[-\frac{Z^3 H_1''(0)}{3}\right] \tag{B-1}$$

$$\Phi_{1,5}(Z) = \left(0.0195491619333433Z + 0.22980950047037Z^4\right) \exp\left[-\frac{Z^3 H_1''(0)}{3}\right] \tag{B-2}$$

$$\Phi_{1,7}(Z) = \big(0.0463852398945 69Z - 0.0818921757306 29Z^4 + 0.0645195119974 33Z^7\big) \exp\left[-\frac{Z^3 H_1''(0)}{3}\right] \tag{B-3}$$

$$\Phi_{1,9}(Z) = \big(0.0371974663055 11Z + 0.0445787500697 12Z^4 - 0.0551976844669 42Z^7 + 0.0135854939195 29Z^{10}\big) \exp\left[-\frac{Z^3 H_1''(0)}{3}\right] \tag{B-4}$$

$$\Phi_{1,11}(Z) = \big(0.0324711750962 86Z + 9.5312102007797 59 \times 10^{-3} Z^4 + 0.0343900611416 28Z^7 - 0.0189855922790 3Z^{10} + 2.2884939990854 38 \times 10^{-3} Z^{13}\big) \exp\left[-\frac{Z^3 H_1''(0)}{3}\right] \tag{B-5}$$

$$\Phi_{1,13}(Z) = \big(0.0294959463884888Z + 0.0137056922103555Z^4$$
$$-8.155404955284953 \times 10^{-3}Z^7 + 0.0159059536800822Z^{10}$$
$$-4.487417750161311 \times 10^{-3}Z^{13}$$
$$+3.212498084888444 \times 10^{-4}Z^{16}\big) \exp\left[-\frac{Z^3 H_1''(0)}{3}\right] \tag{B-6}$$

$$\Phi_{1,15}(Z) = \big(0.0276172570516745Z + 0.0122068005528965Z^4$$
$$+5.601693276335696 \times 10^{-3}Z^7 - 7.914866172102188 \times 10^{-3}Z^{10}$$
$$+4.890007650178375 \times 10^{-3}Z^{13} + 8.148371810924252 \times 10^{-4}Z^{16}$$
$$+3.865353228381212 \times 10^{-5}Z^{19}\big) \exp\left[-\frac{Z^3 H_1''(0)}{3}\right] \tag{B-7}$$

$$\Phi_{1,17}(Z) = \big(0.0264723050234235Z + 0.0117395957542225Z^4$$
$$+2.027511423732476 \times 10^{-3}Z^7 + 3.715610096603022 \times 10^{-3}Z^{10}$$
$$-3.460299105112408 \times 10^{-3}Z^{13} + 1.106919051608306 \times 10^{-3}Z^{16}$$
$$-1.205874826618782 \times 10^{-4}Z^{19}$$
$$+4.069523401160695 \times 10^{-6}Z^{22}\big) \exp\left[-\frac{Z^3 H_1''(0)}{3}\right] \tag{B-8}$$

$$\Phi_{1,19}(Z) = \big(0.0258534812757312Z + 0.0114486642555863Z^4$$
$$+2.626815088536126 \times 10^{-3}Z^7 - 6.718391700859723 \times 10^{-4}Z^{10}$$
$$+1.939689983511778 \times 10^{-3}Z^{13} - 1.001165404851775 \times 10^{-3}Z^{16}$$
$$+1.973508690684787 \times 10^{-4}Z^{19} - 1.508994956957569 \times 10^{-5}Z^{22}$$
$$+3.808424852868884 \times 10^{-7}Z^{25}\big) \exp\left[-\frac{Z^3 H_1''(0)}{3}\right] \tag{B-9}$$

$$\Phi_{1,21}(Z) = \big(0.025635602737 34Z + 0.011340988284241Z^4$$
$$+2.497746698301685 \times 10^{-3}Z^7 + 6.367613726292331 \times 10^{-4}Z^{10}$$
$$-7.735325909614409 \times 10^{-4}Z^{13} + 6.9140412265024 \times 10^{-4}Z^{16}$$
$$-2.16692219795348 \times 10^{-4}Z^{19} + 2.898152277646378 \times 10^{-5}Z^{22}$$
$$-1.637600671725532 \times 10^{-6}Z^{25}$$
$$+3.207670428982255 \times 10^{-8}Z^{28}\big) \exp\left[-\frac{Z^3 H_1''(0)}{3}\right] \qquad \text{(B-10)}$$

$$\Phi_{1,23}(Z) = \big(0.025740812913 81Z + 0.011377417297367Z^4$$
$$+2.516351443908926 \times 10^{-3}Z^7 + 3.145350798309402 \times 10^{-4}Z^{10}$$
$$+3.274581421873338 \times 10^{-4}Z^{13} - 3.708673869516351 \times 10^{-4}Z^{16}$$
$$+1.79925482723237 \times 10^{-4}Z^{19} - 3.742084021147993 \times 10^{-5}Z^{22}$$
$$+3.61674007291003 \times 10^{-6}Z^{25} - 1.569974972993698 \times 10^{-7}Z^{28}$$
$$+2.456073759545927 \times 10^{-9}Z^{31}\big) \exp\left[-\frac{Z^3 H_1''(0)}{3}\right] \qquad \text{(B-11)}$$

$$\Phi_{1,25}(Z) = \big(0.026120175464161Z + 0.011536033857682Z^4$$
$$+2.547990978800542 \times 10^{-3}Z^7 + 3.853204317851295 \times 10^{-4}Z^{10}$$
$$-4.304155660476651 \times 10^{-5}Z^{13} + 1.717737137848556 \times 10^{-4}Z^{16}$$
$$-1.183741696896257 \times 10^{-4}Z^{19} + 3.642822415706468 \times 10^{-5}Z^{22}$$
$$-5.370631661204772 \times 10^{-6}Z^{25} + 3.923930669059197 \times 10^{-7}Z^{28}$$
$$-1.348601314078991 \times 10^{-8}Z^{31}$$
$$+1.723869988743519 \times 10^{-10}Z^{34}\big) \exp\left[-\frac{Z^3 H_1''(0)}{3}\right] \qquad \text{(B-12)}$$

$$\Phi_{1,27}(Z) = \big(0.02674339550 15Z + 0.0118030721088 09Z^4$$
$$+2.605205492382419 \times 10^{-3}Z^7 + 3.819192030568879 \times 10^{-4}Z^{10}$$
$$+6.361457361444786 \times 10^{-5}Z^{13} - 5.999781821003725 \times 10^{-5}Z^{16}$$
$$+6.509008632308619 \times 10^{-5}Z^{19} - 2.826487192450259 \times 10^{-5}Z^{22}$$
$$+6.005663398904835 \times 10^{-6}Z^{25} - 6.590099418671317 \times 10^{-7}Z^{28}$$
$$+3.765622327245689 \times 10^{-8}Z^{31} - 1.04963380277 \times 10^{-9}Z^{34}$$
$$+1.116877408928525 \times 10^{-11}Z^{37}\big) \exp\left[-\frac{Z^3 H_1''(0)}{3}\right] \qquad \text{(B-13)}$$

APPENDIX C
BOUNDARY-LAYER PROGRAM LISTING

The program listing presents all of the FORTRAN code to solve governing equations of the boundary layer fluid model for stationary hemispherical electrode under submerged jet impingement. The program was developed with 'Compaq Visual Fortran, Version 6.1' with double precision accuracy. The main program 'BOUNDARYLAYER' called the subroutine containing governing equations and boundary conditions.

The governing equations for the boundary layer hydrodynamic model were programmed in subroutines INNERH#F#, where # varies from 1 to 27. The boundary conditions for the governing equations at the electrode surface were programmed in subroutines BC1H#F#, and far field boundary conditions are programmed in subroutines BC2H#F#.

The boundary value problem was numerically solved by subroutines BAND and MATINV, which were developed by Newman. The program was iterated until all relative values for H#(i,1),F#(i,1) were within a specified tolerance limit.

C.1 Program Listing

C.1.1 Main Program

```
PROGRAM BOUNDARYLAYER
IMPLICIT REAL*8 (A-H,O-Z)
IMPLICIT INTEGER (I-N)
INCLUDE 'COMMON.f'
DOUBLE PRECISION, ALLOCATABLE :: C(:,:), H1(:,:), F1(:,:)
DOUBLE PRECISION, ALLOCATABLE :: H3(:,:), F3(:,:)
DOUBLE PRECISION, ALLOCATABLE :: H5(:,:), F5(:,:)
DOUBLE PRECISION, ALLOCATABLE :: H7(:,:), F7(:,:)
DOUBLE PRECISION, ALLOCATABLE :: H9(:,:), F9(:,:)
DOUBLE PRECISION, ALLOCATABLE :: H11(:,:), F11(:,:)
DOUBLE PRECISION, ALLOCATABLE :: H13(:,:), F13(:,:)
DOUBLE PRECISION, ALLOCATABLE :: H15(:,:), F15(:,:)
```

```
DOUBLE PRECISION, ALLOCATABLE :: H17(:,:), F17(:,:)
DOUBLE PRECISION, ALLOCATABLE :: H19(:,:), F19(:,:)
DOUBLE PRECISION, ALLOCATABLE :: H21(:,:), F21(:,:)
DOUBLE PRECISION, ALLOCATABLE :: H23(:,:), F23(:,:)
DOUBLE PRECISION, ALLOCATABLE :: H25(:,:), F25(:,:)
DOUBLE PRECISION, ALLOCATABLE :: H27(:,:), F27(:,:)
DOUBLE PRECISION, ALLOCATABLE :: H29(:,:), F29(:,:)
DOUBLE PRECISION, ALLOCATABLE :: DH(:,:),DF(:,:)
DOUBLE PRECISION  maxvalG, Zeta
DOUBLE PRECISION  FP(15),FPP(15)
DOUBLE PRECISION H, H2
INTEGER NJL(20),NJLIST
CHARACTER NAMEFP*15,NAME1*25,NAME2*25,NAME3*25,FNUM*6
CHARACTER NAME4*25,NAME5*25,NAME6*25,NAME7*25,NAME8*25,NAME9*25
CHARACTER NAME10*25,NAME11*25,NAME12*25,NAME13*25,NAME14*25
CHARACTER NAME15*25
NAMELIST/par/ERRSUB,Zeta,NMAX,N
INCLUDE 'COT_TERM.f'
NJLIST=9
NJL(1)=20001
NJL(2)=40001
NJL(3)=80001
NJL(4)=100001
NJL(5)=160001
NJL(6)=200001
NJL(7)=250001
NJL(8)=400001
NJL(9)=500001
NJL(10)=1000001
open(9,FILE='INPUT.DAT',STATUS='UNKNOWN')
READ(9,par)
CLOSE(9)
OPEN(unit=16,file='FP.txt')
CLOSE(unit=16,status='delete')
OPEN(unit=16,file='FP.txt')
OPEN(unit=17,file='FPP.txt')
CLOSE(unit=17,status='delete')
OPEN(unit=17,file='FPP.txt')
DO ii=1,NJLIST
    NJ=NJL(ii)
    H=Zeta/(NJ-1)
    H2=H*H
    INCLUDE 'ALC.f'
    INCLUDE 'HF.f'
    INCLUDE 'CALFP_J1.f'
    INCLUDE 'DAC.f'
END DO
END
```

C.1.2 Main Subroutines

In this section, all the include files which are called in the main program as well as in various subroutimes are listed here.

```
!***************** SUBROUTINE SETUP ****************************
      SUBROUTINE SETUPHF(C,H1,F1,H3,F3,H5,F5,H7,F7,H9,F9,H11,F11
     *,H13,F13,H15,F15,H17,F17,H19,F19,H21,F21,H23,F23,H25,F25,H27,F27
     *,H29,F29)
      INCLUDE 'DEFINEVAR.f'
      DOUBLE PRECISION CONST
      CONST=0.0d0
      F1(1,1)=0.0d0
      H1(1,1)=0.0d0
      F3(1,1)=0.0d0
      H3(1,1)=0.0d0
      F1(1,NJ)=BC(1)
      H1(1,NJ)=0.0d0
      F3(1,NJ)=BC(2)
      H3(1,NJ)=0.0d0
      F5(1,1)=0.0d0
      H5(1,1)=0.0d0
      F5(1,NJ)=BC(3)
      H5(1,NJ)=0.0d0
      F7(1,1)=0.0d0
      H7(1,1)=0.0d0
      F7(1,NJ)=BC(4)
      H7(1,NJ)=0.0d0
      F9(1,1)=0.0d0
      H9(1,1)=0.0d0
      F9(1,NJ)=BC(5)
      H9(1,NJ)=0.0d0
      F11(1,1)=0.0d0
      H11(1,1)=0.0d0
      F11(1,NJ)=BC(6)
      H11(1,NJ)=0.0d0
      H13(1,1)=0.0d0
      F13(1,1)=0.0d0
      H13(1,NJ)=BC(7)
      F13(1,NJ)=0.0d0
      H15(1,1)=0.0d0
      F15(1,1)=0.0d0
      H15(1,NJ)=BC(8)
      F15(1,NJ)=0.0d0
      H17(1,1)=0.0d0
      F17(1,1)=0.0d0
      H17(1,NJ)=BC(9)
      F17(1,NJ)=0.0d0
      H19(1,1)=0.0d0
      F19(1,1)=0.0d0
      H19(1,NJ)=BC(10)
      F19(1,NJ)=0.0d0
      H21(1,1)=0.0d0
      F21(1,1)=0.0d0
      H21(1,NJ)=BC(11)
      F21(1,NJ)=0.0d0
      H23(1,1)=0.0d0
      F23(1,1)=0.0d0
      H23(1,NJ)=BC(12)
      F23(1,NJ)=0.0d0
```

```
      H25(1,1)=0.0d0
      F25(1,1)=0.0d0
      H25(1,NJ)=BC(13)
      F25(1,NJ)=0.0d0
      H27(1,1)=0.0d0
      F27(1,1)=0.0d0
      H27(1,NJ)=BC(14)
      F27(1,NJ)=0.0d0
      H29(1,1)=0.0d0
      F29(1,1)=0.0d0
      H29(1,NJ)=BC(15)
      F29(1,NJ)=0.0d0
      DO 20 II=2,NJ-1
          F1(1,II)=CONST
          H1(1,II)=CONST
          F3(1,II)=CONST
          H3(1,II)=CONST
          H5(1,II)=CONST
          F5(1,II)=CONST
          H7(1,II)=CONST
          F7(1,II)=CONST
          H9(1,II)=CONST
          F9(1,II)=CONST
          H11(1,II)=CONST
          F11(1,II)=CONST
          H13(1,II)=CONST
          F13(1,II)=CONST
          H15(1,II)=CONST
          F15(1,II)=CONST
          H17(1,II)=CONST
          F17(1,II)=CONST
          H19(1,II)=CONST
          F19(1,II)=CONST
          H21(1,II)=CONST
          F21(1,II)=CONST
          H23(1,II)=CONST
          F23(1,II)=CONST
          H25(1,II)=CONST
          F25(1,II)=CONST
          H27(1,II)=CONST
          F27(1,II)=CONST
          H29(1,II)=CONST
          F29(1,II)=CONST
20    CONTINUE
      RETURN
      END
!***************** SUBROUTINE BC1H1F1*****************************
      SUBROUTINE BC1H1F1(J,C,H1,F1)
      INCLUDE 'DEFINEVAR.f'
      DO i=1,N
          G(i)=0.0d0
          DO k=1,N
              A(i,k)=0.0d0
              B(i,k)=0.0d0
              D(i,k)=0.0d0
```

```
        END DO
    END DO
    G(1)=-H1(1,J)
    B(1,1)=1.0d0
    G(2)=-F1(1,J)
    B(2,2)=1.0d0
    RETURN
    END
!***************** SUBROUTINE BC1H3F3*****************************
    SUBROUTINE BC1H3F3(J,C,H3,F3)
    INCLUDE 'DEFINEVAR.f'
    DO i=1,N
        G(i)=0.0d0
        DO k=1,N
            A(i,k)=0.0d0
            B(i,k)=0.0d0
            D(i,k)=0.0d0
        END DO
    END DO
    G(1)=-H3(1,J)
    B(1,1)=1.0d0
    G(2)=-F3(1,J)
    B(2,2)=1.0d0
    RETURN
    END
!***************** SUBROUTINE BC1H5F5*****************************
    SUBROUTINE BC1H5F5(J,C,H5,F5)
    INCLUDE 'DEFINEVAR.f'
    DO i=1,N
        G(i)=0.0d0
        DO k=1,N
            A(i,k)=0.0d0
            B(i,k)=0.0d0
            D(i,k)=0.0d0
        END DO
    END DO
    G(1)=-H5(1,J)
    B(1,1)=1.0d0
    G(2)=-F5(1,J)
    B(2,2)=1.0d0
    RETURN
    END
!***************** SUBROUTINE BC1H7F7*****************************
    SUBROUTINE BC1H7F7(J,C,H7,F7)
    INCLUDE 'DEFINEVAR.f'
    DO i=1,N
        G(i)=0.0d0
        DO k=1,N
            A(i,k)=0.0d0
            B(i,k)=0.0d0
            D(i,k)=0.0d0
        END DO
    END DO
    G(1)=-H7(1,J)
    B(1,1)=1.0d0
```

```
    G(2)=-F7(1,J)
    B(2,2)=1.0d0
    RETURN
    END
!***************** SUBROUTINE BC1H5F5*****************************
    SUBROUTINE BC1H9F9(J,C,H9,F9)
    INCLUDE 'DEFINEVAR.f'
    DO i=1,N
        G(i)=0.0d0
        DO k=1,N
            A(i,k)=0.0d0
            B(i,k)=0.0d0
            D(i,k)=0.0d0
        END DO
    END DO
    G(1)=-H9(1,J)
    B(1,1)=1.0d0
    G(2)=-F9(1,J)
    B(2,2)=1.0d0
    RETURN
    END
!***************** SUBROUTINE BC1H11F11************************%
    SUBROUTINE BC1H11F11(J,C,H11,F11)
    INCLUDE 'DEFINEVAR.f'
    DO i=1,N
        G(i)=0.0d0
        DO k=1,N
            A(i,k)=0.0d0
            B(i,k)=0.0d0
            D(i,k)=0.0d0
        END DO
    END DO
    G(1)=-H11(1,J)
    B(1,1)=1.0d0
    G(2)=-F11(1,J)
    B(2,2)=1.0d0
    RETURN
    END
!***************** SUBROUTINE BC1H13F13 ************************
    SUBROUTINE BC1H13F13(J,C,H13,F13)
    INCLUDE 'DEFINEVAR.f'
    DO i=1,N
        G(i)=0.0d0
        DO k=1,N
            A(i,k)=0.0d0
            B(i,k)=0.0d0
            D(i,k)=0.0d0
        END DO
    END DO
    G(1)=-H13(1,J)
    B(1,1)=1.0d0
    G(2)=-F13(1,J)
    B(2,2)=1.0d0
    RETURN
    END
```

```
!***************** SUBROUTINE BC1H15F15 ************************
    SUBROUTINE BC1H15F15(J,C,H15,F15)
    INCLUDE 'DEFINEVAR.f'
    DO i=1,N
        G(i)=0.0d0
        DO k=1,N
            A(i,k)=0.0d0
            B(i,k)=0.0d0
            D(i,k)=0.0d0
        END DO
    END DO
    G(1)=-H15(1,J)
    B(1,1)=1.0d0
    G(2)=-F15(1,J)
    B(2,2)=1.0d0
    RETURN
    END
!***************** SUBROUTINE BC1H17F17 ************************
    SUBROUTINE BC1H17F17(J,C,H17,F17)
    INCLUDE 'DEFINEVAR.f'
    DO i=1,N
        G(i)=0.0d0
        DO k=1,N
            A(i,k)=0.0d0
            B(i,k)=0.0d0
            D(i,k)=0.0d0
        END DO
    END DO
    G(1)=-H17(1,J)
    B(1,1)=1.0d0
    G(2)=-F17(1,J)
    B(2,2)=1.0d0
    RETURN
    END
!***************** SUBROUTINE BC1H19F19 ************************
    SUBROUTINE BC1H19F19(J,C,H19,F19)
    INCLUDE 'DEFINEVAR.f'
    DO i=1,N
        G(i)=0.0d0
        DO k=1,N
            A(i,k)=0.0d0
            B(i,k)=0.0d0
            D(i,k)=0.0d0
        END DO
    END DO
    G(1)=-H19(1,J)
    B(1,1)=1.0d0
    G(2)=-F19(1,J)
    B(2,2)=1.0d0
    RETURN
    END
!***************** SUBROUTINE BC1H21F21 ************************
    SUBROUTINE BC1H21F21(J,C,H21,F21)
    INCLUDE 'DEFINEVAR.f'
    DO i=1,N
```

```
        G(i)=0.0d0
        DO k=1,N
            A(i,k)=0.0d0
            B(i,k)=0.0d0
            D(i,k)=0.0d0
        END DO
    END DO
    G(1)=-H21(1,J)
    B(1,1)=1.0d0
    G(2)=-F21(1,J)
    B(2,2)=1.0d0
    RETURN
    END
!***************** SUBROUTINE BC1H23F23*************************
    SUBROUTINE BC1H23F23(J,C,H23,F23)
    INCLUDE 'DEFINEVAR.f'
    DO i=1,N
        G(i)=0.0d0
        DO k=1,N
            A(i,k)=0.0d0
            B(i,k)=0.0d0
            D(i,k)=0.0d0
        END DO
    END DO
    G(1)=-H23(1,J)
    B(1,1)=1.0d0
    G(2)=-F23(1,J)
    B(2,2)=1.0d0
    RETURN
    END
!***************** SUBROUTINE BC1H25F25 ************************
    SUBROUTINE BC1H25F25(J,C,H25,F25)
    INCLUDE 'DEFINEVAR.f'
    DO i=1,N
        G(i)=0.0d0
        DO k=1,N
            A(i,k)=0.0d0
            B(i,k)=0.0d0
            D(i,k)=0.0d0
        END DO
    END DO
    G(1)=-H25(1,J)
    B(1,1)=1.0d0
    G(2)=-F25(1,J)
    B(2,2)=1.0d0
    RETURN
    END
!***************** SUBROUTINE BC1H27F27 ************************
    SUBROUTINE BC1H27F27(J,C,H27,F27)
    INCLUDE 'DEFINEVAR.f'
    DO i=1,N
        G(i)=0.0d0
        DO k=1,N
            A(i,k)=0.0d0
            B(i,k)=0.0d0
```

```
            D(i,k)=0.0d0
          END DO
        END DO
        G(1)=-H27(1,J)
        B(1,1)=1.0d0
        G(2)=-F27(1,J)
        B(2,2)=1.0d0
        RETURN
        END
!***************** SUBROUTINE INNERH1F1 ************************
        SUBROUTINE INNERH1F1(J,C,H1,F1)
        INCLUDE 'DEFINEVAR.f'
C       Continuity equation for H1 and F1 !
        G(1)=2.0d0*(H1(1,J)-H1(1,J-1))/H - (F1(1,J)+F1(1,J-1))/2.0d0
        A(1,1)=2.0d0/H
        B(1,1)=-2.0d0/H
        D(1,1)=0.0
        A(1,2)=1.0d0/2.0d0
        B(1,2)=1.0d0/2.0d0
        D(1,2)=0.0d0
C       Momentum equation for H1 and F1 !
        G(2)=(F1(1,J+1)-2.0d0*F1(1,J)+F1(1,J-1))/2.0d0/H2
       *+ FT(1)
       *+ H1(1,J)*(F1(1,J+1)-F1(1,J-1))/H/2.0d0
       *- F1(1,J)*F1(1,J)/4.0d0
        A(2,1)=0.0d0
        B(2,1)=-(F1(1,J+1)-F1(1,J-1))/H/2d0
        D(2,1)=0.0d0
        A(2,2)=-1.0d0/2.0d0/H2 + H1(1,J)/2.0d0/H
        B(2,2)= 1.0d0/H2 + F1(1,J)/2.0d0
        D(2,2)=-1.0d0/2.0d0/H2 - H1(1,J)/2.0d0/H
        RETURN
        END
!***************** SUBROUTINE INNERH3F3 ************************
        SUBROUTINE INNERH3F3(J,C,H1,F1,H3,F3)
        INCLUDE 'DEFINEVAR.f'
C       Continuity equation for H3 and F3
        G(1)=2.0d0*(H3(1,J)-H3(1,J-1))/H - (F3(1,J)+F3(1,J-1))
       *+ t2*(F1(1,J)+F1(1,J-1))/4.0d0
        A(1,1)=2.0d0/H
        B(1,1)=-2.0d0/H
        D(1,1)=0.0
        A(1,2)=1.0d0
        B(1,2)=1.0d0
        D(1,2)=0.0d0
C       Momentum equation for H3 and F3 !
        G(2)=(F3(1,J+1)-2.0d0*F3(1,J)+F3(1,J-1))/2.0d0/H2
       *+ FT(2)
       *+ H1(1,J)*(F3(1,J+1)-F3(1,J-1))/H/2.0d0
       *+ H3(1,J)*(F1(1,J+1)-F1(1,J-1))/H/2.0d0
       *- F1(1,J)*F3(1,J)
        A(2,1)=0.0d0
        B(2,1)=-(F1(1,J+1)-F1(1,J-1))/H/2.0d0
        D(2,1)=0.0d0
        A(2,2)=-1.0d0/2.0d0/H2 + H1(1,J)/2.0d0/H
```

```
      B(2,2)= 1.0d0/H2 + F1(1,J)
      D(2,2)=-1.0d0/2.0d0/H2 - H1(1,J)/2.0d0/H
      RETURN
      END
!***************** SUBROUTINE INNERH5F5 ************************
      SUBROUTINE INNERH5F5(J,C,H1,F1,H3,F3,H5,F5)
      INCLUDE 'DEFINEVAR.f'
C     Continuity equation for H5 and F5 !
      G(1)=2.0d0*(H5(1,J)-H5(1,J-1))/H - 1.5d0*(F5(1,J)+F5(1,J-1))
     *+ t3*(F1(1,J)+F1(1,J-1))/4.0d0
     *+ t2*(F3(1,J)+F3(1,J-1))/4.0d0
      A(1,1)=2.0d0/H
      B(1,1)=-2.0d0/H
      D(1,1)=0.0d0
      A(1,2)=1.5d0
      B(1,2)=1.5d0
      D(1,2)=0.0d0
C     Momentum equation for H5 and F5 !
      G(2)=(F5(1,J+1)-2.0d0*F5(1,J)+F5(1,J-1))/2.0d0/H2
     *+ FT(3)
     *+ H1(1,J)*(F5(1,J+1)-F5(1,J-1))/H/2.0d0
     *+ H3(1,J)*(F3(1,J+1)-F3(1,J-1))/H/2.0d0
     *+ H5(1,J)*(F1(1,J+1)-F1(1,J-1))/H/2.0d0
     *- (6.0d0*F1(1,J)*F5(1,J)+3.0d0*F3(1,J)*F3(1,J))/4.0d0
      A(2,1)=0.0d0
      B(2,1)=-(F1(1,J+1)-F1(1,J-1))/H/2.0d0
      D(2,1)=0.0d0
      A(2,2)=-1.0d0/2.0d0/H2 + H1(1,J)/2.0d0/H
      B(2,2)= 1.0d0/H2 + 6.0d0*F1(1,J)/4.0d0
      D(2,2)=-1.0d0/2.0d0/H2 - H1(1,J)/2.0d0/H
      RETURN
      END
!***************** SUBROUTINE INNERH7F7 ************************
      SUBROUTINE INNERH7F7(J,C,H1,F1,H3,F3,H5,F5,H7,F7)
      INCLUDE 'DEFINEVAR.f'
C     Continuity equation H7 and F7 !
      G(1)=2.0*(H7(1,J)-H7(1,J-1))/H - 2.0d0*(F7(1,J)+F7(1,J-1))
     *+ t4*(F1(1,J)+F1(1,J-1))/4.0d0
     *+ t3*(F3(1,J)+F3(1,J-1))/4.0d0
     *+ t2*(F5(1,J)+F5(1,J-1))/4.0d0
      A(1,1)=2.0d0/H
      B(1,1)=-2.0d0/H
      D(1,1)=0.0d0
      A(1,2)=2.0d0
      B(1,2)=2.0d0
      D(1,2)=0.0d0
C     Momentum equation F7, H7 !
      G(2)=(F7(1,J+1)-2.0d0*F7(1,J)+F7(1,J-1))/2.0d0/H2
     *+ FT(4)
     *+ H1(1,J)*(F7(1,J+1)-F7(1,J-1))/H/2.0d0
     *+ H3(1,J)*(F5(1,J+1)-F5(1,J-1))/H/2.0d0
     *+ H5(1,J)*(F3(1,J+1)-F3(1,J-1))/H/2.0d0
     *+ H7(1,J)*(F1(1,J+1)-F1(1,J-1))/H/2.0d0
     *- (8.0d0*F1(1,J)*F7(1,J)+8.0*F3(1,J)*F5(1,J))/4.0d0
      A(2,1)=0.0
```

```
      B(2,1)=-(F1(1,J+1)-F1(1,J-1))/H/2.0d0
      D(2,1)=0.0
      A(2,2)=-1.0/2.0/H2 + H1(1,J)/2.0/H
      B(2,2)= 1.0/H2 + 8.0d0*F1(1,J)/4.0d0
      D(2,2)=-1.0/2.0/H2 - H1(1,J)/2.0/H
      RETURN
      END
!***************** SUBROUTINE INNERH9F9 ************************
      SUBROUTINE INNERH9F9(J,C,H1,F1,H3,F3,H5,F5,H7,F7,H9,F9)
      INCLUDE 'DEFINEVAR.f'
C     Continuity equation for H9, F9 !
      G(1)=2.0*(H9(1,J)-H9(1,J-1))/H - 2.5d0*(F9(1,J)+F9(1,J-1))
     *+ t5*(F1(1,J)+F1(1,J-1))/4.0d0
     *+ t4*(F3(1,J)+F3(1,J-1))/4.0d0
     *+ t3*(F5(1,J)+F5(1,J-1))/4.0d0
     *+ t2*(F7(1,J)+F7(1,J-1))/4.0d0
      A(1,1)=2.0d0/H
      B(1,1)=-2.0d0/H
      D(1,1)=0.0d0
      A(1,2)=2.5d0
      B(1,2)=2.5d0
      D(1,2)=0.0d0
C     Momentum equation for H9, F9 !
      G(2)=(F9(1,J+1)-2.0d0*F9(1,J)+F9(1,J-1))/2.0d0/H2
     *+ FT(5)
     *+ H1(1,J)*(F9(1,J+1)-F9(1,J-1))/H/2.0d0
     *+ H3(1,J)*(F7(1,J+1)-F7(1,J-1))/H/2.0d0
     *+ H5(1,J)*(F5(1,J+1)-F5(1,J-1))/H/2.0d0
     *+ H7(1,J)*(F3(1,J+1)-F3(1,J-1))/H/2.0d0
     *+ H9(1,J)*(F1(1,J+1)-F1(1,J-1))/H/2.0d0
     *- (10.0d0*F1(1,J)*F9(1,J)+5.0d0*F5(1,J)*F5(1,J)
     *+  10.0*F3(1,J)*F7(1,J))/4.0d0
      A(2,1)=0.0
      B(2,1)=-(F1(1,J+1)-F1(1,J-1))/H/2.0d0
      D(2,1)=0.0
      A(2,2)=-1.0/2.0/H2 + H1(1,J)/2.0/H
      B(2,2)= 1.0/H2 + 10.0d0*F1(1,J)/4.0d0
      D(2,2)=-1.0/2.0/H2 - H1(1,J)/2.0/H
      RETURN
      END
!***************** SUBROUTINE INNERH11F11 **********************
      SUBROUTINE INNERH11F11(J,C,H1,F1,H3,F3,H5,F5,H7,F7,H9,F9,H11,F11)
C     Continuity equation for H11, F11 !
      G(1)=2.0*(H11(1,J)-H11(1,J-1))/H - 3.0d0*(F11(1,J)+F11(1,J-1))
     *+ t6*(F1(1,J)+F1(1,J-1))/4.0d0
     *+ t5*(F3(1,J)+F3(1,J-1))/4.0d0
     *+ t4*(F5(1,J)+F5(1,J-1))/4.0d0
     *+ t3*(F7(1,J)+F7(1,J-1))/4.0d0
     *+ t2*(F9(1,J)+F9(1,J-1))/4.0d0
      A(1,1)=2.0d0/H
      B(1,1)=-2.0d0/H
      D(1,1)=0.0d0
      A(1,2)=3.0d0
      B(1,2)=3.0d0
      D(1,2)=0.0d0
```

```
C   Momentum equation for H11, F11 !
    G(2)=(F11(1,J+1)-2.0d0*F11(1,J)+F11(1,J-1))/2.0d0/H2
   *+ FT(6)
   *+ H1(1,J)*(F11(1,J+1)-F11(1,J-1))/H/2.0d0
   *+ H3(1,J)*(F9(1,J+1)-F9(1,J-1))/H/2.0d0
   *+ H5(1,J)*(F7(1,J+1)-F7(1,J-1))/H/2.0d0
   *+ H7(1,J)*(F5(1,J+1)-F5(1,J-1))/H/2.0d0
   *+ H9(1,J)*(F3(1,J+1)-F3(1,J-1))/H/2.0d0
   *+ H11(1,J)*(F1(1,J+1)-F1(1,J-1))/H/2.0d0
   *- (12.0d0*F5(1,J)*F7(1,J)+12.0d0*F1(1,J)*F11(1,J)
   *+   12.0*F3(1,J)*F9(1,J))/4.0d0
    A(2,1)=0.0
    B(2,1)=-(F1(1,J+1)-F1(1,J-1))/H/2.0d0
    D(2,1)=0.0
    A(2,2)=-1.0/2.0/H2 + H1(1,J)/2.0/H
    B(2,2)= 1.0/H2 + 12.0d0*F1(1,J)/4.0d0
    D(2,2)=-1.0/2.0/H2 - H1(1,J)/2.0/H
    RETURN
    END
!***************** SUBROUTINE INNERH13F13 ***********************
    SUBROUTINE INNERH13F13(J,C,H1,F1,H3,F3,H5,F5,H7,F7,H9,F9,H11,F11
   *,H13,F13)
    INCLUDE 'DEFINEVAR.f'
C   Continuity equation for H13, F13 !
    G(1)=2.0*(H13(1,J)-H13(1,J-1))/H - 3.5d0*(F13(1,J)+F13(1,J-1))
   *+ t7*(F1(1,J)+F1(1,J-1))/4.0d0
   *+ t6*(F3(1,J)+F3(1,J-1))/4.0d0
   *+ t5*(F5(1,J)+F5(1,J-1))/4.0d0
   *+ t4*(F7(1,J)+F7(1,J-1))/4.0d0
   *+ t3*(F9(1,J)+F9(1,J-1))/4.0d0
   *+ t2*(F11(1,J)+F11(1,J-1))/4.0d0
    A(1,1)=2.0d0/H
    B(1,1)=-2.0d0/H
    D(1,1)=0.0d0
    A(1,2)=3.5d0
    B(1,2)=3.5d0
    D(1,2)=0.0d0
C   Momentum equation for H13, F13 !
    G(2)=(F13(1,J+1)-2.0d0*F13(1,J)+F13(1,J-1))/2.0d0/H2
   *+ FT(7)
   *+ H1(1,J)*(F13(1,J+1)-F13(1,J-1))/H/2.0d0
   *+ H3(1,J)*(F11(1,J+1)-F11(1,J-1))/H/2.0d0
   *+ H5(1,J)*(F9(1,J+1)-F9(1,J-1))/H/2.0d0
   *+ H7(1,J)*(F7(1,J+1)-F7(1,J-1))/H/2.0d0
   *+ H9(1,J)*(F5(1,J+1)-F5(1,J-1))/H/2.0d0
   *+ H11(1,J)*(F3(1,J+1)-F3(1,J-1))/H/2.0d0
   *+ H13(1,J)*(F1(1,J+1)-F1(1,J-1))/H/2.0d0
   *- (14.0d0*F3(1,J)*F11(1,J)+14.0d0*F5(1,J)*F9(1,J)
   *+  14.0d0*F1(1,J)*F13(1,J)+7.0d0*F7(1,J)*F7(1,J))/4.0d0
    A(2,1)=0.0
    B(2,1)=-(F1(1,J+1)-F1(1,J-1))/H/2.0d0
    D(2,1)=0.0
    A(2,2)=-1.0/2.0/H2 + H1(1,J)/2.0/H
    B(2,2)= 1.0/H2 + 14.0d0*F1(1,J)/4.0d0
    D(2,2)=-1.0/2.0/H2 - H1(1,J)/2.0/H
```

```
      RETURN
      END
!***************** SUBROUTINE INNERH15F15 **********************
      SUBROUTINE INNERH15F15(J,C,H1,F1,H3,F3,H5,F5,H7,F7,H9,F9,H11,F11
     *,H13,F13,H15,F15)
      INCLUDE 'DEFINEVAR.f'
      DO i=1,N
          G(i)=0.0d0
          DO k=1,N
              A(i,k)=0.0d0
              B(i,k)=0.0d0
              D(i,k)=0.0d0
          END DO
      END DO
C     Continuity equation for H15, F15 !
      G(1)=2.0*(H15(1,J)-H15(1,J-1))/H - 4.0d0*(F15(1,J)+F15(1,J-1))
     *+ t8*(F1(1,J)+F1(1,J-1))/4.0d0
     *+ t7*(F3(1,J)+F3(1,J-1))/4.0d0
     *+ t6*(F5(1,J)+F5(1,J-1))/4.0d0
     *+ t5*(F7(1,J)+F7(1,J-1))/4.0d0
     *+ t4*(F9(1,J)+F9(1,J-1))/4.0d0
     *+ t3*(F11(1,J)+F11(1,J-1))/4.0d0
     *+ t2*(F13(1,J)+F13(1,J-1))/4.0d0
      A(1,1)=2.0d0/H
      B(1,1)=-2.0d0/H
      D(1,1)=0.0d0
      A(1,2)=4.0d0
      B(1,2)=4.0d0
      D(1,2)=0.0d0
C     Momentum equation for H15, F15 !
      G(2)=(F15(1,J+1)-2.0d0*F15(1,J)+F15(1,J-1))/2.0d0/H2
     *+ FT(8)
     *+ H1(1,J)*(F15(1,J+1)-F15(1,J-1))/H/2.0d0
     *+ H3(1,J)*(F13(1,J+1)-F13(1,J-1))/H/2.0d0
     *+ H5(1,J)*(F11(1,J+1)-F11(1,J-1))/H/2.0d0
     *+ H7(1,J)*(F9(1,J+1)-F9(1,J-1))/H/2.0d0
     *+ H9(1,J)*(F7(1,J+1)-F7(1,J-1))/H/2.0d0
     *+ H11(1,J)*(F5(1,J+1)-F5(1,J-1))/H/2.0d0
     *+ H13(1,J)*(F3(1,J+1)-F3(1,J-1))/H/2.0d0
     *+ H15(1,J)*(F1(1,J+1)-F1(1,J-1))/H/2.0d0
     *- (16.0d0*F3(1,J)*F13(1,J)+16.0d0*F7(1,J)*F9(1,J)
     *+  16.0d0*F1(1,J)*F15(1,J)+16.0d0*F5(1,J)*F11(1,J))/4.0d0
      A(2,1)=0.0
      B(2,1)=-(F1(1,J+1)-F1(1,J-1))/H/2.0d0
      D(2,1)=0.0
      A(2,2)=-1.0/2.0/H2 + H1(1,J)/2.0/H
      B(2,2)= 1.0/H2 + 4.0d0*F1(1,J)
      D(2,2)=-1.0/2.0/H2 - H1(1,J)/2.0/H
      RETURN
      END
!***************** SUBROUTINE INNERH17F17 **********************
      SUBROUTINE INNERH17F17(J,C,H1,F1,H3,F3,H5,F5,H7,F7,H9,F9,H11,F11
     *,H13,F13,H15,F15,H17,F17)
      INCLUDE 'DEFINEVAR.f'
C     Continuity equation for H17, F17 !
```

```
      G(1)=2.0*(H17(1,J)-H17(1,J-1))/H - 4.5d0*(F17(1,J)+F17(1,J-1))
     *+ t9*(F1(1,J)+F1(1,J-1))/4.0d0
     *+ t8*(F3(1,J)+F3(1,J-1))/4.0d0
     *+ t7*(F5(1,J)+F5(1,J-1))/4.0d0
     *+ t6*(F7(1,J)+F7(1,J-1))/4.0d0
     *+ t5*(F9(1,J)+F9(1,J-1))/4.0d0
     *+ t4*(F11(1,J)+F11(1,J-1))/4.0d0
     *+ t3*(F13(1,J)+F13(1,J-1))/4.0d0
     *+ t2*(F15(1,J)+F15(1,J-1))/4.0d0
      A(1,1)=2.0d0/H
      B(1,1)=-2.0d0/H
      D(1,1)=0.0d0
      A(1,2)=4.5d0
      B(1,2)=4.5d0
      D(1,2)=0.0d0
C     Momentum equation for H17, F17 !
      G(2)=(F17(1,J+1)-2.0d0*F17(1,J)+F17(1,J-1))/2.0d0/H2
     *+ FT(9)
     *+ H1(1,J)*(F17(1,J+1)-F17(1,J-1))/H/2.0d0
     *+ H3(1,J)*(F15(1,J+1)-F15(1,J-1))/H/2.0d0
     *+ H5(1,J)*(F13(1,J+1)-F13(1,J-1))/H/2.0d0
     *+ H7(1,J)*(F11(1,J+1)-F11(1,J-1))/H/2.0d0
     *+ H9(1,J)*(F9(1,J+1)-F9(1,J-1))/H/2.0d0
     *+ H11(1,J)*(F7(1,J+1)-F7(1,J-1))/H/2.0d0
     *+ H13(1,J)*(F5(1,J+1)-F5(1,J-1))/H/2.0d0
     *+ H15(1,J)*(F3(1,J+1)-F3(1,J-1))/H/2.0d0
     *+ H17(1,J)*(F1(1,J+1)-F1(1,J-1))/H/2.0d0
     *- (18.0d0*F3(1,J)*F15(1,J)+9.0d0*F9(1,J)*F9(1,J)
     *+  18.0d0*F7(1,J)*F11(1,J)
     *+  18.0*F1(1,J)*F17(1,J)+18.0d0*F5(1,J)*F13(1,J))/4.0d0
      A(2,1)=0.0
      B(2,1)=-(F1(1,J+1)-F1(1,J-1))/H/2.0d0
      D(2,1)=0.0
      A(2,2)=-1.0/2.0/H2 + H1(1,J)/2.0/H
      B(2,2)= 1.0/H2 + 18.0d0*F1(1,J)/4.0d0
      D(2,2)=-1.0/2.0/H2 - H1(1,J)/2.0/H
      RETURN
      END
!***************** SUBROUTINE INNERH19F19 **********************
      SUBROUTINE INNERH19F19(J,C,H1,F1,H3,F3,H5,F5,H7,F7,H9,F9,H11,F11
     *,H13,F13,H15,F15,H17,F17,H19,F19)
      INCLUDE 'DEFINEVAR.f'
C     Continuity equation for H19, F19 !
      G(1)=2.0*(H19(1,J)-H19(1,J-1))/H - 5.0d0*(F19(1,J)+F19(1,J-1))
     *+t10*(F1(1,J)+F1(1,J-1))/4.0d0
     *+ t9*(F3(1,J)+F3(1,J-1))/4.0d0
     *+ t8*(F5(1,J)+F5(1,J-1))/4.0d0
     *+ t7*(F7(1,J)+F7(1,J-1))/4.0d0
     *+ t6*(F9(1,J)+F9(1,J-1))/4.0d0
     *+ t5*(F11(1,J)+F11(1,J-1))/4.0d0
     *+ t4*(F13(1,J)+F13(1,J-1))/4.0d0
     *+ t3*(F15(1,J)+F15(1,J-1))/4.0d0
     *+ t2*(F17(1,J)+F17(1,J-1))/4.0d0
      A(1,1)=2.0d0/H
      B(1,1)=-2.0d0/H
```

```
      D(1,1)=0.0d0
      A(1,2)=5.0d0
      B(1,2)=5.0d0
      D(1,2)=0.0d0
C     Momentum equation for H19, F19 !
      G(2)=(F19(1,J+1)-2.0d0*F19(1,J)+F19(1,J-1))/2.0d0/H2
     *+ FT(10)
     *+ H1(1,J)*(F19(1,J+1)-F19(1,J-1))/H/2.0d0
     *+ H3(1,J)*(F17(1,J+1)-F17(1,J-1))/H/2.0d0
     *+ H5(1,J)*(F15(1,J+1)-F15(1,J-1))/H/2.0d0
     *+ H7(1,J)*(F13(1,J+1)-F13(1,J-1))/H/2.0d0
     *+ H9(1,J)*(F11(1,J+1)-F11(1,J-1))/H/2.0d0
     *+ H11(1,J)*(F9(1,J+1)-F9(1,J-1))/H/2.0d0
     *+ H13(1,J)*(F7(1,J+1)-F7(1,J-1))/H/2.0d0
     *+ H15(1,J)*(F5(1,J+1)-F5(1,J-1))/H/2.0d0
     *+ H17(1,J)*(F3(1,J+1)-F3(1,J-1))/H/2.0d0
     *+ H19(1,J)*(F1(1,J+1)-F1(1,J-1))/H/2.0d0
     *- (20.0d0*F3(1,J)*F17(1,J)+20.0d0*F9(1,J)*F11(1,J)
     *+  20.0d0*F7(1,J)*F13(1,J)
     *+  20.0*F1(1,J)*F19(1,J)+20.0d0*F5(1,J)*F15(1,J))/4.0d0
      A(2,1)=0.0
      B(2,1)=-(F1(1,J+1)-F1(1,J-1))/H/2.0d0
      D(2,1)=0.0
      A(2,2)=-1.0/2.0/H2 + H1(1,J)/2.0/H
      B(2,2)= 1.0/H2 + 20.0d0*F1(1,J)/4.0d0
      D(2,2)=-1.0/2.0/H2 - H1(1,J)/2.0/H
      RETURN
      END
!***************** SUBROUTINE INNERH21F21 ***********************
      SUBROUTINE INNERH21F21(J,C,H1,F1,H3,F3,H5,F5,H7,F7,H9,F9,H11,F11
     *,H13,F13,H15,F15,H17,F17,H19,F19,H21,F21)
      INCLUDE 'DEFINEVAR.f'
C     Continuity equation for H21, F21 !
      G(1)=2.0d0*(H21(1,J)-H21(1,J-1))/H - 5.5d0*(F21(1,J)+F21(1,J-1))
     *+t11*(F1(1,J)+F1(1,J-1))/4.0d0
     *+t10*(F3(1,J)+F3(1,J-1))/4.0d0
     *+ t9*(F5(1,J)+F5(1,J-1))/4.0d0
     *+ t8*(F7(1,J)+F7(1,J-1))/4.0d0
     *+ t7*(F9(1,J)+F9(1,J-1))/4.0d0
     *+ t6*(F11(1,J)+F11(1,J-1))/4.0d0
     *+ t5*(F13(1,J)+F13(1,J-1))/4.0d0
     *+ t4*(F15(1,J)+F15(1,J-1))/4.0d0
     *+ t3*(F17(1,J)+F17(1,J-1))/4.0d0
     *+ t2*(F19(1,J)+F19(1,J-1))/4.0d0
      A(1,1)=2.0d0/H
      B(1,1)=-2.0d0/H
      D(1,1)=0.0d0
      A(1,2)=5.5d0
      B(1,2)=5.5d0
      D(1,2)=0.0d0
C     Momentum equation for H21, F21 !
      G(2)=(F21(1,J+1)-2.0d0*F21(1,J)+F21(1,J-1))/2.0d0/H2
     *+ FT(11)
     *+  H1(1,J)*(F21(1,J+1)-F21(1,J-1))/H/2.0d0
     *+  H3(1,J)*(F19(1,J+1)-F19(1,J-1))/H/2.0d0
```

```
     *+  H5(1,J)*(F17(1,J+1)-F17(1,J-1))/H/2.0d0
     *+  H7(1,J)*(F15(1,J+1)-F15(1,J-1))/H/2.0d0
     *+  H9(1,J)*(F13(1,J+1)-F13(1,J-1))/H/2.0d0
     *+ H11(1,J)*(F11(1,J+1)-F11(1,J-1))/H/2.0d0
     *+ H13(1,J)*(F9(1,J+1)-F9(1,J-1))/H/2.0d0
     *+ H15(1,J)*(F7(1,J+1)-F7(1,J-1))/H/2.0d0
     *+ H17(1,J)*(F5(1,J+1)-F5(1,J-1))/H/2.0d0
     *+ H19(1,J)*(F3(1,J+1)-F3(1,J-1))/H/2.0d0
     *+ H21(1,J)*(F1(1,J+1)-F1(1,J-1))/H/2.0d0
     *- (22.0d0*F1(1,J)*F21(1,J)+11.0d0*F11(1,J)*F11(1,J)
     *+  22.0d0*F7(1,J)*F15(1,J)+22.0d0*F5(1,J)*F17(1,J)
     *+  22.0d0*F3(1,J)*F19(1,J)+22.0d0*F9(1,J)*F13(1,J))/4.0d0
      A(2,1)=0.0
      B(2,1)=-(F1(1,J+1)-F1(1,J-1))/H/2.0d0
      D(2,1)=0.0
      A(2,2)=-1.0/2.0/H2 + H1(1,J)/2.0/H
      B(2,2)= 1.0/H2 + 22.0d0*F1(1,J)/4.0d0
      D(2,2)=-1.0/2.0/H2 - H1(1,J)/2.0/H
      RETURN
      END
!***************** SUBROUTINE INNERH23F23 **********************
      SUBROUTINE INNERH23F23(J,C,H1,F1,H3,F3,H5,F5,H7,F7,H9,F9,H11,F11
     *,H13,F13,H15,F15,H17,F17,H19,F19,H21,F21,H23,F23,H25,F25,H27,F27
     *,H29,F29)
      INCLUDE 'DEFINEVAR.f'
C     Continuity equation for H23, F23 !
      G(1)=2.0d0*(H23(1,J)-H23(1,J-1))/H - 6.0d0*(F23(1,J)+F23(1,J-1))
     *+t12*(F1(1,J)+F1(1,J-1))/4.0d0
     *+t11*(F3(1,J)+F3(1,J-1))/4.0d0
     *+t10*(F5(1,J)+F5(1,J-1))/4.0d0
     *+ t9*(F7(1,J)+F7(1,J-1))/4.0d0
     *+ t8*(F9(1,J)+F9(1,J-1))/4.0d0
     *+ t7*(F11(1,J)+F11(1,J-1))/4.0d0
     *+ t6*(F13(1,J)+F13(1,J-1))/4.0d0
     *+ t5*(F15(1,J)+F15(1,J-1))/4.0d0
     *+ t4*(F17(1,J)+F17(1,J-1))/4.0d0
     *+ t3*(F19(1,J)+F19(1,J-1))/4.0d0
     *+ t2*(F21(1,J)+F21(1,J-1))/4.0d0
      A(1,1)=2.0d0/H
      B(1,1)=-2.0d0/H
      D(1,1)=0.0d0
      A(1,2)=6.0d0
      B(1,2)=6.0d0
      D(1,2)=0.0d0
C     Momentum equation for H23, F23 !
      G(2)=(F23(1,J+1)-2.0d0*F23(1,J)+F23(1,J-1))/2.0d0/H2
     *+  FT(12)
     *+  H1(1,J)*(F23(1,J+1)-F23(1,J-1))/H/2.0d0
     *+  H3(1,J)*(F21(1,J+1)-F21(1,J-1))/H/2.0d0
     *+  H5(1,J)*(F19(1,J+1)-F19(1,J-1))/H/2.0d0
     *+  H7(1,J)*(F17(1,J+1)-F17(1,J-1))/H/2.0d0
     *+  H9(1,J)*(F15(1,J+1)-F15(1,J-1))/H/2.0d0
     *+ H11(1,J)*(F13(1,J+1)-F13(1,J-1))/H/2.0d0
     *+ H13(1,J)*(F11(1,J+1)-F11(1,J-1))/H/2.0d0
     *+ H15(1,J)*(F9(1,J+1)-F9(1,J-1))/H/2.0d0
```

```
     *+ H17(1,J)*(F7(1,J+1)-F7(1,J-1))/H/2.0d0
     *+ H19(1,J)*(F5(1,J+1)-F5(1,J-1))/H/2.0d0
     *+ H21(1,J)*(F3(1,J+1)-F3(1,J-1))/H/2.0d0
     *+ H23(1,J)*(F1(1,J+1)-F1(1,J-1))/H/2.0d0
     *- (24.0d0*F1(1,J)*F23(1,J)+24.0d0*F7(1,J)*F17(1,J)
     *+  24.0d0*F5(1,J)*F19(1,J)+24.0d0*F3(1,J)*F21(1,J)
     *+  24.0d0*F11(1,J)*F13(1,J)+24.0d0*F9(1,J)*F15(1,J))/4.0d0
      A(2,1)=0.0
      B(2,1)=-(F1(1,J+1)-F1(1,J-1))/H/2.0d0
      D(2,1)=0.0
      A(2,2)=-1.0/2.0/H2 + H1(1,J)/2.0/H
      B(2,2)= 1.0/H2 + 24.0d0*F1(1,J)/4.0d0
      D(2,2)=-1.0/2.0/H2 - H1(1,J)/2.0/H
      RETURN
      END
!***************** SUBROUTINE INNER ****************************
      SUBROUTINE INNERH25F25(J,C,H1,F1,H3,F3,H5,F5,H7,F7,H9,F9,H11,F11
     *,H13,F13,H15,F15,H17,F17,H19,F19,H21,F21,H23,F23,H25,F25)
C     Continuity equation for H25, F25 !
      G(1)=2.0*(H25(1,J)-H25(1,J-1))/H - 6.5d0*(F25(1,J)+F25(1,J-1))
     *+t13*(F1(1,J)+F1(1,J-1))/4.0d0
     *+t12*(F3(1,J)+F3(1,J-1))/4.0d0
     *+t11*(F5(1,J)+F5(1,J-1))/4.0d0
     *+t10*(F7(1,J)+F7(1,J-1))/4.0d0
     *+ t9*(F9(1,J)+F9(1,J-1))/4.0d0
     *+ t8*(F11(1,J)+F11(1,J-1))/4.0d0
     *+ t7*(F13(1,J)+F13(1,J-1))/4.0d0
     *+ t6*(F15(1,J)+F15(1,J-1))/4.0d0
     *+ t5*(F17(1,J)+F17(1,J-1))/4.0d0
     *+ t4*(F19(1,J)+F19(1,J-1))/4.0d0
     *+ t3*(F21(1,J)+F21(1,J-1))/4.0d0
     *+ t2*(F23(1,J)+F23(1,J-1))/4.0d0
      A(1,1)=2.0d0/H
      B(1,1)=-2.0d0/H
      D(1,1)=0.0d0
      A(1,2)=5.5d0
      B(1,2)=5.5d0
      D(1,2)=0.0d0
C     Momentum equation for H25, F25 !
      G(2)=(F25(1,J+1)-2.0d0*F25(1,J)+F25(1,J-1))/2.0d0/H2
     *+ FT(13)
     *+ H1(1,J)*(F25(1,J+1)-F25(1,J-1))/H/2.0d0
     *+ H3(1,J)*(F23(1,J+1)-F23(1,J-1))/H/2.0d0
     *+ H5(1,J)*(F21(1,J+1)-F21(1,J-1))/H/2.0d0
     *+ H7(1,J)*(F19(1,J+1)-F19(1,J-1))/H/2.0d0
     *+ H9(1,J)*(F17(1,J+1)-F17(1,J-1))/H/2.0d0
     *+ H11(1,J)*(F15(1,J+1)-F15(1,J-1))/H/2.0d0
     *+ H13(1,J)*(F13(1,J+1)-F13(1,J-1))/H/2.0d0
     *+ H15(1,J)*(F11(1,J+1)-F11(1,J-1))/H/2.0d0
     *+ H17(1,J)*(F9(1,J+1)-F9(1,J-1))/H/2.0d0
     *+ H19(1,J)*(F7(1,J+1)-F7(1,J-1))/H/2.0d0
     *+ H21(1,J)*(F5(1,J+1)-F5(1,J-1))/H/2.0d0
     *+ H23(1,J)*(F3(1,J+1)-F3(1,J-1))/H/2.0d0
     *+ H25(1,J)*(F1(1,J+1)-F1(1,J-1))/H/2.0d0
     *- (13.0d0*F13(1,J)*F13(1,J)+26.0d0*F11(1,J)*F15(1,J)
```

```
     *+  26.0d0*F7(1,J)*F19(1,J)+26.0d0*F5(1,J)*F21(1,J)
     *+  26.0d0*F3(1,J)*F23(1,J)+26.0d0*F1(1,J)*F25(1,J)
     *+  26.0d0*F9(1,J)*F17(1,J))/4.0d0
      A(2,1)=0.0
      B(2,1)=-(F1(1,J+1)-F1(1,J-1))/H/2.0d0
      D(2,1)=0.0
      A(2,2)=-1.0/2.0/H2 + H1(1,J)/2.0/H
      B(2,2)= 1.0/H2 + 26.0d0*F1(1,J)/4.0d0
      D(2,2)=-1.0/2.0/H2 - H1(1,J)/2.0/H
      RETURN
      END
!***************** SUBROUTINE INNERH27F27 **********************
      SUBROUTINE INNERH27F27(J,C,H1,F1,H3,F3,H5,F5,H7,F7,H9,F9,H11,F11
     *,H13,F13,H15,F15,H17,F17,H19,F19,H21,F21,H23,F23,H25,F25,H27,F27)
      INCLUDE 'DEFINEVAR.f'
C     Continuity equation for H27, F27 !
      G(1)=2.0*(H27(1,J)-H27(1,J-1))/H - 7.0d0*(F27(1,J)+F27(1,J-1))
     *+t14*(F1(1,J)+F1(1,J-1))/4.0d0
     *+t13*(F3(1,J)+F3(1,J-1))/4.0d0
     *+t12*(F5(1,J)+F5(1,J-1))/4.0d0
     *+t11*(F7(1,J)+F7(1,J-1))/4.0d0
     *+t10*(F9(1,J)+F9(1,J-1))/4.0d0
     *+ t9*(F11(1,J)+F11(1,J-1))/4.0d0
     *+ t8*(F13(1,J)+F13(1,J-1))/4.0d0
     *+ t7*(F15(1,J)+F15(1,J-1))/4.0d0
     *+ t6*(F17(1,J)+F17(1,J-1))/4.0d0
     *+ t5*(F19(1,J)+F19(1,J-1))/4.0d0
     *+ t4*(F21(1,J)+F21(1,J-1))/4.0d0
     *+ t3*(F23(1,J)+F23(1,J-1))/4.0d0
     *+ t2*(F25(1,J)+F25(1,J-1))/4.0d0
      A(1,1)=2.0d0/H
      B(1,1)=-2.0d0/H
      D(1,1)=0.0d0
      A(1,2)=7.0d0
      B(1,2)=7.0d0
      D(1,2)=0.0d0
C     Momentum equation for H27, F27 !
      G(2)=(F27(1,J+1)-2.0d0*F27(1,J)+F27(1,J-1))/2.0d0/H2
     *+ FT(14)
     *+ H1(1,J)*(F27(1,J+1)-F27(1,J-1))/H/2.0d0
     *+ H3(1,J)*(F25(1,J+1)-F25(1,J-1))/H/2.0d0
     *+ H5(1,J)*(F23(1,J+1)-F23(1,J-1))/H/2.0d0
     *+ H7(1,J)*(F21(1,J+1)-F21(1,J-1))/H/2.0d0
     *+ H9(1,J)*(F19(1,J+1)-F19(1,J-1))/H/2.0d0
     *+ H11(1,J)*(F17(1,J+1)-F17(1,J-1))/H/2.0d0
     *+ H13(1,J)*(F15(1,J+1)-F15(1,J-1))/H/2.0d0
     *+ H15(1,J)*(F13(1,J+1)-F13(1,J-1))/H/2.0d0
     *+ H17(1,J)*(F11(1,J+1)-F11(1,J-1))/H/2.0d0
     *+ H19(1,J)*(F9(1,J+1)-F9(1,J-1))/H/2.0d0
     *+ H21(1,J)*(F7(1,J+1)-F7(1,J-1))/H/2.0d0
     *+ H23(1,J)*(F5(1,J+1)-F5(1,J-1))/H/2.0d0
     *+ H25(1,J)*(F3(1,J+1)-F3(1,J-1))/H/2.0d0
     *+ H27(1,J)*(F1(1,J+1)-F1(1,J-1))/H/2.0d0
     *- (28.0d0*F5(1,J)*F23(1,J)+28.0d0*F3(1,J)*F25(1,J)
     *+  28.0d0*F7(1,J)*F21(1,J)+28.0d0*F1(1,J)*F27(1,J)
```

```
     *+  28.0d0*F13(1,J)*F15(1,J)+28.0d0*F11(1,J)*F17(1,J)
     *+  28.0*F9(1,J)*F19(1,J))/4.0d0
      A(2,1)=0.0
      B(2,1)=-(F1(1,J+1)-F1(1,J-1))/H/2.0d0
      D(2,1)=0.0
      A(2,2)=-1.0/2.0/H2 + H1(1,J)/2.0/H
      B(2,2)= 1.0/H2 + 28.0d0*F1(1,J)/4.0d0
      D(2,2)=-1.0/2.0/H2 - H1(1,J)/2.0/H
      RETURN
      END
!********************** SUBROUTINE BC2H1F1 **********************
      SUBROUTINE BC2H1F1(J,C,H1,F1)
      INCLUDE 'DEFINEVAR.f'
C     Boundary Condition on H1 !
      G(1)=2.0d0*(H1(1,J)-H1(1,J-1))/H - (F1(1,J)+F1(1,J-1))/2.0d0
      A(1,1)=2.0d0/H
      B(1,1)=-2.0d0/H
      D(1,1)=0.0
      A(1,2)=1.0d0/2.0d0
      B(1,2)=1.0d0/2.0d0
      D(1,2)=0.0d0
C     Boundary Condition on F1 !
      G(2)=BC(1)-F1(1,J)
      B(2,2)=1.0d0
      RETURN
      END
!********************** SUBROUTINE BC2H3F3 **********************
      SUBROUTINE BC2H3F3(J,C,H1,F1,H3,F3)
      INCLUDE 'DEFINEVAR.f'
C   Boundary Condition on H3 !
      G(1)=2.0d0*(H3(1,J)-H3(1,J-1))/H - (F3(1,J)+F3(1,J-1))
     *+ t2*(F1(1,J)+F1(1,J-1))/4.0d0
      A(1,1)=2.0d0/H
      B(1,1)=-2.0d0/H
      D(1,1)=0.0
      A(1,2)=1.0d0
      B(1,2)=1.0d0
      D(1,2)=0.0d0
C     Boundary Condition on F3 !
      G(2)=BC(2)-F3(1,J)
      B(2,2)=1.0d0
      RETURN
      END
!********************** SUBROUTINE BC2H5F5 **********************
      SUBROUTINE BC2H5F5(J,C,H1,F1,H3,F3,H5,F5)
      INCLUDE 'DEFINEVAR.f'
      G(1)=2.0d0*(H5(1,J)-H5(1,J-1))/H - 1.5d0*(F5(1,J)+F5(1,J-1))
     *+ t3*(F1(1,J)+F1(1,J-1))/4.0d0
     *+ t2*(F3(1,J)+F3(1,J-1))/4.0d0
      A(1,1)=2.0d0/H
      B(1,1)=-2.0d0/H
      D(1,1)=0.0d0
      A(1,2)=1.5d0
      B(1,2)=1.5d0
      D(1,2)=0.0d0
```

```
C   Boundary Condition on F5 !
    G(2)=BC(3)-F5(1,J)
    B(2,2)=1.0d0
    RETURN
    END
!********************** SUBROUTINE BC2H7F7 **********************
    SUBROUTINE BC2H7F7(J,C,H1,F1,H3,F3,H5,F5,H7,F7)
    INCLUDE 'DEFINEVAR.f'
C   Boundary Condition on H7 !
    G(1)=2.0*(H7(1,J)-H7(1,J-1))/H - 2.0d0*(F7(1,J)+F7(1,J-1))
   *+ t4*(F1(1,J)+F1(1,J-1))/4.0d0
   *+ t3*(F3(1,J)+F3(1,J-1))/4.0d0
   *+ t2*(F5(1,J)+F5(1,J-1))/4.0d0
    A(1,1)=2.0d0/H
    B(1,1)=-2.0d0/H
    D(1,1)=0.0d0
    A(1,2)=2.0d0
    B(1,2)=2.0d0
    D(1,2)=0.0d0
C   Boundary Condition on F7 !
    G(2)=BC(4)-F7(1,J)
    B(2,2)=1.0d0
    RETURN
    END
!********************** SUBROUTINE BC2H9F9 **********************
    SUBROUTINE BC2H9F9(J,C,H1,F1,H3,F3,H5,F5,H7,F7,H9,F9)
    INCLUDE 'DEFINEVAR.f'
C   Boundary Condition on H9 !
    G(1)=2.0*(H9(1,J)-H9(1,J-1))/H - 2.5d0*(F9(1,J)+F9(1,J-1))
   *+ t5*(F1(1,J)+F1(1,J-1))/4.0d0
   *+ t4*(F3(1,J)+F3(1,J-1))/4.0d0
   *+ t3*(F5(1,J)+F5(1,J-1))/4.0d0
   *+ t2*(F7(1,J)+F7(1,J-1))/4.0d0
    A(1,1)=2.0d0/H
    B(1,1)=-2.0d0/H
    D(1,1)=0.0d0
    A(1,2)=2.5d0
    B(1,2)=2.5d0
    D(1,2)=0.0d0
C   Boundary Condition on F9 !
    G(2)=BC(5)-F9(1,J)
    B(2,2)=1.0d0
    RETURN
    END
!********************** SUBROUTINE BC2H11F11 ********************
    SUBROUTINE BC2H11F11(J,C,H1,F1,H3,F3,H5,F5,H7,F7,H9,F9,H11,F11)
    INCLUDE 'DEFINEVAR.f'
C   Boundary Condition on H11 !
    G(1)=2.0*(H11(1,J)-H11(1,J-1))/H - 3.0d0*(F11(1,J)+F11(1,J-1))
   *+ t6*(F1(1,J)+F1(1,J-1))/4.0d0
   *+ t5*(F3(1,J)+F3(1,J-1))/4.0d0
   *+ t4*(F5(1,J)+F5(1,J-1))/4.0d0
   *+ t3*(F7(1,J)+F7(1,J-1))/4.0d0
   *+ t2*(F9(1,J)+F9(1,J-1))/4.0d0
    A(1,1)=2.0d0/H
```

```
      B(1,1)=-2.0d0/H
      D(1,1)=0.0d0
      A(1,2)=3.0d0
      B(1,2)=3.0d0
      D(1,2)=0.0d0
C     Boundary Condition on F11 !
      G(2)=BC(6)-F11(1,J)
      B(2,2)=1.0d0
      RETURN
      END
!********************** SUBROUTINE BCH13F13 **********************
      SUBROUTINE BC2H13F13(J,C,H1,F1,H3,F3,H5,F5,H7,F7,H9,F9,H11,F11
     *,H13,F13)
      INCLUDE 'DEFINEVAR.f'
C     Boundary Condition on H13 !
      G(1)=2.0*(H13(1,J)-H13(1,J-1))/H - 3.5d0*(F13(1,J)+F13(1,J-1))
     *+ t7*(F1(1,J)+F1(1,J-1))/4.0d0
     *+ t6*(F3(1,J)+F3(1,J-1))/4.0d0
     *+ t5*(F5(1,J)+F5(1,J-1))/4.0d0
     *+ t4*(F7(1,J)+F7(1,J-1))/4.0d0
     *+ t3*(F9(1,J)+F9(1,J-1))/4.0d0
     *+ t2*(F11(1,J)+F11(1,J-1))/4.0d0
      A(1,1)=2.0d0/H
      B(1,1)=-2.0d0/H
      D(1,1)=0.0d0
      A(1,2)=3.5d0
      B(1,2)=3.5d0
      D(1,2)=0.0d0
C     Boundary Condition on F13 !
      G(2)=BC(7)-F13(1,J)
      B(2,2)=1.0d0
      RETURN
      END
!********************** SUBROUTINE BC2H15F15 *******************
      SUBROUTINE BC2H15F15(J,C,H1,F1,H3,F3,H5,F5,H7,F7,H9,F9,H11,F11
     *,H13,F13,H15,F15)
      INCLUDE 'DEFINEVAR.f'
C     Boundary Condition on H15 !
      G(1)=2.0*(H15(1,J)-H15(1,J-1))/H - 4.0d0*(F15(1,J)+F15(1,J-1))
     *+ t8*(F1(1,J)+F1(1,J-1))/4.0d0
     *+ t7*(F3(1,J)+F3(1,J-1))/4.0d0
     *+ t6*(F5(1,J)+F5(1,J-1))/4.0d0
     *+ t5*(F7(1,J)+F7(1,J-1))/4.0d0
     *+ t4*(F9(1,J)+F9(1,J-1))/4.0d0
     *+ t3*(F11(1,J)+F11(1,J-1))/4.0d0
     *+ t2*(F13(1,J)+F13(1,J-1))/4.0d0
      A(1,1)=2.0d0/H
      B(1,1)=-2.0d0/H
      D(1,1)=0.0d0
      A(1,2)=4.0d0
      B(1,2)=4.0d0
      D(1,2)=0.0d0
C     Boundary Condition on F15 !
      G(2)=BC(8)-F15(1,J)
      B(2,2)=1.0d0
```

```
      RETURN
      END
!***************** SUBROUTINE BC2H17F17 ************************
      SUBROUTINE BC2H17F17(J,C,H1,F1,H3,F3,H5,F5,H7,F7,H9,F9,H11,F11
     *,H13,F13,H15,F15,H17,F17)
      INCLUDE 'DEFINEVAR.f'
      DO i=1,N
          G(i)=0.0d0
          DO k=1,N
              A(i,k)=0.0d0
              B(i,k)=0.0d0
              D(i,k)=0.0d0
          END DO
      END DO
C     Boundary Condition on H17 !
      G(1)=2.0*(H17(1,J)-H17(1,J-1))/H - 4.5d0*(F17(1,J)+F17(1,J-1))
     *+ t9*(F1(1,J)+F1(1,J-1))/4.0d0
     *+ t8*(F3(1,J)+F3(1,J-1))/4.0d0
     *+ t7*(F5(1,J)+F5(1,J-1))/4.0d0
     *+ t6*(F7(1,J)+F7(1,J-1))/4.0d0
     *+ t5*(F9(1,J)+F9(1,J-1))/4.0d0
     *+ t4*(F11(1,J)+F11(1,J-1))/4.0d0
     *+ t3*(F13(1,J)+F13(1,J-1))/4.0d0
     *+ t2*(F15(1,J)+F15(1,J-1))/4.0d0
      A(1,1)=2.0d0/H
      B(1,1)=-2.0d0/H
      D(1,1)=0.0d0
      A(1,2)=4.5d0
      B(1,2)=4.5d0
      D(1,2)=0.0d0
C     Boundary Condition on F17 !
      G(2)=BC(9)-F17(1,J)
      B(2,2)=1.0d0
      RETURN
      END
!********************** SUBROUTINE BC2H19F19 *********************
      SUBROUTINE BC2H19F19(J,C,H1,F1,H3,F3,H5,F5,H7,F7,H9,F9,H11,F11
     *,H13,F13,H15,F15,H17,F17,H19,F19)
      INCLUDE 'DEFINEVAR.f'
C     Boundary Condition on H19 !
      G(1)=2.0*(H19(1,J)-H19(1,J-1))/H - 5.0d0*(F19(1,J)+F19(1,J-1))
     *+t10*(F1(1,J)+F1(1,J-1))/4.0d0
     *+ t9*(F3(1,J)+F3(1,J-1))/4.0d0
     *+ t8*(F5(1,J)+F5(1,J-1))/4.0d0
     *+ t7*(F7(1,J)+F7(1,J-1))/4.0d0
     *+ t6*(F9(1,J)+F9(1,J-1))/4.0d0
     *+ t5*(F11(1,J)+F11(1,J-1))/4.0d0
     *+ t4*(F13(1,J)+F13(1,J-1))/4.0d0
     *+ t3*(F15(1,J)+F15(1,J-1))/4.0d0
     *+ t2*(F17(1,J)+F17(1,J-1))/4.0d0
      A(1,1)=2.0d0/H
      B(1,1)=-2.0d0/H
      D(1,1)=0.0d0
      A(1,2)=5.0d0
      B(1,2)=5.0d0
```

```
      D(1,2)=0.0d0
C     Boundary Condition on F19 !
      G(2)=BC(10)-F19(1,J)
      B(2,2)=1.0d0
      RETURN
      END
!********************** SUBROUTINE BC2H21F21 ********************
      SUBROUTINE BC2H21F21(J,C,H1,F1,H3,F3,H5,F5,H7,F7,H9,F9,H11,F11
     *,H13,F13,H15,F15,H17,F17,H19,F19,H21,F21)
C   Boundary Condition on H21 !
      G(1)=2.0d0*(H21(1,J)-H21(1,J-1))/H - 5.5d0*(F21(1,J)+F21(1,J-1))
     *+t11*(F1(1,J)+F1(1,J-1))/4.0d0
     *+t10*(F3(1,J)+F3(1,J-1))/4.0d0
     *+ t9*(F5(1,J)+F5(1,J-1))/4.0d0
     *+ t8*(F7(1,J)+F7(1,J-1))/4.0d0
     *+ t7*(F9(1,J)+F9(1,J-1))/4.0d0
     *+ t6*(F11(1,J)+F11(1,J-1))/4.0d0
     *+ t5*(F13(1,J)+F13(1,J-1))/4.0d0
     *+ t4*(F15(1,J)+F15(1,J-1))/4.0d0
     *+ t3*(F17(1,J)+F17(1,J-1))/4.0d0
     *+ t2*(F19(1,J)+F19(1,J-1))/4.0d0
      A(1,1)=2.0d0/H
      B(1,1)=-2.0d0/H
      D(1,1)=0.0d0
      A(1,2)=5.5d0
      B(1,2)=5.5d0
      D(1,2)=0.0d0
C     Boundary Condition on F21 !
      G(2)=BC(11)-F21(1,J)
      B(2,2)=1.0d0
      RETURN
      END
!********************** SUBROUTINE BC2H23F23 ********************
      SUBROUTINE BC2H23F23(J,C,H1,F1,H3,F3,H5,F5,H7,F7,H9,F9,H11,F11
     *,H13,F13,H15,F15,H17,F17,H19,F19,H21,F21,H23,F23)
      INCLUDE 'DEFINEVAR.f'
C     Boundary Condition on H23 !
      G(1)=2.0*(H23(1,J)-H23(1,J-1))/H - 6.0d0*(F23(1,J)+F23(1,J-1))
     *+t12*(F1(1,J)+F1(1,J-1))/4.0d0
     *+t11*(F3(1,J)+F3(1,J-1))/4.0d0
     *+t10*(F5(1,J)+F5(1,J-1))/4.0d0
     *+ t9*(F7(1,J)+F7(1,J-1))/4.0d0
     *+ t8*(F9(1,J)+F9(1,J-1))/4.0d0
     *+ t7*(F11(1,J)+F11(1,J-1))/4.0d0
     *+ t6*(F13(1,J)+F13(1,J-1))/4.0d0
     *+ t5*(F15(1,J)+F15(1,J-1))/4.0d0
     *+ t4*(F17(1,J)+F17(1,J-1))/4.0d0
     *+ t3*(F19(1,J)+F19(1,J-1))/4.0d0
     *+ t2*(F21(1,J)+F21(1,J-1))/4.0d0
      A(1,1)=2.0d0/H
      B(1,1)=-2.0d0/H
      D(1,1)=0.0d0
      A(1,2)=6.0d0
      B(1,2)=6.0d0
      D(1,2)=0.0d0
```

```
C    Boundary Condition on F23 !
     G(2)=BC(12)-F23(1,J)
     B(2,2)=1.0d0
     RETURN
     END
!********************** SUBROUTINE BC2H25F25 *********************
     SUBROUTINE BC2H25F25(J,C,H1,F1,H3,F3,H5,F5,H7,F7,H9,F9,H11,F11
    *,H13,F13,H15,F15,H17,F17,H19,F19,H21,F21,H23,F23,H25,F25)
C    Boundary Condition on H25 !
     G(1)=2.0*(H25(1,J)-H25(1,J-1))/H - 6.5d0*(F25(1,J)+F25(1,J-1))
    *+t13*(F1(1,J)+F1(1,J-1))/4.0d0
    *+t12*(F3(1,J)+F3(1,J-1))/4.0d0
    *+t11*(F5(1,J)+F5(1,J-1))/4.0d0
    *+t10*(F7(1,J)+F7(1,J-1))/4.0d0
    *+ t9*(F9(1,J)+F9(1,J-1))/4.0d0
    *+ t8*(F11(1,J)+F11(1,J-1))/4.0d0
    *+ t7*(F13(1,J)+F13(1,J-1))/4.0d0
    *+ t6*(F15(1,J)+F15(1,J-1))/4.0d0
    *+ t5*(F17(1,J)+F17(1,J-1))/4.0d0
    *+ t4*(F19(1,J)+F19(1,J-1))/4.0d0
    *+ t3*(F21(1,J)+F21(1,J-1))/4.0d0
    *+ t2*(F23(1,J)+F23(1,J-1))/4.0d0
     A(1,1)=2.0d0/H
     B(1,1)=-2.0d0/H
     D(1,1)=0.0d0
     A(1,2)=5.5d0
     B(1,2)=5.5d0
     D(1,2)=0.0d0
C    Boundary Condition on F25 !
     G(2)=BC(13)-F25(1,J)
     B(2,2)=1.0d0
     RETURN
     END
!********************** SUBROUTINE BC2H27F27 *********************
     SUBROUTINE BC2H27F27(J,C,H1,F1,H3,F3,H5,F5,H7,F7,H9,F9,H11,F11
    *,H13,F13,H15,F15,H17,F17,H19,F19,H21,F21
    *,H23,F23,H25,F25,H27,F27)
     INCLUDE 'DEFINEVAR.f'
C   Boundary Condition on H27 !
     G(1)=2.0*(H27(1,J)-H27(1,J-1))/H - 7.0d0*(F27(1,J)+F27(1,J-1))
    *+t14*(F1(1,J)+F1(1,J-1))/4.0d0
    *+t13*(F3(1,J)+F3(1,J-1))/4.0d0
    *+t12*(F5(1,J)+F5(1,J-1))/4.0d0
    *+t11*(F7(1,J)+F7(1,J-1))/4.0d0
    *+t10*(F9(1,J)+F9(1,J-1))/4.0d0
    *+ t9*(F11(1,J)+F11(1,J-1))/4.0d0
    *+ t8*(F13(1,J)+F13(1,J-1))/4.0d0
    *+ t7*(F15(1,J)+F15(1,J-1))/4.0d0
    *+ t6*(F17(1,J)+F17(1,J-1))/4.0d0
    *+ t5*(F19(1,J)+F19(1,J-1))/4.0d0
    *+ t4*(F21(1,J)+F21(1,J-1))/4.0d0
    *+ t3*(F23(1,J)+F23(1,J-1))/4.0d0
    *+ t2*(F25(1,J)+F25(1,J-1))/4.0d0
     A(1,1)=2.0d0/H
     B(1,1)=-2.0d0/H
```

```
      D(1,1)=0.0d0
      A(1,2)=7.0d0
      B(1,2)=7.0d0
      D(1,2)=0.0d0
C     Boundary Condition on F27 !
      G(2)=BC(14)-F27(1,J)
      B(2,2)=1.0d0
      RETURN
      END
!************ SUBROUTINE GETMAXG*********************
      SUBROUTINE GETMAXG_DHDF(N,NJ,NJP,DH,DF,maxval)
      INTEGER N,NJ,NJP,NN
      DOUBLE PRECISION DH(1,NJ),DF(1,NJ), maxval
      NJP=1
      maxval=0.0d0
      NN=N/2
      DO 20 j=1,NN
          DO 10 i=2,NJ-1
              IF (dabs(DH(j,i)).GT.maxval) THEN
                  maxval=dabs(DH(j,i))
                  NJP=i
              END IF
   10         CONTINUE
   20     CONTINUE
       DO 30 j=1,NN
          DO 40 i=2,NJ-1
              IF (dabs(DF(j,i)).GT.maxval) THEN
                  maxval=dabs(DF(j,i))
                  NJP=i
              END IF
   40         CONTINUE
   30     CONTINUE
       RETURN
       END
!************factrl.for*********************
        FUNCTION factrl(n)
        INTEGER n
        REAL*8 factrl
        INTEGER j,ntop
        DOUBLE PRECISION a(33)
        SAVE ntop,a
        a(1)=1.0d0
        DO 11 j=1,n
            a(j+1)=j*a(j)
11      CONTINUE
      factrl=a(n+1)
        return
        END
!***********************************************
```

C.1.3 Include Files

In this section, all the include files which are called in the main program as well as in various subroutimes are listed here.

```
!***************** Include File ALC.f ***********************
    ALLOCATE (C(2,NJ),H1(1,NJ),F1(1,NJ))
    ALLOCATE (H3(1,NJ),F3(1,NJ))
    ALLOCATE (H5(1,NJ),F5(1,NJ))
    ALLOCATE (H7(1,NJ),F7(1,NJ))
    ALLOCATE (H9(1,NJ),F9(1,NJ))
    ALLOCATE (H11(1,NJ),F11(1,NJ))
    ALLOCATE (H13(1,NJ),F13(1,NJ))
    ALLOCATE (H15(1,NJ),F15(1,NJ))
    ALLOCATE (H17(1,NJ),F17(1,NJ))
    ALLOCATE (H19(1,NJ),F19(1,NJ))
    ALLOCATE (H21(1,NJ),F21(1,NJ))
    ALLOCATE (H23(1,NJ),F23(1,NJ))
    ALLOCATE (H25(1,NJ),F25(1,NJ))
    ALLOCATE (H27(1,NJ),F27(1,NJ))
    ALLOCATE (DH(1,NJ),DF(1,NJ))
!***************** Include File COTTERM.f ***********************
C Defining Cot term
    t2=1.0d0/3.0d0
    t3=1.0d0/45.0d0
    t4=2.0d0/945.0d0
    t5=1.0d0/4725.0d0
    t6=2.0d0/93555.0d0
    t7=1382.0d0/638512875.0d0
    t8=4.0d0/18243225.0d0
    t9=3617.0d0/162820783125.0d0
    t10=87734.0d0/38979295480125.0d0
    t11=349222.0d0/1531329465290625.0d0
    t12=310732.0d0/13447856940643125.0d0
    t13=472728182.0d0/201919571963756521875.0d0
    t14=2631724.0d0/110944819760305781250.0d0
    t15=13571120588.0d0/5646536601700762736718750.0d0
C Defininging forcing term
    FT(1)=1.0d0
    FT(2)=-((4.0d0)**(3-1))/factrl(3)
    FT(3)=((4.0d0)**(5-1))/factrl(5)
    FT(4)=-((4.0d0)**(7-1))/factrl(7)
    FT(5)=((4.0d0)**(9-1))/factrl(9)
    FT(6)=-((4.0d0)**(11-1))/factrl(11)
    FT(7)=((4.0d0)**(13-1))/factrl(13)
    FT(8)=-((4.0d0)**(15-1))/factrl(15)
    FT(9)=((4.0d0)**(17-1))/factrl(17)
    FT(10)=-((4.0d0)**(19-1))/factrl(19)
    FT(11)=((4.0d0)**(21-1))/factrl(21)
    FT(12)=-((4.0d0)**(23-1))/factrl(23)
    FT(13)=((4.0d0)**(25-1))/factrl(25)
    FT(14)=-((4.0d0)**(27-1))/factrl(27)
    FT(15)=((4.0d0)**(29-1))/factrl(29)
! Defininging Boundary Condition on $F_{2i-1}(\infty)$
```

```
      BC(1)=2.0d0
      BC(2)=-((2.0d0)**3)/factrl(3)
      BC(3)=((2.0d0)**5)/factrl(5)
      BC(4)=-((2.0d0)**7)/factrl(7)
      BC(5)=((2.0d0)**9)/factrl(9)
      BC(6)=-((2.0d0)**11)/factrl(11)
      BC(7)=((2.0d0)**13)/factrl(13)
      BC(8)=-((2.0d0)**15)/factrl(15)
      BC(9)=((2.0d0)**17)/factrl(17)
      BC(10)=-((2.0d0)**19)/factrl(19)
      BC(11)=((2.0d0)**21)/factrl(21)
      BC(12)=-((2.0d0)**23)/factrl(23)
      BC(13)=((2.0d0)**25)/factrl(25)
      BC(14)=-((2.0d0)**27)/factrl(27)
      BC(15)=((2.0d0)**29)/factrl(29)
!********** INCLUDE FILE HF.f for main program ************
      NAME15(1:10)='VelHF_ALL_'
      CALL fnumber(NJ,FNUM)
      NAME15(11:16)=FNUM
      NAME15(17:20)='.txt'
      OPEN(unit=15,file=NAME15)
      CLOSE(unit=15,status='delete')
      OPEN(unit=15,file=NAME15)
C     Setup initial velocity profile for H and F !
      CALL SETUPHF(C,H1,F1,H3,F3,H5,F5,H7,F7,H9,F9,H11,F11
     *,H13,F13,H15,F15,H17,F17,H19,F19,H21,F21,H23,F23,H25,F25,H27,F27
     *,H29,F29)
C     INITILIZE ALL COEFFICIENT MATRIX !
      DO I=1,N
          DO K=1,N
              X(I,K)=0.0d0
              Y(I,K)=0.0d0
          END DO
      END DO
      JJ= 1
101   J=0
351   J=J+1
      SUMH=SUMH+H
      DO I=1,N
          G(I)=0.0d0
          DO K=1,N
              A(I,K)=0.0d0
              B(I,K)=0.0d0
              D(I,K)=0.0d0
          ENDDO
      ENDDO
C     Call BC1 for J=1 !
      IF(J.EQ.1) CALL BC1H1F1(J,C,H1,F1)
C     Equation for interior region !
      IF((J.GT.1).AND.(J.LT.NJ)) THEN
      CALL INNERH1F1(J,C,H1,F1)
      END IF
C     Equation for second boundary condition !
      IF (J.EQ.NJ)  THEN
      CALL BC2H1F1(J,C,H1,F1)
```

```
      END IF
      CALL BAND(J,C)
      IF(J.NE.NJ) GOTO 351
      DO I=1,NJ
          H1(1,I)=H1(1,I)+C(1,I)
          F1(1,I)=F1(1,I)+C(2,I)
      END DO
      DO i=1,NJ
          IF (dabs(H1(1,i)).GT.0.0d0) THEN
              DH(1,i)=dabs(C(1,i)/H1(1,i))
          ELSE
              DH(1,i)=1.0d0
          ENDIF
          IF (dabs(F1(1,i)).GT.0.0d0) THEN
              DF(1,i)=dabs(C(2,i)/F1(1,i))
          ELSE
              DF(1,i)=1.0d0
          ENDIF
      END DO
      CALL GETMAXG_DHDF(N,NJ,NJP,DH,DF,maxvalG)
      JJ=JJ+1
      IF ((maxvalG.GT.ERRSUB).AND.(JJ.LT.NMAX)) GO TO 101
!********** For H3 and F3 ************ !
      JJ= 1
102   J=0
352   J=J+1
      SUMH=SUMH+H
      DO I=1,N
          G(I)=0.0d0
          DO K=1,N
              A(I,K)=0.0d0
              B(I,K)=0.0d0
              D(I,K)=0.0d0
          ENDDO
      ENDDO
!     Call BC1 for J=1 !
      IF(J.EQ.1) CALL BC1H3F3(J,C,H1,F1,H3,F3)
!     Equation for interior region !
      IF((J.GT.1).AND.(J.LT.NJ)) THEN
      CALL INNERH3F3(J,C,H1,F1,H3,F3)
      END IF
!     Equation for second boundary condition !
      IF (J.EQ.NJ)  THEN
      CALL BC2H3F3(J,C,H1,F1,H3,F3)
      END IF
      CALL BAND(J,C)
      IF(J.NE.NJ) GOTO 352
      DO I=1,NJ
          H3(1,I)=H3(1,I)+C(1,I)
          F3(1,I)=F3(1,I)+C(2,I)
      END DO
      DO i=1,NJ
          IF (dabs(H3(1,i)).GT.0.0d0) THEN
              DH(1,i)=dabs(C(1,i)/H3(1,i))
          ELSE
```

```
            DH(1,i)=1.0d0
        ENDIF
        IF (dabs(F3(1,i)).GT.0.0d0) THEN
            DF(1,i)=dabs(C(2,i)/F3(1,i))
        ELSE
            DF(1,i)=1.0d0
        ENDIF
    END DO
    CALL GETMAXG_DHDF(N,NJ,NJP,DH,DF,maxvalG)
    JJ=JJ+1
    IF ((maxvalG.GT.ERRSUB).AND.(JJ.LT.NMAX)) GO TO 102
!********** For H5 and F5 ************
    JJ= 1
103 J=0
353 J=J+1
    SUMH=SUMH+H
    DO I=1,N
        G(I)=0.0d0
        DO K=1,N
            A(I,K)=0.0d0
            B(I,K)=0.0d0
            D(I,K)=0.0d0
        ENDDO
    ENDDO
!   Call BC1 for J=1 !
    IF(J.EQ.1) CALL BC1H5F5(J,C,H1,F1,H3,F3,H5,F5)
!   Equation for interior region !
    IF((J.GT.1).AND.(J.LT.NJ)) THEN
    CALL INNERH5F5(J,C,H1,F1,H3,F3,H5,F5)
    END IF
!   Equation for second boundary condition !
    IF (J.EQ.NJ)  THEN
    CALL BC2H5F5(J,C,H1,F1,H3,F3,H5,F5)
    END IF
    CALL BAND(J,C)
    IF(J.NE.NJ) GOTO 353
    DO I=1,NJ
        H5(1,I)=H5(1,I)+C(1,I)
        F5(1,I)=F5(1,I)+C(2,I)
    END DO
    DO i=1,NJ
        IF (dabs(H5(1,i)).GT.0.0d0) THEN
            DH(1,i)=dabs(C(1,i)/H5(1,i))
        ELSE
            DH(1,i)=1.0d0
        ENDIF
        IF (dabs(F5(1,i)).GT.0.0d0) THEN
            DF(1,i)=dabs(C(2,i)/F5(1,i))
        ELSE
            DF(1,i)=1.0d0
        ENDIF
    END DO
    CALL GETMAXG_DHDF(N,NJ,NJP,DH,DF,maxvalG)
    JJ=JJ+1
    IF ((maxvalG.GT.ERRSUB).AND.(JJ.LT.NMAX)) GO TO 103
```

```
!********** For H7 and F7 ************
    JJ= 1
104 J=0
354 J=J+1
    SUMH=SUMH+H
    DO I=1,N
        G(I)=0.0d0
        DO K=1,N
            A(I,K)=0.0d0
            B(I,K)=0.0d0
            D(I,K)=0.0d0
        ENDDO
    ENDDO
!   Call BC1 for J=1 !
    IF(J.EQ.1) CALL BC1H7F7(J,C,H1,F1,H3,F3,H5,F5,H7,F7)
!   Equation for interior region !
    IF((J.GT.1).AND.(J.LT.NJ)) THEN
    CALL INNERH7F7(J,C,H1,F1,H3,F3,H5,F5,H7,F7)
    END IF
!   Equation for second boundary condition !
    IF (J.EQ.NJ)  THEN
    CALL BC2H7F7(J,C,H1,F1,H3,F3,H5,F5,H7,F7)
    END IF
    CALL BAND(J,C) !
    IF(J.NE.NJ) GOTO 354
    DO I=1,NJ
        H7(1,I)=H7(1,I)+C(1,I)
        F7(1,I)=F7(1,I)+C(2,I)
    END DO
    DO i=1,NJ
        IF (dabs(H7(1,i)).GT.0.0d0) THEN
            DH(1,i)=dabs(C(1,i)/H7(1,i))
        ELSE
            DH(1,i)=1.0d0
        ENDIF
        IF (dabs(F7(1,i)).GT.0.0d0) THEN
            DF(1,i)=dabs(C(2,i)/F7(1,i))
        ELSE
            DF(1,i)=1.0d0
        ENDIF
    END DO
    CALL GETMAXG_DHDF(N,NJ,NJP,DH,DF,maxvalG)
    JJ=JJ+1
    IF ((maxvalG.GT.ERRSUB).AND.(JJ.LT.NMAX)) GO TO 104
!********** For H9 and F9 ************
    JJ= 1
105 J=0
355 J=J+1
    SUMH=SUMH+H
    DO I=1,N
        G(I)=0.0d0
        DO K=1,N
            A(I,K)=0.0d0
            B(I,K)=0.0d0
            D(I,K)=0.0d0
```

```
        ENDDO
      ENDDO
C     Call BC1 for J=1 !
      IF(J.EQ.1) CALL BC1H9F9(J,C,H1,F1,H3,F3,H5,F5,H7,F7,H9,F9)
C     Equation for interior region !
      IF((J.GT.1).AND.(J.LT.NJ)) THEN
      CALL INNERH9F9(J,C,H1,F1,H3,F3,H5,F5,H7,F7,H9,F9)
      END IF
C     Equation for second boundary condition !
      IF (J.EQ.NJ)  THEN
      CALL BC2H9F9(J,C,H1,F1,H3,F3,H5,F5,H7,F7,H9,F9)
      END IF
      CALL BAND(J,C)
      IF(J.NE.NJ) GOTO 355
      DO I=1,NJ
          H9(1,I)=H9(1,I)+C(1,I)
          F9(1,I)=F9(1,I)+C(2,I)
      END DO
      DO i=1,NJ
          IF (dabs(H9(1,i)).GT.0.0d0) THEN
              DH(1,i)=dabs(C(1,i)/H9(1,i))
          ELSE
              DH(1,i)=1.0d0
          ENDIF
          IF (dabs(F9(1,i)).GT.0.0d0) THEN
              DF(1,i)=dabs(C(2,i)/F9(1,i))
          ELSE
              DF(1,i)=1.0d0
          ENDIF
      END DO
      CALL GETMAXG_DHDF(N,NJ,NJP,DH,DF,maxvalG)
      JJ=JJ+1
      IF ((maxvalG.GT.ERRSUB).AND.(JJ.LT.NMAX)) GO TO 105
!********** For H11 and F11 ************
      JJ= 1
106   J=0
356   J=J+1
      SUMH=SUMH+H
      DO I=1,N
          G(I)=0.0d0
          DO K=1,N
              A(I,K)=0.0d0
              B(I,K)=0.0d0
              D(I,K)=0.0d0
          ENDDO
      ENDDO
C     Call BC1 for J=1 !
      IF(J.EQ.1) CALL BC1H11F11(J,C,H1,F1,H3,F3,H5,F5,H7,F7,H9,F9,H11
     *,F11)
C     Equation for interior region !
      IF((J.GT.1).AND.(J.LT.NJ)) THEN
      CALL INNERH11F11(J,C,H1,F1,H3,F3,H5,F5,H7,F7,H9,F9,H11,F11)
      END IF
C   Equation for second boundary condition !
      IF (J.EQ.NJ)  THEN
```

```
      CALL BC2H11F11(J,C,H1,F1,H3,F3,H5,F5,H7,F7,H9,F9,H11,F11)
      END IF
      CALL BAND(J,C)
      IF(J.NE.NJ) GOTO 356
      DO I=1,NJ
          H11(1,I)=H11(1,I)+C(1,I)
          F11(1,I)=F11(1,I)+C(2,I)
      END DO
      DO i=1,NJ
          IF (dabs(H11(1,i)).GT.0.0d0) THEN
              DH(1,i)=dabs(C(1,i)/H11(1,i))
          ELSE
              DH(1,i)=1.0d0
          ENDIF
          IF (dabs(F11(1,i)).GT.0.0d0) THEN
              DF(1,i)=dabs(C(2,i)/F11(1,i))
          ELSE
              DF(1,i)=1.0d0
          ENDIF
      END DO
      CALL GETMAXG_DHDF(N,NJ,NJP,DH,DF,maxvalG)
      JJ=JJ+1
      IF ((maxvalG.GT.ERRSUB).AND.(JJ.LT.NMAX)) GO TO 106
!********** For H13 and F13 ************
      JJ= 1
107   J=0
357   J=J+1
      SUMH=SUMH+H
      DO I=1,N
          G(I)=0.0d0
          DO K=1,N
              A(I,K)=0.0d0
              B(I,K)=0.0d0
              D(I,K)=0.0d0
          ENDDO
      ENDDO
!     Call BC1 for J=1 !
      IF(J.EQ.1) CALL BC1H13F13(J,C,H1,F1,H3,F3,H5,F5,H7,F7,H9,F9,H11
     *,F11,H13,F13)
!     Equation for interior region !
      IF((J.GT.1).AND.(J.LT.NJ)) THEN
      CALL INNERH13F13(J,C,H1,F1,H3,F3,H5,F5,H7,F7,H9,F9,H11,F11
     *,H13,F13)
      END IF
!     Equation for second boundary condition !
      IF (J.EQ.NJ)  THEN
      CALL BC2H13F13(J,C,H1,F1,H3,F3,H5,F5,H7,F7,H9,F9,H11,F11
       *,H13,F13,H15,F15,H17,F17,H19,F19,H21,F21
       *,H23,F23,H25,F25,H27,F27,H29,F29)
      END IF
      CALL BAND(J,C)
      IF(J.NE.NJ) GOTO 357
      DO I=1,NJ
          H13(1,I)=H13(1,I)+C(1,I)
          F13(1,I)=F13(1,I)+C(2,I)
```

```
      END DO
      DO i=1,NJ
          IF (dabs(H13(1,i)).GT.0.0d0) THEN
              DH(1,i)=dabs(C(1,i)/H13(1,i))
          ELSE
              DH(1,i)=1.0d0
          ENDIF
          IF (dabs(F13(1,i)).GT.0.0d0) THEN
              DF(1,i)=dabs(C(2,i)/F13(1,i))
          ELSE
              DF(1,i)=1.0d0
          ENDIF
      END DO
      CALL GETMAXG_DHDF(N,NJ,NJP,DH,DF,maxvalG)
      JJ=JJ+1
      IF ((maxvalG.GT.ERRSUB).AND.(JJ.LT.NMAX)) GO TO 107
!********** Solving for H15 and F15 ************
      JJ= 1
108   J=0
358   J=J+1
      SUMH=SUMH+H
      DO I=1,N
          G(I)=0.0d0
          DO K=1,N
              A(I,K)=0.0d0
              B(I,K)=0.0d0
              D(I,K)=0.0d0
          ENDDO
      ENDDO
!     Call BC1 for J=1 !
      IF(J.EQ.1) CALL BC1H15F15(J,C,H15,F15)
!     Equation for interior region !
      IF((J.GT.1).AND.(J.LT.NJ)) THEN
      CALL INNERH15F15(J,C,H1,F1,H3,F3,H5,F5,H7,F7,H9,F9,H11,F11
     *,H13,F13,H15,F15)
      END IF
!     Equation for second boundary condition !
      IF (J.EQ.NJ)  THEN
      CALL BC2H15F15(J,C,H1,F1,H3,F3,H5,F5,H7,F7,H9,F9,H11,F11
     *,H13,F13,H15,F15)
      END IF
      CALL BAND(J,C)
      IF(J.NE.NJ) GOTO 358
      DO I=1,NJ
          H15(1,I)=H15(1,I)+C(1,I)
          F15(1,I)=F15(1,I)+C(2,I)
      END DO
      DO i=1,NJ
          IF (dabs(H15(1,i)).GT.0.0d0) THEN
              DH(1,i)=dabs(C(1,i)/H15(1,i))
          ELSE
              DH(1,i)=1.0d0
          ENDIF
          IF (dabs(F15(1,i)).GT.0.0d0) THEN
              DF(1,i)=dabs(C(2,i)/F15(1,i))
```

```
        ELSE
            DF(1,i)=1.0d0
        ENDIF
    END DO
    CALL GETMAXG_DHDF(N,NJ,NJP,DH,DF,maxvalG)
    JJ=JJ+1
    IF ((maxvalG.GT.ERRSUB).AND.(JJ.LT.NMAX)) GO TO 108
!********** For H17 and F17 ************
    JJ= 1
109 J=0
359 J=J+1
    SUMH=SUMH+H
    DO I=1,N
        G(I)=0.0d0
        DO K=1,N
            A(I,K)=0.0d0
            B(I,K)=0.0d0
            D(I,K)=0.0d0
        ENDDO
    ENDDO
C   Call BC1 for J=1 !
    IF(J.EQ.1) CALL BC1H17F17(J,C,H1,F1,H3,F3,H5,F5,H7,F7,H9,F9,H11
   *,F11,H13,F13,H15,F15,H17,F17)
C   Equation for interior region !
    IF((J.GT.1).AND.(J.LT.NJ)) THEN
    CALL INNERH17F17(J,C,H1,F1,H3,F3,H5,F5,H7,F7,H9,F9,H11,F11
   *,H13,F13,H15,F15,H17,F17)
    END IF
C   Equation for second boundary condition !
    IF (J.EQ.NJ)  THEN
    CALL BC2H17F17(J,C,H1,F1,H3,F3,H5,F5,H7,F7,H9,F9,H11,F11
   *,H13,F13,H15,F15,H17,F17)
    END IF
    CALL BAND(J,C)
    IF(J.NE.NJ) GOTO 359
    DO I=1,NJ
        H17(1,I)=H17(1,I)+C(1,I)
        F17(1,I)=F17(1,I)+C(2,I)
    END DO
    DO i=1,NJ
        IF (dabs(H17(1,i)).GT.0.0d0) THEN
            DH(1,i)=dabs(C(1,i)/H17(1,i))
        ELSE
            DH(1,i)=1.0d0
        ENDIF
        IF (dabs(F17(1,i)).GT.0.0d0) THEN
            DF(1,i)=dabs(C(2,i)/F17(1,i))
        ELSE
            DF(1,i)=1.0d0
        ENDIF
    END DO
    CALL GETMAXG_DHDF(N,NJ,NJP,DH,DF,maxvalG)
    JJ=JJ+1
    IF ((maxvalG.GT.ERRSUB).AND.(JJ.LT.NMAX)) GO TO 109
!********** For H19 and F19 ************
```

```
    JJ= 1
110 J=0
360 J=J+1
    SUMH=SUMH+H
    DO I=1,N
        G(I)=0.0d0
        DO K=1,N
            A(I,K)=0.0d0
            B(I,K)=0.0d0
            D(I,K)=0.0d0
        ENDDO
    ENDDO
C   Call BC1 for J=1 !
    IF(J.EQ.1) CALL BC1H19F19(J,C,H19,F19)
C   Equation for interior region
    IF((J.GT.1).AND.(J.LT.NJ)) THEN
    CALL INNERH19F19(J,C,H1,F1,H3,F3,H5,F5,H7,F7,H9,F9,H11,F11
   *,H13,F13,H15,F15,H17,F17,H19,F19)
    END IF
C   Equation for second boundary condition
    IF (J.EQ.NJ)  THEN
    CALL BC2H19F19(J,C,H1,F1,H3,F3,H5,F5,H7,F7,H9,F9,H11,F11
   *,H13,F13,H15,F15,H17,F17,H19,F19)
    END IF
    CALL BAND(J,C)
    IF(J.NE.NJ) GOTO 360
    DO I=1,NJ
        H19(1,I)=H19(1,I)+C(1,I)
        F19(1,I)=F19(1,I)+C(2,I)
    END DO
    DO i=1,NJ
        IF (dabs(H19(1,i)).GT.0.0d0) THEN
            DH(1,i)=dabs(C(1,i)/H19(1,i))
        ELSE
            DH(1,i)=1.0d0
        ENDIF
        IF (dabs(F19(1,i)).GT.0.0d0) THEN
            DF(1,i)=dabs(C(2,i)/F19(1,i))
        ELSE
            DF(1,i)=1.0d0
        ENDIF
    END DO
    CALL GETMAXG_DHDF(N,NJ,NJP,DH,DF,maxvalG)
    JJ=JJ+1
    IF ((maxvalG.GT.ERRSUB).AND.(JJ.LT.NMAX)) GO TO 110
!********** For H21 and F21 ************
    JJ= 1
111 J=0
361 J=J+1
    SUMH=SUMH+H
    DO I=1,N
        G(I)=0.0d0
        DO K=1,N
            A(I,K)=0.0d0
            B(I,K)=0.0d0
```

```
            D(I,K)=0.0d0
          ENDDO
        ENDDO
C  Call BC1 for J=1 !
        IF(J.EQ.1) CALL BC1H21F21(J,C,H1,F1,H3,F3,H5,F5,H7,F7,H9,F9,H11
       *,F11,H13,F13,H15,F15,H17,F17,H19,F19,H21,F21)
C    Equation for interior region !
        IF((J.GT.1).AND.(J.LT.NJ)) THEN
        CALL INNERH21F21(J,C,H1,F1,H3,F3,H5,F5,H7,F7,H9,F9,H11,F11
       *,H13,F13,H15,F15,H17,F17,H19,F19,H21,F21)
        END IF
C    Equation for second boundary condition !
        IF (J.EQ.NJ)  THEN
        CALL BC2H21F21(J,C,H1,F1,H3,F3,H5,F5,H7,F7,H9,F9,H11,F11
       *,H13,F13,H15,F15,H17,F17,H19,F19,H21,F21)
        END IF
        CALL BAND(J,C)
        IF(J.NE.NJ) GOTO 361
        DO I=1,NJ
            H21(1,I)=H21(1,I)+C(1,I)
            F21(1,I)=F21(1,I)+C(2,I)
        END DO
        DO i=1,NJ
            IF (dabs(H21(1,i)).GT.0.0d0) THEN
                DH(1,i)=dabs(C(1,i)/H21(1,i))
            ELSE
                DH(1,i)=1.0d0
            ENDIF
            IF (dabs(F21(1,i)).GT.0.0d0) THEN
                DF(1,i)=dabs(C(2,i)/F21(1,i))
            ELSE
                DF(1,i)=1.0d0
            ENDIF
        END DO
        CALL GETMAXG_DHDF(N,NJ,NJP,DH,DF,maxvalG)
        JJ=JJ+1
        IF ((maxvalG.GT.ERRSUB).AND.(JJ.LT.NMAX)) GO TO 111
!********** For H23 and F23 ************
        JJ= 1
112     J=0
362     J=J+1
        SUMH=SUMH+H
        DO I=1,N
            G(I)=0.0d0
            DO K=1,N
                A(I,K)=0.0d0
                B(I,K)=0.0d0
                D(I,K)=0.0d0
            ENDDO
        ENDDO
C    Call BC1 for J=1 !
        IF(J.EQ.1) CALL BC1H23F23(J,C,H1,F1,H3,F3,H5,F5,H7,F7,H9,F9,H11
       *,F11,H13,F13,H15,F15,H17,F17,H19,F19,H21,F21,H23,F23)
C    Equation for interior region !
        IF((J.GT.1).AND.(J.LT.NJ)) THEN
```

```
      CALL INNERH23F23(J,C,H1,F1,H3,F3,H5,F5,H7,F7,H9,F9,H11,F11
     *,H13,F13,H15,F15,H17,F17,H19,F19,H21,F21,H23,F23)
      END IF
C     Equation for second boundary condition !
      IF (J.EQ.NJ)  THEN
      CALL BC2H23F23(J,C,H1,F1,H3,F3,H5,F5,H7,F7,H9,F9,H11,F11
     *,H13,F13,H15,F15,H17,F17,H19,F19,H21,F21,H23,F23)
      END IF
      CALL BAND(J,C)
      IF(J.NE.NJ) GOTO 362
      DO I=1,NJ
          H23(1,I)=H23(1,I)+C(1,I)
          F23(1,I)=F23(1,I)+C(2,I)
      END DO
      DO i=1,NJ
          IF (dabs(H23(1,i)).GT.0.0d0) THEN
              DH(1,i)=dabs(C(1,i)/H23(1,i))
          ELSE
              DH(1,i)=1.0d0
          ENDIF
          IF (dabs(F23(1,i)).GT.0.0d0) THEN
              DF(1,i)=dabs(C(2,i)/F23(1,i))
          ELSE
              DF(1,i)=1.0d0
          ENDIF
      END DO
      CALL GETMAXG_DHDF(N,NJ,NJP,DH,DF,maxvalG)
      JJ=JJ+1
      IF ((maxvalG.GT.ERRSUB).AND.(JJ.LT.NMAX)) GO TO 112
!********** For H25 and F25 ************
      JJ= 1
113   J=0
363   J=J+1
      SUMH=SUMH+H
      DO I=1,N
          G(I)=0.0d0
          DO K=1,N
              A(I,K)=0.0d0
              B(I,K)=0.0d0
              D(I,K)=0.0d0
          ENDDO
      ENDDO
!     Call BC1 for J=1 !
      IF(J.EQ.1) CALL BC1H25F25(J,C,H25,F25)
! Equation for interior region !
      IF((J.GT.1).AND.(J.LT.NJ)) THEN
      CALL INNERH25F25(J,C,H1,F1,H3,F3,H5,F5,H7,F7,H9,F9,H11,F11
     *,H13,F13,H15,F15,H17,F17,H19,F19,H21,F21,H23,F23,H25,F25)
      END IF
!     Equation for second boundary condition !
      IF (J.EQ.NJ)  THEN
      CALL BC2H25F25(J,C,H1,F1,H3,F3,H5,F5,H7,F7,H9,F9,H11,F11
     *,H13,F13,H15,F15,H17,F17,H19,F19,H21,F21
     *,H23,F23,H25,F25)
      END IF
```

```
      CALL BAND(J,C)
      IF(J.NE.NJ) GOTO 363
      DO I=1,NJ
          H25(1,I)=H25(1,I)+C(1,I)
          F25(1,I)=F25(1,I)+C(2,I)
      END DO
      DO i=1,NJ
          IF (dabs(H25(1,i)).GT.0.0d0) THEN
              DH(1,i)=dabs(C(1,i)/H25(1,i))
          ELSE
              DH(1,i)=1.0d0
          ENDIF
          IF (dabs(F25(1,i)).GT.0.0d0) THEN
              DF(1,i)=dabs(C(2,i)/F25(1,i))
          ELSE
              DF(1,i)=1.0d0
          ENDIF
      END DO
      CALL GETMAXG_DHDF(N,NJ,NJP,DH,DF,maxvalG)
      JJ=JJ+1
      IF ((maxvalG.GT.ERRSUB).AND.(JJ.LT.NMAX)) GO TO 113
!********** For H27 and F27 ************
      JJ= 1
114   J=0
364   J=J+1
      SUMH=SUMH+H
      DO I=1,N
          G(I)=0.0d0
          DO K=1,N
              A(I,K)=0.0d0
              B(I,K)=0.0d0
              D(I,K)=0.0d0
          ENDDO
      ENDDO
!     Call BC1 for J=1 !
      IF(J.EQ.1) CALL BC1H27F27(J,C,H27,F27)
!     Equation for interior region !
      IF((J.GT.1).AND.(J.LT.NJ)) THEN
      CALL INNERH27F27(J,C,H1,F1,H3,F3,H5,F5,H7,F7,H9,F9,H11,F11
     *,H13,F13,H15,F15,H17,F17,H19,F19,H21,F21,H23,F23,H25,F25,H27,F27)
      END IF
!     Equation for second boundary condition !
      IF (J.EQ.NJ)  THEN
      CALL BC2H27F27(J,C,H1,F1,H3,F3,H5,F5,H7,F7,H9,F9,H11,F11
     *,H13,F13,H15,F15,H17,F17,H19,F19,H21,F21
     *,H23,F23,H25,F25,H27,F27)
      END IF
      CALL BAND(J,C)
      IF(J.NE.NJ) GOTO 364
      DO I=1,NJ
          H27(1,I)=H27(1,I)+C(1,I)
          F27(1,I)=F27(1,I)+C(2,I)
      END DO
      DO i=1,NJ
          IF (dabs(H27(1,i)).GT.0.0d0) THEN
```

```
            DH(1,i)=dabs(C(1,i)/H27(1,i))
          ELSE
            DH(1,i)=1.0d0
          ENDIF
          IF (dabs(F27(1,i)).GT.0.0d0) THEN
            DF(1,i)=dabs(C(2,i)/F27(1,i))
          ELSE
            DF(1,i)=1.0d0
          ENDIF
        END DO
        CALL GETMAXG_DHDF(N,NJ,NJP,DH,DF,maxvalG)
        JJ=JJ+1
        IF ((maxvalG.GT.ERRSUB).AND.(JJ.LT.NMAX)) GO TO 114
!******************  Include file COMMON.f ****************
        COMMON/BA/A(2,2),B(2,2),D(2,5),G(2),X(2,2),Y(2,2),N,NJ
        COMMON/BB/H,H2
        COMMON/COTTERM/t2,t3,t4,t5,t6,t7,t8,t9,t10,t11,t12,t13,t14,t15
        COMMON/FANDBCTERM/FT(15),BC(15)
!******************* Include File Cotterm.f ***************
        FP(1)=(-F1(1,3)+4.0d0*F1(1,2))/2.0d0/H
        FP(2)=(-F3(1,3)+4.0d0*F3(1,2))/2.0d0/H
        FP(3)=(-F5(1,3)+4.0d0*F5(1,2))/2.0d0/H
        FP(4)=(-F7(1,3)+4.0d0*F7(1,2))/2.0d0/H
        FP(5)=(-F9(1,3)+4.0d0*F9(1,2))/2.0d0/H
        FP(6)=(-F11(1,3)+4.0d0*F11(1,2))/2.0d0/H
        FP(7)=(-F13(1,3)+4.0d0*F13(1,2))/2.0d0/H
        FP(8)=(-F15(1,3)+4.0d0*F15(1,2))/2.0d0/H
        FP(9)=(-F17(1,3)+4.0d0*F17(1,2))/2.0d0/H
        FP(10)=(-F19(1,3)+4.0d0*F19(1,2))/2.0d0/H
        FP(11)=(-F21(1,3)+4.0d0*F21(1,2))/2.0d0/H
        FP(12)=(-F23(1,3)+4.0d0*F23(1,2))/2.0d0/H
        FP(13)=(-F25(1,3)+4.0d0*F25(1,2))/2.0d0/H
        FP(14)=(-F27(1,3)+4.0d0*F27(1,2))/2.0d0/H
        FP(15)=(-F29(1,3)+4.0d0*F29(1,2))/2.0d0/H
        WRITE(16,1410)H,H2,(FP(ij),ij=1,15)
        FPP(1)=(-F1(1,4)+4.0d0*F1(1,3)-5.0d0*F1(1,2))/H2
        FPP(2)=(-F3(1,4)+4.0d0*F3(1,3)-5.0d0*F3(1,2))/H2
        FPP(3)=(-F5(1,4)+4.0d0*F5(1,3)-5.0d0*F5(1,2))/H2
        FPP(4)=(-F7(1,4)+4.0d0*F7(1,3)-5.0d0*F7(1,2))/H2
        FPP(5)=(-F9(1,4)+4.0d0*F9(1,3)-5.0d0*F9(1,2))/H2
        FPP(6)=(-F11(1,4)+4.0d0*F11(1,3)-5.0d0*F11(1,2))/H2
        FPP(7)=(-F13(1,4)+4.0d0*F13(1,3)-5.0d0*F13(1,2))/H2
        FPP(8)=(-F15(1,4)+4.0d0*F15(1,3)-5.0d0*F15(1,2))/H2
        FPP(9)=(-F17(1,4)+4.0d0*F17(1,3)-5.0d0*F17(1,2))/H2
        FPP(10)=(-F19(1,4)+4.0d0*F19(1,3)-5.0d0*F19(1,2))/H2
        FPP(11)=(-F21(1,4)+4.0d0*F21(1,3)-5.0d0*F21(1,2))/H2
        FPP(12)=(-F23(1,4)+4.0d0*F23(1,3)-5.0d0*F23(1,2))/H2
        FPP(13)=(-F25(1,4)+4.0d0*F25(1,3)-5.0d0*F25(1,2))/H2
        FPP(14)=(-F27(1,4)+4.0d0*F27(1,3)-5.0d0*F27(1,2))/H2
        FPP(15)=(-F29(1,4)+4.0d0*F29(1,3)-5.0d0*F29(1,2))/H2
        WRITE(17,*)H,H2,(FPP(ij),ij=1,15)
1410    FORMAT(17(f57.52,2x))
```

APPENDIX D
PROGRAM LISTING FOR CONVECTIVE DIFFUSION CALCULATIONS

The program listing presents all of the FORTRAN code to calculate the convective diffusion model for stationary hemispherical electrode under submerged jet impingement. The program was developed with 'Compaq Visual Fortran, Version 6.1' with double precision accuracy. The main program 'SOLUTIONOFCONVECTIVE' called the subroutine containing governing equations and boundary conditions.

The governing equations for the convective diffusion model were programmed in subroutines 'INNERPALL' and 'INNERPALLSC'. Varible $\Phi_{1,2i-1}$ were programmed in 'INNERPALL', while $\Phi_{2,2i-1}$ were programmed in 'INNERPALLSC'. The electrode surface and far field boundary conditions for the subroutines 'INNERPALL' were programmed in 'BC1PALL' and 'BC2PALL', respectively. Similarly, The electrode surface and far field boundary conditions for the subroutines 'INNERPALLSC' were programmed in 'BC1PALL' and 'BC2PALLSC', respectively.

The boundary value problem was numerically solved by subroutines BAND and MATINV, which were developed by Newman. The program was iterated until all relative values for $\Phi_(1, 2i-1)$, $\Phi(2, 2i-1)$ were within a specified tolerance limit.

D.1 Program Listing

D.1.1 Main Program

```
IMPLICIT REAL*8 (A-H,O-Z)
IMPLICIT INTEGER (I-N)
INCLUDE 'COMMON.f'
DOUBLE PRECISION, ALLOCATABLE :: C(:,:), P1(:)
DOUBLE PRECISION, ALLOCATABLE :: P3(:),P5(:),P7(:),P9(:)
```

```
    DOUBLE PRECISION, ALLOCATABLE :: P11(:),P13(:),P15(:),P17(:)
    DOUBLE PRECISION, ALLOCATABLE :: P19(:),P21(:),P23(:),P25(:)
    DOUBLE PRECISION, ALLOCATABLE :: GG(:), P27(:)
    DOUBLE PRECISION, ALLOCATABLE :: P1C(:),P3C(:),P5C(:),P7C(:)
    DOUBLE PRECISION, ALLOCATABLE :: P9C(:),P11C(:),P13C(:),P15C(:)
    DOUBLE PRECISION, ALLOCATABLE :: P17C(:),P19C(:),P21C(:),P23C(:)
    DOUBLE PRECISION, ALLOCATABLE :: P25C(:), P27C(:), DP(:,:)
    DOUBLE PRECISION  maxvalG, Z , PP(14), PCP(14)
    DOUBLE PRECISION FP(14),FPP(14),HPP(14),HPPP(14)
    DOUBLE PRECISION H, H2
    INTEGER NJL(20),NJLIST, ITMAX
    INCLUDE 'VELOCITYDATA.f'
    NJLIST=1
    NJL(1)=2001
    NJL(2)=100001
    NJL(3)=120001
    NJL(4)=140001
    NJL(5)=160001
    NJL(6)=20001
    NJL(7)=80001
    ERREQN = 0.0
    ERRSUB = 1.0E-12
    Z=20.0d0
    N=14
    ITMAX=1000
    OPEN(unit=16,file='PHP.txt')
    CLOSE(unit=16,status='delete')
    OPEN(unit=16,file='PHP.txt')
    OPEN(unit=161,file='PCHP.txt')
    CLOSE(unit=161,status='delete')
    OPEN(unit=161,file='PCHP.txt')
    DO ii=1,NJLIST
        NJ=NJL(ii)
        H=Z/(NJ-1)
        H2=H*H
        INCLUDE 'ALC.f'
        INCLUDE 'GETFNAME.f'
        INCLUDE 'PALL.f'
        INCLUDE 'CAL_PP.f'
        INCLUDE 'DLC.f'
    END DO
    END
```

D.1.2 Main Subroutines

In this section, all the include files which are called in the main program as well as in various subroutimes are listed here.

```
C***************** SUBROUTINE SETUP ****************************
    SUBROUTINE SETUPPALL(P1,P3,P5,P7,P9,P11,P13,P15,P17,P19,P21,P23
     *                  ,P25,P27,P1C,P3C,P5C,P7C,P9C,P11C,P13C,P15C
     *                  ,P17C,P19C,P21C,P23C,P25C,P27C)
    IMPLICIT DOUBLE PRECISION (A-H,O-Z)
    IMPLICIT INTEGER (I-N)
```

```
      DOUBLE PRECISION P1(*),P3(*),P5(*),P7(*),P9(*),P11(*),P13(*)
      DOUBLE PRECISION P15(*),P17(*),P19(*),P21(*),P23(*),P25(*),P27(*)
      DOUBLE PRECISION P1C(*),P3C(*),P5C(*),P7C(*),P9C(*),P11C(*)
      DOUBLE PRECISION P13C(*),P15C(*),P17C(*),P19C(*)
      DOUBLE PRECISION P21C(*),P23C(*),P25C(*),P27C(*)
      COMMON/BA/A(14,14),B(14,14),D(14,29),G(14),X(14,14),Y(14,14),N,NJ
      DO 20 II=1,NJ
          P1(II)=0.0d0
          P3(II)=0.0d0
          P5(II)=0.0d0
          P7(II)=0.0d0
          P9(II)=0.0d0
          P11(II)=0.0d0
          P13(II)=0.0d0
          P15(II)=0.0d0
          P17(II)=0.0d0
          P19(II)=0.00d0
          P21(II)=0.00d0
          P23(II)=0.00d0
          P25(II)=0.00d0
          P27(II)=0.00d0
          P1C(II)=0.0d0
          P3C(II)=0.0d0
          P5C(II)=0.0d0
          P7C(II)=0.0d0
          P9C(II)=0.0d0
          P11C(II)=0.0d0
          P13C(II)=0.0d0
          P15C(II)=0.0d0
          P17C(II)=0.0d0
          P19C(II)=0.00d0
          P21C(II)=0.00d0
          P23C(II)=0.00d0
          P25C(II)=0.00d0
          P27C(II)=0.00d0
20    CONTINUE
      P1(1)=1.0d0
      RETURN
      END
!***************** SUBROUTINE BC1PALL************************
      SUBROUTINE BC1PALL(J,C,P1,P3,P5,P7,P9,P11,P13,P15,P17,P19,P21,P23
     *                  ,P25,P27)
      IMPLICIT DOUBLE PRECISION (A-H,O-Z)
      IMPLICIT INTEGER (I-N)
      COMMON/BA/A(14,14),B(14,14),D(14,29),G(14),X(14,14),Y(14,14),N,NJ
      DOUBLE PRECISION C(14,*)
      DOUBLE PRECISION P1(*),P3(*),P5(*),P7(*),P9(*),P11(*),P13(*)
      DOUBLE PRECISION P15(*),P17(*),P19(*),P21(*),P23(*),P25(*),P27(*)
      G(1)=1.0d0-P1(J)
      B(1,1)=1.0d0
      G(2)=0.0d0-P3(J)
      B(2,2)=1.0d0
      G(3)=0.0d0-P5(J)
      B(3,3)=1.0d0
      G(4)=0.0d0-P7(J)
```

```
      B(4,4)=1.0d0
      G(5)=0.0d0-P9(J)
      B(5,5)=1.0d0
      G(6)=0.0d0-P11(J)
      B(6,6)=1.0d0
      G(7)=0.0d0-P13(J)
      B(7,7)=1.0d0
      G(8)=0.0d0-P15(J)
      B(8,8)=1.0d0
      G(9)=0.0d0-P17(J)
      B(9,9)=1.0d0
      G(10)=0.0d0-P19(J)
      B(10,10)=1.0d0
      G(11)=0.0d0-P21(J)
      B(11,11)=1.0d0
      G(12)=0.0d0-P23(J)
      B(12,12)=1.0d0
      G(13)=0.0d0-P25(J)
      B(13,13)=1.0d0
      G(14)=0.0d0-P27(J)
      B(14,14)=1.0d0
      RETURN
      END
!***************** SUBROUTINE INNER *****************************
      SUBROUTINE INNERPALL(J,C,P1,P3,P5,P7,P9,P11,P13,P15,P17,P19,P21
     *                    ,P23,P25,P27)
      IMPLICIT DOUBLE PRECISION (A-H,O-Z)
      IMPLICIT INTEGER (I-N)
      INCLUDE 'COMMON.f'
      DOUBLE PRECISION C(14,*)
      DOUBLE PRECISION P1(*),P3(*),P5(*),P7(*),P9(*),P11(*),P13(*)
      DOUBLE PRECISION P15(*),P17(*),P19(*),P21(*),P23(*),P25(*),P27(*)
      DOUBLE PRECISION Z
      Z=(J-1)*H
      DO i=1,N
          DO jj=1,N
              A(i,jj)=0.0d0
              B(i,jj)=0.0d0
              D(i,jj)=0.0d0
          END DO
      END DO
      G(1)=(P1(J+1)-2.0d0*P1(J)+P1(J-1))/H2
     *+Z*Z*HPP1*(P1(J+1)-P1(J-1))/2.0d0/H
      A(1,1)=-1.0d0/H2+Z*Z*HPP1/2.0d0/H
      B(1,1)=2.0d0/H2
      D(1,1)=-1.0d0/H2-Z*Z*HPP1/2.0d0/H
      G(2)=(P3(J+1)-2.0d0*P3(J)+P3(J-1))/H2
     *+Z*Z*HPP1*(P3(J+1)-P3(J-1))/2.0d0/H
     *+Z*Z*HPP3*(P1(J+1)-P1(J-1))/2.0d0/H
     *-Z*FP1*P3(J)
      A(2,1)= Z*Z*HPP3/2.0d0/H
      B(2,1)= 0.0d0
      D(2,1)=-Z*Z*HPP3/2.0d0/H
      A(2,2)=-1.0d0/H2+Z*Z*HPP1/2.0d0/H
      B(2,2)=2.0d0/H2+Z*FP1
```

```
 D(2,2)=-1.0d0/H2-Z*Z*HPP1/2.0d0/H
 G(3)=(P5(J+1)-2.0d0*P5(J)+P5(J-1))/H2
*+Z*Z*HPP1*(P5(J+1)-P5(J-1))/2.0d0/H
*+Z*Z*HPP3*(P3(J+1)-P3(J-1))/2.0d0/H
*+Z*Z*HPP5*(P1(J+1)-P1(J-1))/2.0d0/H
*-Z*FP3*P3(J)
*-2.0d0*Z*FP1*P5(J)
 A(3,1)= Z*Z*HPP5/2.0d0/H
 B(3,1)= 0.0d0
 D(3,1)=-Z*Z*HPP5/2.0d0/H
 A(3,2)= Z*Z*HPP3/2.0d0/H
 B(3,2)= Z*FP3
 D(3,2)=-Z*Z*HPP3/2.0d0/H
 A(3,3)=-1.0d0/H2+Z*Z*HPP1/2.0d0/H
 B(3,3)=2.0d0/H2+2.0d0*Z*FP1
 D(3,3)=-1.0d0/H2-Z*Z*HPP1/2.0d0/H
 G(4)=(P7(J+1)-2.0d0*P7(J)+P7(J-1))/H2
*+Z*Z*HPP1*(P7(J+1)-P7(J-1))/2.0d0/H
*+Z*Z*HPP3*(P5(J+1)-P5(J-1))/2.0d0/H
*+Z*Z*HPP5*(P3(J+1)-P3(J-1))/2.0d0/H
*+Z*Z*HPP7*(P1(J+1)-P1(J-1))/2.0d0/H
*-Z*FP5*P3(J)-2.0d0*Z*FP3*P5(J)-3.0d0*Z*FP1*P7(J)
 A(4,1)= Z*Z*HPP7/2.0d0/H
 B(4,1)= 0.0d0
 D(4,1)=-Z*Z*HPP7/2.0d0/H
 A(4,2)= Z*Z*HPP5/2.0d0/H
 B(4,2)= Z*FP5
 D(4,2)=-Z*Z*HPP7/2.0d0/H
 A(4,3)= Z*Z*HPP3/2.0d0/H
 B(4,3)= 2.0d0*Z*FP3
 D(4,3)=-Z*Z*HPP3/2.0d0/H
 A(4,4)=-1.0d0/H2+Z*Z*HPP1/2.0d0/H
 B(4,4)=2.0d0/H2+3.0d0*Z*FP1
 D(4,4)=-1.0d0/H2-Z*Z*HPP1/2.0d0/H
 G(5)=(P9(J+1)-2.0d0*P9(J)+P9(J-1))/H2
*+Z*Z*HPP1*(P9(J+1)-P9(J-1))/2.0d0/H
*+Z*Z*HPP3*(P7(J+1)-P7(J-1))/2.0d0/H
*+Z*Z*HPP5*(P5(J+1)-P5(J-1))/2.0d0/H
*+Z*Z*HPP7*(P3(J+1)-P3(J-1))/2.0d0/H
*+Z*Z*HPP9*(P1(J+1)-P1(J-1))/2.0d0/H
*-1.0d0*Z*FP7*P3(J)-2.0d0*Z*FP5*P5(J)-3.0d0*Z*FP3*P7(J)
*-4.0d0*Z*FP1*P9(J)
 A(5,1)= Z*Z*HPP9/2.0d0/H
 B(5,1)= 0.0d0
 D(5,1)=-Z*Z*HPP9/2.0d0/H
 A(5,2)= Z*Z*HPP7/2.0d0/H
 B(5,2)= 1.0d0*Z*FP7
 D(5,2)=-Z*Z*HPP7/2.0d0/H
 A(5,3)= Z*Z*HPP5/2.0d0/H
 B(5,3)= 2.0d0*Z*FP5
 D(5,3)=-Z*Z*HPP5/2.0d0/H
 A(5,4)= Z*Z*HPP3/2.0d0/H
 B(5,4)= 3.0d0*Z*FP3
 D(5,4)=-Z*Z*HPP3/2.0d0/H
 A(5,5)=-1.0d0/H2+Z*Z*HPP1/2.0d0/H
```

```
 B(5,5)=2.0d0/H2+4.0d0*Z*FP1
 D(5,5)=-1.0d0/H2-Z*Z*HPP1/2.0d0/H
 G(6)=(P11(J+1)-2.0d0*P11(J)+P11(J-1))/H2
*+Z*Z*HPP1*(P11(J+1)-P11(J-1))/2.0d0/H
*+Z*Z*HPP3*(P9(J+1)-P9(J-1))/2.0d0/H
*+Z*Z*HPP5*(P7(J+1)-P7(J-1))/2.0d0/H
*+Z*Z*HPP7*(P5(J+1)-P5(J-1))/2.0d0/H
*+Z*Z*HPP9*(P3(J+1)-P3(J-1))/2.0d0/H
*+Z*Z*HPP11*(P1(J+1)-P1(J-1))/2.0d0/H
*-1.0d0*Z*FP9*P3(J)-2.0d0*Z*FP7*P5(J)-3.0d0*Z*FP5*P7(J)
*-4.0d0*Z*FP3*P9(J)-5.0d0*Z*FP1*P11(J)
 A(6,1)= Z*Z*HPP11/2.0d0/H
 B(6,1)= 0.0d0
 D(6,1)=-Z*Z*HPP11/2.0d0/H
 A(6,2)= Z*Z*HPP9/2.0d0/H
 B(6,2)= 1.0d0*Z*FP9
 D(6,2)=-Z*Z*HPP9/2.0d0/H
 A(6,3)= Z*Z*HPP7/2.0d0/H
 B(6,3)= 2.0d0*Z*FP7
 D(6,3)=-Z*Z*HPP7/2.0d0/H
 A(6,4)= Z*Z*HPP5/2.0d0/H
 B(6,4)= 3.0d0*Z*FP5
 D(6,4)=-Z*Z*HPP5/2.0d0/H
 A(6,5)= Z*Z*HPP3/2.0d0/H
 B(6,5)= 4.0d0*Z*FP3
 D(6,5)=-Z*Z*HPP3/2.0d0/H
 A(6,6)=-1.0d0/H2+Z*Z*HPP1/2.0d0/H
 B(6,6)=2.0d0/H2+5.0d0*Z*FP1
 D(6,6)=-1.0d0/H2-Z*Z*HPP1/2.0d0/H
 G(7)=(P13(J+1)-2.0d0*P13(J)+P13(J-1))/H2
*+Z*Z*HPP1*(P13(J+1)-P13(J-1))/2.0d0/H
*+Z*Z*HPP3*(P11(J+1)-P11(J-1))/2.0d0/H
*+Z*Z*HPP5*(P9(J+1)-P9(J-1))/2.0d0/H
*+Z*Z*HPP7*(P7(J+1)-P7(J-1))/2.0d0/H
*+Z*Z*HPP9*(P5(J+1)-P5(J-1))/2.0d0/H
*+Z*Z*HPP11*(P3(J+1)-P3(J-1))/2.0d0/H
*+Z*Z*HPP13*(P1(J+1)-P1(J-1))/2.0d0/H
*-1.0d0*Z*FP11*P3(J)-2.0d0*Z*FP9*P5(J)-3.0d0*Z*FP7*P7(J)
*-4.0d0*Z*FP5*P9(J)-5.0d0*Z*FP3*P11(J)-6.0d0*Z*FP1*P13(J)
 A(7,1)= Z*Z*HPP13/2.0d0/H
 B(7,1)= 0.0d0
 D(7,1)=-Z*Z*HPP13/2.0d0/H
 A(7,2)= Z*Z*HPP11/2.0d0/H
 B(7,2)= 1.0d0*Z*FP11
 D(7,2)=-Z*Z*HPP11/2.0d0/H
 A(7,3)= Z*Z*HPP9/2.0d0/H
 B(7,3)= 2.0d0*Z*FP9
 D(7,3)=-Z*Z*HPP9/2.0d0/H
 A(7,4)= Z*Z*HPP7/2.0d0/H
 B(7,4)= 3.0d0*Z*FP7
 D(7,4)=-Z*Z*HPP7/2.0d0/H
 A(7,5)= Z*Z*HPP5/2.0d0/H
 B(7,5)= 4.0d0*Z*FP5
 D(7,5)=-Z*Z*HPP5/2.0d0/H
 A(7,6)= Z*Z*HPP3/2.0d0/H
```

```
 B(7,6)= 5.0d0*Z*FP3
 D(7,6)=-Z*Z*HPP3/2.0d0/H
 A(7,7)=-1.0d0/H2 + Z*Z*HPP1/2.0d0/H
 B(7,7)=2.0d0/H2 + 6.0d0*Z*FP1
 D(7,7)=-1.0d0/H2 - Z*Z*HPP1/2.0d0/H
 G(8)=(P15(J+1)-2.0d0*P15(J)+P15(J-1))/H2
*+Z*Z*HPP1*(P15(J+1)-P15(J-1))/2.0d0/H
*+Z*Z*HPP3*(P13(J+1)-P13(J-1))/2.0d0/H
*+Z*Z*HPP5*(P11(J+1)-P11(J-1))/2.0d0/H
*+Z*Z*HPP7*(P9(J+1)-P9(J-1))/2.0d0/H
*+Z*Z*HPP9*(P7(J+1)-P7(J-1))/2.0d0/H
*+Z*Z*HPP11*(P5(J+1)-P5(J-1))/2.0d0/H
*+Z*Z*HPP13*(P3(J+1)-P3(J-1))/2.0d0/H
*+Z*Z*HPP15*(P1(J+1)-P1(J-1))/2.0d0/H
*-1.0d0*Z*FP13*P3(J)-2.0d0*Z*FP11*P5(J)-3.0d0*Z*FP9*P7(J)
*-4.0d0*Z*FP7*P9(J)-5.0d0*Z*FP5*P11(J)-6.0d0*Z*FP3*P13(J)
*-7.0d0*Z*FP1*P15(J)
 A(8,1)= Z*Z*HPP15/2.0d0/H
 B(8,1)= 0.0d0
 D(8,1)=-Z*Z*HPP15/2.0d0/H
 A(8,2)= Z*Z*HPP13/2.0d0/H
 B(8,2)= 1.0d0*Z*FP13
 D(8,2)=-Z*Z*HPP13/2.0d0/H
 A(8,3)= Z*Z*HPP11/2.0d0/H
 B(8,3)= 2.0d0*Z*FP11
 D(8,3)=-Z*Z*HPP11/2.0d0/H
 A(8,4)= Z*Z*HPP9/2.0d0/H
 B(8,4)= 3.0d0*Z*FP9
 D(8,4)=-Z*Z*HPP9/2.0d0/H
 A(8,5)= Z*Z*HPP7/2.0d0/H
 B(8,5)= 4.0d0*Z*FP7
 D(8,5)=-Z*Z*HPP7/2.0d0/H
 A(8,6)= Z*Z*HPP5/2.0d0/H
 B(8,6)= 5.0d0*Z*FP5
 D(8,6)=-Z*Z*HPP5/2.0d0/H
 A(8,7)= Z*Z*HPP3/2.0d0/H
 B(8,7)= 6.0d0*Z*FP3
 D(8,7)=-Z*Z*HPP3/2.0d0/H
 A(8,8)=-1.0d0/H2 + Z*Z*HPP1/2.0d0/H
 B(8,8)=2.0d0/H2 + 7.0d0*Z*FP1
 D(8,8)=-1.0d0/H2 - Z*Z*HPP1/2.0d0/H
 G(9)=(P17(J+1)-2.0d0*P17(J)+P17(J-1))/H2
*+Z*Z*HPP1*(P17(J+1)-P17(J-1))/2.0d0/H
*+Z*Z*HPP3*(P15(J+1)-P15(J-1))/2.0d0/H
*+Z*Z*HPP5*(P13(J+1)-P13(J-1))/2.0d0/H
*+Z*Z*HPP7*(P11(J+1)-P11(J-1))/2.0d0/H
*+Z*Z*HPP9*(P9(J+1)-P9(J-1))/2.0d0/H
*+Z*Z*HPP11*(P7(J+1)-P7(J-1))/2.0d0/H
*+Z*Z*HPP13*(P5(J+1)-P5(J-1))/2.0d0/H
*+Z*Z*HPP15*(P3(J+1)-P3(J-1))/2.0d0/H
*+Z*Z*HPP17*(P1(J+1)-P1(J-1))/2.0d0/H
*-1.0d0*Z*FP15*P3(J)-2.0d0*Z*FP13*P5(J)-3.0d0*Z*FP11*P7(J)
*-4.0d0*Z*FP9*P9(J)-5.0d0*Z*FP7*P11(J)-6.0d0*Z*FP5*P13(J)
*-7.0d0*Z*FP3*P15(J)-8.0d0*Z*FP1*P17(J)
 A(9,1)= Z*Z*HPP17/2.0d0/H
```

```
 B(9,1)= 0.0d0
 D(9,1)=-Z*Z*HPP17/2.0d0/H
 A(9,2)= Z*Z*HPP15/2.0d0/H
 B(9,2)= 1.0d0*Z*FP15
 D(9,2)=-Z*Z*HPP15/2.0d0/H
 A(9,3)= Z*Z*HPP13/2.0d0/H
 B(9,3)= 2.0d0*Z*FP13
 D(9,3)=-Z*Z*HPP13/2.0d0/H
 A(9,4)= Z*Z*HPP11/2.0d0/H
 B(9,4)= 3.0d0*Z*FP11
 D(9,4)=-Z*Z*HPP11/2.0d0/H
 A(9,5)= Z*Z*HPP9/2.0d0/H
 B(9,5)= 4.0d0*Z*FP9
 D(9,5)=-Z*Z*HPP9/2.0d0/H
 A(9,6)= Z*Z*HPP7/2.0d0/H
 B(9,6)= 5.0d0*Z*FP7
 D(9,6)=-Z*Z*HPP7/2.0d0/H
 A(9,7)= Z*Z*HPP5/2.0d0/H
 B(9,7)= 6.0d0*Z*FP5
 D(9,7)=-Z*Z*HPP5/2.0d0/H
 A(9,8)= Z*Z*HPP3/2.0d0/H
 B(9,8)= 7.0d0*Z*FP3
 D(9,8)=-Z*Z*HPP3/2.0d0/H
 A(9,9)=-1.0d0/H2 + Z*Z*HPP1/2.0d0/H
 B(9,9)=2.0d0/H2 + 8.0d0*Z*FP1
 D(9,9)=-1.0d0/H2 - Z*Z*HPP1/2.0d0/H
 G(10)=(P19(J+1)-2.0d0*P19(J)+P19(J-1))/H2
*+Z*Z*HPP1*(P19(J+1)-P19(J-1))/2.0d0/H
*+Z*Z*HPP3*(P17(J+1)-P17(J-1))/2.0d0/H
*+Z*Z*HPP5*(P15(J+1)-P15(J-1))/2.0d0/H
*+Z*Z*HPP7*(P13(J+1)-P13(J-1))/2.0d0/H
*+Z*Z*HPP9*(P11(J+1)-P11(J-1))/2.0d0/H
*+Z*Z*HPP11*(P9(J+1)-P9(J-1))/2.0d0/H
*+Z*Z*HPP13*(P7(J+1)-P7(J-1))/2.0d0/H
*+Z*Z*HPP15*(P5(J+1)-P5(J-1))/2.0d0/H
*+Z*Z*HPP17*(P3(J+1)-P3(J-1))/2.0d0/H
*+Z*Z*HPP19*(P1(J+1)-P1(J-1))/2.0d0/H
*-1.0d0*Z*FP17*P3(J)-2.0d0*Z*FP15*P5(J)-3.0d0*Z*FP13*P7(J)
*-4.0d0*Z*FP11*P9(J)-5.0d0*Z*FP9*P11(J)-6.0d0*Z*FP7*P13(J)
*-7.0d0*Z*FP5*P15(J)-8.0d0*Z*FP3*P17(J)-9.0d0*Z*FP1*P19(J)
 A(10,1)= Z*Z*HPP19/2.0d0/H
 B(10,1)= 0.0d0
 D(10,1)=-Z*Z*HPP19/2.0d0/H
 A(10,2)= Z*Z*HPP17/2.0d0/H
 B(10,2)= 1.0d0*Z*FP17
 D(10,2)=-Z*Z*HPP17/2.0d0/H
 A(10,3)= Z*Z*HPP15/2.0d0/H
 B(10,3)= 2.0d0*Z*FP15
 D(10,3)=-Z*Z*HPP15/2.0d0/H
 A(10,4)= Z*Z*HPP13/2.0d0/H
 B(10,4)= 3.0d0*Z*FP13
 D(10,4)=-Z*Z*HPP13/2.0d0/H
 A(10,5)= Z*Z*HPP11/2.0d0/H
 B(10,5)= 4.0d0*Z*FP11
 D(10,5)=-Z*Z*HPP11/2.0d0/H
```

```
 A(10,6)= Z*Z*HPP9/2.0d0/H
 B(10,6)= 5.0d0*Z*FP9
 D(10,6)=-Z*Z*HPP9/2.0d0/H
 A(10,7)= Z*Z*HPP7/2.0d0/H
 B(10,7)= 6.0d0*Z*FP7
 D(10,7)=-Z*Z*HPP7/2.0d0/H
 A(10,8)= Z*Z*HPP5/2.0d0/H
 B(10,8)= 7.0d0*Z*FP5
 D(10,8)=-Z*Z*HPP5/2.0d0/H
 A(10,9)= Z*Z*HPP3/2.0d0/H
 B(10,9)= 8.0d0*Z*FP3
 D(10,9)=-Z*Z*HPP3/2.0d0/H
 A(10,10)=-1.0d0/H2 + Z*Z*HPP1/2.0d0/H
 B(10,10)=2.0d0/H2 + 9.0d0*Z*FP1
 D(10,10)=-1.0d0/H2 - Z*Z*HPP1/2.0d0/H
 G(11)=(P21(J+1)-2.0d0*P21(J)+P21(J-1))/H2
*+Z*Z*HPP1*(P21(J+1)-P21(J-1))/2.0d0/H
*+Z*Z*HPP3*(P19(J+1)-P19(J-1))/2.0d0/H
*+Z*Z*HPP5*(P17(J+1)-P17(J-1))/2.0d0/H
*+Z*Z*HPP7*(P15(J+1)-P15(J-1))/2.0d0/H
*+Z*Z*HPP9*(P13(J+1)-P13(J-1))/2.0d0/H
*+Z*Z*HPP11*(P11(J+1)-P11(J-1))/2.0d0/H
*+Z*Z*HPP13*(P9(J+1)-P9(J-1))/2.0d0/H
*+Z*Z*HPP15*(P7(J+1)-P7(J-1))/2.0d0/H
*+Z*Z*HPP17*(P5(J+1)-P5(J-1))/2.0d0/H
*+Z*Z*HPP19*(P3(J+1)-P3(J-1))/2.0d0/H
*+Z*Z*HPP21*(P1(J+1)-P1(J-1))/2.0d0/H
*-1.0d0*Z*FP19*P3(J)-2.0d0*Z*FP17*P5(J)-3.0d0*Z*FP15*P7(J)
*-4.0d0*Z*FP13*P9(J)-5.0d0*Z*FP11*P11(J)-6.0d0*Z*FP9*P13(J)
*-7.0d0*Z*FP7*P15(J)-8.0d0*Z*FP5*P17(J)-9.0d0*Z*FP3*P19(J)
*-10.0d0*Z*FP1*P21(J)
 A(11,1)= Z*Z*HPP21/2.0d0/H
 B(11,1)= 0.0d0
 D(11,1)=-Z*Z*HPP21/2.0d0/H
 A(11,2)= Z*Z*HPP19/2.0d0/H
 B(11,2)= 1.0d0*Z*FP19
 D(11,2)=-Z*Z*HPP19/2.0d0/H
 A(11,3)= Z*Z*HPP17/2.0d0/H
 B(11,3)= 2.0d0*Z*FP17
 D(11,3)=-Z*Z*HPP17/2.0d0/H
 A(11,4)= Z*Z*HPP15/2.0d0/H
 B(11,4)= 3.0d0*Z*FP15
 D(11,4)=-Z*Z*HPP15/2.0d0/H
 A(11,5)= Z*Z*HPP13/2.0d0/H
 B(11,5)= 4.0d0*Z*FP13
 D(11,5)=-Z*Z*HPP13/2.0d0/H
 A(11,6)= Z*Z*HPP11/2.0d0/H
 B(11,6)= 5.0d0*Z*FP11
 D(11,6)=-Z*Z*HPP11/2.0d0/H
 A(11,7)= Z*Z*HPP9/2.0d0/H
 B(11,7)= 6.0d0*Z*FP9
 D(11,7)=-Z*Z*HPP9/2.0d0/H
 A(11,8)= Z*Z*HPP7/2.0d0/H
 B(11,8)= 7.0d0*Z*FP7
 D(11,8)=-Z*Z*HPP7/2.0d0/H
```

```
 A(11,9)= Z*Z*HPP5/2.0d0/H
 B(11,9)= 8.0d0*Z*FP5
 D(11,9)=-Z*Z*HPP5/2.0d0/H
 A(11,10)= Z*Z*HPP3/2.0d0/H
 B(11,10)= 9.0d0*Z*FP3
 D(11,10)=-Z*Z*HPP3/2.0d0/H
 A(11,11)=-1.0d0/H2 + Z*Z*HPP1/2.0d0/H
 B(11,11)=2.0d0/H2 + 10.0d0*Z*FP1
 D(11,11)=-1.0d0/H2 - Z*Z*HPP1/2.0d0/H
 G(12)=(P23(J+1)-2.0d0*P23(J)+P23(J-1))/H2
*+Z*Z*HPP1*(P23(J+1)-P23(J-1))/2.0d0/H
*+Z*Z*HPP3*(P21(J+1)-P21(J-1))/2.0d0/H
*+Z*Z*HPP5*(P19(J+1)-P19(J-1))/2.0d0/H
*+Z*Z*HPP7*(P17(J+1)-P17(J-1))/2.0d0/H
*+Z*Z*HPP9*(P15(J+1)-P15(J-1))/2.0d0/H
*+Z*Z*HPP11*(P13(J+1)-P13(J-1))/2.0d0/H
*+Z*Z*HPP13*(P11(J+1)-P11(J-1))/2.0d0/H
*+Z*Z*HPP15*(P9(J+1)-P9(J-1))/2.0d0/H
*+Z*Z*HPP17*(P7(J+1)-P7(J-1))/2.0d0/H
*+Z*Z*HPP19*(P5(J+1)-P5(J-1))/2.0d0/H
*+Z*Z*HPP21*(P3(J+1)-P3(J-1))/2.0d0/H
*+Z*Z*HPP23*(P1(J+1)-P1(J-1))/2.0d0/H
*-1.0d0*Z*FP21*P3(J)-2.0d0*Z*FP19*P5(J)-3.0d0*Z*FP17*P7(J)
*-4.0d0*Z*FP15*P9(J)-5.0d0*Z*FP13*P11(J)-6.0d0*Z*FP11*P13(J)
*-7.0d0*Z*FP9*P15(J)-8.0d0*Z*FP7*P17(J)-9.0d0*Z*FP5*P19(J)
*-10.0d0*Z*FP3*P21(J)-11.0d0*Z*FP1*P23(J)
 A(12,1)= Z*Z*HPP23/2.0d0/H
 B(12,1)= 0.0d0
 D(12,1)=-Z*Z*HPP23/2.0d0/H
 A(12,2)= Z*Z*HPP21/2.0d0/H
 B(12,2)= 1.0d0*Z*FP21
 D(12,2)=-Z*Z*HPP21/2.0d0/H
 A(12,3)= Z*Z*HPP19/2.0d0/H
 B(12,3)= 2.0d0*Z*FP19
 D(12,3)=-Z*Z*HPP19/2.0d0/H
 A(12,4)= Z*Z*HPP17/2.0d0/H
 B(12,4)= 3.0d0*Z*FP17
 D(12,4)=-Z*Z*HPP17/2.0d0/H
 A(12,5)= Z*Z*HPP15/2.0d0/H
 B(12,5)= 4.0d0*Z*FP15
 D(12,5)=-Z*Z*HPP15/2.0d0/H
 A(12,6)= Z*Z*HPP13/2.0d0/H
 B(12,6)= 5.0d0*Z*FP13
 D(12,6)=-Z*Z*HPP13/2.0d0/H
 A(12,7)= Z*Z*HPP11/2.0d0/H
 B(12,7)= 6.0d0*Z*FP11
 D(12,7)=-Z*Z*HPP11/2.0d0/H
 A(12,8)= Z*Z*HPP9/2.0d0/H
 B(12,8)= 7.0d0*Z*FP9
 D(12,8)=-Z*Z*HPP9/2.0d0/H
 A(12,9)= Z*Z*HPP7/2.0d0/H
 B(12,9)= 8.0d0*Z*FP7
 D(12,9)=-Z*Z*HPP7/2.0d0/H
 A(12,10)= Z*Z*HPP5/2.0d0/H
 B(12,10)= 9.0d0*Z*FP5
```

```
 D(12,10)=-Z*Z*HPP5/2.0d0/H
 A(12,11)= Z*Z*HPP3/2.0d0/H
 B(12,11)= 10.0d0*Z*FP3
 D(12,11)=-Z*Z*HPP3/2.0d0/H
 A(12,12)=-1.0d0/H2 + Z*Z*HPP1/2.0d0/H
 B(12,12)=2.0d0/H2 + 11.0d0*Z*FP1
 D(12,12)=-1.0d0/H2 - Z*Z*HPP1/2.0d0/H
 G(13)=(P25(J+1)-2.0d0*P25(J)+P25(J-1))/H2
*+Z*Z*HPP1*(P25(J+1)-P25(J-1))/2.0d0/H
*+Z*Z*HPP3*(P23(J+1)-P23(J-1))/2.0d0/H
*+Z*Z*HPP5*(P21(J+1)-P21(J-1))/2.0d0/H
*+Z*Z*HPP7*(P19(J+1)-P19(J-1))/2.0d0/H
*+Z*Z*HPP9*(P17(J+1)-P17(J-1))/2.0d0/H
*+Z*Z*HPP11*(P15(J+1)-P15(J-1))/2.0d0/H
*+Z*Z*HPP13*(P13(J+1)-P13(J-1))/2.0d0/H
*+Z*Z*HPP15*(P11(J+1)-P11(J-1))/2.0d0/H
*+Z*Z*HPP17*(P9(J+1)-P9(J-1))/2.0d0/H
*+Z*Z*HPP19*(P7(J+1)-P7(J-1))/2.0d0/H
*+Z*Z*HPP21*(P5(J+1)-P5(J-1))/2.0d0/H
*+Z*Z*HPP23*(P3(J+1)-P3(J-1))/2.0d0/H
*+Z*Z*HPP25*(P1(J+1)-P1(J-1))/2.0d0/H
*-1.0d0*Z*FP23*P3(J)-2.0d0*Z*FP21*P5(J)-3.0d0*Z*FP19*P7(J)
*-4.0d0*Z*FP17*P9(J)-5.0d0*Z*FP15*P11(J)-6.0d0*Z*FP13*P13(J)
*-7.0d0*Z*FP11*P15(J)-8.0d0*Z*FP9*P17(J)-9.0d0*Z*FP7*P19(J)
*-10.0d0*Z*FP5*P21(J)-11.0d0*Z*FP3*P23(J)-12.0d0*Z*FP1*P25(J)
 A(13,1)= Z*Z*HPP25/2.0d0/H
 B(13,1)= 0.0d0
 D(13,1)=-Z*Z*HPP25/2.0d0/H
 A(13,2)= Z*Z*HPP23/2.0d0/H
 B(13,2)= 1.0d0*Z*FP23
 D(13,2)=-Z*Z*HPP23/2.0d0/H
 A(13,3)= Z*Z*HPP21/2.0d0/H
 B(13,3)= 2.0d0*Z*FP21
 D(13,3)=-Z*Z*HPP21/2.0d0/H
 A(13,4)= Z*Z*HPP21/2.0d0/H
 B(13,4)= 3.0d0*Z*FP21
 D(13,4)=-Z*Z*HPP21/2.0d0/H
 A(13,5)= Z*Z*HPP17/2.0d0/H
 B(13,5)= 4.0d0*Z*FP17
 D(13,5)=-Z*Z*HPP17/2.0d0/H
 A(13,6)= Z*Z*HPP15/2.0d0/H
 B(13,6)= 5.0d0*Z*FP15
 D(13,6)=-Z*Z*HPP15/2.0d0/H
 A(13,7)= Z*Z*HPP13/2.0d0/H
 B(13,7)= 6.0d0*Z*FP13
 D(13,7)=-Z*Z*HPP13/2.0d0/H
 A(13,8)= Z*Z*HPP11/2.0d0/H
 B(13,8)= 7.0d0*Z*FP11
 D(13,8)=-Z*Z*HPP11/2.0d0/H
 A(13,9)= Z*Z*HPP9/2.0d0/H
 B(13,9)= 8.0d0*Z*FP9
 D(13,9)=-Z*Z*HPP9/2.0d0/H
 A(13,10)= Z*Z*HPP7/2.0d0/H
 B(13,10)= 9.0d0*Z*FP7
 D(13,10)=-Z*Z*HPP7/2.0d0/H
```

```
 A(13,11)= Z*Z*HPP5/2.0d0/H
 B(13,11)= 10.0d0*Z*FP5
 D(13,11)=-Z*Z*HPP5/2.0d0/H
 A(13,12)= Z*Z*HPP3/2.0d0/H
 B(13,12)= 11.0d0*Z*FP3
 D(13,12)=-Z*Z*HPP3/2.0d0/H
 A(13,13)=-1.0d0/H2 + Z*Z*HPP1/2.0d0/H
 B(13,13)=2.0d0/H2 + 12.0d0*Z*FP1
 D(13,13)=-1.0d0/H2 - Z*Z*HPP1/2.0d0/H
 G(14)=(P27(J+1)-2.0d0*P27(J)+P27(J-1))/H2
*+Z*Z*HPP1*(P27(J+1)-P27(J-1))/2.0d0/H
*+Z*Z*HPP3*(P25(J+1)-P25(J-1))/2.0d0/H
*+Z*Z*HPP5*(P23(J+1)-P23(J-1))/2.0d0/H
*+Z*Z*HPP7*(P21(J+1)-P21(J-1))/2.0d0/H
*+Z*Z*HPP9*(P19(J+1)-P19(J-1))/2.0d0/H
*+Z*Z*HPP11*(P17(J+1)-P17(J-1))/2.0d0/H
*+Z*Z*HPP13*(P15(J+1)-P15(J-1))/2.0d0/H
*+Z*Z*HPP15*(P13(J+1)-P13(J-1))/2.0d0/H
*+Z*Z*HPP17*(P11(J+1)-P11(J-1))/2.0d0/H
*+Z*Z*HPP19*(P9(J+1)-P9(J-1))/2.0d0/H
*+Z*Z*HPP21*(P7(J+1)-P7(J-1))/2.0d0/H
*+Z*Z*HPP23*(P5(J+1)-P5(J-1))/2.0d0/H
*+Z*Z*HPP25*(P3(J+1)-P3(J-1))/2.0d0/H
*+Z*Z*HPP27*(P1(J+1)-P1(J-1))/2.0d0/H
*-1.0d0*Z*FP25*P3(J)-2.0d0*Z*FP23*P5(J)-3.0d0*Z*FP21*P7(J)
*-4.0d0*Z*FP19*P9(J)-5.0d0*Z*FP17*P11(J)-6.0d0*Z*FP15*P13(J)
*-7.0d0*Z*FP13*P15(J)-8.0d0*Z*FP11*P17(J)-9.0d0*Z*FP9*P19(J)
*-10.0d0*Z*FP7*P21(J)-11.0d0*Z*FP5*P23(J)-12.0d0*Z*FP3*P25(J)
*-13.0d0*Z*FP1*P27(J)
 A(14,1)= Z*Z*HPP27/2.0d0/H
 B(14,1)= 0.0d0
 D(14,1)=-Z*Z*HPP27/2.0d0/H
 A(14,2)= Z*Z*HPP25/2.0d0/H
 B(14,2)= 1.0d0*Z*FP25
 D(14,2)=-Z*Z*HPP25/2.0d0/H
 A(14,3)= Z*Z*HPP23/2.0d0/H
 B(14,3)= 2.0d0*Z*FP23
 D(14,3)=-Z*Z*HPP23/2.0d0/H
 A(14,4)= Z*Z*HPP21/2.0d0/H
 B(14,4)= 3.0d0*Z*FP21
 D(14,4)=-Z*Z*HPP21/2.0d0/H
 A(14,5)= Z*Z*HPP19/2.0d0/H
 B(14,5)= 4.0d0*Z*FP19
 D(14,5)=-Z*Z*HPP19/2.0d0/H
 A(14,6)= Z*Z*HPP17/2.0d0/H
 B(14,6)= 5.0d0*Z*FP17
 D(14,6)=-Z*Z*HPP17/2.0d0/H
 A(14,7)= Z*Z*HPP15/2.0d0/H
 B(14,7)= 6.0d0*Z*FP15
 D(14,7)=-Z*Z*HPP15/2.0d0/H
 A(14,8)= Z*Z*HPP13/2.0d0/H
 B(14,8)= 7.0d0*Z*FP13
 D(14,8)=-Z*Z*HPP13/2.0d0/H
 A(14,9)= Z*Z*HPP11/2.0d0/H
 B(14,9)= 8.0d0*Z*FP11
```

```
      D(14,9)=-Z*Z*HPP11/2.0d0/H
      A(14,10)= Z*Z*HPP9/2.0d0/H
      B(14,10)= 9.0d0*Z*FP9
      D(14,10)=-Z*Z*HPP9/2.0d0/H
      A(14,11)= Z*Z*HPP7/2.0d0/H
      B(14,11)= 10.0d0*Z*FP7
      D(14,11)=-Z*Z*HPP7/2.0d0/H
      A(14,12)= Z*Z*HPP5/2.0d0/H
      B(14,12)= 11.0d0*Z*FP5
      D(14,12)=-Z*Z*HPP5/2.0d0/H
      A(14,13)= Z*Z*HPP3/2.0d0/H
      B(14,13)= 12.0d0*Z*FP3
      D(14,13)= Z*Z*HPP3/2.0d0/H
      A(14,14)=-1.0d0/H2 + Z*Z*HPP1/2.0d0/H
      B(14,14)=2.0d0/H2 + 13.0d0*Z*FP1
      D(14,14)=-1.0d0/H2 - Z*Z*HPP1/2.0d0/H
      RETURN
      END
!********************** SUBROUTINE BC2PALL **********************
      SUBROUTINE BC2PALL(J,C,P1,P3,P5,P7,P9,P11,P13,P15,P17,P19,P21
     *                  ,P23,P25,P27)
      IMPLICIT DOUBLE PRECISION (A-H,O-Z)
      IMPLICIT INTEGER (I-N)
      COMMON/BA/A(14,14),B(14,14),D(14,29),G(14),X(14,14),Y(14,14),N,NJ
      DOUBLE PRECISION C(14,*)
      DOUBLE PRECISION P1(*),P3(*),P5(*),P7(*),P9(*),P11(*),P13(*)
      DOUBLE PRECISION P15(*),P17(*),P19(*),P21(*),P23(*),P25(*),P27(*)
          G(1)=0.0d0-P1(J)
          B(1,1)=1.0d0
          G(2)=0.0d0-P3(J)
          B(2,2)=1.0d0
          G(3)=0.0d0-P5(J)
          B(3,3)=1.0d0
          G(4)=0.0d0-P7(J)
          B(4,4)=1.0d0
          G(5)=0.0d0-P9(J)
          B(5,5)=1.0d0
          G(6)=0.0d0-P11(J)
          B(6,6)=1.0d0
          G(7)=0.0d0-P13(J)
          B(7,7)=1.0d0
          G(8)=0.0d0-P15(J)
          B(8,8)=1.0d0
          G(9)=0.0d0-P17(J)
          B(9,9)=1.0d0
          G(10)=0.0d0-P19(J)
          B(10,10)=1.0d0
          G(11)=0.0d0-P21(J)
          B(11,11)=1.0d0
          G(12)=0.0d0-P23(J)
          B(12,12)=1.0d0
          G(13)=0.0d0-P25(J)
          B(13,13)=1.0d0
          G(14)=0.0d0-P27(J)
          B(14,14)=1.0d0
```

```
      RETURN
      END
!*************** SUBROUTINE BC1PALLSC***********************
      SUBROUTINE BC1PALLSC(J,C,P1C,P3C,P5C,P7C,P9C,P11C,P13C,
     *                 P15C,P17C,P19C,P21C,P23C,P25C,P27C)
      IMPLICIT REAL*8 (A-H,O-Z)
      IMPLICIT INTEGER (I-N)
      COMMON/BA/A(14,14),B(14,14),D(14,29),G(14),X(14,14),Y(14,14),N,NJ
      COMMON/BB/H,H2
      DOUBLE PRECISION C(14,*)
      DOUBLE PRECISION P1C(*),P3C(*),P5C(*),P7C(*),P9C(*),P11C(*)
      DOUBLE PRECISION P13C(*),P15C(*),P17C(*),P19C(*)
      DOUBLE PRECISION P21C(*),P23C(*),P25C(*),P27C(*)
      DO i=1,N
          DO jj=1,N
              A(i,jj)=0.0d0
              B(i,jj)=0.0d0
              D(i,jj)=0.0d0
          END DO
      END DO
          G(1)=0.0d0-P1C(J)
          B(1,1)=1.0d0
          G(2)=0.0d0-P3C(J)
          B(2,2)=1.0d0
          G(3)=0.0d0-P5C(J)
          B(3,3)=1.0d0
          G(4)=0.0d0-P7C(J)
          B(4,4)=1.0d0
          G(5)=0.0d0-P9C(J)
          B(5,5)=1.0d0
          G(6)=0.0d0-P11C(J)
          B(6,6)=1.0d0
          G(7)=0.0d0-P13C(J)
          B(7,7)=1.0d0
          G(8)=0.0d0-P15C(J)
          B(8,8)=1.0d0
          G(9)=0.0d0-P17C(J)
          B(9,9)=1.0d0
          G(10)=0.0d0-P19C(J)
          B(10,10)=1.0d0
          G(11)=0.0d0-P21C(J)
          B(11,11)=1.0d0
          G(12)=0.0d0-P23C(J)
          B(12,12)=1.0d0
          G(13)=0.0d0-P25C(J)
          B(13,13)=1.0d0
          G(14)=0.0d0-P27C(J)
          B(14,14)=1.0d0
      RETURN
      END
!*************** SUBROUTINE INNERPALLSC*********************
      SUBROUTINE INNERPALLSC(J,C,P1,P3,P5,P7,P9,P11,P13,P15,P17,P19,
     *                    P21,P23,P25,P27,P1C,P3C,P5C,P7C,P9C,P11C,
     *                    P13C,P15C,P17C,P19C,P21C,P23C,P25C,P27C)
      IMPLICIT REAL*8 (A-H,O-Z)
```

```
      IMPLICIT INTEGER (I-N)
      INCLUDE 'COMMON.f'
      DOUBLE PRECISION C(14,*)
      DOUBLE PRECISION P1(*),P3(*),P5(*),P7(*),P9(*),P11(*),P13(*)
      DOUBLE PRECISION P15(*),P17(*),P19(*),P21(*),P23(*),P25(*),P27(*)
      DOUBLE PRECISION P1C(*),P3C(*),P5C(*),P7C(*),P9C(*),P11C(*)
      DOUBLE PRECISION P13C(*),P15C(*),P17C(*),P19C(*)
      DOUBLE PRECISION P21C(*),P23C(*),P25C(*),P27C(*)
      DOUBLE PRECISION Z
      Z=(J-1)*H
      DO i=1,N
          DO jj=1,N
              A(i,jj)=0.0d0
              B(i,jj)=0.0d0
              D(i,jj)=0.0d0
          END DO
      END DO
      G(1)=(P1C(J+1)-2.0d0*P1C(J)+P1C(J-1))/H2
     *+Z*Z*HPP1*(P1C(J+1)-P1C(J-1))/2.0d0/H
     *+Z*Z*Z*HPPP1*(P1(J+1)-P1(J-1))/2.0d0/H/3.0d0
      A(1,1)=-1.0d0/H2+Z*Z*HPP1/2.0d0/H
      B(1,1)=2.0d0/H2
      D(1,1)=-1.0d0/H2-Z*Z*HPP1/2.0d0/H
      G(2)=(P3C(J+1)-2.0d0*P3C(J)+P3C(J-1))/H2
     *+Z*Z*HPP1*(P3C(J+1)-P3C(J-1))/2.0d0/H
     *+Z*Z*HPP3*(P1C(J+1)-P1C(J-1))/2.0d0/H
     *+Z*Z*Z*HPPP1*(P3(J+1)-P3(J-1))/2.0d0/H/3.0d0
     *+Z*Z*Z*HPPP3*(P1(J+1)-P1(J-1))/2.0d0/H/3.0d0
     *-Z*FP1*P3C(J)-0.50d0*Z*Z*FPP1*P3(J)
      A(2,1)= Z*Z*HPP3/2.0d0/H
      B(2,1)= 0.0d0
      D(2,1)=-Z*Z*HPP3/2.0d0/H
      A(2,2)=-1.0d0/H2 + Z*Z*HPP1/2.0d0/H
      B(2,2)= 2.0d0/H2 + Z*FP1
      D(2,2)=-1.0d0/H2 - Z*Z*HPP1/2.0d0/H
      G(3)=(P5C(J+1)-2.0d0*P5C(J)+P5C(J-1))/H2
     *+Z*Z*HPP1*(P5C(J+1)-P5C(J-1))/2.0d0/H
     *+Z*Z*HPP3*(P3C(J+1)-P3C(J-1))/2.0d0/H
     *+Z*Z*HPP5*(P1C(J+1)-P1C(J-1))/2.0d0/H
     *+Z*Z*Z*HPPP1*(P5(J+1)-P5(J-1))/2.0d0/H/3.0d0
     *+Z*Z*Z*HPPP3*(P3(J+1)-P3(J-1))/2.0d0/H/3.0d0
     *+Z*Z*Z*HPPP5*(P1(J+1)-P1(J-1))/2.0d0/H/3.0d0
     *-1.0d0*Z*FP3*P3C(J)-2.0d0*Z*FP1*P5C(J)
     *-0.50d0*Z*Z*FPP3*P3(J)-1.00d0*Z*Z*FPP1*P5(J)
      A(3,1)= Z*Z*HPP5/2.0d0/H
      B(3,1)= 0.0d0
      D(3,1)=-Z*Z*HPP5/2.0d0/H
      A(3,2)= Z*Z*HPP3/2.0d0/H
      B(3,2)= Z*FP3
      D(3,2)=-Z*Z*HPP3/2.0d0/H
      A(3,3)=-1.0d0/H2+Z*Z*HPP1/2.0d0/H
      B(3,3)=2.0d0/H2+2.0d0*Z*FP1
      D(3,3)=-1.0d0/H2-Z*Z*HPP1/2.0d0/H
      G(4)=(P7C(J+1)-2.0d0*P7C(J)+P7C(J-1))/H2
     *+Z*Z*HPP1*(P7C(J+1)-P7C(J-1))/2.0d0/H
```

```
*+Z*Z*HPP3*(P5C(J+1)-P5C(J-1))/2.0d0/H
*+Z*Z*HPP5*(P3C(J+1)-P3C(J-1))/2.0d0/H
*+Z*Z*HPP7*(P1C(J+1)-P1C(J-1))/2.0d0/H
*+Z*Z*Z*HPPP1*(P7(J+1)-P7(J-1))/2.0d0/H/3.0d0
*+Z*Z*Z*HPPP3*(P5(J+1)-P5(J-1))/2.0d0/H/3.0d0
*+Z*Z*Z*HPPP5*(P3(J+1)-P3(J-1))/2.0d0/H/3.0d0
*+Z*Z*Z*HPPP7*(P1(J+1)-P1(J-1))/2.0d0/H/3.0d0
*-1.0d0*Z*FP5*P3C(J)-2.0d0*Z*FP3*P5C(J)-3.0d0*Z*FP1*P7C(J)
*-0.50d0*Z*Z*FPP5*P3(J)-1.00d0*Z*Z*FPP3*P5(J)-1.50d0*Z*Z*FPP1*P7(J)
 A(4,1)= Z*Z*HPP7/2.0d0/H
 B(4,1)= 0.0d0
 D(4,1)=-Z*Z*HPP7/2.0d0/H
 A(4,2)= Z*Z*HPP5/2.0d0/H
 B(4,2)= Z*FP5
 D(4,2)=-Z*Z*HPP7/2.0d0/H
 A(4,3)= Z*Z*HPP3/2.0d0/H
 B(4,3)= 2.0d0*Z*FP3
 D(4,3)=-Z*Z*HPP3/2.0d0/H
 A(4,4)=-1.0d0/H2+Z*Z*HPP1/2.0d0/H
 B(4,4)=2.0d0/H2+3.0d0*Z*FP1
 D(4,4)=-1.0d0/H2-Z*Z*HPP1/2.0d0/H
 G(5)=(P9C(J+1)-2.0d0*P9C(J)+P9C(J-1))/H2
*+Z*Z*HPP1*(P9C(J+1)-P9C(J-1))/2.0d0/H
*+Z*Z*HPP3*(P7C(J+1)-P7C(J-1))/2.0d0/H
*+Z*Z*HPP5*(P5C(J+1)-P5C(J-1))/2.0d0/H
*+Z*Z*HPP7*(P3C(J+1)-P3C(J-1))/2.0d0/H
*+Z*Z*HPP9*(P1C(J+1)-P1C(J-1))/2.0d0/H
*+Z*Z*Z*HPPP1*(P9(J+1)-P9(J-1))/2.0d0/H/3.0d0
*+Z*Z*Z*HPPP3*(P7(J+1)-P7(J-1))/2.0d0/H/3.0d0
*+Z*Z*Z*HPPP5*(P5(J+1)-P5(J-1))/2.0d0/H/3.0d0
*+Z*Z*Z*HPPP7*(P3(J+1)-P3(J-1))/2.0d0/H/3.0d0
*+Z*Z*Z*HPPP9*(P1(J+1)-P1(J-1))/2.0d0/H/3.0d0
*-1.0d0*Z*FP7*P3C(J)-2.0d0*Z*FP5*P5C(J)-3.0d0*Z*FP3*P7C(J)
*-4.0d0*Z*FP1*P9C(J)-0.50d0*Z*Z*FPP7*P3(J)-1.00d0*Z*Z*FPP5*P5(J)
*-1.50d0*Z*Z*FPP3*P7(J)-2.00d0*Z*Z*FPP1*P9(J)
 A(5,1)= Z*Z*HPP9/2.0d0/H
 B(5,1)= 0.0d0
 D(5,1)=-Z*Z*HPP9/2.0d0/H
 A(5,2)= Z*Z*HPP7/2.0d0/H
 B(5,2)= 1.0d0*Z*FP7
 D(5,2)=-Z*Z*HPP7/2.0d0/H
 A(5,3)= Z*Z*HPP5/2.0d0/H
 B(5,3)= 2.0d0*Z*FP5
 D(5,3)=-Z*Z*HPP5/2.0d0/H
 A(5,4)= Z*Z*HPP3/2.0d0/H
 B(5,4)= 3.0d0*Z*FP3
 D(5,4)=-Z*Z*HPP3/2.0d0/H
 A(5,5)=-1.0d0/H2+Z*Z*HPP1/2.0d0/H
 B(5,5)=2.0d0/H2+4.0d0*Z*FP1
 D(5,5)=-1.0d0/H2-Z*Z*HPP1/2.0d0/H
 G(6)=(P11C(J+1)-2.0d0*P11C(J) + P11C(J-1))/H2
*+Z*Z*HPP1 *(P11C(J+1)-P11C(J-1))/2.0d0/H
*+Z*Z*HPP3 *( P9C(J+1)- P9C(J-1))/2.0d0/H
*+Z*Z*HPP5 *( P7C(J+1)- P7C(J-1))/2.0d0/H
*+Z*Z*HPP7 *( P5C(J+1)- P5C(J-1))/2.0d0/H
```

```
*+Z*Z*HPP9 *( P3C(J+1)- P3C(J-1))/2.0d0/H
*+Z*Z*HPP11*( P1C(J+1)- P1C(J-1))/2.0d0/H
*+Z*Z*Z*HPPP1 *(P11(J+1)-P11(J-1))/2.0d0/H/3.0d0
*+Z*Z*Z*HPPP3 *( P9(J+1)- P9(J-1))/2.0d0/H/3.0d0
*+Z*Z*Z*HPPP5 *( P7(J+1)- P7(J-1))/2.0d0/H/3.0d0
*+Z*Z*Z*HPPP7 *( P5(J+1)- P5(J-1))/2.0d0/H/3.0d0
*+Z*Z*Z*HPPP9 *( P3(J+1)- P3(J-1))/2.0d0/H/3.0d0
*+Z*Z*Z*HPPP11*( P1(J+1)- P1(J-1))/2.0d0/H/3.0d0
*-1.0d0*Z*FP9* P3C(J)-2.0d0*Z*FP7* P5C(J)-3.0d0*Z*FP5* P7C(J)
*-4.0d0*Z*FP3* P9C(J)-5.0d0*Z*FP1*P11C(J)-0.50d0*Z*Z*FPP9* P3(J)
*-1.00d0*Z*Z*FPP7* P5(J)-1.50d0*Z*Z*FPP5* P7(J)
*-2.00d0*Z*Z*FPP3* P9(J)-2.50d0*Z*Z*FPP1*P11(J)
 A(6,1)= Z*Z*HPP11/2.0d0/H
 B(6,1)= 0.0d0
 D(6,1)=-Z*Z*HPP11/2.0d0/H
 A(6,2)= Z*Z*HPP9/2.0d0/H
 B(6,2)= 1.0d0*Z*FP9
 D(6,2)=-Z*Z*HPP9/2.0d0/H
 A(6,3)= Z*Z*HPP7/2.0d0/H
 B(6,3)= 2.0d0*Z*FP7
 D(6,3)=-Z*Z*HPP7/2.0d0/H
 A(6,4)= Z*Z*HPP5/2.0d0/H
 B(6,4)= 3.0d0*Z*FP5
 D(6,4)=-Z*Z*HPP5/2.0d0/H
 A(6,5)= Z*Z*HPP3/2.0d0/H
 B(6,5)= 4.0d0*Z*FP3
 D(6,5)=-Z*Z*HPP3/2.0d0/H
 A(6,6)=-1.0d0/H2+Z*Z*HPP1/2.0d0/H
 B(6,6)=2.0d0/H2+5.0d0*Z*FP1
 D(6,6)=-1.0d0/H2-Z*Z*HPP1/2.0d0/H
 G(7)=(P13C(J+1)-2.0d0*P13C(J) + P13C(J-1))/H2
*+Z*Z*HPP1 *(P13C(J+1)-P13C(J-1))/2.0d0/H
*+Z*Z*HPP3 *(P11C(J+1)-P11C(J-1))/2.0d0/H
*+Z*Z*HPP5 *( P9C(J+1)- P9C(J-1))/2.0d0/H
*+Z*Z*HPP7 *( P7C(J+1)- P7C(J-1))/2.0d0/H
*+Z*Z*HPP9 *( P5C(J+1)- P5C(J-1))/2.0d0/H
*+Z*Z*HPP11*( P3C(J+1)- P3C(J-1))/2.0d0/H
*+Z*Z*HPP13*( P1C(J+1)- P1C(J-1))/2.0d0/H
*+Z*Z*Z*HPPP1 *(P13(J+1)-P13(J-1))/2.0d0/H/3.0d0
*+Z*Z*Z*HPPP3 *(P11(J+1)-P11(J-1))/2.0d0/H/3.0d0
*+Z*Z*Z*HPPP5 *( P9(J+1)- P9(J-1))/2.0d0/H/3.0d0
*+Z*Z*Z*HPPP7 *( P7(J+1)- P7(J-1))/2.0d0/H/3.0d0
*+Z*Z*Z*HPPP9 *( P5(J+1)- P5(J-1))/2.0d0/H/3.0d0
*+Z*Z*Z*HPPP11*( P3(J+1)- P3(J-1))/2.0d0/H/3.0d0
*+Z*Z*Z*HPPP13*( P1(J+1)- P1(J-1))/2.0d0/H/3.0d0
*-1.0d0*Z*FP11*P3C(J)-2.0d0*Z*FP9*P5C(J)-3.0d0*Z*FP7*P7C(J)
*-4.0d0*Z*FP5*P9C(J)-5.0d0*Z*FP3*P11C(J)-6.0d0*Z*FP1*P13C(J)
*-0.50d0*Z*Z*FPP11*P3(J)-1.00d0*Z*Z*FPP9* P5(J)-1.50d0*Z*Z*FPP7* P7(J)
*-2.00d0*Z*Z*FPP5*P9(J)-2.50d0*Z*Z*FPP3*P11(J)-3.00d0*Z*Z*FPP1*P13(J)
 A(7,1)= Z*Z*HPP13/2.0d0/H
 B(7,1)= 0.0d0
 D(7,1)=-Z*Z*HPP13/2.0d0/H
 A(7,2)= Z*Z*HPP11/2.0d0/H
 B(7,2)= 1.0d0*Z*FP11
 D(7,2)=-Z*Z*HPP11/2.0d0/H
```

```
 A(7,3)= Z*Z*HPP9/2.0d0/H
 B(7,3)= 2.0d0*Z*FP9
 D(7,3)=-Z*Z*HPP9/2.0d0/H
 A(7,4)= Z*Z*HPP7/2.0d0/H
 B(7,4)= 3.0d0*Z*FP7
 D(7,4)=-Z*Z*HPP7/2.0d0/H
 A(7,5)= Z*Z*HPP5/2.0d0/H
 B(7,5)= 4.0d0*Z*FP5
 D(7,5)=-Z*Z*HPP5/2.0d0/H
 A(7,6)= Z*Z*HPP3/2.0d0/H
 B(7,6)= 5.0d0*Z*FP3
 D(7,6)=-Z*Z*HPP3/2.0d0/H
 A(7,7)=-1.0d0/H2+Z*Z*HPP1/2.0d0/H
 B(7,7)=2.0d0/H2+6.0d0*Z*FP1
 D(7,7)=-1.0d0/H2-Z*Z*HPP1/2.0d0/H
 G(8)=(P15C(J+1)-2.0d0*P15C(J) + P15C(J-1))/H2
*+Z*Z*HPP1 *(P15C(J+1)-P15C(J-1))/2.0d0/H
*+Z*Z*HPP3 *(P13C(J+1)-P13C(J-1))/2.0d0/H
*+Z*Z*HPP5 *(P11C(J+1)-P11C(J-1))/2.0d0/H
*+Z*Z*HPP7 *( P9C(J+1)- P9C(J-1))/2.0d0/H
*+Z*Z*HPP9 *( P7C(J+1)- P7C(J-1))/2.0d0/H
*+Z*Z*HPP11*( P5C(J+1)- P5C(J-1))/2.0d0/H
*+Z*Z*HPP13*( P3C(J+1)- P3C(J-1))/2.0d0/H
*+Z*Z*HPP15*( P1C(J+1)- P1C(J-1))/2.0d0/H
*+Z*Z*Z*HPPP1 *(P15(J+1)-P15(J-1))/2.0d0/H/3.0d0
*+Z*Z*Z*HPPP3 *(P13(J+1)-P13(J-1))/2.0d0/H/3.0d0
*+Z*Z*Z*HPPP5 *(P11(J+1)-P11(J-1))/2.0d0/H/3.0d0
*+Z*Z*Z*HPPP7 *( P9(J+1)- P9(J-1))/2.0d0/H/3.0d0
*+Z*Z*Z*HPPP9 *( P7(J+1)- P7(J-1))/2.0d0/H/3.0d0
*+Z*Z*Z*HPPP11*( P5(J+1)- P5(J-1))/2.0d0/H/3.0d0
*+Z*Z*Z*HPPP13*( P3(J+1)- P3(J-1))/2.0d0/H/3.0d0
*+Z*Z*Z*HPPP15*( P1(J+1)- P1(J-1))/2.0d0/H/3.0d0
*-1.0d0*Z*FP13*P3C(J)-2.0d0*Z*FP11*P5C(J)*-3.0d0*Z*FP9*P7C(J)
*-4.0d0*Z*FP7*P9C(J)-5.0d0*Z*FP5*P11C(J)*-6.0d0*Z*FP3*P13C(J)
*-7.0d0*Z*FP1*P15C(J)-0.50d0*Z*Z*FPP13*P3(J)-1.0d0*Z*Z*FPP11*P5(J)
*-1.50d0*Z*Z*FPP9*P7(J)-2.0d0*Z*Z*FPP7*P9(J)-2.50d0*Z*Z*FPP5*P11(J)
*-3.0d0*Z*Z*FPP3*P13(J)-3.50d0*Z*Z*FPP1*P15(J)
 A(8,1)= Z*Z*HPP15/2.0d0/H
 B(8,1)= 0.0d0
 D(8,1)=-Z*Z*HPP15/2.0d0/H
 A(8,2)= Z*Z*HPP13/2.0d0/H
 B(8,2)= 1.0d0*Z*FP13
 D(8,2)=-Z*Z*HPP13/2.0d0/H
 A(8,3)= Z*Z*HPP11/2.0d0/H
 B(8,3)= 2.0d0*Z*FP11
 D(8,3)=-Z*Z*HPP11/2.0d0/H
 A(8,4)= Z*Z*HPP9/2.0d0/H
 B(8,4)= 3.0d0*Z*FP9
 D(8,4)=-Z*Z*HPP9/2.0d0/H
 A(8,5)= Z*Z*HPP7/2.0d0/H
 B(8,5)= 4.0d0*Z*FP7
 D(8,5)=-Z*Z*HPP7/2.0d0/H
 A(8,6)= Z*Z*HPP5/2.0d0/H
 B(8,6)= 5.0d0*Z*FP5
 D(8,6)=-Z*Z*HPP5/2.0d0/H
```

```
 A(8,7)= Z*Z*HPP3/2.0d0/H
 B(8,7)= 6.0d0*Z*FP3
 D(8,7)=-Z*Z*HPP3/2.0d0/H
 A(8,8)=-1.0d0/H2+Z*Z*HPP1/2.0d0/H
 B(8,8)=2.0d0/H2+7.0d0*Z*FP1
 D(8,8)=-1.0d0/H2-Z*Z*HPP1/2.0d0/H
 G(9)=(P17C(J+1)-2.0d0*P17C(J) + P17C(J-1))/H2
*+Z*Z*HPP1 *(P17C(J+1)-P17C(J-1))/2.0d0/H
*+Z*Z*HPP3 *(P15C(J+1)-P15C(J-1))/2.0d0/H
*+Z*Z*HPP5 *(P13C(J+1)-P13C(J-1))/2.0d0/H
*+Z*Z*HPP7 *(P11C(J+1)-P11C(J-1))/2.0d0/H
*+Z*Z*HPP9 *( P9C(J+1)- P9C(J-1))/2.0d0/H
*+Z*Z*HPP11*( P7C(J+1)- P7C(J-1))/2.0d0/H
*+Z*Z*HPP13*( P5C(J+1)- P5C(J-1))/2.0d0/H
*+Z*Z*HPP15*( P3C(J+1)- P3C(J-1))/2.0d0/H
*+Z*Z*HPP17*( P1C(J+1)- P1C(J-1))/2.0d0/H
*+Z*Z*Z*HPPP1 *(P17(J+1)-P17(J-1))/2.0d0/H/3.0d0
*+Z*Z*Z*HPPP3 *(P15(J+1)-P15(J-1))/2.0d0/H/3.0d0
*+Z*Z*Z*HPPP5 *(P13(J+1)-P13(J-1))/2.0d0/H/3.0d0
*+Z*Z*Z*HPPP7 *(P11(J+1)-P11(J-1))/2.0d0/H/3.0d0
*+Z*Z*Z*HPPP9 *( P9(J+1)- P9(J-1))/2.0d0/H/3.0d0
*+Z*Z*Z*HPPP11*( P7(J+1)- P7(J-1))/2.0d0/H/3.0d0
*+Z*Z*Z*HPPP13*( P5(J+1)- P5(J-1))/2.0d0/H/3.0d0
*+Z*Z*Z*HPPP15*( P3(J+1)- P3(J-1))/2.0d0/H/3.0d0
*+Z*Z*Z*HPPP17*( P1(J+1)- P1(J-1))/2.0d0/H/3.0d0
*-1.0d0*Z*FP15*P3C(J)-2.0d0*Z*FP13*P5C(J)-3.0d0*Z*FP11*P7C(J)
*-4.0d0*Z*FP9*P9C(J)-5.0d0*Z*FP7*P11C(J)-6.0d0*Z*FP5*P13C(J)
*-7.0d0*Z*FP3*P15C(J)-8.0d0*Z*FP1*P17C(J)-0.50d0*Z*Z*FPP15*P3(J)
*-1.0d0*Z*Z*FPP13*P5(J)-1.50d0*Z*Z*FPP11*P7(J)-2.0d0*Z*Z*FPP9*P9(J)
*-2.50d0*Z*Z*FPP7*P11(J)-3.0d0*Z*Z*FPP5*P13(J)
*-3.50d0*Z*Z*FPP3*P15(J)-4.00d0*Z*Z*FPP1*P17(J)
 A(9,1)= Z*Z*HPP17/2.0d0/H
 B(9,1)= 0.0d0
 D(9,1)=-Z*Z*HPP17/2.0d0/H
 A(9,2)= Z*Z*HPP15/2.0d0/H
 B(9,2)= 1.0d0*Z*FP15
 D(9,2)=-Z*Z*HPP15/2.0d0/H
 A(9,3)= Z*Z*HPP13/2.0d0/H
 B(9,3)= 2.0d0*Z*FP13
 D(9,3)=-Z*Z*HPP13/2.0d0/H
 A(9,4)= Z*Z*HPP11/2.0d0/H
 B(9,4)= 3.0d0*Z*FP11
 D(9,4)=-Z*Z*HPP11/2.0d0/H
 A(9,5)= Z*Z*HPP9/2.0d0/H
 B(9,5)= 4.0d0*Z*FP9
 D(9,5)=-Z*Z*HPP9/2.0d0/H
 A(9,6)= Z*Z*HPP7/2.0d0/H
 B(9,6)= 5.0d0*Z*FP7
 D(9,6)=-Z*Z*HPP7/2.0d0/H
 A(9,7)= Z*Z*HPP5/2.0d0/H
 B(9,7)= 6.0d0*Z*FP5
 D(9,7)=-Z*Z*HPP5/2.0d0/H
 A(9,8)= Z*Z*HPP3/2.0d0/H
 B(9,8)= 7.0d0*Z*FP3
 D(9,8)=-Z*Z*HPP3/2.0d0/H
```

```
 A(9,9)=-1.0d0/H2+Z*Z*HPP1/2.0d0/H
 B(9,9)=2.0d0/H2+8.0d0*Z*FP1
 D(9,9)=-1.0d0/H2-Z*Z*HPP1/2.0d0/H
 G(10)=(P19C(J+1)-2.0d0*P19C(J) + P19C(J-1))/H2
*+Z*Z*HPP1 *(P19C(J+1)-P19C(J-1))/2.0d0/H
*+Z*Z*HPP3 *(P17C(J+1)-P17C(J-1))/2.0d0/H
*+Z*Z*HPP5 *(P15C(J+1)-P15C(J-1))/2.0d0/H
*+Z*Z*HPP7 *(P13C(J+1)-P13C(J-1))/2.0d0/H
*+Z*Z*HPP9 *(P11C(J+1)-P11C(J-1))/2.0d0/H
*+Z*Z*HPP11*( P9C(J+1)- P9C(J-1))/2.0d0/H
*+Z*Z*HPP13*( P7C(J+1)- P7C(J-1))/2.0d0/H
*+Z*Z*HPP15*( P5C(J+1)- P5C(J-1))/2.0d0/H
*+Z*Z*HPP17*( P3C(J+1)- P3C(J-1))/2.0d0/H
*+Z*Z*HPP19*( P1C(J+1)- P1C(J-1))/2.0d0/H
*+Z*Z*Z*HPPP1 *(P19(J+1)-P19(J-1))/2.0d0/H/3.0d0
*+Z*Z*Z*HPPP3 *(P17(J+1)-P17(J-1))/2.0d0/H/3.0d0
*+Z*Z*Z*HPPP5 *(P15(J+1)-P15(J-1))/2.0d0/H/3.0d0
*+Z*Z*Z*HPPP7 *(P13(J+1)-P13(J-1))/2.0d0/H/3.0d0
*+Z*Z*Z*HPPP9 *(P11(J+1)-P11(J-1))/2.0d0/H/3.0d0
*+Z*Z*Z*HPPP11*( P9(J+1)- P9(J-1))/2.0d0/H/3.0d0
*+Z*Z*Z*HPPP13*( P7(J+1)- P7(J-1))/2.0d0/H/3.0d0
*+Z*Z*Z*HPPP15*( P5(J+1)- P5(J-1))/2.0d0/H/3.0d0
*+Z*Z*Z*HPPP17*( P3(J+1)- P3(J-1))/2.0d0/H/3.0d0
*+Z*Z*Z*HPPP19*( P1(J+1)- P1(J-1))/2.0d0/H/3.0d0
*-1.0d0*Z*FP17*P3C(J)-2.0d0*Z*FP15*P5C(J)-3.0d0*Z*FP13*P7C(J)
*-4.0d0*Z*FP11*P9C(J)-5.0d0*Z*FP9*P11C(J)-6.0d0*Z*FP7*P13C(J)
*-7.0d0*Z*FP5*P15C(J)-8.0d0*Z*FP3*P17C(J)-9.0d0*Z*FP1*P19C(J)
*-0.50d0*Z*Z*FPP17*P3(J)-1.00d0*Z*Z*FPP15*P5(J)
*-1.50d0*Z*Z*FPP13*P7(J)-2.00d0*Z*Z*FPP11*P9(J)
*-2.50d0*Z*Z*FPP9*P11(J)-3.00d0*Z*Z*FPP7*P13(J)
*-3.50d0*Z*Z*FPP5*P15(J)-4.00d0*Z*Z*FPP3*P17(J)
*-4.50d0*Z*Z*FPP1 * P19(J)
 A(10,1)= Z*Z*HPP19/2.0d0/H
 B(10,1)= 0.0d0
 D(10,1)=-Z*Z*HPP19/2.0d0/H
 A(10,2)= Z*Z*HPP17/2.0d0/H
 B(10,2)= 1.0d0*Z*FP17
 D(10,2)=-Z*Z*HPP17/2.0d0/H
 A(10,3)= Z*Z*HPP15/2.0d0/H
 B(10,3)= 2.0d0*Z*FP15
 D(10,3)=-Z*Z*HPP15/2.0d0/H
 A(10,4)= Z*Z*HPP13/2.0d0/H
 B(10,4)= 3.0d0*Z*FP13
 D(10,4)=-Z*Z*HPP13/2.0d0/H
 A(10,5)= Z*Z*HPP11/2.0d0/H
 B(10,5)= 4.0d0*Z*FP11
 D(10,5)=-Z*Z*HPP11/2.0d0/H
 A(10,6)= Z*Z*HPP9/2.0d0/H
 B(10,6)= 5.0d0*Z*FP9
 D(10,6)=-Z*Z*HPP9/2.0d0/H
 A(10,7)= Z*Z*HPP7/2.0d0/H
 B(10,7)= 6.0d0*Z*FP7
 D(10,7)=-Z*Z*HPP7/2.0d0/H
 A(10,8)= Z*Z*HPP5/2.0d0/H
 B(10,8)= 7.0d0*Z*FP5
```

```
 D(10,8)=-Z*Z*HPP5/2.0d0/H
 A(10,9)= Z*Z*HPP3/2.0d0/H
 B(10,9)= 8.0d0*Z*FP3
 D(10,9)=-Z*Z*HPP3/2.0d0/H
 A(10,10)=-1.0d0/H2+Z*Z*HPP1/2.0d0/H
 B(10,10)=2.0d0/H2+9.0d0*Z*FP1
 D(10,10)=-1.0d0/H2-Z*Z*HPP1/2.0d0/H
 G(11)=(P21C(J+1)-2.0d0*P21C(J) + P21C(J-1))/H2
*+Z*Z*HPP1 *(P21C(J+1)-P21C(J-1))/2.0d0/H
*+Z*Z*HPP3 *(P19C(J+1)-P19C(J-1))/2.0d0/H
*+Z*Z*HPP5 *(P17C(J+1)-P17C(J-1))/2.0d0/H
*+Z*Z*HPP7 *(P15C(J+1)-P15C(J-1))/2.0d0/H
*+Z*Z*HPP9 *(P13C(J+1)-P13C(J-1))/2.0d0/H
*+Z*Z*HPP11*(P11C(J+1)-P11C(J-1))/2.0d0/H
*+Z*Z*HPP13*( P9C(J+1)- P9C(J-1))/2.0d0/H
*+Z*Z*HPP15*( P7C(J+1)- P7C(J-1))/2.0d0/H
*+Z*Z*HPP17*( P5C(J+1)- P5C(J-1))/2.0d0/H
*+Z*Z*HPP19*( P3C(J+1)- P3C(J-1))/2.0d0/H
*+Z*Z*HPP21*( P1C(J+1)- P1C(J-1))/2.0d0/H
*+Z*Z*Z*HPPP1 *(P21(J+1)-P21(J-1))/2.0d0/H/3.0d0
*+Z*Z*Z*HPPP3 *(P19(J+1)-P19(J-1))/2.0d0/H/3.0d0
*+Z*Z*Z*HPPP5 *(P17(J+1)-P17(J-1))/2.0d0/H/3.0d0
*+Z*Z*Z*HPPP7 *(P15(J+1)-P15(J-1))/2.0d0/H/3.0d0
*+Z*Z*Z*HPPP9 *(P13(J+1)-P13(J-1))/2.0d0/H/3.0d0
*+Z*Z*Z*HPPP11*(P11(J+1)-P11(J-1))/2.0d0/H/3.0d0
*+Z*Z*Z*HPPP13*( P9(J+1)- P9(J-1))/2.0d0/H/3.0d0
*+Z*Z*Z*HPPP15*( P7(J+1)- P7(J-1))/2.0d0/H/3.0d0
*+Z*Z*Z*HPPP17*( P5(J+1)- P5(J-1))/2.0d0/H/3.0d0
*+Z*Z*Z*HPPP19*( P3(J+1)- P3(J-1))/2.0d0/H/3.0d0
*+Z*Z*Z*HPPP21*( P1(J+1)- P1(J-1))/2.0d0/H/3.0d0
*-1.0d0*Z*FP19*P3C(J)-2.0d0*Z*FP17*P5C(J)-3.0d0*Z*FP15*P7C(J)
*-4.0d0*Z*FP13*P9C(J)-5.0d0*Z*FP11*P11C(J)-6.0d0*Z*FP9*P13C(J)
*-7.0d0*Z*FP7*P15C(J)-8.0d0*Z*FP5*P17C(J)-9.0d0*Z*FP3*P19C(J)
*-10.0d0*Z*FP1*P21C(J)-0.50d0*Z*Z*FPP19*P3(J)
*-1.00d0*Z*Z*FPP17*P5(J)-1.50d0*Z*Z*FPP15*P7(J)
*-2.00d0*Z*Z*FPP13*P9(J)-2.50d0*Z*Z*FPP11*P11(J)
*-3.00d0*Z*Z*FPP9*P13(J)-3.50d0*Z*Z*FPP7*P15(J)
*-4.00d0*Z*Z*FPP5*P17(J)-4.50d0*Z*Z*FPP3*P19(J)
*-5.00d0*Z*Z*FPP1 * P21(J)
 A(11,1)= Z*Z*HPP21/2.0d0/H
 B(11,1)= 0.0d0
 D(11,1)=-Z*Z*HPP21/2.0d0/H
 A(11,2)= Z*Z*HPP19/2.0d0/H
 B(11,2)= 1.0d0*Z*FP19
 D(11,2)=-Z*Z*HPP19/2.0d0/H
 A(11,3)= Z*Z*HPP17/2.0d0/H
 B(11,3)= 2.0d0*Z*FP17
 D(11,3)=-Z*Z*HPP17/2.0d0/H
 A(11,4)= Z*Z*HPP15/2.0d0/H
 B(11,4)= 3.0d0*Z*FP15
 D(11,4)=-Z*Z*HPP15/2.0d0/H
 A(11,5)= Z*Z*HPP13/2.0d0/H
 B(11,5)= 4.0d0*Z*FP13
 D(11,5)=-Z*Z*HPP13/2.0d0/H
 A(11,6)= Z*Z*HPP11/2.0d0/H
```

```
 B(11,6)= 5.0d0*Z*FP11
 D(11,6)=-Z*Z*HPP11/2.0d0/H
 A(11,7)= Z*Z*HPP9/2.0d0/H
 B(11,7)= 6.0d0*Z*FP9
 D(11,7)=-Z*Z*HPP9/2.0d0/H
 A(11,8)= Z*Z*HPP7/2.0d0/H
 B(11,8)= 7.0d0*Z*FP7
 D(11,8)=-Z*Z*HPP7/2.0d0/H
 A(11,9)= Z*Z*HPP5/2.0d0/H
 B(11,9)= 8.0d0*Z*FP5
 D(11,9)=-Z*Z*HPP5/2.0d0/H
 A(11,10)= Z*Z*HPP3/2.0d0/H
 B(11,10)= 9.0d0*Z*FP3
 D(11,10)=-Z*Z*HPP3/2.0d0/H
 A(11,11)=-1.0d0/H2+Z*Z*HPP1/2.0d0/H
 B(11,11)=2.0d0/H2+10.0d0*Z*FP1
 D(11,11)=-1.0d0/H2-Z*Z*HPP1/2.0d0/H
 G(12)=(P23C(J+1)-2.0d0*P23C(J) + P23C(J-1))/H2
*+Z*Z*HPP1 *(P23C(J+1)-P23C(J-1))/2.0d0/H
*+Z*Z*HPP3 *(P21C(J+1)-P21C(J-1))/2.0d0/H
*+Z*Z*HPP5 *(P19C(J+1)-P19C(J-1))/2.0d0/H
*+Z*Z*HPP7 *(P17C(J+1)-P17C(J-1))/2.0d0/H
*+Z*Z*HPP9 *(P15C(J+1)-P15C(J-1))/2.0d0/H
*+Z*Z*HPP11*(P13C(J+1)-P13C(J-1))/2.0d0/H
*+Z*Z*HPP13*(P11C(J+1)-P11C(J-1))/2.0d0/H
*+Z*Z*HPP15*( P9C(J+1)- P9C(J-1))/2.0d0/H
*+Z*Z*HPP17*( P7C(J+1)- P7C(J-1))/2.0d0/H
*+Z*Z*HPP19*( P5C(J+1)- P5C(J-1))/2.0d0/H
*+Z*Z*HPP21*( P3C(J+1)- P3C(J-1))/2.0d0/H
*+Z*Z*HPP23*( P1C(J+1)- P1C(J-1))/2.0d0/H
*+Z*Z*Z*HPPP1 *(P23(J+1)-P23(J-1))/2.0d0/H/3.0d0
*+Z*Z*Z*HPPP3 *(P21(J+1)-P21(J-1))/2.0d0/H/3.0d0
*+Z*Z*Z*HPPP5 *(P19(J+1)-P19(J-1))/2.0d0/H/3.0d0
*+Z*Z*Z*HPPP7 *(P17(J+1)-P17(J-1))/2.0d0/H/3.0d0
*+Z*Z*Z*HPPP9 *(P15(J+1)-P15(J-1))/2.0d0/H/3.0d0
*+Z*Z*Z*HPPP11*(P13(J+1)-P13(J-1))/2.0d0/H/3.0d0
*+Z*Z*Z*HPPP13*(P11(J+1)-P11(J-1))/2.0d0/H/3.0d0
*+Z*Z*Z*HPPP15*( P9(J+1)- P9(J-1))/2.0d0/H/3.0d0
*+Z*Z*Z*HPPP17*( P7(J+1)- P7(J-1))/2.0d0/H/3.0d0
*+Z*Z*Z*HPPP19*( P5(J+1)- P5(J-1))/2.0d0/H/3.0d0
*+Z*Z*Z*HPPP21*( P3(J+1)- P3(J-1))/2.0d0/H/3.0d0
*+Z*Z*Z*HPPP23*( P1(J+1)- P1(J-1))/2.0d0/H/3.0d0
*-1.0d0*Z*FP21*P3C(J)-2.0d0*Z*FP19*P5C(J)-3.0d0*Z*FP17*P7C(J)
*-4.0d0*Z*FP15*P9C(J)-5.0d0*Z*FP13*P11C(J)-6.0d0*Z*FP11* P13C(J)
*-7.0d0*Z*FP9*P15C(J)-8.0d0*Z*FP7*P17C(J)-9.0d0*Z*FP5*P19C(J)
*-10.0d0*Z*FP3*P21C(J)-11.0d0*Z*FP1*P23C(J)
*-0.50d0*Z*Z*FPP21*P3(J)-1.0d0*Z*Z*FPP19*P5(J)
*-1.50d0*Z*Z*FPP17*P7(J)-2.00d0*Z*Z*FPP15*P9(J)
*-2.50d0*Z*Z*FPP13*P11(J)-3.0d0*Z*Z*FPP11*P13(J)
*-3.50d0*Z*Z*FPP9*P15(J)-4.0d0*Z*Z*FPP7*P17(J)
*-4.50d0*Z*Z*FPP5*P19(J)-5.00d0*Z*Z*FPP3*P21(J)
*-5.50d0*Z*Z*FPP1*P23(J)
 A(12,1)= Z*Z*HPP23/2.0d0/H
 B(12,1)= 0.0d0
 D(12,1)=-Z*Z*HPP23/2.0d0/H
```

```
 A(12,2)= Z*Z*HPP21/2.0d0/H
 B(12,2)= 1.0d0*Z*FP21
 D(12,2)=-Z*Z*HPP21/2.0d0/H
 A(12,3)= Z*Z*HPP19/2.0d0/H
 B(12,3)= 2.0d0*Z*FP19
 D(12,3)=-Z*Z*HPP19/2.0d0/H
 A(12,4)= Z*Z*HPP17/2.0d0/H
 B(12,4)= 3.0d0*Z*FP17
 D(12,4)=-Z*Z*HPP17/2.0d0/H
 A(12,5)= Z*Z*HPP15/2.0d0/H
 B(12,5)= 4.0d0*Z*FP15
 D(12,5)=-Z*Z*HPP15/2.0d0/H
 A(12,6)= Z*Z*HPP13/2.0d0/H
 B(12,6)= 5.0d0*Z*FP13
 D(12,6)=-Z*Z*HPP13/2.0d0/H
 A(12,7)= Z*Z*HPP11/2.0d0/H
 B(12,7)= 6.0d0*Z*FP11
 D(12,7)=-Z*Z*HPP11/2.0d0/H
 A(12,8)= Z*Z*HPP9/2.0d0/H
 B(12,8)= 7.0d0*Z*FP9
 D(12,8)=-Z*Z*HPP9/2.0d0/H
 A(12,9)= Z*Z*HPP7/2.0d0/H
 B(12,9)= 8.0d0*Z*FP7
 D(12,9)=-Z*Z*HPP7/2.0d0/H
 A(12,10)= Z*Z*HPP5/2.0d0/H
 B(12,10)= 9.0d0*Z*FP5
 D(12,10)=-Z*Z*HPP5/2.0d0/H
 A(12,11)= Z*Z*HPP3/2.0d0/H
 B(12,11)= 10.0d0*Z*FP3
 D(12,11)=-Z*Z*HPP3/2.0d0/H
 A(12,12)=-1.0d0/H2+Z*Z*HPP1/2.0d0/H
 B(12,12)=2.0d0/H2+11.0d0*Z*FP1
 D(12,12)=-1.0d0/H2-Z*Z*HPP1/2.0d0/H
 G(13)=(P25C(J+1)-2.0d0*P25C(J) + P25C(J-1))/H2
*+Z*Z*HPP1 *(P25C(J+1)-P25C(J-1))/2.0d0/H
*+Z*Z*HPP3 *(P23C(J+1)-P23C(J-1))/2.0d0/H
*+Z*Z*HPP5 *(P21C(J+1)-P21C(J-1))/2.0d0/H
*+Z*Z*HPP7 *(P19C(J+1)-P19C(J-1))/2.0d0/H
*+Z*Z*HPP9 *(P17C(J+1)-P17C(J-1))/2.0d0/H
*+Z*Z*HPP11*(P15C(J+1)-P15C(J-1))/2.0d0/H
*+Z*Z*HPP13*(P13C(J+1)-P13C(J-1))/2.0d0/H
*+Z*Z*HPP15*(P11C(J+1)-P11C(J-1))/2.0d0/H
*+Z*Z*HPP17*( P9C(J+1)- P9C(J-1))/2.0d0/H
*+Z*Z*HPP19*( P7C(J+1)- P7C(J-1))/2.0d0/H
*+Z*Z*HPP21*( P5C(J+1)- P5C(J-1))/2.0d0/H
*+Z*Z*HPP23*( P3C(J+1)- P3C(J-1))/2.0d0/H
*+Z*Z*HPP25*( P1C(J+1)- P1C(J-1))/2.0d0/H
*+Z*Z*Z*HPPP1 *(P25(J+1)-P25(J-1))/2.0d0/H/3.0d0
*+Z*Z*Z*HPPP3 *(P23(J+1)-P23(J-1))/2.0d0/H/3.0d0
*+Z*Z*Z*HPPP5 *(P21(J+1)-P21(J-1))/2.0d0/H/3.0d0
*+Z*Z*Z*HPPP7 *(P19(J+1)-P19(J-1))/2.0d0/H/3.0d0
*+Z*Z*Z*HPPP9 *(P17(J+1)-P17(J-1))/2.0d0/H/3.0d0
*+Z*Z*Z*HPPP11*(P15(J+1)-P15(J-1))/2.0d0/H/3.0d0
*+Z*Z*Z*HPPP13*(P13(J+1)-P13(J-1))/2.0d0/H/3.0d0
*+Z*Z*Z*HPPP15*(P11(J+1)-P11(J-1))/2.0d0/H/3.0d0
```

```
*+Z*Z*Z*HPPP17*( P9(J+1)- P9(J-1))/2.0d0/H/3.0d0
*+Z*Z*Z*HPPP19*( P7(J+1)- P7(J-1))/2.0d0/H/3.0d0
*+Z*Z*Z*HPPP21*( P5(J+1)- P5(J-1))/2.0d0/H/3.0d0
*+Z*Z*Z*HPPP23*( P3(J+1)- P3(J-1))/2.0d0/H/3.0d0
*+Z*Z*Z*HPPP25*( P1(J+1)- P1(J-1))/2.0d0/H/3.0d0
*-1.0d0*Z*FP23*P3C(J)-2.0d0*Z*FP21*P5C(J)-3.0d0*Z*FP19*P7C(J)
*-4.0d0*Z*FP17*P9C(J)-5.0d0*Z*FP15*P11C(J)-6.0d0*Z*FP13*P13C(J)
*-7.0d0*Z*FP11*P15C(J)-8.0d0*Z*FP9*P17C(J)-9.0d0*Z*FP7*P19C(J)
*-10.0d0*Z*FP5*P21C(J)-11.0d0*Z*FP3*P23C(J)-12.0d0*Z*FP1*P25C(J)
*-0.50d0*Z*Z*FPP23*P3(J)-1.00d0*Z*Z*FPP21*P5(J)
*-1.50d0*Z*Z*FPP19*P7(J)-2.00d0*Z*Z*FPP17*P9(J)
*-2.50d0*Z*Z*FPP15*P11(J)-3.00d0*Z*Z*FPP13*P13(J)
*-3.50d0*Z*Z*FPP11*P15(J)-4.00d0*Z*Z*FPP9*P17(J)
*-4.50d0*Z*Z*FPP7*P19(J)-5.00d0*Z*Z*FPP5*P21(J)
*-5.50d0*Z*Z*FPP3*P23(J)-6.00d0*Z*Z*FPP1*P25(J)
 A(13,1)= Z*Z*HPP25/2.0d0/H
 B(13,1)= 0.0d0
 D(13,1)=-Z*Z*HPP25/2.0d0/H
 A(13,2)= Z*Z*HPP23/2.0d0/H
 B(13,2)= 1.0d0*Z*FP23
 D(13,2)=-Z*Z*HPP23/2.0d0/H
 A(13,3)= Z*Z*HPP21/2.0d0/H
 B(13,3)= 2.0d0*Z*FP21
 D(13,3)=-Z*Z*HPP21/2.0d0/H
 A(13,4)= Z*Z*HPP19/2.0d0/H
 B(13,4)= 3.0d0*Z*FP19
 D(13,4)=-Z*Z*HPP19/2.0d0/H
 A(13,5)= Z*Z*HPP17/2.0d0/H
 B(13,5)= 4.0d0*Z*FP17
 D(13,5)=-Z*Z*HPP17/2.0d0/H
 A(13,6)= Z*Z*HPP15/2.0d0/H
 B(13,6)= 5.0d0*Z*FP15
 D(13,6)=-Z*Z*HPP15/2.0d0/H
 A(13,7)= Z*Z*HPP13/2.0d0/H
 B(13,7)= 6.0d0*Z*FP13
 D(13,7)=-Z*Z*HPP13/2.0d0/H
 A(13,8)= Z*Z*HPP11/2.0d0/H
 B(13,8)= 7.0d0*Z*FP11
 D(13,8)=-Z*Z*HPP11/2.0d0/H
 A(13,9)= Z*Z*HPP9/2.0d0/H
 B(13,9)= 8.0d0*Z*FP9
 D(13,9)=-Z*Z*HPP9/2.0d0/H
 A(13,10)= Z*Z*HPP7/2.0d0/H
 B(13,10)= 9.0d0*Z*FP7
 D(13,10)=-Z*Z*HPP7/2.0d0/H
 A(13,11)= Z*Z*HPP5/2.0d0/H
 B(13,11)= 10.0d0*Z*FP5
 D(13,11)=-Z*Z*HPP5/2.0d0/H
 A(13,12)= Z*Z*HPP3/2.0d0/H
 B(13,12)= 11.0d0*Z*FP3
 D(13,12)=-Z*Z*HPP3/2.0d0/H
 A(13,13)=-1.0d0/H2+Z*Z*HPP1/2.0d0/H
 B(13,13)=2.0d0/H2+12.0d0*Z*FP1
 D(13,13)=-1.0d0/H2-Z*Z*HPP1/2.0d0/H
 G(14)=(P27C(J+1)-2.0d0*P27C(J) + P27C(J-1))/H2
```

```
*+Z*Z*HPP1 *(P27C(J+1)-P27C(J-1))/2.0d0/H
*+Z*Z*HPP3 *(P25C(J+1)-P25C(J-1))/2.0d0/H
*+Z*Z*HPP5 *(P23C(J+1)-P23C(J-1))/2.0d0/H
*+Z*Z*HPP7 *(P21C(J+1)-P21C(J-1))/2.0d0/H
*+Z*Z*HPP9 *(P19C(J+1)-P19C(J-1))/2.0d0/H
*+Z*Z*HPP11*(P17C(J+1)-P17C(J-1))/2.0d0/H
*+Z*Z*HPP13*(P15C(J+1)-P15C(J-1))/2.0d0/H
*+Z*Z*HPP15*(P13C(J+1)-P13C(J-1))/2.0d0/H
*+Z*Z*HPP17*(P11C(J+1)-P11C(J-1))/2.0d0/H
*+Z*Z*HPP19*( P9C(J+1)- P9C(J-1))/2.0d0/H
*+Z*Z*HPP21*( P7C(J+1)- P7C(J-1))/2.0d0/H
*+Z*Z*HPP23*( P5C(J+1)- P5C(J-1))/2.0d0/H
*+Z*Z*HPP25*( P3C(J+1)- P3C(J-1))/2.0d0/H
*+Z*Z*HPP27*( P1C(J+1)- P1C(J-1))/2.0d0/H
*+Z*Z*Z*HPPP1 *(P27(J+1)-P27(J-1))/2.0d0/H/3.0d0
*+Z*Z*Z*HPPP3 *(P25(J+1)-P25(J-1))/2.0d0/H/3.0d0
*+Z*Z*Z*HPPP5 *(P23(J+1)-P23(J-1))/2.0d0/H/3.0d0
*+Z*Z*Z*HPPP7 *(P21(J+1)-P21(J-1))/2.0d0/H/3.0d0
*+Z*Z*Z*HPPP9 *(P19(J+1)-P19(J-1))/2.0d0/H/3.0d0
*+Z*Z*Z*HPPP11*(P17(J+1)-P17(J-1))/2.0d0/H/3.0d0
*+Z*Z*Z*HPPP13*(P15(J+1)-P15(J-1))/2.0d0/H/3.0d0
*+Z*Z*Z*HPPP15*(P13(J+1)-P13(J-1))/2.0d0/H/3.0d0
*+Z*Z*Z*HPPP17*(P11(J+1)-P11(J-1))/2.0d0/H/3.0d0
*+Z*Z*Z*HPPP19*( P9(J+1)- P9(J-1))/2.0d0/H/3.0d0
*+Z*Z*Z*HPPP21*( P7(J+1)- P7(J-1))/2.0d0/H/3.0d0
*+Z*Z*Z*HPPP23*( P5(J+1)- P5(J-1))/2.0d0/H/3.0d0
*+Z*Z*Z*HPPP25*( P3(J+1)- P3(J-1))/2.0d0/H/3.0d0
*+Z*Z*Z*HPPP27*( P1(J+1)- P1(J-1))/2.0d0/H/3.0d0
*-1.0d0*Z*FP25*P3C(J)-2.0d0*Z*FP23*P5C(J)-3.0d0*Z*FP21*P7C(J)
*-4.0d0*Z*FP19*P9C(J)-5.0d0*Z*FP17*P11C(J)-6.0d0*Z*FP15*P13C(J)
*-7.0d0*Z*FP13*P15C(J)-8.0d0*Z*FP11*P17C(J)-9.0d0*Z*FP9*P19C(J)
*-10.0d0*Z*FP7*P21C(J)-11.0d0*Z*FP5*P23C(J)-12.0d0*Z*FP3*P25C(J)
*-13.0d0*Z*FP1*P27C(J)
*-0.50d0*Z*Z*FPP25*P3(J)-1.00d0*Z*Z*FPP23*P5(J)
*-1.50d0*Z*Z*FPP21*P7(J)-2.00d0*Z*Z*FPP19*P9(J)
*-2.50d0*Z*Z*FPP17*P11(J)-3.00d0*Z*Z*FPP15*P13(J)
*-3.50d0*Z*Z*FPP13*P15(J)-4.00d0*Z*Z*FPP11*P17(J)
*-4.50d0*Z*Z*FPP9*P19(J)-5.00d0*Z*Z*FPP7*P21(J)
*-5.50d0*Z*Z*FPP5*P23(J)-6.00d0*Z*Z*FPP3*P25(J)
*-6.50d0*Z*Z*FPP1*P25(J)
 A(14,1)= Z*Z*HPP27/2.0d0/H
 B(14,1)= 0.0d0
 D(14,1)=-Z*Z*HPP27/2.0d0/H
 A(14,2)= Z*Z*HPP25/2.0d0/H
 B(14,2)= 1.0d0*Z*FP25
 D(14,2)=-Z*Z*HPP25/2.0d0/H
 A(14,3)= Z*Z*HPP23/2.0d0/H
 B(14,3)= 2.0d0*Z*FP23
 D(14,3)=-Z*Z*HPP23/2.0d0/H
 A(14,4)= Z*Z*HPP21/2.0d0/H
 B(14,4)= 3.0d0*Z*FP21
 D(14,4)=-Z*Z*HPP21/2.0d0/H
 A(14,5)= Z*Z*HPP19/2.0d0/H
 B(14,5)= 4.0d0*Z*FP19
 D(14,5)=-Z*Z*HPP19/2.0d0/H
```

```
      A(14,6)= Z*Z*HPP17/2.0d0/H
      B(14,6)= 5.0d0*Z*FP17
      D(14,6)=-Z*Z*HPP17/2.0d0/H
      A(14,7)= Z*Z*HPP15/2.0d0/H
      B(14,7)= 6.0d0*Z*FP15
      D(14,7)=-Z*Z*HPP15/2.0d0/H
      A(14,8)= Z*Z*HPP13/2.0d0/H
      B(14,8)= 7.0d0*Z*FP13
      D(14,8)=-Z*Z*HPP13/2.0d0/H
      A(14,9)= Z*Z*HPP11/2.0d0/H
      B(14,9)= 8.0d0*Z*FP11
      D(14,9)=-Z*Z*HPP11/2.0d0/H
      A(14,10)= Z*Z*HPP9/2.0d0/H
      B(14,10)= 9.0d0*Z*FP9
      D(14,10)=-Z*Z*HPP9/2.0d0/H
      A(14,11)= Z*Z*HPP7/2.0d0/H
      B(14,11)= 10.0d0*Z*FP7
      D(14,11)=-Z*Z*HPP7/2.0d0/H
      A(14,12)= Z*Z*HPP5/2.0d0/H
      B(14,12)= 11.0d0*Z*FP5
      D(14,12)=-Z*Z*HPP5/2.0d0/H
      A(14,13)= Z*Z*HPP3/2.0d0/H
      B(14,13)= 12.0d0*Z*FP3
      D(14,13)=-Z*Z*HPP3/2.0d0/H
      A(14,14)=-1.0d0/H2+Z*Z*HPP1/2.0d0/H
      B(14,14)=2.0d0/H2+13.0d0*Z*FP1
      D(14,14)=-1.0d0/H2-Z*Z*HPP1/2.0d0/H
      RETURN
      END
!****************** SUBROUTINE BC2PALLSC*********************
      SUBROUTINE BC2PALLSC(J,C,P1C,P3C,P5C,P7C,P9C,P11C,
     *                  P13C,P15C,P17C,P19C,P21C,P23C,P25C,P27C)
      IMPLICIT REAL*8 (A-H,O-Z)
      IMPLICIT INTEGER (I-N)
      COMMON/BA/A(14,14),B(14,14),D(14,29),G(14),X(14,14),Y(14,14),N,NJ
      DOUBLE PRECISION C(14,*)
      DOUBLE PRECISION P1C(*),P3C(*),P5C(*),P7C(*),P9C(*),P11C(*)
      DOUBLE PRECISION P13C(*),P15C(*),P17C(*),P19C(*)
      DOUBLE PRECISION P21C(*),P23C(*),P25C(*),P27C(*)
      DO i=1,N
          DO jj=1,N
              A(i,jj)=0.0d0
              B(i,jj)=0.0d0
              D(i,jj)=0.0d0
          END DO
      END DO
          G(1)=0.0d0-P1C(J)
          B(1,1)=1.0d0
          G(2)=0.0d0-P3C(J)
          B(2,2)=1.0d0
          G(3)=0.0d0-P5C(J)
          B(3,3)=1.0d0
          G(4)=0.0d0-P7C(J)
          B(4,4)=1.0d0
          G(5)=0.0d0-P9C(J)
```

```
        B(5,5)=1.0d0
        G(6)=0.0d0-P11C(J)
        B(6,6)=1.0d0
        G(7)=0.0d0-P13C(J)
        B(7,7)=1.0d0
        G(8)=0.0d0-P15C(J)
        B(8,8)=1.0d0
        G(9)=0.0d0-P17C(J)
        B(9,9)=1.0d0
        G(10)=0.0d0-P19C(J)
        B(10,10)=1.0d0
        G(11)=0.0d0-P21C(J)
        B(11,11)=1.0d0
        G(12)=0.0d0-P23C(J)
        B(12,12)=1.0d0
        G(13)=0.0d0-P25C(J)
        B(13,13)=1.0d0
        G(14)=0.0d0-P27C(J)
        B(14,14)=1.0d0
    RETURN
    END
!*************** SUBROUTINE GETMAXG_CONC**********************
    SUBROUTINE GETMAXG_CONC(NJ,NJP,DP,maxval)
    INTEGER NJ,NJP
    DOUBLE PRECISION DP(14,*), maxval
    NJP=1
    maxval=0.0d0
    DO 20 j=1,14
        DO 10 i=2,NJ-1
            IF (dabs(DP(j,i)).GT.maxval) THEN
                maxval=dabs(DP(j,i))
                NJP=i
            END IF
10       CONTINUE
20    CONTINUE
    RETURN
    END
```

D.1.3 Include Files

In this section, all the include files which are called in the main program as well as in various subroutimes are listed here.

```
!********** INCLUDE FILE PALL.f for main program ************
    maxvalG=1.0d0
    DO I=1,N
        DO K=1,N
            X(I,K)=0.0d0
            Y(I,K)=0.0d0
        END DO
    END DO
    JJ= 1
110 J=0
```

```
360 J=J+1
    SUMH=SUMH+H
    DO I=1,N
        G(I)=0.0d0
        DO K=1,N
            A(I,K)=0.0d0
            B(I,K)=0.0d0
            D(I,K)=0.0d0
        ENDDO
    ENDDO
!   Call BC1PALL for J=1
    IF(J.EQ.1) CALL BC1PALL(J,C,P1,P3,P5,P7,P9,P11,P13,P15,P17,P19,P21
   *              ,P23,P25,P27)
!   Equation for interior region
    IF((J.GT.1).AND.(J.LT.NJ)) THEN
    CALL INNERPALL(J,C,P1,P3,P5,P7,P9,P11,P13,P15,P17,P19,P21
   *                  ,P23,P25,P27)
    END IF
!   Equation for second boundary condition C
    IF (J.EQ.NJ)  THEN
    CALL BC2PALL(J,C,P1,P3,P5,P7,P9,P11,P13,P15,P17,P19,P21
   *                  ,P23,P25,P27)
    END IF
    CALL BAND(J,C)
    IF(J.NE.NJ) GOTO 360
    DO I=1,NJ
        P1(I) =P1(I) +C(1,I)
        P3(I) =P3(I) +C(2,I)
        P5(I) =P5(I) +C(3,I)
        P7(I) =P7(I) +C(4,I)
        P9(I) =P9(I) +C(5,I)
        P11(I)=P11(I)+C(6,I)
        P13(I)=P13(I)+C(7,I)
        P15(I)=P15(I)+C(8,I)
        P17(I)=P17(I)+C(9,I)
        P19(I)=P19(I)+C(10,I)
        P21(I)=P21(I)+C(11,I)
        P23(I)=P23(I)+C(12,I)
        P25(I)=P25(I)+C(13,I)
        P27(I)=P27(I)+C(14,I)
    END DO
    INCLUDE 'CHECKCONVERGE.f'
    JJ=JJ+1
    IF ((maxvalG.GT.ERRSUB).AND.(JJ.LT.ITMAX)) GO TO 110
    maxvalG=1.0d0
    DO I=1,N
        DO K=1,N
            X(I,K)=0.0d0
            Y(I,K)=0.0d0
        END DO
    END DO
    JJ= 1
111 J=0
361 J=J+1
    SUMH=SUMH+H
```

```
      DO I=1,N
          G(I)=0.0d0
          DO K=1,N
              A(I,K)=0.0d0
              B(I,K)=0.0d0
              D(I,K)=0.0d0
          ENDDO
      ENDDO
!     Call BC1PALLSC for J=1 C
      IF(J.EQ.1) CALL BC1PALLSC(J,C,P1C,P3C,P5C,P7C,P9C,P11C,P13C,
     *                  P15C,P17C,P19C,P21C,P23C,P25C,P27C)
!     Equation for interior region C
      IF((J.GT.1).AND.(J.LT.NJ)) THEN
      CALL INNERPALLSC(J,C,P1,P3,P5,P7,P9,P11,P13,P15,P17,P19,
     *               P21,P23,P25,P27,P1C,P3C,P5C,P7C,P9C,P11C,
     *                P13C,P15C,P17C,P19C,P21C,P23C,P25C,P27C)
      END IF
!     Equation for second boundary condition C
      IF (J.EQ.NJ)  THEN
      CALL BC2PALLSC(J,C,P1C,P3C,P5C,P7C,P9C,P11C,
     *             P13C,P15C,P17C,P19C,P21C,P23C,P25C,P27C)
      END IF
      CALL BAND(J,C)
      IF(J.NE.NJ) GOTO 361
      DO I=1,NJ
          P1C(I) =P1C(I) +C(1,I)
          P3C(I) =P3C(I) +C(2,I)
          P5C(I) =P5C(I) +C(3,I)
          P7C(I) =P7C(I) +C(4,I)
          P9C(I) =P9C(I) +C(5,I)
          P11C(I)=P11C(I)+C(6,I)
          P13C(I)=P13C(I)+C(7,I)
          P15C(I)=P15C(I)+C(8,I)
          P17C(I)=P17C(I)+C(9,I)
          P19C(I)=P19C(I)+C(10,I)
          P21C(I)=P21C(I)+C(11,I)
          P23C(I)=P23C(I)+C(12,I)
          P25C(I)=P25C(I)+C(13,I)
          P27C(I)=P27C(I)+C(14,I)
      END DO
      INCLUDE 'CHECKCONVERGE1.f'
      JJ=JJ+1
      IF ((maxvalG.GT.ERRSUB).AND.(JJ.LT.ITMAX)) GO TO 111
!****** INCLUDE FILE VELOCITYDATA.f for main program **********
      OPEN(unit=2,file='HFP.txt')
      DO i=1,14
          READ(2,*)ii,FP(i),FPP(i),HPP(i),HPPP(i)
      ENDDO
      HPP1=HPP(1)
      HPP3=HPP(2)
      HPP5=HPP(3)
      HPP7=HPP(4)
      HPP9=HPP(5)
      HPP11=HPP(6)
      HPP13=HPP(7)
```

```
      HPP15=HPP(8)
      HPP17=HPP(9)
      HPP19=HPP(10)
      HPP21=HPP(11)
      HPP23=HPP(12)
      HPP25=HPP(13)
      HPP27=HPP(14)
      FP1=FP(1)
      FP3=FP(2)
      FP5=FP(3)
      FP7=FP(4)
      FP9=FP(5)
      FP11=FP(6)
      FP13=FP(7)
      FP15=FP(8)
      FP17=FP(9)
      FP19=FP(10)
      FP21=FP(11)
      FP23=FP(12)
      FP25=FP(13)
      FP27=FP(14)
      HPPP1=HPPP(1)
      HPPP3=HPPP(2)
      HPPP5=HPPP(3)
      HPPP7=HPPP(4)
      HPPP9=HPPP(5)
      HPPP11=HPPP(6)
      HPPP13=HPPP(7)
      HPPP15=HPPP(8)
      HPPP17=HPPP(9)
      HPPP19=HPPP(10)
      HPPP21=HPPP(11)
      HPPP23=HPPP(12)
      HPPP25=HPPP(13)
      HPPP27=HPPP(14)
      FPP1=FPP(1)
      FPP3=FPP(2)
      FPP5=FPP(3)
      FPP7=FPP(4)
      FPP9=FPP(5)
      FPP11=FPP(6)
      FPP13=FPP(7)
      FPP15=FPP(8)
      FPP17=FPP(9)
      FPP19=FPP(10)
      FPP21=FPP(11)
      FPP23=FPP(12)
      FPP25=FPP(13)
      FPP27=FPP(14)
      CLOSE(2)
!****** INCLUDE FILE CAL_PP.f for main program **********
      PP(1)=(-P1(3)+4.0d0*P1(2)-3.0d0*P1(1))/2.0d0/H
      PP(2)=(-P3(3)+4.0d0*P3(2))/2.0d0/H
      PP(3)=(-P5(3)+4.0d0*P5(2))/2.0d0/H
      PP(4)=(-P7(3)+4.0d0*P7(2))/2.0d0/H
```

```
      PP(5)=(-P9(3)+4.0d0*P9(2))/2.0d0/H
      PP(6)=(-P11(3)+4.0d0*P11(2))/2.0d0/H
      PP(7)=(-P13(3)+4.0d0*P13(2))/2.0d0/H
      PP(8)=(-P15(3)+4.0d0*P15(2))/2.0d0/H
      PP(9)=(-P17(3)+4.0d0*P17(2))/2.0d0/H
      PP(10)=(-P19(3)+4.0d0*P19(2))/2.0d0/H
      PP(11)=(-P21(3)+4.0d0*P21(2))/2.0d0/H
      PP(12)=(-P23(3)+4.0d0*P23(2))/2.0d0/H
      PP(13)=(-P25(3)+4.0d0*P25(2))/2.0d0/H
      PP(14)=(-P27(3)+4.0d0*P27(2))/2.0d0/H
      WRITE(16,*)H,H2,PP(1),PP(2),PP(3),PP(4),PP(5),PP(6),PP(7),PP(8)
     *                ,PP(9),PP(10),PP(11),PP(12),PP(13),PP(14)
      PCP(1)=(-P1C(3)+4.0d0*P1C(2))/2.0d0/H
      PCP(2)=(-P3C(3)+4.0d0*P3C(2))/2.0d0/H
      PCP(3)=(-P5C(3)+4.0d0*P5C(2))/2.0d0/H
      PCP(4)=(-P7C(3)+4.0d0*P7C(2))/2.0d0/H
      PCP(5)=(-P9C(3)+4.0d0*P9C(2))/2.0d0/H
      PCP(6)=(-P11C(3)+4.0d0*P11C(2))/2.0d0/H
      PCP(7)=(-P13C(3)+4.0d0*P13C(2))/2.0d0/H
      PCP(8)=(-P15C(3)+4.0d0*P15C(2))/2.0d0/H
      PCP(9)=(-P17C(3)+4.0d0*P17C(2))/2.0d0/H
      PCP(10)=(-P19C(3)+4.0d0*P19C(2))/2.0d0/H
      PCP(11)=(-P21C(3)+4.0d0*P21C(2))/2.0d0/H
      PCP(12)=(-P23C(3)+4.0d0*P23C(2))/2.0d0/H
      PCP(13)=(-P25C(3)+4.0d0*P25C(2))/2.0d0/H
      PCP(14)=(-P27C(3)+4.0d0*P27C(2))/2.0d0/H
      WRITE(161,*)H,H2,PCP(1),PCP(2),PCP(3),PCP(4),PCP(5),PCP(6),PCP(7),
     *PCP(8),PCP(9),PCP(10),PCP(11),PCP(12),PCP(13),PCP(14)
!****** INCLUDE FILE ALC.f for main program **********
      ALLOCATE (C(14,NJ),P1(NJ))
      ALLOCATE (P3(NJ),P5(NJ),P7(NJ),P9(NJ))
      ALLOCATE (P11(NJ),P13(NJ),P15(NJ),P17(NJ))
      ALLOCATE (P19(NJ),P21(NJ),P23(NJ),P25(NJ))
      ALLOCATE (GG(NJ),P27(NJ))
      ALLOCATE (P1C(NJ),P3C(NJ),P5C(NJ),P7C(NJ))
      ALLOCATE (P9C(NJ),P11C(NJ),P13C(NJ),P15C(NJ))
      ALLOCATE (P17C(NJ),P19C(NJ),P21C(NJ),P23C(NJ))
      ALLOCATE (P25C(NJ), P27C(NJ), DP(14,NJ))
!****** INCLUDE FILE DLC.f for main program **********
      DEALLOCATE (C,P1)
      DEALLOCATE (P3,P5,P7,P9)
      DEALLOCATE (P11,P13,P15,P17)
      DEALLOCATE (P19,P21,P23,P25)
      DEALLOCATE (GG,P27)
      DEALLOCATE (P1C,P3C,P5C,P7C)
      DEALLOCATE (P9C,P11C,P13C,P15C)
      DEALLOCATE (P17C,P19C,P21C,P23C)
      DEALLOCATE (P25C,P27C,DP)
!****** INCLUDE FILE COMMON.f for main program **********
      COMMON/BA/A(14,14),B(14,14),D(14,29),G(14),X(14,14),Y(14,14),N,NJ
      COMMON/BB/H,H2
      COMMON/VELOCITY/HPP1,HPP3,HPP5,HPP7,HPP9,HPP11,HPP13,
     *HPP15,HPP17,HPP19,HPP21,HPP23,HPP25,HPP27,
     *HPPP1,HPPP3,HPPP5,HPPP7,HPPP9,HPPP11,HPPP13,
     *HPPP15,HPPP17,HPPP19,HPPP21,HPPP23,HPPP25,HPPP27,
```

```
   *FP1,FP3,FP5,FP7,FP9,FP11,FP13,FP15,FP17,FP19,FP21,
   *FP23,FP25,FP27,FPP1,FPP3,FPP5,FPP7,FPP9,FPP11,FPP13,
   *FPP15,FPP17,FPP19,FPP21,FPP23,FPP25,FPP27
!****** INCLUDE FILE CHECHCONVERGE.f for main program **********
    DO i=1,NJ
        IF (dabs(P1(i)).GT.0.0d0) THEN
            DP(1,i)=dabs(C(1,i)/P1(i))
        ELSE
            DP(1,i)=1.0d0
        ENDIF
        IF (dabs(P3(i)).GT.0.0d0) THEN
            DP(2,i)=dabs(C(2,i)/P3(i))
        ELSE
            DP(2,i)=1.0d0
        ENDIF
        IF (dabs(P5(i)).GT.0.0d0) THEN
            DP(3,i)=dabs(C(3,i)/P5(i))
        ELSE
            DP(3,i)=1.0d0
        ENDIF
        IF (dabs(P7(i)).GT.0.0d0) THEN
            DP(4,i)=dabs(C(4,i)/P7(i))
        ELSE
            DP(4,i)=1.0d0
        ENDIF
        IF (dabs(P9(i)).GT.0.0d0) THEN
            DP(5,i)=dabs(C(5,i)/P9(i))
        ELSE
            DP(5,i)=1.0d0
        ENDIF
        IF (dabs(P11(i)).GT.0.0d0) THEN
            DP(6,i)=dabs(C(6,i)/P11(i))
        ELSE
            DP(6,i)=1.0d0
        ENDIF
        IF (dabs(P13(i)).GT.0.0d0) THEN
            DP(7,i)=dabs(C(7,i)/P13(i))
        ELSE
            DP(7,i)=1.0d0
        ENDIF
        IF (dabs(P15(i)).GT.0.0d0) THEN
            DP(8,i)=dabs(C(8,i)/P15(i))
        ELSE
            DP(8,i)=1.0d0
        ENDIF
        IF (dabs(P17(i)).GT.0.0d0) THEN
            DP(9,i)=dabs(C(9,i)/P17(i))
        ELSE
            DP(9,i)=1.0d0
        ENDIF
        IF (dabs(P19(i)).GT.0.0d0) THEN
            DP(10,i)=dabs(C(10,i)/P19(i))
        ELSE
            DP(10,i)=1.0d0
        ENDIF
```

```
            IF (dabs(P21(i)).GT.0.0d0) THEN
                DP(11,i)=dabs(C(11,i)/P21(i))
            ELSE
                DP(11,i)=1.0d0
            ENDIF
            IF (dabs(P23(i)).GT.0.0d0) THEN
                DP(12,i)=dabs(C(12,i)/P23(i))
            ELSE
                DP(12,i)=1.0d0
            ENDIF
            IF (dabs(P25(i)).GT.0.0d0) THEN
                DP(13,i)=dabs(C(13,i)/P25(i))
            ELSE
                DP(13,i)=1.0d0
            ENDIF
            IF (dabs(P27(i)).GT.0.0d0) THEN
                DP(14,i)=dabs(C(14,i)/P27(i))
            ELSE
                DP(14,i)=1.0d0
            ENDIF
        END DO
        CALL GETMAXG_CONC(NJ,NJP,DP,maxvalG)
!****** INCLUDE FILE CHECHCONVERGE1.f for main program **********
        DO i=1,NJ
            IF (dabs(P1C(i)).GT.0.0d0) THEN
                DP(1,i)=dabs(C(1,i)/P1C(i))
            ELSE
                DP(1,i)=1.0d0
            ENDIF
            IF (dabs(P3C(i)).GT.0.0d0) THEN
                DP(2,i)=dabs(C(2,i)/P3C(i))
            ELSE
                DP(2,i)=1.0d0
            ENDIF
            IF (dabs(P5C(i)).GT.0.0d0) THEN
                DP(3,i)=dabs(C(3,i)/P5C(i))
            ELSE
                DP(3,i)=1.0d0
            ENDIF
            IF (dabs(P7C(i)).GT.0.0d0) THEN
                DP(4,i)=dabs(C(4,i)/P7C(i))
            ELSE
                DP(4,i)=1.0d0
            ENDIF
            IF (dabs(P9C(i)).GT.0.0d0) THEN
                DP(5,i)=dabs(C(5,i)/P9C(i))
            ELSE
                DP(5,i)=1.0d0
            ENDIF
            IF (dabs(P11C(i)).GT.0.0d0) THEN
                DP(6,i)=dabs(C(6,i)/P11C(i))
            ELSE
                DP(6,i)=1.0d0
            ENDIF
            IF (dabs(P13C(i)).GT.0.0d0) THEN
```

```
            DP(7,i)=dabs(C(7,i)/P13C(i))
        ELSE
            DP(7,i)=1.0d0
        ENDIF
        IF (dabs(P15C(i)).GT.0.0d0) THEN
            DP(8,i)=dabs(C(8,i)/P15C(i))
        ELSE
            DP(8,i)=1.0d0
        ENDIF
        IF (dabs(P17C(i)).GT.0.0d0) THEN
            DP(9,i)=dabs(C(9,i)/P17C(i))
        ELSE
            DP(9,i)=1.0d0
        ENDIF
        IF (dabs(P19C(i)).GT.0.0d0) THEN
            DP(10,i)=dabs(C(10,i)/P19C(i))
        ELSE
            DP(10,i)=1.0d0
        ENDIF
        IF (dabs(P21C(i)).GT.0.0d0) THEN
            DP(11,i)=dabs(C(11,i)/P21C(i))
        ELSE
            DP(11,i)=1.0d0
        ENDIF
        IF (dabs(P23C(i)).GT.0.0d0) THEN
            DP(12,i)=dabs(C(12,i)/P23C(i))
        ELSE
            DP(12,i)=1.0d0
        ENDIF
        IF (dabs(P25C(i)).GT.0.0d0) THEN
            DP(13,i)=dabs(C(13,i)/P25C(i))
        ELSE
            DP(13,i)=1.0d0
        ENDIF
        IF (dabs(P27C(i)).GT.0.0d0) THEN
            DP(14,i)=dabs(C(14,i)/P27C(i))
        ELSE
            DP(14,i)=1.0d0
        ENDIF
    END DO
    CALL GETMAXG_CONC(NJ,NJP,DP,maxvalG)
```

APPENDIX E
PROGRAM LISTING FOR CALCULATING THE CURRENT DISTRIBUTION AT THE STATIONARY HEMISPHERICAL ELECTRODE UNDER SUBMERGED JET IMPINGEMENT

The program listing presents all of the FORTRAN code to solve governing equations for calculating the current distribution at the stationary hemispherical electrode under submerged jet impingement. The program was developed with 'Compaq Visual Fortran, Version 6.1' with double precision accuracy. The main program 'CURRDISTIJHSE' called the subroutine containing governing equations.

The governing equations were programmed in subroutines 'THETA' and 'CSOLPONT'. The subroutine 'THETA' calculated the current at the electrode surface due to electrode kinetics and mass-transfer. The subroutine 'CSOLPONT' calculated the potential distribution along the electrode surface. The value of electrode potential was calculated at grid point in each iteration. The program was terminated once electrode potential became uniform for the entire electrode surface.

E.1 Program Listing

E.1.1 Main Program

```
IMPLICIT REAL*8 (A-H,O-Z)
IMPLICIT INTEGER (I-N)
DOUBLE PRECISION,ALLOCATABLE::SOLPONT(:)
DOUBLE PRECISION,ALLOCATABLE::CI(:),THC(:),ZCI(:)
DOUBLE PRECISION,ALLOCATABLE::CONC(:),CURT1(:),CURT2(:),ILIM(:)
DOUBLE PRECISION,ALLOCATABLE::AA(:),BB(:)
DOUBLE PRECISION,ALLOCATABLE::EACT(:),CUR(:),ETEST(:),ESOLPONT(:)
DOUBLE PRECISION,ALLOCATABLE::BM(:),RESV(:)
DOUBLE PRECISION,ALLOCATABLE::PPN(:)
DOUBLE PRECISION,ALLOCATABLE::XGAUSS(:),WGAUSS(:)
DOUBLE PRECISION  maxvalG,Z,LP,PP(10),ILIM_AVG,IAVG
DOUBLE PRECISION FP(14),FPP(14),HPP(14),HPPP(14)
DOUBLE PRECISION H, H2 , percent , percent1, percent2
INTEGER SUR_CONC, SUR_DER ,N_STEP,IPP(1),JMID,JMAX
```

```
      DOUBLE PRECISION SC(10), SD(10),ESOLPONTP(401),TH(401)
      INTEGER NJL(20),NJLIST,NGAUSS,LMAX,NMAX
      DOUBLE PRECISION DCI,XL,XU,T,ZZ
      DOUBLE PRECISION CURR_NN,EJJ,alpha,beta,gamma,pi2
      DOUBLE PRECISION tplus,ETAC0,ETAS0,CONC0,CUR0,TAF,res
      DOUBLE PRECISION dpi2,BOLD,DB,DAMP,DAMP1,PHI,V,XACC,CUR_AVG
      CHARACTER filename*13
      CHARACTER filename1*13
      REAL*8 GRADT
      NAMELIST/par/ CURR_NN,EJJ,alpha,beta,gamma,tplus,LMAX,NMAX,IPMAX,
     &              NGAUSS,DAMP,DAMP1,JMID,JMAX,XACC,CONC0,filename,
     &            filename1
      EXTERNAL LP, GRADT
!     Read input parameters
      open(9,FILE='INPUT.DAT',STATUS='UNKNOWN')
      READ(9,par)
      CLOSE(9)
      pi2=acos(-1.0d0)/2.0d0
      ALLOCATE (CI(LMAX),THC(LMAX),ZCI(LMAX))
      ALLOCATE (CONC(LMAX),CURT1(LMAX),CURT2(LMAX),ILIM(LMAX))
      ALLOCATE (AA(LMAX),BB(LMAX))
      ALLOCATE (EACT(LMAX),CUR(LMAX),ETEST(LMAX),ESOLPONT(LMAX))
      ALLOCATE (BM(NMAX),RESV(IPMAX-1))
      ALLOCATE (XGAUSS(NGAUSS),WGAUSS(NGAUSS))
      BM(1)=0.0d0
      JCOUNT=0
      CALL gauleg(0.0d0,pi2,XGAUSS,WGAUSS,NGAUSS)
      CALL GETCITHC(LMAX,CI,THC,ZCI,AA,BB,CIMAX,TH)
      CALL CALINIPONT(EJJ,CURR_NN,alpha,beta,gamma,tplus,CONC0,ETAC0
     *               ,ETAS0,CUR0,TAF)
      DO i=1,LMAX
          CONC(i)=CONC0
          EACT(i)=ETAS0+ETAC0
      END DO
      CUR(1)=CUR0
   12   BOLD=BM(1)
        JCOUNT=JCOUNT+1
      CALL THETA(LMAX,CIMAX,EJJ,CURR_NN,alpha,beta,gamma,tplus,TAF,
     *           CONC,EACT,CUR,ZCI,AA,BB)
      INCLUDE 'POLYFIT.f'
      CALL CSOLPONT(LMAX,CUR,THC,NMAX,BM,ESOLPONT,IP,PPN,
     *            WGAUSS,XGAUSS,NGAUSS,TH,ESOLPONTP)
      DEALLOCATE(PPN)
      V=ESOLPONT(1)+EACT(1)
      IF(JCOUNT.LT.JMID) THEN
          DO 18 i=2,LMAX
              PHI=V
              PHI=PHI-ESOLPONT(i)
              EACT(i)=EACT(i)+DAMP*(PHI-EACT(i))
   18       CONTINUE
      END IF
      IF(JCOUNT.GE.JMID) THEN
          DO 19 i=2,LMAX
              PHI=V
              PHI=PHI-ESOLPONT(i)
```

```
          EACT(i)=EACT(i)+DAMP1*(PHI-EACT(i))
 19       CONTINUE
   END IF
   DB=dabs(BOLD-BM(1))/dabs(BM(1))
   IF ((DABS(DB).GE.XACC).AND.(JCOUNT.LE.JMAX)) GO TO 12
   PRINT*,"CALCULATION␣COMPLETE"
   PRINT*,"BOLD=␣␣", BOLD
   INCLUDE 'WRITEOUTPUT.f'
   DEALLOCATE (BM,RESV)
   DEALLOCATE (EACT,CUR,ETEST,ESOLPONT)
   DEALLOCATE (AA,BB)
   DEALLOCATE (CI,THC,ZCI)
   DEALLOCATE (CONC,CURT1,CURT2,ILIM)
   DEALLOCATE (XGAUSS,WGAUSS)
   END
```

E.1.2 Main Subroutines

In this section, all the include files which are called in the main program as well as in various subroutines are listed here.

```
!***************** SUBROUTINE GETCITHC ***************************
    SUBROUTINE GETCITHC(LMAX,CI,THC,ZCI,A,B,CIMAX,TH)
    INTEGER LMAX,NSTEP
    DOUBLE PRECISION CI(LMAX),THC(LMAX),ZCI(LMAX),TH(401)
    DOUBLE PRECISION A(LMAX),B(LMAX),EX,EX1,CIMAX,pi2
    DOUBLE PRECISION,ALLOCATABLE :: CI_FF(:),THC_FF(:)
    ALLOCATE (CI_FF(10001),THC_FF(10001))
    pi2=dacos(-1.0d0)/2.0d0
    DO i=1,400
        TH(i)=dfloat(i-1)*pi2/400.0d0
    END DO
    TH(401)=pi2
    OPEN(unit=10,file='CITH.txt')
    DO i=1,10001
        READ(10,*)CI_FF(i),THC_FF(i)
    END DO
    NSTEP=(10001-1)/(LMAX-1)
    CIMAX=CI_FF(10001)
    DO i=1,LMAX
        j=(i-1)*NSTEP+1
        CI(i)=CI_FF(j)
        THC(i)=THC_FF(j)
    END DO
    DO i=1,LMAX
        ZCI(i)=SQRT(GRADT(THC(i)))
    END DO
    ZCI(LMAX)=0.12
    EX=2.0d0/3.0d0
    EX1=1.0d0/3.0d0
    DO L=1,LMAX
        AA=DFLOAT(L)
        A(L)=2.0*AA**EX-(AA+1.0d0)**EX-(AA-1.0d0)**EX
        B(L)=AA**EX-(AA-1.0d0)**EX
```

```
      END DO
      DEALLOCATE (CI_FF,THC_FF)
      RETURN
      END
!********** SUBROUTINE CALINIPONT *************************
      SUBROUTINE CALINIPONT(EJJ,CURR_NN,ALPHA,BETA,GAMMA,TPLUS,
     *                      C0,ETAC,ETAS,CUR0,TAF)
      DOUBLE PRECISION EJJ,C1,C2,EXCH,CURR_NN
      DOUBLE PRECISION ALPHA,BETA,GAMMA,TPLUS,C0
      DOUBLE PRECISION ETAC,ETAS,TAF,CUR0,xacc,DETAS
      DOUBLE PRECISION F,FP
      C1=1.5788643711074880d0
      C2=1.1198465217221860d0*CURR_NN
      xacc=1.0e-14
      EXCH=1/EJJ
      TAF=1.0d0
      IF (EXCH-400) 7,7,6
    6   TAF=0.0d0
      EXCH=1.0d0
    7 ETAC=DLOG(C0) + TPLUS*(1-C0)
      CUR0=-(1.0d0-C0)*C1*C2*EXCH/(C0**GAMMA)
      ETAS=DLOG(TAF-CUR0)/BETA
      IF(CUR0) 8,10,8
    8   DO 9 J=1,100
          F=TAF*DEXP(ALPHA*ETAS)-DEXP(-BETA*ETAS)
          FP=TAF*ALPHA*DEXP(ALPHA*ETAS)+BETA*DEXP(-BETA*ETAS)
          DETAS=(F-CUR0)/FP
          IF(DABS(DETAS).LT.xacc) GO TO 10
          ETAS=ETAS-DETAS
    9 CONTINUE
   10 CUR0=-(1.0d0-C0)*C1*C2
      RETURN
      END
!***************** SUBROUTINE INNERP1 *************************
      SUBROUTINE THETA(LMAX,CIMAX,EJJ,CURR_NN,al,be,ga,tp,TAF,
     *                 CONC,EACT,CUR,ZC,A,B)
      INTEGER LMAX
      DOUBLE PRECISION EJJ,CURR_NN,al,be,ga,tp
      DOUBLE PRECISION CONC(LMAX),EACT(LMAX),CUR(LMAX)
      DOUBLE PRECISION ALPHA,BETA,GAMMA,TPLUS,EXCH
      DOUBLE PRECISION ZC(LMAX),A(LMAX),B(LMAX)
      DOUBLE PRECISION C1,C2,C3,EX,EX1,AA,PN,DTH
      DOUBLE PRECISION CIMAX,DCI,Z,TAF,S,DZ,ETA,XACC
      DOUBLE PRECISION DX3,X3,DS
      INTEGER N,i,J,K,NZ,NJ
      C2=1.1198465217221860d0
      C1=C2*(1.0d0-CONC(1))
      EX=2.0d0/3.0d0
      EX1=1.0d0/3.0d0
      DCI=CIMAX/DFLOAT(LMAX-1)
      ALPHA=al
      BETA=be
      GAMMA=ga
      TPLUS=tp
      EXCH=1.0d0/EJJ
```

```
      DZ=CIMAX/DFLOAT(LMAX-1)
      S=CONC(1)
      PN=CURR_NN
      XACC=1.0e-15
      S=CONC(2)
      DO 60 NZ=2,LMAX
          Z=(NZ-1)*DZ
          SUM=0.0d0
          IF (NZ.LE.2) GO TO 42
          DO 40 J=3,NZ
              K=NZ-J+1
              SUM=SUM+CONC(J-1)*A(K)
   40        CONTINUE
   42        ETA=EACT(NZ)
          NJ=NZ-1
          DO 56 N=1,100
              X1=EJJ*TAF*(S**(GAMMA-ALPHA))
     *            *DEXP(ALPHA*ETA)*DEXP(ALPHA*TPLUS*(S-1.0d0))
              X2=EJJ*TAF*(S**(GAMMA+BETA))
     *            *DEXP(-BETA*ETA)*DEXP(BETA*TPLUS*(1.0d0-S))
              DX1=X1*((GAMMA-ALPHA)/S + ALPHA*TPLUS)
              DX2=X2*((GAMMA+BETA )/S - BETA*TPLUS)
              C3=1.50d0*C2*ZC(NZ)/(DZ**EX1)
              X3=-C3*PN*(CONC(1)*B(NJ)+SUM-S)-C1*PN*ZC(NZ)/(Z**EX1)
              DX3=C3*PN
              DS=((X1-X2)-X3)/((DX1-DX2)-DX3)
              CUR(NZ)=X3
              IF(DABS(DS).LE.XACC) GO TO 10
              S=S-DS
   56        CONTINUE
   10        CONC(NZ)=S
   60   CONTINUE
        RETURN
        END
!************ SUBROUTINE CSOLPONT ********************************
      SUBROUTINE CSOLPONT(LMAX,CUR,THC,NMAX,BM,ESOLPONT,IP,PPN,
     *                    W,X,NGAUSS,TH,ESOLPONTP)
      INTEGER LMAX,NMAX,N,i,j,IP,NGAUSS
      DOUBLE PRECISION CUR(LMAX),ESOLPONT(LMAX),BM(NMAX),THC(LMAX)
      DOUBLE PRECISION LP,PPN(IP),BMM(NMAX),ESOLPONT1(LMAX)
      DOUBLE PRECISION W(NGAUSS),X(NGAUSS),ss
      DO N=1,NMAX
          BM(N)=0.0d0
          CALL qgauss(2*(N-1),ss,IP,PPN,W,X,NGAUSS)
          BM(N)=ss*dfloat(4*N-3)/dfloat(2*N-1)
      END DO
      DO 20 i=1,LMAX
          ESOLPONT(i)=0.0d0
          DO N=1,NMAX
              ESOLPONT(i)=ESOLPONT(i)+BM(N)*LP(2*(N-1),dcos(THC(i)))
          END DO
   20 CONTINUE
      RETURN
      END
!***************SUBROUTINE POLYFITCURTHETA*********************
```

```
      SUBROUTINE POLYFITCURTHETA(LMAX,CUR,THC,IP,PPN,res)
      INTEGER LMAX,IP
      DOUBLE PRECISION CUR(LMAX),THC(LMAX),PPN(IP),DET(2),sig,res
      DOUBLE PRECISION, ALLOCATABLE :: Y(:,:),X(:,:),XX(:,:),XXINV(:,:)
      DOUBLE PRECISION, ALLOCATABLE :: PC(:,:),CURC(:,:)
      ALLOCATE(Y(LMAX,1),X(LMAX,IP),XX(IP,IP),XXINV(IP,IP))
      ALLOCATE(PC(IP,1),CURC(LMAX,1))
      res=0.0d0
      DO 10 i=1,LMAX
          sig=1.0d0
          Y(i,1)=CUR(i)/sig
          TH=THC(i)
          DO 20 j=1,IP
              X(i,j)=TH**(dfloat(2*j-2))/sig
20        CONTINUE
10    CONTINUE
      XX=MATMUL(TRANSPOSE(X),X)
      CALL CALINVERSE(XX,IP,XXINV,DET)
      PC=MATMUL(XXINV,MATMUL(TRANSPOSE(X),Y))
      CURC=MATMUL(X,PC)
      DO 40 j=1,IP
          PPN(j)=PC(j,1)
40    CONTINUE
      DEALLOCATE(PC,CURC)
      DEALLOCATE(Y,X,XX,XXINV)
      RETURN
      END
!*************** SUBROUTINE qgauss ****************************
      SUBROUTINE qgauss(NC,ss,IP,PP,W,X,NGAUSS)
      DOUBLE PRECISION a,b,ss,func
      INTEGER j,NC,IP,NGAUSS
      DOUBLE PRECISION dx,xm,xr
      DOUBLE PRECISION W(NGAUSS),X(NGAUSS),PP(IP)
      ss=0.0d0
        DO 11 j=1,NGAUSS
          dx=X(j)
          CALL get_func(NC,dx,func,IP,PP)
          ss=ss+W(j)*func
11      CONTINUE
      RETURN
      END
!********************  SUBROUTINE get_func  ******************
      SUBROUTINE get_func(N,x,func,IP,PP)
      INTEGER N,IP
      DOUBLE PRECISION x,func,cur,LP,xstar
      DOUBLE PRECISION PP(IP)
      DOUBLE PRECISION PPN(IP,1),XX(1,IP),curr(1,1)
      XX(1,1)=1.0d0
      PPN(1,1)=PP(1)
      xstar=0.9562841591392380d0
      DO i=2,IP
          IF (x.le.xstar) THEN
              XX(1,i)=x**(dfloat(2*i-2))
          ELSE
              XX(1,i)=xstar**(dfloat(2*i-2))
```

```
        END IF
        PPN(i,1)=PP(i)
    END DO
    curr=MATMUL(XX,PPN)
    cur=curr(1,1)
    func=cur*dsin(x)*LP(N,dcos(x))
    RETURN
    END
!****************FUNCTION LP ***********************************
    REAL*8 FUNCTION  LP*8(N,X)
    DOUBLE PRECISION P1,P2,P,X
    INTEGER NM1,NU,N
    P1=1.0
    P2=X
    IF (N-1) 1,2,3
  1 LP=P1
    RETURN
  2 LP=P2
    RETURN
  3 NM1=N-1
    DO 4 NU=1,NM1,1
        P=(X*dfloat(2*NU+1)*P2-dfloat(NU)*P1)/dfloat(NU+1)
        P1=P2
        P2=P
  4 CONTINUE
    LP=P
    RETURN
    END
!********************** SUBROUTINE gauleg **********************
    SUBROUTINE gauleg(x1,x2,x,w,n)
    INTEGER n
    DOUBLE PRECISION x1,x2,x(*),w(*)
    DOUBLE PRECISION EPS
    PARAMETER (EPS=3.d-14)
    INTEGER i,j,m
    DOUBLE PRECISION p1,p2,p3,pp,xl,xm,z,z1
    m=(n+1)/2
    xm=0.5d0*(x2+x1)
    xl=0.5d0*(x2-x1)
    do 12 i=1,m
        z=cos(3.141592654d0*(i-.25d0)/(n+.5d0))
1       continue
        p1=1.d0
        p2=0.d0
        do 11 j=1,n
            p3=p2
            p2=p1
            p1=((2.d0*j-1.d0)*z*p2-(j-1.d0)*p3)/j
11      continue
        pp=n*(z*p1-p2)/(z*z-1.d0)
        z1=z
        z=z1-p1/pp
        if(abs(z-z1).gt.EPS)goto 1
        x(i)=xm-xl*z
        x(n+1-i)=xm+xl*z
```

```
        w(i)=2.d0*xl/((1.d0-z*z)*pp*pp)
        w(n+1-i)=w(i)
12  continue
    RETURN
    END
!*************** SUBROUTINE CALILIMAVG **************************
    SUBROUTINE CALILIMIAVG(LMAX,CIMAX,CURR_NN,
   *               CONC,CUR,THC,ZC,ILIM,ILIM_AVG,CUR_AVG)
    INTEGER LMAX
    DOUBLE PRECISION CURR_NN
    DOUBLE PRECISION CONC(LMAX),THC(LMAX),CUR(LMAX)
    DOUBLE PRECISION ZC(LMAX),ILIM(LMAX),ILIM_AVG,ILIMAVG(LMAX)
    DOUBLE PRECISION C1,C2,C3,EX,EX1,AA,PN,DTH,CURAVG(LMAX)
    DOUBLE PRECISION CIMAX,Z,TAF,S,DZ,pi2,BETA,CUR_AVG
    INTEGER N,i,J,K,NZ,NJ
    pi2=acos(-1.0d0)
    BETA=1.0
    C1=1.5788643711074880d0
    C2=1.1198465217221860d0*CURR_NN
    EX=2.0d0/3.0d0
    EX1=1.0d0/3.0d0
    DZ=CIMAX/DFLOAT(LMAX-1)
    ILIM(1)=-C1*C2
    DO 60 NZ=2,LMAX
        Z=(NZ-1)*DZ
        ILIM(NZ)=-C2*ZC(NZ)/(Z**EX1)
60 CONTINUE
    DO i=1,LMAX
        ILIMAVG(i)=dsin(THC(i))*ILIM(i)
        CURAVG(i)=dsin(THC(i))*CUR(i)
    END DO
    ILIM_AVG=0.0d0
    CUR_AVG=0.0d0
    DO i=2,LMAX
        DTH=(THC(i)-THC(i-1))
        ILIM_AVG=(ILIMAVG(i)+ILIMAVG(i-1))*DTH*0.50d0+ILIM_AVG
        CUR_AVG =(CURAVG(i) +CURAVG(i-1)) *DTH*0.50d0+CUR_AVG
    END DO
    DTH=pi2-THC(LMAX)
    ILIM_AVG=ILIM_AVG+BETA*ILIM(LMAX)*dcos(THC(LMAX))
    CUR_AVG =CUR_AVG +BETA* CUR(LMAX)*dcos(THC(LMAX))
    RETURN
    END
```

E.1.3 Include Files

In this section, all the include files which are called in the main program as well as in various subroutimes are listed here.

```
C**************** INCLUDE FILE WRITEOUTPUT.f *****************
    CALL CALILIMIAVG(LMAX,CIMAX,CURR_NN,
   *                 CONC,CUR,THC,ZCI,ILIM,ILIM_AVG,CUR_AVG)
900 FORMAT(' THETA     CONC    CURRENT    ILIM  CURRENT/AVG
```

```
   * CURRENT/ILIMVAG   ILIM/ILIMAVG  IAVG/ILIMAVG
   * EACTS    EACTC   ESOL  ETOT')
901 FORMAT(' THETA     ESOL')
    OPEN(unit=10,file=filename)
    OPEN(unit=11,file=filename1)
    WRITE(10,900)
    WRITE(11,901)
1410FORMAT(12(e13.5,2x)) 1411        FORMAT(2(e13.5,2x))
    CURAVG=-BOLD/
   *1.50d0/CURR_NN/(CIMAX**(2.0d0/3.0d0))/1.1198465217221860d0
    CURAVG=-BOLD
    pi2=dacos(-1.0d0)/2.0d0
    DO i=1,LMAX
        ETAC0=DLOG(CONC(i)) + TPLUS*(1-CONC(i))
        WRITE(10,1410)THC(i)*90.0d0/pi2,CONC(i),CUR(i),ILIM(i),
   *               CUR(i)/CUR_AVG,CUR(i)/ILIM_AVG,ILIM(i)/ILIM_AVG
   *                ,CUR_AVG/ILIM_AVG,EACT(i)-ETAC0,ETAC0,ESOLPONT(i)
   *               ,ESOLPONT(i)+EACT(i)
    END DO
    DO i=1,401
        WRITE(11,1411)TH(i)*90.0d0/pi2,ESOLPONTP(i)
    END DO
    CLOSE(10)
    CLOSE(11)
```

E.1.4 Input File

The following variables were read in the main program by the following input file. .

```
!************************INPUT.DAT*************************
    CURR_NN=     20.0d0
    EJJ=         5.0d0
    alpha=       0.50d0
    beta=        0.50d0
    gamma=       0.50d0
    tplus=       0.50d0
    LMAX=        201
    NMAX=        51
    IPMAX=       20
    NGAUSS=      400
    DAMP=        0.02
    DAMP1=       0.0200
    JMID=        1000
    JMAX=        10000
    XACC=        1.0e-8
    CONC0=       0.50d0
    filename=    'N20J5NCP5.txt'
    filename1=   'N20J5NPP5.txt'
```

APPENDIX F
PROGRAM LISTING FOR CALCULATING THE CURRENT DISTRIBUTION AT THE ROTATING HEMISPHERICAL ELECTRODE

The program listing presents all of the FORTRAN code to solve governing equations for calculation of current distribution at the rotating hemispherical electrode with finite Schmidt number. The program was developed with 'Compaq Visual Fortran, Version 6.1' with double precision accuracy. The main program 'CURRDISTRHEWITHSCCORR' called the subroutine containing governing equations.

The input parameters for the main program were read from the file 'INPUT.DAT'. An initial surface concentration distribution was established. The convective-diffusion governing equation for the current distribution were solved by calling the include file 'PALL.f' and 'CALCONCCURR.f'. The surface potential along the electrode surface was estimated by subroutine 'CSOLPONT'. The electrode potential was calculated and total over potential was updated at each node. Assuming the current along the electrode surface from previous iteration, a new surface concentration distribution was estimated in the subroutine 'THETA'

A polynomial was regressed to the obtained concentration distribution. The coefficients of the polynomial were used to calculate the current distribution due to mass-transfer again using subroutine 'CALCONCCURR.f'. The procedure was iterated until quantities converged.

F.1 Program Listing

F.1.1 Main Program

```
IMPLICIT REAL*8 (A-H,O-Z)
```

```
      IMPLICIT INTEGER (I-N)
      INCLUDE 'COMMON.f'
      DOUBLE PRECISION,ALLOCATABLE::C(:,:),GG(:),DP(:,:)
      DOUBLE PRECISION,ALLOCATABLE::P1(:),P3(:),P5(:),P7(:),P9(:)
      DOUBLE PRECISION,ALLOCATABLE::P11(:),P13(:),P15(:),P17(:)
      DOUBLE PRECISION,ALLOCATABLE::P19(:)
      DOUBLE PRECISION,ALLOCATABLE::P1C(:),P3C(:),P5C(:),P7C(:),P9C(:)
      DOUBLE PRECISION,ALLOCATABLE::P11C(:),P13C(:),P15C(:),P17C(:)
      DOUBLE PRECISION,ALLOCATABLE::P19C(:)
      DOUBLE PRECISION,ALLOCATABLE::THC(:),CONC(:)
      DOUBLE PRECISION,ALLOCATABLE::EACT(:),CUR(:),ETEST(:),ESOLPONT(:)
      DOUBLE PRECISION,ALLOCATABLE::BM(:),RESV(:)
      DOUBLE PRECISION,ALLOCATABLE::XGAUSS(:),WGAUSS(:)
      DOUBLE PRECISION,ALLOCATABLE::CI(:),ZCI(:),AA(:),BB(:)
      DOUBLE PRECISION,ALLOCATABLE::CUR1(:), CUR2(:)
      DOUBLE PRECISION maxvalG,Z,LP,PP(10),PPC(10),CUR_NN,TH
      DOUBLE PRECISION FP(10),FPP(10),HPP(10),HPPP(10)
      DOUBLE PRECISION H, H2 , percent , percent1, percent2
      INTEGER SUR_CONC, SUR_DER ,N_STEP,IPP(1),NJP,NT
      DOUBLE PRECISION SC(10), SD(10), SCOLD(10), DSCMAX
      INTEGER NJL(20),NJLIST,NGAUSS,LMAX,NMAX,IP
      DOUBLE PRECISION DCI,XL,XU,T,ZZ,SCN,SCNTERM
      DOUBLE PRECISION CURR_NN,EJJ,alpha,beta,gamma,pi2
      DOUBLE PRECISION tplus,ETAC0,ETAS0,CONC0,CUR0,TAF,res
      CHARACTER filename*15
      DOUBLE PRECISION dpi2,BOLD,DB,DAMP,PHI,V,XACC1,XACC2,CIMAX,ERRSUB
      NAMELIST/par/CURR_NN,EJJ,alpha,beta,gamma,tplus,LMAX,NMAX,IPMAX,NT
     &            ,NGAUSS,DAMP,XACC1,XACC2,CONC0,Z,NJ,ERRSUB,filename,SCN
      EXTERNAL LP
!     Reading the parameters
      open(9,FILE='INPUT.DAT',STATUS='UNKNOWN')
      READ(9,par)
      CLOSE(9)
      pi2=acos(-1.0d0)/2.0d0
      IP=10
      ALLOCATE (THC(LMAX),CONC(LMAX))
      ALLOCATE (EACT(LMAX),CUR(LMAX),ETEST(LMAX),ESOLPONT(LMAX))
      ALLOCATE (BM(NMAX),RESV(IPMAX-1))
      ALLOCATE (XGAUSS(NGAUSS),WGAUSS(NGAUSS))
      ALLOCATE (CI(LMAX),ZCI(LMAX),AA(LMAX),BB(LMAX))
      ALLOCATE (CUR1(LMAX),CUR2(LMAX))
      INCLUDE 'VELOCITYDATA.f'
      SUR_CONC=1
      SUR_DER=0
      DO i=1,10
          SC(i)=0.0d0
          SD(i)=0.0d0
          SCOLD(i)=0.0d0
      END DO
      SC(1)=1.0d0-CONC0
      INCLUDE 'ALC.f'
      CALL SETUPPALL(P1,P3,P5,P7,P9,P11,P13,P15,P17,P19,
     *                    P1C,P3C,P5C,P7C,P9C,P11C,P13C,P15C,P17C,P19C)
      CALL GETCITHC(LMAX,THC,pi2)
      CALL gauleg(0.0d0,pi2,XGAUSS,WGAUSS,NGAUSS)
```

```
    BM(1)=0.0d0
    JCOUNT=0
12  BOLD=BM(1)
    N=10
    H=Z/(NJ-1)
    H2=H*H
    INCLUDE 'PALL.f'
    INCLUDE 'CALCONCCURR.f'
    CUR0=CUR(1)
    CALL CALINIPONT(LMAX,EJJ,CURR_NN,alpha,beta,gamma,tplus,CONC,ETAC0
   *              ,ETAS0,CUR,EACT,TAF)
    CALL CSOLPONT(LMAX,CUR,THC,NMAX,BM,ESOLPONT,IP,PP,PPC,SCN,
   *            WGAUSS,XGAUSS,NGAUSS)
    V=ESOLPONT(1)+EACT(1)
    DO 18 i=2,LMAX
        PHI=V
        PHI=PHI-ESOLPONT(i)
        EACT(i)=EACT(i)+DAMP*(PHI-EACT(i))
18  CONTINUE
    CALL THETA(LMAX,EJJ,CURR_NN,alpha,beta,gamma,tplus,TAF,
   *               CONC,EACT,CUR,THC)
    CALL POLYFITCONCTHETA2(LMAX,CONC,THC,NT,IP,SC,res)
    CALL FINDDSCMAX(IP,SC,SCOLD,DSCMAX)
    SC(1)=1.0d0-CONC0
    JCOUNT=JCOUNT+1
    DB=dabs(BOLD-BM(1))/dabs(BM(1))
    IF ((DABS(DB).GE.XACC1).OR.(DSCMAX.GE.XACC2)) GO TO 12
    INCLUDE 'WRITEOUTPUT.f'
    INCLUDE 'DLC.f'
    DEALLOCATE (CUR1,CUR2)
    DEALLOCATE (CI,ZCI,AA,BB)
    DEALLOCATE (XGAUSS,WGAUSS)
    DEALLOCATE (BM,RESV)
    DEALLOCATE (EACT,CUR,ETEST,ESOLPONT)
    DEALLOCATE (THC,CONC)
    END
```

F.1.2 Main Subroutines

In this section, all the include files which are called in the main program as well as in various subroutimes are listed here.

```
!***************** SUBROUTINE SETUPPALL ************************
    SUBROUTINE SETUPPALL(P1,P3,P5,P7,P9,P11,P13,P15,P17,P19,
   *                   P1C,P3C,P5C,P7C,P9C,P11C,P13C,P15C,P17C,P19C)
    IMPLICIT REAL*8 (A-H,O-Z)
    IMPLICIT INTEGER (I-N)
    COMMON/BA/A(6,6),B(6,6),D(6,13),G(6),X(6,6),Y(6,6),N,NJ
    DOUBLE PRECISION P1(*),P3(*),P5(*),P7(*),P9(*),P11(*),P13(*)
    DOUBLE PRECISION P15(*),P17(*),P19(*),P1C(*),P3C(*),P5C(*),P7C(*)
    DOUBLE PRECISION P9C(*),P11C(*),P13C(*),P15C(*),P17C(*),P19C(*)
    DO 20 II=1,NJ
        P1(II)=0.0d0
        P3(II)=0.0d0
```

```
          P5(II)=0.0d0
          P7(II)=0.0d0
          P9(II)=0.0d0
          P11(II)=0.0d0
          P13(II)=0.0d0
          P15(II)=0.0d0
          P17(II)=0.0d0
          P19(II)=0.00d0
          P1C(II)=0.0d0
          P3C(II)=0.0d0
          P5C(II)=0.0d0
          P7C(II)=0.0d0
          P9C(II)=0.0d0
          P11C(II)=0.0d0
          P13C(II)=0.0d0
          P15C(II)=0.0d0
          P17C(II)=0.0d0
          P19C(II)=0.00d0
       20 CONTINUE
          RETURN
          END
!***************** SUBROUTINE BC1PALL *************************
          SUBROUTINE BC1PALL(J,C,P1,P3,P5,P7,P9,P11,P13,P15,P17,P19,
         *                   SUR_CONC,SUR_DER,SC,SD)
          IMPLICIT REAL*8 (A-H,O-Z)
          IMPLICIT INTEGER (I-N)
          COMMON/BA/A(10,10),B(10,10),D(10,21),G(10),X(10,10),Y(10,10),N,NJ
          COMMON/BB/H,H2
          DOUBLE PRECISION C(10,*)
          DOUBLE PRECISION P1(*),P3(*),P5(*),P7(*),P9(*),P11(*),P13(*)
          DOUBLE PRECISION P15(*),P17(*),P19(*)
          INTEGER SUR_CONC, SUR_DER
          DOUBLE PRECISION SC(*), SD(*)
          DO i=1,10
              DO jj=1,10
                  A(i,jj)=0.0d0
                  B(i,jj)=0.0d0
                  D(i,jj)=0.0d0
              END DO
          END DO
          IF (SUR_CONC.EQ.1) THEN
              G(1)=SC(1)-P1(J)
              B(1,1)=1.0d0
              G(2)=SC(2)-P3(J)
              B(2,2)=1.0d0
              G(3)=SC(3)-P5(J)
              B(3,3)=1.0d0
              G(4)=SC(4)-P7(J)
              B(4,4)=1.0d0
              G(5)=SC(5)-P9(J)
              B(5,5)=1.0d0
              G(6)=SC(6)-P11(J)
              B(6,6)=1.0d0
              G(7)=SC(7)-P13(J)
              B(7,7)=1.0d0
```

```
          G(8)=SC(8)-P15(J)
          B(8,8)=1.0d0
          G(9)=SC(9)-P17(J)
          B(9,9)=1.0d0
          G(10)=SC(10)-P19(J)
          B(10,10)=1.0d0
      END IF
      RETURN
      END
!***************** SUBROUTINE INNERPALL ***********************
      SUBROUTINE INNERPALL(J,C,P1,P3,P5,P7,P9,P11,P13,P15,P17,P19)
      IMPLICIT REAL*8 (A-H,O-Z)
      IMPLICIT INTEGER (I-N)
      INCLUDE 'COMMON.f'
      DOUBLE PRECISION C(10,*)
      DOUBLE PRECISION P1(*),P3(*),P5(*),P7(*),P9(*),P11(*),P13(*)
      DOUBLE PRECISION P15(*),P17(*),P19(*)
      DOUBLE PRECISION Z
      Z=(J-1)*H
      DO i=1,10
          DO jj=1,10
              A(i,jj)=0.0d0
              B(i,jj)=0.0d0
              D(i,jj)=0.0d0
          END DO
      END DO
      G(1)=(P1(J+1)-2.0d0*P1(J)+P1(J-1))/H2
     *+Z*Z*HPP1*(P1(J+1)-P1(J-1))/2.0d0/H
      A(1,1)=-1.0d0/H2+Z*Z*HPP1/2.0d0/H
      B(1,1)=2.0d0/H2
      D(1,1)=-1.0d0/H2-Z*Z*HPP1/2.0d0/H
      G(2)=(P3(J+1)-2.0d0*P3(J)+P3(J-1))/H2
     *+Z*Z*HPP1*(P3(J+1)-P3(J-1))/2.0d0/H
     *+Z*Z*HPP3*(P1(J+1)-P1(J-1))/2.0d0/H-Z*FP1*P3(J)
      A(2,1)= Z*Z*HPP3/2.0d0/H
      B(2,1)= 0.0d0
      D(2,1)=-Z*Z*HPP3/2.0d0/H
      A(2,2)=-1.0d0/H2+Z*Z*HPP1/2.0d0/H
      B(2,2)= 2.0d0/H2+Z*FP1
      D(2,2)=-1.0d0/H2-Z*Z*HPP1/2.0d0/H
      G(3)=(P5(J+1)-2.0d0*P5(J)+P5(J-1))/H2
     *+Z*Z*HPP1*(P5(J+1)-P5(J-1))/2.0d0/H
     *+Z*Z*HPP3*(P3(J+1)-P3(J-1))/2.0d0/H
     *+Z*Z*HPP5*(P1(J+1)-P1(J-1))/2.0d0/H
     *-Z*FP3*P3(J)-2.0d0*Z*FP1*P5(J)
      A(3,1)= Z*Z*HPP5/2.0d0/H
      B(3,1)= 0.0d0
      D(3,1)=-Z*Z*HPP5/2.0d0/H
      A(3,2)= Z*Z*HPP3/2.0d0/H
      B(3,2)= Z*FP3
      D(3,2)=-Z*Z*HPP3/2.0d0/H
      A(3,3)=-1.0d0/H2+Z*Z*HPP1/2.0d0/H
      B(3,3)= 2.0d0/H2+2.0d0*Z*FP1
      D(3,3)=-1.0d0/H2-Z*Z*HPP1/2.0d0/H
      G(4)=(P7(J+1)-2.0d0*P7(J)+P7(J-1))/H2
```

```
*+Z*Z*HPP1*(P7(J+1)-P7(J-1))/2.0d0/H
*+Z*Z*HPP3*(P5(J+1)-P5(J-1))/2.0d0/H
*+Z*Z*HPP5*(P3(J+1)-P3(J-1))/2.0d0/H
*+Z*Z*HPP7*(P1(J+1)-P1(J-1))/2.0d0/H
*-Z*FP5*P3(J)-2.0d0*Z*FP3*P5(J)-3.0d0*Z*FP1*P7(J)
 A(4,1)= Z*Z*HPP7/2.0d0/H
 B(4,1)= 0.0d0
 D(4,1)=-Z*Z*HPP7/2.0d0/H
 A(4,2)= Z*Z*HPP5/2.0d0/H
 B(4,2)= Z*FP5
 D(4,2)=-Z*Z*HPP7/2.0d0/H
 A(4,3)= Z*Z*HPP3/2.0d0/H
 B(4,3)= 2.0d0*Z*FP3
 D(4,3)=-Z*Z*HPP3/2.0d0/H
 A(4,4)=-1.0d0/H2+Z*Z*HPP1/2.0d0/H
 B(4,4)= 2.0d0/H2+3.0d0*Z*FP1
 D(4,4)=-1.0d0/H2-Z*Z*HPP1/2.0d0/H
 G(5)=(P9(J+1)-2.0d0*P9(J)+P9(J-1))/H2
*+Z*Z*HPP1*(P9(J+1)-P9(J-1))/2.0d0/H
*+Z*Z*HPP3*(P7(J+1)-P7(J-1))/2.0d0/H
*+Z*Z*HPP5*(P5(J+1)-P5(J-1))/2.0d0/H
*+Z*Z*HPP7*(P3(J+1)-P3(J-1))/2.0d0/H
*+Z*Z*HPP9*(P1(J+1)-P1(J-1))/2.0d0/H
*-1.0d0*Z*FP7*P3(J)-2.0d0*Z*FP5*P5(J)-3.0d0*Z*FP3*P7(J)
*-4.0d0*Z*FP1*P9(J)
 A(5,1)= Z*Z*HPP9/2.0d0/H
 B(5,1)= 0.0d0
 D(5,1)=-Z*Z*HPP9/2.0d0/H
 A(5,2)= Z*Z*HPP7/2.0d0/H
 B(5,2)= 1.0d0*Z*FP7
 D(5,2)=-Z*Z*HPP7/2.0d0/H
 A(5,3)= Z*Z*HPP5/2.0d0/H
 B(5,3)= 2.0d0*Z*FP5
 D(5,3)=-Z*Z*HPP5/2.0d0/H
 A(5,4)= Z*Z*HPP3/2.0d0/H
 B(5,4)= 3.0d0*Z*FP3
 D(5,4)=-Z*Z*HPP3/2.0d0/H
 A(5,5)=-1.0d0/H2+Z*Z*HPP1/2.0d0/H
 B(5,5)=2.0d0/H2+4.0d0*Z*FP1
 D(5,5)=-1.0d0/H2-Z*Z*HPP1/2.0d0/H
 G(6)=(P11(J+1)-2.0d0*P11(J)+P11(J-1))/H2
*+Z*Z*HPP1*(P11(J+1)-P11(J-1))/2.0d0/H
*+Z*Z*HPP3*(P9(J+1)-P9(J-1))/2.0d0/H
*+Z*Z*HPP5*(P7(J+1)-P7(J-1))/2.0d0/H
*+Z*Z*HPP7*(P5(J+1)-P5(J-1))/2.0d0/H
*+Z*Z*HPP9*(P3(J+1)-P3(J-1))/2.0d0/H
*+Z*Z*HPP11*(P1(J+1)-P1(J-1))/2.0d0/H
*-1.0d0*Z*FP9*P3(J)-2.0d0*Z*FP7*P5(J)-3.0d0*Z*FP5*P7(J)
*-4.0d0*Z*FP3*P9(J)-5.0d0*Z*FP1*P11(J)
 A(6,1)= Z*Z*HPP11/2.0d0/H
 B(6,1)= 0.0d0
 D(6,1)=-Z*Z*HPP11/2.0d0/H
 A(6,2)= Z*Z*HPP9/2.0d0/H
 B(6,2)= 1.0d0*Z*FP9
 D(6,2)=-Z*Z*HPP9/2.0d0/H
```

```
 A(6,3)= Z*Z*HPP7/2.0d0/H
 B(6,3)= 2.0d0*Z*FP7
 D(6,3)=-Z*Z*HPP7/2.0d0/H
 A(6,4)= Z*Z*HPP5/2.0d0/H
 B(6,4)= 3.0d0*Z*FP5
 D(6,4)=-Z*Z*HPP5/2.0d0/H
 A(6,5)= Z*Z*HPP3/2.0d0/H
 B(6,5)= 4.0d0*Z*FP3
 D(6,5)=-Z*Z*HPP3/2.0d0/H
 A(6,6)=-1.0d0/H2+Z*Z*HPP1/2.0d0/H
 B(6,6)=2.0d0/H2+5.0d0*Z*FP1
 D(6,6)=-1.0d0/H2-Z*Z*HPP1/2.0d0/H
 G(7)=(P13(J+1)-2.0d0*P13(J)+P13(J-1))/H2
*+Z*Z*HPP1*(P13(J+1)-P13(J-1))/2.0d0/H
*+Z*Z*HPP3*(P11(J+1)-P11(J-1))/2.0d0/H
*+Z*Z*HPP5*(P9(J+1)-P9(J-1))/2.0d0/H
*+Z*Z*HPP7*(P7(J+1)-P7(J-1))/2.0d0/H
*+Z*Z*HPP9*(P5(J+1)-P5(J-1))/2.0d0/H
*+Z*Z*HPP11*(P3(J+1)-P3(J-1))/2.0d0/H
*+Z*Z*HPP13*(P1(J+1)-P1(J-1))/2.0d0/H
*-1.0d0*Z*FP11*P3(J)-2.0d0*Z*FP9*P5(J)-3.0d0*Z*FP7*P7(J)
*-4.0d0*Z*FP5*P9(J)-5.0d0*Z*FP3*P11(J)-6.0d0*Z*FP1*P13(J)
 A(7,1)= Z*Z*HPP13/2.0d0/H
 B(7,1)= 0.0d0
 D(7,1)=-Z*Z*HPP13/2.0d0/H
 A(7,2)= Z*Z*HPP11/2.0d0/H
 B(7,2)= 1.0d0*Z*FP11
 D(7,2)=-Z*Z*HPP11/2.0d0/H
 A(7,3)= Z*Z*HPP9/2.0d0/H
 B(7,3)= 2.0d0*Z*FP9
 D(7,3)=-Z*Z*HPP9/2.0d0/H
 A(7,4)= Z*Z*HPP7/2.0d0/H
 B(7,4)= 3.0d0*Z*FP7
 D(7,4)=-Z*Z*HPP7/2.0d0/H
 A(7,5)= Z*Z*HPP5/2.0d0/H
 B(7,5)= 4.0d0*Z*FP5
 D(7,5)=-Z*Z*HPP5/2.0d0/H
 A(7,6)= Z*Z*HPP3/2.0d0/H
 B(7,6)= 5.0d0*Z*FP3
 D(7,6)=-Z*Z*HPP3/2.0d0/H
 A(7,7)=-1.0d0/H2 + Z*Z*HPP1/2.0d0/H
 B(7,7)=2.0d0/H2 + 6.0d0*Z*FP1
 D(7,7)=-1.0d0/H2 - Z*Z*HPP1/2.0d0/H
 G(8)=(P15(J+1)-2.0d0*P15(J)+P15(J-1))/H2
*+Z*Z*HPP1*(P15(J+1)-P15(J-1))/2.0d0/H
*+Z*Z*HPP3*(P13(J+1)-P13(J-1))/2.0d0/H
*+Z*Z*HPP5*(P11(J+1)-P11(J-1))/2.0d0/H
*+Z*Z*HPP7*(P9(J+1)-P9(J-1))/2.0d0/H
*+Z*Z*HPP9*(P7(J+1)-P7(J-1))/2.0d0/H
*+Z*Z*HPP11*(P5(J+1)-P5(J-1))/2.0d0/H
*+Z*Z*HPP13*(P3(J+1)-P3(J-1))/2.0d0/H
*+Z*Z*HPP15*(P1(J+1)-P1(J-1))/2.0d0/H
*-1.0d0*Z*FP13*P3(J)-2.0d0*Z*FP11*P5(J)-3.0d0*Z*FP9*P7(J)
*-4.0d0*Z*FP7*P9(J)-5.0d0*Z*FP5*P11(J)-6.0d0*Z*FP3*P13(J)
*-7.0d0*Z*FP1*P15(J)
```

```
 A(8,1)= Z*Z*HPP15/2.0d0/H
 B(8,1)= 0.0d0
 D(8,1)=-Z*Z*HPP15/2.0d0/H
 A(8,2)= Z*Z*HPP13/2.0d0/H
 B(8,2)= 1.0d0*Z*FP13
 D(8,2)=-Z*Z*HPP13/2.0d0/H
 A(8,3)= Z*Z*HPP11/2.0d0/H
 B(8,3)= 2.0d0*Z*FP11
 D(8,3)=-Z*Z*HPP11/2.0d0/H
 A(8,4)= Z*Z*HPP9/2.0d0/H
 B(8,4)= 3.0d0*Z*FP9
 D(8,4)=-Z*Z*HPP9/2.0d0/H
 A(8,5)= Z*Z*HPP7/2.0d0/H
 B(8,5)= 4.0d0*Z*FP7
 D(8,5)=-Z*Z*HPP7/2.0d0/H
 A(8,6)= Z*Z*HPP5/2.0d0/H
 B(8,6)= 5.0d0*Z*FP5
 D(8,6)=-Z*Z*HPP5/2.0d0/H
 A(8,7)= Z*Z*HPP3/2.0d0/H
 B(8,7)= 6.0d0*Z*FP3
 D(8,7)=-Z*Z*HPP3/2.0d0/H
 A(8,8)=-1.0d0/H2 + Z*Z*HPP1/2.0d0/H
 B(8,8)=2.0d0/H2 + 7.0d0*Z*FP1
 D(8,8)=-1.0d0/H2 - Z*Z*HPP1/2.0d0/H
 G(9)=(P17(J+1)-2.0d0*P17(J)+P17(J-1))/H2
*+Z*Z*HPP1*(P17(J+1)-P17(J-1))/2.0d0/H
*+Z*Z*HPP3*(P15(J+1)-P15(J-1))/2.0d0/H
*+Z*Z*HPP5*(P13(J+1)-P13(J-1))/2.0d0/H
*+Z*Z*HPP7*(P11(J+1)-P11(J-1))/2.0d0/H
*+Z*Z*HPP9*(P9(J+1)-P9(J-1))/2.0d0/H
*+Z*Z*HPP11*(P7(J+1)-P7(J-1))/2.0d0/H
*+Z*Z*HPP13*(P5(J+1)-P5(J-1))/2.0d0/H
*+Z*Z*HPP15*(P3(J+1)-P3(J-1))/2.0d0/H
*+Z*Z*HPP17*(P1(J+1)-P1(J-1))/2.0d0/H
*-1.0d0*Z*FP15*P3(J)-2.0d0*Z*FP13*P5(J)-3.0d0*Z*FP11*P7(J)
*-4.0d0*Z*FP9*P9(J)-5.0d0*Z*FP7*P11(J)-6.0d0*Z*FP5*P13(J)
*-7.0d0*Z*FP3*P15(J)-8.0d0*Z*FP1*P17(J)
 A(9,1)= Z*Z*HPP17/2.0d0/H
 B(9,1)= 0.0d0
 D(9,1)=-Z*Z*HPP17/2.0d0/H
 A(9,2)= Z*Z*HPP15/2.0d0/H
 B(9,2)= 1.0d0*Z*FP15
 D(9,2)=-Z*Z*HPP15/2.0d0/H
 A(9,3)= Z*Z*HPP13/2.0d0/H
 B(9,3)= 2.0d0*Z*FP13
 D(9,3)=-Z*Z*HPP13/2.0d0/H
 A(9,4)= Z*Z*HPP11/2.0d0/H
 B(9,4)= 3.0d0*Z*FP11
 D(9,4)=-Z*Z*HPP11/2.0d0/H
 A(9,5)= Z*Z*HPP9/2.0d0/H
 B(9,5)= 4.0d0*Z*FP9
 D(9,5)=-Z*Z*HPP9/2.0d0/H
 A(9,6)= Z*Z*HPP7/2.0d0/H
 B(9,6)= 5.0d0*Z*FP7
 D(9,6)=-Z*Z*HPP7/2.0d0/H
```

```
 A(9,7)= Z*Z*HPP5/2.0d0/H
 B(9,7)= 6.0d0*Z*FP5
 D(9,7)=-Z*Z*HPP5/2.0d0/H
 A(9,8)= Z*Z*HPP3/2.0d0/H
 B(9,8)= 7.0d0*Z*FP3
 D(9,8)=-Z*Z*HPP3/2.0d0/H
 A(9,9)=-1.0d0/H2 + Z*Z*HPP1/2.0d0/H
 B(9,9)=2.0d0/H2 + 8.0d0*Z*FP1
 D(9,9)=-1.0d0/H2 - Z*Z*HPP1/2.0d0/H
 G(10)=(P19(J+1)-2.0d0*P19(J)+P19(J-1))/H2
*+Z*Z*HPP1*(P19(J+1)-P19(J-1))/2.0d0/H
*+Z*Z*HPP3*(P17(J+1)-P17(J-1))/2.0d0/H
*+Z*Z*HPP5*(P15(J+1)-P15(J-1))/2.0d0/H
*+Z*Z*HPP7*(P13(J+1)-P13(J-1))/2.0d0/H
*+Z*Z*HPP9*(P11(J+1)-P11(J-1))/2.0d0/H
*+Z*Z*HPP11*(P9(J+1)-P9(J-1))/2.0d0/H
*+Z*Z*HPP13*(P7(J+1)-P7(J-1))/2.0d0/H
*+Z*Z*HPP15*(P5(J+1)-P5(J-1))/2.0d0/H
*+Z*Z*HPP17*(P3(J+1)-P3(J-1))/2.0d0/H
*+Z*Z*HPP19*(P1(J+1)-P1(J-1))/2.0d0/H
*-1.0d0*Z*FP17*P3(J)-2.0d0*Z*FP15*P5(J)-3.0d0*Z*FP13*P7(J)
*-4.0d0*Z*FP11*P9(J)-5.0d0*Z*FP9*P11(J)-6.0d0*Z*FP7*P13(J)
*-7.0d0*Z*FP5*P15(J)-8.0d0*Z*FP3*P17(J)-9.0d0*Z*FP1*P19(J)
 A(10,1)= Z*Z*HPP19/2.0d0/H
 B(10,1)= 0.0d0
 D(10,1)=-Z*Z*HPP19/2.0d0/H
 A(10,2)= Z*Z*HPP17/2.0d0/H
 B(10,2)= 1.0d0*Z*FP17
 D(10,2)=-Z*Z*HPP17/2.0d0/H
 A(10,3)= Z*Z*HPP15/2.0d0/H
 B(10,3)= 2.0d0*Z*FP15
 D(10,3)=-Z*Z*HPP15/2.0d0/H
 A(10,4)= Z*Z*HPP13/2.0d0/H
 B(10,4)= 3.0d0*Z*FP13
 D(10,4)=-Z*Z*HPP13/2.0d0/H
 A(10,5)= Z*Z*HPP11/2.0d0/H
 B(10,5)= 4.0d0*Z*FP11
 D(10,5)=-Z*Z*HPP11/2.0d0/H
 A(10,6)= Z*Z*HPP9/2.0d0/H
 B(10,6)= 5.0d0*Z*FP9
 D(10,6)=-Z*Z*HPP9/2.0d0/H
 A(10,7)= Z*Z*HPP7/2.0d0/H
 B(10,7)= 6.0d0*Z*FP7
 D(10,7)=-Z*Z*HPP7/2.0d0/H
 A(10,8)= Z*Z*HPP5/2.0d0/H
 B(10,8)= 7.0d0*Z*FP5
 D(10,8)=-Z*Z*HPP5/2.0d0/H
 A(10,9)= Z*Z*HPP3/2.0d0/H
 B(10,9)= 8.0d0*Z*FP3
 D(10,9)=-Z*Z*HPP3/2.0d0/H
 A(10,10)=-1.0d0/H2 + Z*Z*HPP1/2.0d0/H
 B(10,10)=2.0d0/H2 + 9.0d0*Z*FP1
 D(10,10)=-1.0d0/H2 - Z*Z*HPP1/2.0d0/H
 RETURN
 END
```

```
!********************** SUBROUTINE BC2 *************************
    SUBROUTINE BC2ALL(J,C,P1,P3,P5,P7,P9,P11,P13,P15,P17,P19)
    IMPLICIT REAL*8 (A-H,O-Z)
    IMPLICIT INTEGER (I-N)
    COMMON/BA/A(10,10),B(10,10),D(10,21),G(10),X(10,10),Y(10,10),N,NJ
    DOUBLE PRECISION C(10,*)
    DOUBLE PRECISION P1(*),P3(*),P5(*),P7(*),P9(*),P11(*),P13(*)
    DOUBLE PRECISION P15(*),P17(*),P19(*)
    DO i=1,10
        DO jj=1,10
            A(i,jj)=0.0d0
            B(i,jj)=0.0d0
            D(i,jj)=0.0d0
        END DO
    END DO
        G(1)=0.0d0-P1(J)
        B(1,1)=1.0d0
        G(2)=0.0d0-P3(J)
        B(2,2)=1.0d0
        G(3)=0.0d0-P5(J)
        B(3,3)=1.0d0
        G(4)=0.0d0-P7(J)
        B(4,4)=1.0d0
        G(5)=0.0d0-P9(J)
        B(5,5)=1.0d0
        G(6)=0.0d0-P11(J)
        B(6,6)=1.0d0
        G(7)=0.0d0-P13(J)
        B(7,7)=1.0d0
        G(8)=0.0d0-P15(J)
        B(8,8)=1.0d0
        G(9)=0.0d0-P17(J)
        B(9,9)=1.0d0
        G(10)=0.0d0-P19(J)
        B(10,10)=1.0d0
    RETURN
    END
!***************** SUBROUTINE BC1PALLSC **********************
    SUBROUTINE BC1PALLSC(J,C,P1C,P3C,P5C,P7C,P9C,P11C,P13C,
   *                     P15C,P17C,P19C)
    IMPLICIT REAL*8 (A-H,O-Z)
    IMPLICIT INTEGER (I-N)
    COMMON/BA/A(10,10),B(10,10),D(10,21),G(10),X(10,10),Y(10,10),N,NJ
    COMMON/BB/H,H2
    DOUBLE PRECISION C(10,*)
    DOUBLE PRECISION P1C(*),P3C(*),P5C(*),P7C(*),P9C(*),P11C(*)
    DOUBLE PRECISION P13C(*),P15C(*),P17C(*),P19C(*)
    DO i=1,10
        DO jj=1,10
            A(i,jj)=0.0d0
            B(i,jj)=0.0d0
            D(i,jj)=0.0d0
        END DO
    END DO
    G(1)=0.0d0-P1C(J)
```

```
      B(1,1)=1.0d0
      G(2)=0.0d0-P3C(J)
      B(2,2)=1.0d0
      G(3)=0.0d0-P5C(J)
      B(3,3)=1.0d0
      G(4)=0.0d0-P7C(J)
      B(4,4)=1.0d0
      G(5)=0.0d0-P9C(J)
      B(5,5)=1.0d0
      G(6)=0.0d0-P11C(J)
      B(6,6)=1.0d0
      G(7)=0.0d0-P13C(J)
      B(7,7)=1.0d0
      G(8)=0.0d0-P15C(J)
      B(8,8)=1.0d0
      G(9)=0.0d0-P17C(J)
      B(9,9)=1.0d0
      G(10)=0.0d0-P19C(J)
      B(10,10)=1.0d0
      RETURN
      END
!***************** SUBROUTINE INNERPALLSC*********************
      SUBROUTINE INNERPALLSC(J,C,P1,P3,P5,P7,P9,P11,P13,P15,P17,P19,P1C,
     *                       P3C,P5C,P7C,P9C,P11C,P13C,P15C,P17C,P19C)
      IMPLICIT REAL*8 (A-H,O-Z)
      IMPLICIT INTEGER (I-N)
      INCLUDE 'COMMON.f'
      DOUBLE PRECISION C(10,*)
      DOUBLE PRECISION P1(*),P3(*),P5(*),P7(*),P9(*),P11(*),P13(*)
      DOUBLE PRECISION P15(*),P17(*),P19(*)
      DOUBLE PRECISION P1C(*),P3C(*),P5C(*),P7C(*),P9C(*),P11C(*)
      DOUBLE PRECISION P13C(*),P15C(*),P17C(*),P19C(*)
      DOUBLE PRECISION Z
      Z=(J-1)*H
      DO i=1,10
          DO jj=1,10
              A(i,jj)=0.0d0
              B(i,jj)=0.0d0
              D(i,jj)=0.0d0
          END DO
      END DO
      G(1)=(P1C(J+1)-2.0d0*P1C(J)+P1C(J-1))/H2
     *+Z*Z*HPP1*(P1C(J+1)-P1C(J-1))/2.0d0/H
     *+Z*Z*Z*HPPP1*(P1(J+1)-P1(J-1))/2.0d0/H/3.0d0
      A(1,1)=-1.0d0/H2+Z*Z*HPP1/2.0d0/H
      B(1,1)=2.0d0/H2
      D(1,1)=-1.0d0/H2-Z*Z*HPP1/2.0d0/H
      G(2)=(P3C(J+1)-2.0d0*P3C(J)+P3C(J-1))/H2
     *+Z*Z*HPP1*(P3C(J+1)-P3C(J-1))/2.0d0/H
     *+Z*Z*HPP3*(P1C(J+1)-P1C(J-1))/2.0d0/H
     *+Z*Z*Z*HPPP1*(P3(J+1)-P3(J-1))/2.0d0/H/3.0d0
     *+Z*Z*Z*HPPP3*(P1(J+1)-P1(J-1))/2.0d0/H/3.0d0
     *-Z*FP1*P3C(J)-0.50d0*Z*Z*FPP1*P3(J)
        A(2,1)= Z*Z*HPP3/2.0d0/H
      B(2,1)= 0.0d0
```

```
 D(2,1)=-Z*Z*HPP3/2.0d0/H
 A(2,2)=-1.0d0/H2 + Z*Z*HPP1/2.0d0/H
 B(2,2)= 2.0d0/H2 + Z*FP1
 D(2,2)=-1.0d0/H2 - Z*Z*HPP1/2.0d0/H
 G(3)=(P5C(J+1)-2.0d0*P5C(J)+P5C(J-1))/H2
*+Z*Z*HPP1*(P5C(J+1)-P5C(J-1))/2.0d0/H
*+Z*Z*HPP3*(P3C(J+1)-P3C(J-1))/2.0d0/H
*+Z*Z*HPP5*(P1C(J+1)-P1C(J-1))/2.0d0/H
*+Z*Z*Z*HPPP1*(P5(J+1)-P5(J-1))/2.0d0/H/3.0d0
*+Z*Z*Z*HPPP3*(P3(J+1)-P3(J-1))/2.0d0/H/3.0d0
*+Z*Z*Z*HPPP5*(P1(J+1)-P1(J-1))/2.0d0/H/3.0d0
*-1.0d0*Z*FP3*P3C(J)-2.0d0*Z*FP1*P5C(J)
*-0.50d0*Z*Z*FPP3*P3(J)-1.00d0*Z*Z*FPP1*P5(J)
 A(3,1)= Z*Z*HPP5/2.0d0/H
 B(3,1)= 0.0d0
 D(3,1)=-Z*Z*HPP5/2.0d0/H
 A(3,2)= Z*Z*HPP3/2.0d0/H
 B(3,2)= Z*FP3
 D(3,2)=-Z*Z*HPP3/2.0d0/H
 A(3,3)=-1.0d0/H2+Z*Z*HPP1/2.0d0/H
 B(3,3)=2.0d0/H2+2.0d0*Z*FP1
 D(3,3)=-1.0d0/H2-Z*Z*HPP1/2.0d0/H
 G(4)=(P7C(J+1)-2.0d0*P7C(J)+P7C(J-1))/H2
*+Z*Z*HPP1*(P7C(J+1)-P7C(J-1))/2.0d0/H
*+Z*Z*HPP3*(P5C(J+1)-P5C(J-1))/2.0d0/H
*+Z*Z*HPP5*(P3C(J+1)-P3C(J-1))/2.0d0/H
*+Z*Z*HPP7*(P1C(J+1)-P1C(J-1))/2.0d0/H
*+Z*Z*Z*HPPP1*(P7(J+1)-P7(J-1))/2.0d0/H/3.0d0
*+Z*Z*Z*HPPP3*(P5(J+1)-P5(J-1))/2.0d0/H/3.0d0
*+Z*Z*Z*HPPP5*(P3(J+1)-P3(J-1))/2.0d0/H/3.0d0
*+Z*Z*Z*HPPP7*(P1(J+1)-P1(J-1))/2.0d0/H/3.0d0
*-1.0d0*Z*FP5*P3C(J)-2.0d0*Z*FP3*P5C(J)-3.0d0*Z*FP1*P7C(J)
*-0.50d0*Z*Z*FPP5*P3(J)-1.00d0*Z*Z*FPP3*P5(J)-1.50d0*Z*Z*FPP1*P7(J)
 A(4,1)= Z*Z*HPP7/2.0d0/H
 B(4,1)= 0.0d0
 D(4,1)=-Z*Z*HPP7/2.0d0/H
 A(4,2)= Z*Z*HPP5/2.0d0/H
 B(4,2)= Z*FP5
 D(4,2)=-Z*Z*HPP7/2.0d0/H
 A(4,3)= Z*Z*HPP3/2.0d0/H
 B(4,3)= 2.0d0*Z*FP3
 D(4,3)=-Z*Z*HPP3/2.0d0/H
 A(4,4)=-1.0d0/H2+Z*Z*HPP1/2.0d0/H
 B(4,4)=2.0d0/H2+3.0d0*Z*FP1
 D(4,4)=-1.0d0/H2-Z*Z*HPP1/2.0d0/H
 G(5)=(P9C(J+1)-2.0d0*P9C(J)+P9C(J-1))/H2
*+Z*Z*HPP1*(P9C(J+1)-P9C(J-1))/2.0d0/H
*+Z*Z*HPP3*(P7C(J+1)-P7C(J-1))/2.0d0/H
*+Z*Z*HPP5*(P5C(J+1)-P5C(J-1))/2.0d0/H
*+Z*Z*HPP7*(P3C(J+1)-P3C(J-1))/2.0d0/H
*+Z*Z*HPP9*(P1C(J+1)-P1C(J-1))/2.0d0/H
*+Z*Z*Z*HPPP1*(P9(J+1)-P9(J-1))/2.0d0/H/3.0d0
*+Z*Z*Z*HPPP3*(P7(J+1)-P7(J-1))/2.0d0/H/3.0d0
*+Z*Z*Z*HPPP5*(P5(J+1)-P5(J-1))/2.0d0/H/3.0d0
*+Z*Z*Z*HPPP7*(P3(J+1)-P3(J-1))/2.0d0/H/3.0d0
```

```
*+Z*Z*Z*HPPP9*(P1(J+1)-P1(J-1))/2.0d0/H/3.0d0
*-1.0d0*Z*FP7*P3C(J)-2.0d0*Z*FP5*P5C(J)-3.0d0*Z*FP3*P7C(J)
*-4.0d0*Z*FP1*P9C(J)-0.50d0*Z*Z*FPP7*P3(J)
*-1.00d0*Z*Z*FPP5*P5(J)-1.50d0*Z*Z*FPP3*P7(J)
*-2.00d0*Z*Z*FPP1*P9(J)
 A(5,1)= Z*Z*HPP9/2.0d0/H
 B(5,1)= 0.0d0
 D(5,1)=-Z*Z*HPP9/2.0d0/H
 A(5,2)= Z*Z*HPP7/2.0d0/H
 B(5,2)= 1.0d0*Z*FP7
 D(5,2)=-Z*Z*HPP7/2.0d0/H
 A(5,3)= Z*Z*HPP5/2.0d0/H
 B(5,3)= 2.0d0*Z*FP5
 D(5,3)=-Z*Z*HPP5/2.0d0/H
 A(5,4)= Z*Z*HPP3/2.0d0/H
 B(5,4)= 3.0d0*Z*FP3
 D(5,4)=-Z*Z*HPP3/2.0d0/H
 A(5,5)=-1.0d0/H2+Z*Z*HPP1/2.0d0/H
 B(5,5)=2.0d0/H2+4.0d0*Z*FP1
 D(5,5)=-1.0d0/H2-Z*Z*HPP1/2.0d0/H
 G(6)=(P11C(J+1)-2.0d0*P11C(J) + P11C(J-1))/H2
*+Z*Z*HPP1 *(P11C(J+1)-P11C(J-1))/2.0d0/H
*+Z*Z*HPP3 *( P9C(J+1)- P9C(J-1))/2.0d0/H
*+Z*Z*HPP5 *( P7C(J+1)- P7C(J-1))/2.0d0/H
*+Z*Z*HPP7 *( P5C(J+1)- P5C(J-1))/2.0d0/H
*+Z*Z*HPP9 *( P3C(J+1)- P3C(J-1))/2.0d0/H
*+Z*Z*HPP11*( P1C(J+1)- P1C(J-1))/2.0d0/H
*+Z*Z*Z*HPPP1 *(P11(J+1)-P11(J-1))/2.0d0/H/3.0d0
*+Z*Z*Z*HPPP3 *( P9(J+1)- P9(J-1))/2.0d0/H/3.0d0
*+Z*Z*Z*HPPP5 *( P7(J+1)- P7(J-1))/2.0d0/H/3.0d0
*+Z*Z*Z*HPPP7 *( P5(J+1)- P5(J-1))/2.0d0/H/3.0d0
*+Z*Z*Z*HPPP9 *( P3(J+1)- P3(J-1))/2.0d0/H/3.0d0
*+Z*Z*Z*HPPP11*( P1(J+1)- P1(J-1))/2.0d0/H/3.0d0
*-1.0d0*Z*FP9* P3C(J)-2.0d0*Z*FP7* P5C(J)-3.0d0*Z*FP5* P7C(J)
*-4.0d0*Z*FP3* P9C(J)-5.0d0*Z*FP1*P11C(J)
*-0.50d0*Z*Z*FPP9*P3(J)-1.00d0*Z*Z*FPP7*P5(J)-1.50d0*Z*Z*FPP5*P7(J)
*-2.00d0*Z*Z*FPP3*P9(J)-2.50d0*Z*Z*FPP1*P11(J)
 A(6,1)= Z*Z*HPP11/2.0d0/H
 B(6,1)= 0.0d0
 D(6,1)=-Z*Z*HPP11/2.0d0/H
 A(6,2)= Z*Z*HPP9/2.0d0/H
 B(6,2)= 1.0d0*Z*FP9
 D(6,2)=-Z*Z*HPP9/2.0d0/H
 A(6,3)= Z*Z*HPP7/2.0d0/H
 B(6,3)= 2.0d0*Z*FP7
 D(6,3)=-Z*Z*HPP7/2.0d0/H
 A(6,4)= Z*Z*HPP5/2.0d0/H
 B(6,4)= 3.0d0*Z*FP5
 D(6,4)=-Z*Z*HPP5/2.0d0/H
 A(6,5)= Z*Z*HPP3/2.0d0/H
 B(6,5)= 4.0d0*Z*FP3
 D(6,5)=-Z*Z*HPP3/2.0d0/H
 A(6,6)=-1.0d0/H2+Z*Z*HPP1/2.0d0/H
 B(6,6)=2.0d0/H2+5.0d0*Z*FP1
 D(6,6)=-1.0d0/H2-Z*Z*HPP1/2.0d0/H
```

```
 G(7)=(P13C(J+1)-2.0d0*P13C(J) + P13C(J-1))/H2
*+Z*Z*HPP1 *(P13C(J+1)-P13C(J-1))/2.0d0/H
*+Z*Z*HPP3 *(P11C(J+1)-P11C(J-1))/2.0d0/H
*+Z*Z*HPP5 *( P9C(J+1)- P9C(J-1))/2.0d0/H
*+Z*Z*HPP7 *( P7C(J+1)- P7C(J-1))/2.0d0/H
*+Z*Z*HPP9 *( P5C(J+1)- P5C(J-1))/2.0d0/H
*+Z*Z*HPP11*( P3C(J+1)- P3C(J-1))/2.0d0/H
*+Z*Z*HPP13*( P1C(J+1)- P1C(J-1))/2.0d0/H
*+Z*Z*Z*HPPP1 *(P13(J+1)-P13(J-1))/2.0d0/H/3.0d0
*+Z*Z*Z*HPPP3 *(P11(J+1)-P11(J-1))/2.0d0/H/3.0d0
*+Z*Z*Z*HPPP5 *( P9(J+1)- P9(J-1))/2.0d0/H/3.0d0
*+Z*Z*Z*HPPP7 *( P7(J+1)- P7(J-1))/2.0d0/H/3.0d0
*+Z*Z*Z*HPPP9 *( P5(J+1)- P5(J-1))/2.0d0/H/3.0d0
*+Z*Z*Z*HPPP11*( P3(J+1)- P3(J-1))/2.0d0/H/3.0d0
*+Z*Z*Z*HPPP13*( P1(J+1)- P1(J-1))/2.0d0/H/3.0d0
*-1.0d0*Z*FP11*P3C(J)-2.0d0*Z*FP9*P5C(J)-3.0d0*Z*FP7*P7C(J)
*-4.0d0*Z*FP5*P9C(J)-5.0d0*Z*FP3*P11C(J)-6.0d0*Z*FP1*P13C(J)
*-0.50d0*Z*Z*FPP11*P3(J)-1.0d0*Z*Z*FPP9*P5(J)-1.50d0*Z*Z*FPP7*P7(J)
*-2.0d0*Z*Z*FPP5*P9(J)-2.50d0*Z*Z*FPP3*P11(J)-3.0d0*Z*Z*FPP1*P13(J)
 A(7,1)= Z*Z*HPP13/2.0d0/H
 B(7,1)= 0.0d0
 D(7,1)=-Z*Z*HPP13/2.0d0/H
 A(7,2)= Z*Z*HPP11/2.0d0/H
 B(7,2)= 1.0d0*Z*FP11
 D(7,2)=-Z*Z*HPP11/2.0d0/H
 A(7,3)= Z*Z*HPP9/2.0d0/H
 B(7,3)= 2.0d0*Z*FP9
 D(7,3)=-Z*Z*HPP9/2.0d0/H
 A(7,4)= Z*Z*HPP7/2.0d0/H
 B(7,4)= 3.0d0*Z*FP7
 D(7,4)=-Z*Z*HPP7/2.0d0/H
 A(7,5)= Z*Z*HPP5/2.0d0/H
 B(7,5)= 4.0d0*Z*FP5
 D(7,5)=-Z*Z*HPP5/2.0d0/H
 A(7,6)= Z*Z*HPP3/2.0d0/H
 B(7,6)= 5.0d0*Z*FP3
 D(7,6)=-Z*Z*HPP3/2.0d0/H
 A(7,7)=-1.0d0/H2+Z*Z*HPP1/2.0d0/H
 B(7,7)=2.0d0/H2+6.0d0*Z*FP1
 D(7,7)=-1.0d0/H2-Z*Z*HPP1/2.0d0/H
 G(8)=(P15C(J+1)-2.0d0*P15C(J) + P15C(J-1))/H2
*+Z*Z*HPP1 *(P15C(J+1)-P15C(J-1))/2.0d0/H
*+Z*Z*HPP3 *(P13C(J+1)-P13C(J-1))/2.0d0/H
*+Z*Z*HPP5 *(P11C(J+1)-P11C(J-1))/2.0d0/H
*+Z*Z*HPP7 *( P9C(J+1)- P9C(J-1))/2.0d0/H
*+Z*Z*HPP9 *( P7C(J+1)- P7C(J-1))/2.0d0/H
*+Z*Z*HPP11*( P5C(J+1)- P5C(J-1))/2.0d0/H
*+Z*Z*HPP13*( P3C(J+1)- P3C(J-1))/2.0d0/H
*+Z*Z*HPP15*( P1C(J+1)- P1C(J-1))/2.0d0/H
*+Z*Z*Z*HPPP1 *(P15(J+1)-P15(J-1))/2.0d0/H/3.0d0
*+Z*Z*Z*HPPP3 *(P13(J+1)-P13(J-1))/2.0d0/H/3.0d0
*+Z*Z*Z*HPPP5 *(P11(J+1)-P11(J-1))/2.0d0/H/3.0d0
*+Z*Z*Z*HPPP7 *( P9(J+1)- P9(J-1))/2.0d0/H/3.0d0
*+Z*Z*Z*HPPP9 *( P7(J+1)- P7(J-1))/2.0d0/H/3.0d0
*+Z*Z*Z*HPPP11*( P5(J+1)- P5(J-1))/2.0d0/H/3.0d0
```

```
*+Z*Z*Z*HPPP13*( P3(J+1)- P3(J-1))/2.0d0/H/3.0d0
*+Z*Z*Z*HPPP15*( P1(J+1)- P1(J-1))/2.0d0/H/3.0d0
*-1.0d0*Z*FP13*P3C(J)-2.0d0*Z*FP11*P5C(J)-3.0d0*Z*FP9*P7C(J)
*-4.0d0*Z*FP7*P9C(J)-5.0d0*Z*FP5*P11C(J)-6.0d0*Z*FP3*P13C(J)
*-7.0d0*Z*FP1*P15C(J)
*-0.50d0*Z*Z*FPP13*P3(J)-1.0d0*Z*Z*FPP11*P5(J)-1.50d0*Z*Z*FPP9*P7(J)
*-2.0d0*Z*Z*FPP7*P9(J)-2.50d0*Z*Z*FPP5*P11(J)-3.0d0*Z*Z*FPP3*P13(J)
*-3.50d0*Z*Z*FPP1*P15(J)
 A(8,1)= Z*Z*HPP15/2.0d0/H
 B(8,1)= 0.0d0
 D(8,1)=-Z*Z*HPP15/2.0d0/H
 A(8,2)= Z*Z*HPP13/2.0d0/H
 B(8,2)= 1.0d0*Z*FP13
 D(8,2)=-Z*Z*HPP13/2.0d0/H
 A(8,3)= Z*Z*HPP11/2.0d0/H
 B(8,3)= 2.0d0*Z*FP11
 D(8,3)=-Z*Z*HPP11/2.0d0/H
 A(8,4)= Z*Z*HPP9/2.0d0/H
 B(8,4)= 3.0d0*Z*FP9
 D(8,4)=-Z*Z*HPP9/2.0d0/H
 A(8,5)= Z*Z*HPP7/2.0d0/H
 B(8,5)= 4.0d0*Z*FP7
 D(8,5)=-Z*Z*HPP7/2.0d0/H
 A(8,6)= Z*Z*HPP5/2.0d0/H
 B(8,6)= 5.0d0*Z*FP5
 D(8,6)=-Z*Z*HPP5/2.0d0/H
 A(8,7)= Z*Z*HPP3/2.0d0/H
 B(8,7)= 6.0d0*Z*FP3
 D(8,7)=-Z*Z*HPP3/2.0d0/H
 A(8,8)=-1.0d0/H2+Z*Z*HPP1/2.0d0/H
 B(8,8)=2.0d0/H2+7.0d0*Z*FP1
 D(8,8)=-1.0d0/H2-Z*Z*HPP1/2.0d0/H
 G(9)=(P17C(J+1)-2.0d0*P17C(J) + P17C(J-1))/H2
*+Z*Z*HPP1 *(P17C(J+1)-P17C(J-1))/2.0d0/H
*+Z*Z*HPP3 *(P15C(J+1)-P15C(J-1))/2.0d0/H
*+Z*Z*HPP5 *(P13C(J+1)-P13C(J-1))/2.0d0/H
*+Z*Z*HPP7 *(P11C(J+1)-P11C(J-1))/2.0d0/H
*+Z*Z*HPP9 *( P9C(J+1)- P9C(J-1))/2.0d0/H
*+Z*Z*HPP11*( P7C(J+1)- P7C(J-1))/2.0d0/H
*+Z*Z*HPP13*( P5C(J+1)- P5C(J-1))/2.0d0/H
*+Z*Z*HPP15*( P3C(J+1)- P3C(J-1))/2.0d0/H
*+Z*Z*HPP17*( P1C(J+1)- P1C(J-1))/2.0d0/H
*+Z*Z*Z*HPPP1 *(P17(J+1)-P17(J-1))/2.0d0/H/3.0d0
*+Z*Z*Z*HPPP3 *(P15(J+1)-P15(J-1))/2.0d0/H/3.0d0
*+Z*Z*Z*HPPP5 *(P13(J+1)-P13(J-1))/2.0d0/H/3.0d0
*+Z*Z*Z*HPPP7 *(P11(J+1)-P11(J-1))/2.0d0/H/3.0d0
*+Z*Z*Z*HPPP9 *( P9(J+1)- P9(J-1))/2.0d0/H/3.0d0
*+Z*Z*Z*HPPP11*( P7(J+1)- P7(J-1))/2.0d0/H/3.0d0
*+Z*Z*Z*HPPP13*( P5(J+1)- P5(J-1))/2.0d0/H/3.0d0
*+Z*Z*Z*HPPP15*( P3(J+1)- P3(J-1))/2.0d0/H/3.0d0
*+Z*Z*Z*HPPP17*( P1(J+1)- P1(J-1))/2.0d0/H/3.0d0
*-1.0d0*Z*FP15*P3C(J)-2.0d0*Z*FP13*P5C(J)-3.0d0*Z*FP11*P7C(J)
*-4.0d0*Z*FP9*P9C(J)-5.0d0*Z*FP7*P11C(J)-6.0d0*Z*FP5*P13C(J)
*-7.0d0*Z*FP3*P15C(J)-8.0d0*Z*FP1*P17C(J)
*-0.50d0*Z*Z*FPP15*P3(J)-1.0d0*Z*Z*FPP13*P5(J)-1.50d0*Z*Z*FPP11*P7(J)
```

```
*-2.0d0*Z*Z*FPP9*P9(J)-2.50d0*Z*Z*FPP7*P11(J)-3.0d0*Z*Z*FPP5*P13(J)
*-3.50d0*Z*Z*FPP3*P15(J)-4.0d0*Z*Z*FPP1*P17(J)
 A(9,1)= Z*Z*HPP17/2.0d0/H
 B(9,1)= 0.0d0
 D(9,1)=-Z*Z*HPP17/2.0d0/H
 A(9,2)= Z*Z*HPP15/2.0d0/H
 B(9,2)= 1.0d0*Z*FP15
 D(9,2)=-Z*Z*HPP15/2.0d0/H
 A(9,3)= Z*Z*HPP13/2.0d0/H
 B(9,3)= 2.0d0*Z*FP13
 D(9,3)=-Z*Z*HPP13/2.0d0/H
 A(9,4)= Z*Z*HPP11/2.0d0/H
 B(9,4)= 3.0d0*Z*FP11
 D(9,4)=-Z*Z*HPP11/2.0d0/H
 A(9,5)= Z*Z*HPP9/2.0d0/H
 B(9,5)= 4.0d0*Z*FP9
 D(9,5)=-Z*Z*HPP9/2.0d0/H
 A(9,6)= Z*Z*HPP7/2.0d0/H
 B(9,6)= 5.0d0*Z*FP7
 D(9,6)=-Z*Z*HPP7/2.0d0/H
 A(9,7)= Z*Z*HPP5/2.0d0/H
 B(9,7)= 6.0d0*Z*FP5
 D(9,7)=-Z*Z*HPP5/2.0d0/H
 A(9,8)= Z*Z*HPP3/2.0d0/H
 B(9,8)= 7.0d0*Z*FP3
 D(9,8)=-Z*Z*HPP3/2.0d0/H
 A(9,9)=-1.0d0/H2+Z*Z*HPP1/2.0d0/H
 B(9,9)=2.0d0/H2+8.0d0*Z*FP1
 D(9,9)=-1.0d0/H2-Z*Z*HPP1/2.0d0/H
 G(10)=(P19C(J+1)-2.0d0*P19C(J) + P19C(J-1))/H2
*+Z*Z*HPP1 *(P19C(J+1)-P19C(J-1))/2.0d0/H
*+Z*Z*HPP3 *(P17C(J+1)-P17C(J-1))/2.0d0/H
*+Z*Z*HPP5 *(P15C(J+1)-P15C(J-1))/2.0d0/H
*+Z*Z*HPP7 *(P13C(J+1)-P13C(J-1))/2.0d0/H
*+Z*Z*HPP9 *(P11C(J+1)-P11C(J-1))/2.0d0/H
*+Z*Z*HPP11*( P9C(J+1)- P9C(J-1))/2.0d0/H
*+Z*Z*HPP13*( P7C(J+1)- P7C(J-1))/2.0d0/H
*+Z*Z*HPP15*( P5C(J+1)- P5C(J-1))/2.0d0/H
*+Z*Z*HPP17*( P3C(J+1)- P3C(J-1))/2.0d0/H
*+Z*Z*HPP19*( P1C(J+1)- P1C(J-1))/2.0d0/H
*+Z*Z*Z*HPPP1 *(P19(J+1)-P19(J-1))/2.0d0/H/3.0d0
*+Z*Z*Z*HPPP3 *(P17(J+1)-P17(J-1))/2.0d0/H/3.0d0
*+Z*Z*Z*HPPP5 *(P15(J+1)-P15(J-1))/2.0d0/H/3.0d0
*+Z*Z*Z*HPPP7 *(P13(J+1)-P13(J-1))/2.0d0/H/3.0d0
*+Z*Z*Z*HPPP9 *(P11(J+1)-P11(J-1))/2.0d0/H/3.0d0
*+Z*Z*Z*HPPP11*( P9(J+1)- P9(J-1))/2.0d0/H/3.0d0
*+Z*Z*Z*HPPP13*( P7(J+1)- P7(J-1))/2.0d0/H/3.0d0
*+Z*Z*Z*HPPP15*( P5(J+1)- P5(J-1))/2.0d0/H/3.0d0
*+Z*Z*Z*HPPP17*( P3(J+1)- P3(J-1))/2.0d0/H/3.0d0
*+Z*Z*Z*HPPP19*( P1(J+1)- P1(J-1))/2.0d0/H/3.0d0
*-1.0d0*Z*FP17*P3C(J)-2.0d0*Z*FP15*P5C(J)-3.0d0*Z*FP13*P7C(J)
*-4.0d0*Z*FP11*P9C(J)-5.0d0*Z*FP9*P11C(J)-6.0d0*Z*FP7*P13C(J)
*-7.0d0*Z*FP5*P15C(J)-8.0d0*Z*FP3*P17C(J)-9.0d0*Z*FP1*P19C(J)
*-0.50d0*Z*Z*FPP17*P3(J)-1.0d0*Z*Z*FPP15*P5(J)-1.50d0*Z*Z*FPP13*P7(J)
*-2.0d0*Z*Z*FPP11*P9(J)-2.50d0*Z*Z*FPP9*P11(J)-3.0d0*Z*Z*FPP7*P13(J)
```

```
     *-3.50d0*Z*Z*FPP5*P15(J)-4.0d0*Z*Z*FPP3*P17(J)-4.50d0*Z*Z*FPP1*P19(J)
      A(10,1)= Z*Z*HPP19/2.0d0/H
      B(10,1)= 0.0d0
      D(10,1)=-Z*Z*HPP19/2.0d0/H
      A(10,2)= Z*Z*HPP17/2.0d0/H
      B(10,2)= 1.0d0*Z*FP17
      D(10,2)=-Z*Z*HPP17/2.0d0/H
      A(10,3)= Z*Z*HPP15/2.0d0/H
      B(10,3)= 2.0d0*Z*FP15
      D(10,3)=-Z*Z*HPP15/2.0d0/H
      A(10,4)= Z*Z*HPP13/2.0d0/H
      B(10,4)= 3.0d0*Z*FP13
      D(10,4)=-Z*Z*HPP13/2.0d0/H
      A(10,5)= Z*Z*HPP11/2.0d0/H
      B(10,5)= 4.0d0*Z*FP11
      D(10,5)=-Z*Z*HPP11/2.0d0/H
      A(10,6)= Z*Z*HPP9/2.0d0/H
      B(10,6)= 5.0d0*Z*FP9
      D(10,6)=-Z*Z*HPP9/2.0d0/H
      A(10,7)= Z*Z*HPP7/2.0d0/H
      B(10,7)= 6.0d0*Z*FP7
      D(10,7)=-Z*Z*HPP7/2.0d0/H
      A(10,8)= Z*Z*HPP5/2.0d0/H
      B(10,8)= 7.0d0*Z*FP5
      D(10,8)=-Z*Z*HPP5/2.0d0/H
      A(10,9)= Z*Z*HPP3/2.0d0/H
      B(10,9)= 8.0d0*Z*FP3
      D(10,9)=-Z*Z*HPP3/2.0d0/H
      A(10,10)=-1.0d0/H2+Z*Z*HPP1/2.0d0/H
      B(10,10)=2.0d0/H2+9.0d0*Z*FP1
      D(10,10)=-1.0d0/H2-Z*Z*HPP1/2.0d0/H
      RETURN
      END
    !********************** SUBROUTINE BC2 *************************
      SUBROUTINE BC2ALLSC(J,C,P1C,P3C,P5C,P7C,P9C,P11C,
     *                  P13C,P15C,P17C,P19C)
      IMPLICIT REAL*8 (A-H,O-Z)
      IMPLICIT INTEGER (I-N)
        COMMON/BA/A(10,10),B(10,10),D(10,21),G(10),X(10,10),Y(10,10),N,NJ
      DOUBLE PRECISION C(10,*)
      DOUBLE PRECISION P1C(*),P3C(*),P5C(*),P7C(*),P9C(*),P11C(*)
      DOUBLE PRECISION P13C(*),P15C(*),P17C(*),P19C(*)
      DO i=1,10
          DO jj=1,10
              A(i,jj)=0.0d0
              B(i,jj)=0.0d0
              D(i,jj)=0.0d0
          END DO
      END DO
      G(1)=0.0d0-P1C(J)
      B(1,1)=1.0d0
      G(2)=0.0d0-P3C(J)
      B(2,2)=1.0d0
      G(3)=0.0d0-P5C(J)
      B(3,3)=1.0d0
```

```
      G(4)=0.0d0-P7C(J)
      B(4,4)=1.0d0
      G(5)=0.0d0-P9C(J)
      B(5,5)=1.0d0
      G(6)=0.0d0-P11C(J)
      B(6,6)=1.0d0
      G(7)=0.0d0-P13C(J)
      B(7,7)=1.0d0
      G(8)=0.0d0-P15C(J)
      B(8,8)=1.0d0
      G(9)=0.0d0-P17C(J)
      B(9,9)=1.0d0
      G(10)=0.0d0-P19C(J)
      B(10,10)=1.0d0
      RETURN
      END
!******************** SUBROUTINE THETA *************************
      SUBROUTINE THETA(LMAX,EJJ,CURR_NN,al,be,ga,tp,TAF,
     *               CONC,EACT,CUR,THC)
      INTEGER LMAX
      DOUBLE PRECISION EJJ,CURR_NN,al,be,ga,tp
      DOUBLE PRECISION CONC(LMAX),EACT(LMAX),CUR(LMAX),THC(LMAX)
      DOUBLE PRECISION ALPHA,BETA,GAMMA,TPLUS,EXCH
      DOUBLE PRECISION CUR0,DX1,DX2
      DOUBLE PRECISION TAF,S,ETA,XACC,DS
      INTEGER N,NZ,NJ
      ALPHA=al
      BETA=be
      GAMMA=ga
      TPLUS=tp
      EXCH=1.0d0/EJJ
      XACC=1.0e-15
      S=CONC(1)
      DO 60 NZ=2,LMAX
          ETA=EACT(NZ)
          CUR0=CUR(NZ)
          DO 56 N=1,100
              X1=EJJ*TAF*(S**(GAMMA-ALPHA))
     *           *DEXP(ALPHA*ETA)*DEXP(ALPHA*TPLUS*(S-1.0d0))
              X2=EJJ*TAF*(S**(GAMMA+BETA))
     *           *DEXP(-BETA*ETA)*DEXP(BETA*TPLUS*(1.0d0-S))
              DX1=X1*((GAMMA-ALPHA)/S + ALPHA*TPLUS)
              DX2=X2*((GAMMA+BETA )/S - BETA*TPLUS)
              DS=((X1-X2)-CUR0)/(DX1-DX2)
              IF(DABS(DS).LE.XACC) GO TO 10
              S=S-DS
     56       CONTINUE
     10       CONC(NZ)=S
     60   CONTINUE
      RETURN
      END
```

F.1.3 Include Files

In this section, all the include files which are called in the main program as well as in various subroutimes are listed here.

```
!*************** INCLUDE FILE VELOCITYDATA.f***************
    OPEN(unit=2,file='HFP_Benard.txt')
    DO i=1,10
        READ(2,*)ii,FP(i),FPP(i),HPP(i),HPPP(i)
    ENDDO
    HPP1=HPP(1)
    HPP3=HPP(2)
    HPP5=HPP(3)
    HPP7=HPP(4)
    HPP9=HPP(5)
    HPP11=HPP(6)
    HPP13=HPP(7)
    HPP15=HPP(8)
    HPP17=HPP(9)
    HPP19=HPP(10)
    FP1=FP(1)
    FP3=FP(2)
    FP5=FP(3)
    FP7=FP(4)
    FP9=FP(5)
    FP11=FP(6)
    FP13=FP(7)
    FP15=FP(8)
    FP17=FP(9)
    FP19=FP(10)
    HPPP1=HPPP(1)
    HPPP3=HPPP(2)
    HPPP5=HPPP(3)
    HPPP7=HPPP(4)
    HPPP9=HPPP(5)
    HPPP11=HPPP(6)
    HPPP13=HPPP(7)
    HPPP15=HPPP(8)
    HPPP17=HPPP(9)
    HPPP19=HPPP(10)
    FPP1=FPP(1)
    FPP3=FPP(2)
    FPP5=FPP(3)
    FPP7=FPP(4)
    FPP9=FPP(5)
    FPP11=FPP(6)
    FPP13=FPP(7)
    FPP15=FPP(8)
    FPP17=FPP(9)
    FPP19=FPP(10)
    CLOSE(2)
!******************** INCLUDE FILE ALC.f *****************
    ALLOCATE (C(10,NJ),GG(NJ),DP(10,NJ))
    ALLOCATE (P1(NJ),P3(NJ),P5(NJ),P7(NJ),P9(NJ))
```

```
      ALLOCATE (P11(NJ),P13(NJ),P15(NJ),P17(NJ))
      ALLOCATE (P19(NJ))
      ALLOCATE (P1C(NJ),P3C(NJ),P5C(NJ),P7C(NJ),P9C(NJ))
      ALLOCATE (P11C(NJ),P13C(NJ),P15C(NJ),P17C(NJ))
      ALLOCATE (P19C(NJ))
      NJLIST=1
      NJL(1)=50001
      ERREQN = 0.0
      N=10
!******************** INCLUDE FILE PALL.f *****************
      maxvalG=1.0d0
!     INITILIZE ALL COEFFICIENT MATRIX C
      DO I=1,N
          DO K=1,N
              X(I,K)=0.0d0
              Y(I,K)=0.0d0
          END DO
      END DO
      JJ= 1
110   J=0
360   J=J+1
      SUMH=SUMH+H
      DO I=1,N
          G(I)=0.0d0
          DO K=1,N
              A(I,K)=0.0d0
              B(I,K)=0.0d0
              D(I,K)=0.0d0
          ENDDO
      ENDDO
!     Call BC1 for J=1
      IF(J.EQ.1) CALL BC1PALL(J,C,P1,P3,P5,P7,P9,P11,P13,P15,P17,P19,
     *                        SUR_CONC,SUR_DER,SC,SD)
!     Equation for interior region C
      IF((J.GT.1).AND.(J.LT.NJ)) THEN
      CALL INNERPALL(J,C,P1,P3,P5,P7,P9,P11,P13,P15,P17,P19)
      END IF
!     Equation for second boundary condition C
      IF (J.EQ.NJ)  THEN
      CALL BC2ALL(J,C,P1,P3,P5,P7,P9,P11,P13,P15,P17,P19)
      END IF
      CALL BAND(J,C)
      IF(J.NE.NJ) GOTO 360
      DO I=1,NJ
          P1(I) =P1(I) +C(1,I)
          P3(I) =P3(I) +C(2,I)
          P5(I) =P5(I) +C(3,I)
          P7(I) =P7(I) +C(4,I)
          P9(I) =P9(I) +C(5,I)
          P11(I)=P11(I)+C(6,I)
          P13(I)=P13(I)+C(7,I)
          P15(I)=P15(I)+C(8,I)
          P17(I)=P17(I)+C(9,I)
          P19(I)=P19(I)+C(10,I)
      END DO
```

```
      INCLUDE 'CHECKCONVERGE.f'
      JJ=JJ+1
      IF ((maxvalG.GT.ERRSUB).AND.(JJ.LT.25)) GO TO 110
      maxvalG=1.0d0
!     INITILIZE ALL COEFFICIENT MATRIX C
      DO I=1,N
          DO K=1,N
              X(I,K)=0.0d0
              Y(I,K)=0.0d0
          END DO
      END DO
      JJ= 1
      IF (SCN.GT.0.0d0) THEN
111   J=0
361   J=J+1
      SUMH=SUMH+H
      DO I=1,N
          G(I)=0.0d0
          DO K=1,N
              A(I,K)=0.0d0
              B(I,K)=0.0d0
              D(I,K)=0.0d0
          ENDDO
      ENDDO
!     Call BC1 for J=1 C
      IF(J.EQ.1) CALL BC1PALLSC(J,C,P1C,P3C,P5C,P7C,P9C,P11C,
     *                          P13C,P15C,P17C,P19C)
!     Equation for interior region C
      IF((J.GT.1).AND.(J.LT.NJ)) THEN
      CALL INNERPALLSC(J,C,P1,P3,P5,P7,P9,P11,P13,P15,P17,P19,P1C,
     *               P3C,P5C,P7C,P9C,P11C,P13C,P15C,P17C,P19C)
      END IF
!     Equation for second boundary condition C
      IF (J.EQ.NJ)  THEN
      CALL BC2ALLSC(J,C,P1C,P3C,P5,P7,P9,P11,P13,P15,P17,P19)
      END IF
      CALL BAND(J,C)
      IF(J.NE.NJ) GOTO 361
      DO I=1,NJ
          P1C(I) =P1C(I) +C(1,I)
          P3C(I) =P3C(I) +C(2,I)
          P5C(I) =P5C(I) +C(3,I)
          P7C(I) =P7C(I) +C(4,I)
          P9C(I) =P9C(I) +C(5,I)
          P11C(I)=P11C(I)+C(6,I)
          P13C(I)=P13C(I)+C(7,I)
          P15C(I)=P15C(I)+C(8,I)
          P17C(I)=P17C(I)+C(9,I)
          P19C(I)=P19C(I)+C(10,I)
      END DO
      INCLUDE 'CHECKCONVERGE1.f'
      JJ=JJ+1
      IF ((maxvalG.GT.ERRSUB).AND.(JJ.LT.25)) GO TO 111
```

F.1.4 Input File

The following variables were read in the main program by the following input file. .

```
!***********************INPUT.DAT************************%
    CURR_NN=     125.0d0
    EJJ=         5.0d0
    alpha=       0.50d0
    beta=        0.50d0
    gamma=       0.50d0
    tplus=       0.50d0
    LMAX=        501
    NMAX=        51
    IPMAX=       20
    NT=          6
    NGAUSS=      400
    DAMP=        0.05
    XACC1=       1.0e-6
    XACC2=       1.0e-5
    CONC0=       0.50d0
    Z=           10.0d0
    NJ=          10001
    ERRSUB=      1.0e-7
    filename=    'NSCY125C0P5.txt'
    SCN=         1000.0d0
```

REFERENCES

1. W. G. Cochran, "The Flow due to a Rotating Disc," *Proceedings of the Cambridge Philosophical Society*, **30** (1934) 365–375.

2. D.-T. Chin and C.-H. Tsang, "Mass Transfer to an Impinging Jet Electrode," *Journal of the Electrochemical Society*, **125** (1978) 1461–1470.

3. J. M. Esteban, G. Hickey, and M. E. Orazem, "The Impinging Jet Electrode: Measurement of the Hydrodynamic Constant and Its Use for Evaluating Film Persistency," *Corrosion*, **46** (1990) 896–901.

4. J. Newman, "Resistance for Flow of Current to a Rotating Disk," *Journal of the Electrochemical Society*, **113** (1966) 501–502.

5. J. Newman, "Current Distribution on a Rotating Disk below the Limiting Current," *Journal of the Electrochemical Society*, **113** (1966) 1235.

6. M. Durbha and M. E. Orazem, "Current Distribution on a Rotating Disk Electrode Below the Mass-Transfer Limited Current: Correction for Finite Schmidt Number and Determination of Surface Charge Distribution," *Journal of the Electrochemical Society*, **145** (1998) 1940–1949.

7. W. H. Smyrl and J. Newman, "Detection of Nonuniform Current Distribution on a Disk Electrode," *Journal of the Electrochemical Society*, **119** (1972) 208–212.

8. J. Estaban, M. Lowry, and M. E. Orazem, "Correction of Experimental Data for the Ohmic Potential Drop Corresponding to a Secondary Current Distribution on a Disk Electrode," *American Society for Testing and Materials*, (1990) 127–141.

9. W. H. Tiedemann, J. Newman, and D. N. Bennion, "The Error in Measurements of Electrode Kinetics Caused by Nonuniform Ohmic-Potential Drop to a Disk Electrode," *Journal of the Electrochemical Society*, **120** (1973) 256–258.

10. B. Tribollet and J. Newman, "The Modulated Flow at a Rotating Disk Electrode," *Journal of the Electrochemical Society*, **130** (1983) 2016–2026.

11. M. E. Orazem and B. Tribollet, "Error Analysis for Interpretation of Impedance Data Using Mathematical Models," in *Design and Mathematical Modeling of Electrochemical Systems*, J. W. V. Zee and M. E. Orazem, editors (Pennington, NJ: the Electrochemical Society, 2003) in press.

12. M. E. Orazem, J. C. C. Filho, and B. Tribollet, "Application of a Submerged Impinging Jet for Corrosion Studies: Development of Models for the Impedance Response," *Electrochimica Acta*, **46** (2001) 3685–3698.

13. P. W. Appel and J. Newman, "Radially Dependent Convective Warburg Problem for a Rotating Disk," *Journal of the Electrochemical Society*, **124** (1977) 1864–1868.

14. M. Durbha, M. E. Orazem, and B. Tribollet, "A Mathematical Model for the Radially Dependent Impedance of a Rotating Disk Electrode," *Journal of The Electrochemical Society*, **146** (1999) 2199–2208.

15. M. E. Orazem, M. Durbha, C. Deslouis, H. Takenouti, and B. Tribollet, "Influence of Surface Phenomena on the Impedance Response of a Rotating Disk Electrode," *Electrochimica Acta*, **44** (1999) 4403–4412.

16. J. B. Matos, E. D'Elia, O. E. Barcia, O. R. Mattos, N. P eb ere, and B. Tribollet, "Rotating Disc and Hemispherical Electrodes for Copper Dissolution Study in Hydrochloric Solution in the Presence of Benzotriazole," *Electrochimica Acta*, **46** (2001) 1377–1383.

17. D.-T. Chin, "Convective Diffusion on a Rotating Spherical Electrode," *Journal of the Electrochemical Society*, **118** (1971) 1434–1438.

18. K. Nisançiöglu and J. Newman, "Current Distribution on a Rotating Sphere below the Limiting Current," *Journal of the Electrochemical Society*, **121** (1974) 241–246.

19. O. E. Barcia, J. S. Godinez, L. R. S. Lamego, O. R. Mattos, and B. Tribollet, "Rotating Hemispherical Electrode," *Journal of the Electrochemical Society*, **145** (1998) 4189–4195.

20. M. E. Orazem, J. C. C. Filho, and B. Tribollet, "Application of a submerged impinging jet for corrosion studies: development of models for the impedance response," *Electrochimica Acta*, **46** (2001) 3685–3698.

21. C. B. Diem and M. E. Orazem, "The Influence of Velocity on the Corrosion of Copper in Alkaline Chloride Solutions," *Corrosion*, **50** (1994) 290–300.

22. R. C. Alkire and A. Cangellari, "Formation of Salt Films during Anodic Metal Dissolution in the Presence of Fluid Flow," *Journal of the Electrochemical Society*, **130** (1983) 1252–1259.

23. J. S. Newman, *Electrochemical Systems*, 2nd edition (Prentice Hall International, Englewood Cliffs, NJ, 1991).

24. V. G. Levich, "The Theory of Concentration Polarization," *Acta Physicochimica URSS*, **17** (1942) 257–307.

25. M. Eisenberg, C. W. Tobais, and C. R. Wilke, "Ionic Mass Transfer and Concentration Polarization at Rotating Electrodes," *Journal of the Electrochemical Society*, **101** (1954) 306–319.

26. A. C. Riddiford, "The Rotating Disk System," in *Advances in Electrochemistry and Electrochemical Engineering*, volume 4 (1966) 47–116.

27. J. S. Newman, "Current Distribution on a Rotating Disk Below the Limiting Current," *Journal of the Electrochemical Society*, (1966) 1235–1241.

28. M. Matlosz, O. Chene, and D. Landolt, "Design and Construction of a Rotating Disk-Hemispherical Electrode," *Journal of the Electrochemical Society*, **137** (1990) 3033–3038.

29. C. Madore, A. C. West, M. Matlosz, and D. Landolt, "Design Considerations for a Cylindrical Hull Cell with Forced Convection," *Electrochimica Acta*, **37** (1992) 69–74.

30. T. E. Dinan, M. Matlosz, and D. Landolt, "Experimental Investigation of the Current Distribution on a Recessed Rotating Disk Electrode," *Journal of the Electrochemical Society*, **138** (1991) 2947–2952.

31. P. Agarwal, M. E. Orazem, and L. H. García-Rubio, "Measurement Models for Electrochemical Impedance Spectroscopy: I. Demonstration of Applicability," *Journal of the Electrochemical Society*, **139** (1992) 1917–1927.

32. P. Agarwal, O. D. Crisalle, M. E. Orazem, and L. H. García-Rubio, "Measurement Models for Electrochemical Impedance Spectroscopy: 2. Determination of the Stochastic Contribution to the Error Structure," *Journal of the Electrochemical Society*, **142** (1995) 4149–4158.

33. P. Agarwal, M. E. Orazem, and L. H. García-Rubio, "Measurement Models for Electrochemical Impedance Spectroscopy: 3. Evaluation of Consistency with the Kramers-Kronig Relations," *Journal of the Electrochemical Society*, **142** (1995) 4159–4168.

34. L. Pauwels, W. Simons, A. Hubin, J. Schoukens, and R. Pintelon, "Key Issues for Reproducible Impedance Measurements and their Wellfounded Error Analysis in a Silver Electrodeposition System," *Electrochimica Acta*, **47** (2002) 2135–2141.

35. M. T. Scholtz and O. Trass, "Mass Transfer in a Nonuniform Impinging Jet: Part I. Stagnation Flow-Velocity and Pressure Distribution," *AIChE Journal*, **16** (1970) 82–90.

36. L. Howarth, "Note on a Boundary Layer on a Rotating Sphere," *Philosophical Magazine*, **42** (1951) 1308–1315.

37. H. Schlichting and G. Gresten, *Boundary Layer Theory*, 9th edition (Springer Verlag, New York, NY, 2000).

38. J. S. Marshall, *Invicid Incompressible Flow* (John Wiley and Sons, New York, NY, 2001).

39. J. S. Newman, "Numerical Solution of Coupled, Ordinary Differential Equations," *Industrial and Engineering Chemistry Fundamentals*, **7** (1968) 517–517.

40. F. Homann, "Der Einfluid groider Zähihkeit bei der Strömung um den Zylinder und um die Kugel," *Zeitschrift für Angewandte Mathematik und Mechanik*, (1936) 153–164.

41. S. C. Chapra, *Numerical Methods for Engineers*, 4th edition (McGraw-Hill, New York, NY, 1988).

42. G. Nelissen, B. V. D. Bossche, J. Deconinck, A. V. Theemsche, and C. Dan, "Laminar and Turbulent Mass Transfer Simulations in a Parallel Plate Reactor," *Journal of Applied Electrochemistry*, **33** (2003) 863–873.

43. R. Abgrall, "Towards the Ultimate Conservative Scheme: Following the Quest," *Journal of Computational Physics*, **167** (2001) 277–315.

44. D. Chin and C. Tsang, "Mass Transfer to an Impinging Jet Electrode," *Journal of the Electrochemical Society*, **125** (1978) 1461–1470.

45. G. Nelissen, A. V. Theemsche, C. Dan, B. V. D. Bossche, and J. Deconinck, "Multi-ion Transport and Reaction Simulations in Turbulent Parallel Plate Flow," *Journal of Electroanalytical Chemistry*, **563** (2004) 213–220.

46. J. R. Cray, "The Determination of Local Forced-Convection Coefficients for Spheres," *Transactions of the ASME*, **75** (1953) 483–487.

47. D.-T. Chin, *Theory and Experimental Aspects of the Rotating Hemispherical Electrode*, volume 1 of *Advances in Electrochemical Science and Engineering* (VCH Publishers, New York, NY, 1990).

48. S. D. Nigam, "Note on the Boundary Layer on a Rotating Sphere," *ZAMP*, **V** (1954) 151–155.

49. K. Stewartson, "On Rotating Laminar Boundary Layer," in *Boundary Layer Research*, H. Gortler, editor, International Union of Theoretical and Applied Mechanics (Springer-Verlag, New York, NY, 1957) 59–71.

50. W. H. H. Banks, "The Boundary Layer On a Rotating Sphere," *Quart. Journal of Mechnics and Applied Mathematics*, **18** (1964) 443–454.

51. R. Manohar, "The Boundary Layer on a Rotating Sphere," *ZAMP*, **18** (1967) 320–330.

52. J. S. Newman, "Mass Transfer to a Rotating Sphere at High Schmidt Numbers," *Journal of the Electrochemical Society*, **119** (1972) 69–71.

53. M. Abramowitz and I. A. Stegun, *Handbook of Mathematical Functions* (Dover Publications, New York, NY, 1972).

54. J. S. Newman, *Electrochemical Engineering*, 2nd edition (Prentice-Hall International, Englewood Cliffs, NJ, 1991).

55. M. Datta and D. Landolt, "Fundamental Aspects and Application of Electrochemical Microfabrication," *Electrochimica Acta*, **45** (2000) 2535–2558.

56. D. Landolt, "Electrochemical and Materials Science Aspects of Alloy Deposition," *Electrochimica Acta*, **39** (1994) 1075–1090.

57. M. J. Lighthill, "Contributions to the Theory of Heat Transfer Through a Laminar Boundary Layer," *Proceedings of Royal Society of London. Seires A, Mathematical and Physical Sciences*, **202** (1950) 359–377.

58. C. R. Wylie, *Advanced Engineering Mathematics*, 3rd edition (McGraw-Hill, New York, NY, 1966).

59. A. Acrivos and P. L. Chambré, "Laminar Boundary Layer Flows with Surface Reactions," *Industrial and Engineering Chemistry*, **49** (1957) 1025–1029.

60. W. H. Press, S. A. Teukolsky, W. T. Vetterling, and B. P. Flannery, *Numerical Recipes in Fortran 77*, 2nd edition (Press Syndicate of the University of Cambridge, Cambridge, UK, 1992).

61. G. E. P. Box and N. R. Draper, *Empirical Model-Building and Response Surfaces* (John Wiley and Sons, New York, NY, 1987).

62. R. W. Christy, "Classical Theory of Optical Dispersion," *American Journal of Physics*, **40** (1972) 1403–1419.

63. A. Jutan and L. H. García-Rubio, "Spectroscopic Data Resolution Using Discriminant and Eigenvalue Analysis," *Process Control and Quality*, **4** (1993) 235–243.

64. H. A. Kramers, "Die Dispersion und Absorption von Röntgenstrahlen," *Physik. Zeitschr*, **30** (1929) 522–523.

65. R. de L. Kronig, "Dispersionstheorie im Röntgengebeit," *Physik Zeitschrift*, **30** (1929) 521–522.

66. P. Agarwal, *Application of Measurement Models to Impedance Spectroscopy*, Ph.D. dissertation, University of Florida, Gainesville, Florida (1994).

67. M. K. Brachman and J. R. Macdonald, "Generalized Immitance Kernels and the Kronig-Kramers Transforms," *Physica*, **20** (1956) 141–148.

68. J. R. Macdonald, *Impedance Spectroscopy: Emphasizing Solid Materials and Systems* (John Wiley and Sons, New York, NY, 1987).

69. B. A. Boukamp and J. R. Macdonald, "Alternatives to Kronig-Kramers Transformation and Testing, and Estimation of Distribtuions," *Solid State Ionics*, **74** (1994) 85–101.

70. B. A. Boukamp, "A Linear Kronig-Kramers Transform Test for Immittance Data Validation," *Journal of the Electrochemical Society*, **142** (1995) 1885–1894.

71. D. D. MacDonald, "Kramers-Kronig Transformation of Constant Phase Impedances," *Journal of the Electrochemical Society*, **137** (1990) 3303–3307.

72. R. de L. Kronig, "On the Theory of Dispersion of X-Rays," *Journal of the Optical Society of America and Review of Scientific Instruments*, **12** (1926) 547–557.

73. A. Lasia, "Electrochemical Impedance Spectroscopy and its Applications," in *Modern Aspects of Electrochemistry*, R. E. White, B. E. Conway, and J. O. Bockris, editors, volume 32 (Plenum Press, New York, NY, 1999).

74. R. J. Sheppard, B. P. Jordan, and E. H. Grant, "Least Squares Analysis of Complex Data with Applications to Permittivity Measurements," *Journal of Physics D: Applied Physics*, **3** (1970) 1759–1764.

75. R. J. Sheppard, "Least-Squares Analysis of Complex Weighted Data with Dielectric Applications," *Journal of Physics D-Applied Physics*, **6** (1973) 790–794.

76. J. R. Macdonald and J. A. Garber, "Analysis of Impedance and Admittance Data for Solids and Liquids," *Journal of the Electrochemical Society*, **124** (1977) 1022–1030.

77. W. Press, S. A. Teukolsky, W. T. Vetterling, and B. P. Flannery, *Numerical Recipes in C: the Art of Scientific Computing*, 2nd edition (Cambridge University Press, New York, NY, 1992).

78. N. R. Draper and H. Smith, *Applied Regression Analysis*, 3rd edition (Wiley Interscience, New York, NY, 1998).

79. D. M. Himmelblau, *Applied Nonlinear Programming*, 6th edition (McGraw-Hill, New York, NY, 1972).

80. D. W. Marquardt, "An Algorithm for Least-Squares Estimation of Nonlinear Parameters," *Journal of the Society for Industrial and Applied Mathematics*, **11** (1963) 431–441.

81. P. Zoltowski, "The Error Function for Fitting of Models to Immitance Data," *Journal of Electroanalytical Chemistry*, **178** (1984) 11–19.

82. P. Zoltowski, "An Immitance Study of the Mechanism of Hydrogen Reactions on a Tungsten Carbide Electrode. Part II," *Journal of Electroanalytical Chemistry*, **287** (1989) 260.

83. P. Zoltowski, "An Immitance Study of the Mechanism of Hydrogen Reactions on a Tungsten Carbide Electrode. Part I," *Journal of Electroanalytical Chemistry*, **260** (1989) 269.

84. B. A. Boukamp, "A Nonlinear Least Squares Fit Procedure for Analysis of Immittance Data of Electrochemical Systems," *Solid State Ionics*, **20** (1986) 31–44.

85. J. R. Macdonald and J. L. D. Potter, "A Flexible Procedure for Analyzing Impedance Spectroscopy Results: Description and Illustrations," *Solid State Ionics*, **23** (1987) 61–79.

86. M. E. Orazem, P. Agarwal, C. Deslouis, and T. B., "Application of Measurement Models to Electrohydrodynamic Impedance Spectroscopy," *Journal of the Electrochemical Society*, **143** (1996) 948–960.

87. M. E. Orazem, T. E. Moustafid, C. Deslouis, and B. Tribollet, "The Error Structure of Impedance Spectroscopy Measurements for Systems with a Large Ohmic Resistance with Respect to the Polarization Impedance," *Journal of the Electrochemical Society*, **143** (1996) 3880–3890.

88. M. Durbha, M. E. Orazem, and L. H. García-Rubio, "Spectroscopy Applications of the Kramers-Kronig Relations: Implications for Error Structure Identification," *Journal of the Electrochemical Society*, **144** (1997) 48–55.

89. D. S. Bunch, D. M. Gay, and R. E. Welsh, "Algorithm 717: Subroutine for Maximum Likelihood and Quasi-Likelihood Estimation of Parameter in Nonlinear Regression Model," *ACM Transactions on Mathematical Software*, **19** (1997) 109–130.

90. D. M. Gay, *Usage Summary for Selected Optimization Software*, AT&T Bell Laboratories, Murry Hill, NJ (1990).

91. S. L. Carson, M. E. Orazem, O. D. Crisalle, and L. H. García-Rubio, "On the Error Structure of Impedance Measurements: Simulation of Frequency Response Analysis (FRA) Instrumentation," *Journal of the Electrochemical Society*, **150** (2003) E477–E490.

92. S. L. Carson, M. E. Orazem, O. D. Crisalle, and L. H. García-Rubio, "On the Error Structure of Impedance Measurements: Simulation of Phase Sensitive Detection (PSD) Instrumentation," *Journal of the Electrochemical Society*, **150** (2003) E491–E500.

93. S. L. Carson, M. E. Orazem, O. D. Crisalle, and L. H. García-Rubio, "On the Error Structure of Impedance Measurements: Series Expansions," *Journal of the Electrochemical Society*, **150** (2003) E501–E511.

94. R. E. Kirk and D. F. Othmer, *Encyclopedia of Chemical Technology*, volume 17, 4th edition (Wiley International, New York, NY, 1997).

95. M. G. Fontana, *Corrosion Engineering*, 3rd edition (McGraw Hill, New York, NY, 1986).

96. D. Jones, *Corrosion*, 2nd edition (Prentice Hall, Upper Saddle River, NJ, 1992).

97. J. O. M. Bockris and A. K. N. Reddy, *Modern Electrochemistry -2* (Plenum Press, New York, NY, 1970).

98. A. Hammous and J. Guindet, *The CRC HandBook of Solid State Electrochemistry* (CRC Press, Boca Raton, FL, 1997).

99. A. J. Bard and L. R. Faulkner, *Electrochemical Methods: Fundamentals and Applications* (John Wiley and Sons, New York, NY, 1980).

100. F. King, M. Quinn, and C. D. Litke, "Oxygen Reduction on Copper in Neutral Nacl Solution," *Journal of Electroanalytic Chemistry*, **385** (1995) 45–55.

101. V. Jovancicevic and J. O. M. Bockris, "The Mechanism of Oxygen Reduction on Iron in Neutral Solution," *Journal of Electrochemical Society*, **133** (1986) 1797–1807.

102. N. A. Anastasijevic, V. Vesovic, and R. R. Adzic, "Detrmination of Kinetic Parameters of the Oxygen Reduction Reaction using Rotating Ring-Disk Electrode Part 1. Theory," *Journal of Electroanalytic Chemistry*, **229** (1987) 306–316.

103. N. A. Anastasijevic, V. Vesovic, and R. R. Adzic, "Detrmination of Kinetic Parameters of the Oxygen Reduction Reaction using Rotating Ring-Disk Electrode Part 2. Applications," *Journal of Electroanalytic Chemistry*, **229** (1987) 317–325.

104. V. Vesovic, N. Anastasijevic, and R. R. Adzic, "Rotating Disk Electrode: A Re-examination of some kineric criteria with a special reference to oxygen reduction," *Journal of Electroanalytic Chemistry*, **218** (1987) 53–63.

105. K.-L. Hsueh, E. R. Gonzalez, and S. Srinivasan, "Electrolyte Effects on Oxygen Reduction Kinetics at Platinum: A Rotating Ring-Disk Electrode Analysis," *Electochimica Acta*, **28** (1983) 691–697.

106. M. B. Vukmirovic, N. Vasijevic, N. Dimitrov, and K. Sieradzki, "Diffusion-Limited Current Density of Oxygen Reduction on Copper," *Journal of the Electrochemical Society*, **150** (2003) B10–B15.

107. N. A. Shumilova and V. S. Bagotzky, "Oxygen Ionization on Nickel in Alkaline Solutions," *Electochimica Acta*, **13** (1968) 285–293.

108. V. S. Batotgky, N. A. Shumilova, G. P. Samoilov, and E. I. Khrushcheva, "Electrochemical Oxygen Reduction on Nickel Electrodes in Alkaline Solutions-II," *Electochimica Acta*, **17** (1972) 1625–1635.

109. P. T. Wojcik, P. Agarwal, and M. E. Orazem, "A Method For Maintaining A Constant Potential Variation During Galvanostatic Regulation of Electrochemical Impedance Measurements," *Electrochimica Acta*, **41** (1996) 977–983.

110. M. Pourbaix, *Atlas of Electrochemical Equilibria in Aqueous Solutions* (NACE International: The Corrosion Society, Houston, TX, 1974).

111. P. T. Wojcik, *The Electrochemical Behavior of Copper and Copper Nickel Alloys in Synthetic Seawater*, Ph.D. dissertation, University of Florida, Gainesville, Florida (1997).

112. *1250 Frequency Response Analyser: Operating Manual*, Schlumberger Instruments, 6th edition (1985).

113. G. J. Burg, A. L. G. V. D. Feden, M. Sluyters-Rehbach, and J. H. Sluyters, "The Analysis of Electrode Impedance Complicated by the Presence of a Constant Phase Element," *Journal of Electroanalytic Chemistry*, (1984) 275–295.

114. G. Lang and K. E. Heusler, "Remarks on the Energetics of Interfaces Exhibiting Constant Phase Element Behaviour," *Journal of Electroanalytical Chemistry*, **457** (1998) 257–260.

115. Z. Lukacs, "Evaluation of Model and Dispersion Parameters and Their Effects on the Formation of Constant-Phase Elements in Equivalent Circuits," *Journal of Electroanalytical Chemistry*, **464** (1999) 68–75.

116. T. Nahir and E. Bowden, "The Distribution of Standard Rate Constants for Electron Transfer between Thiol-Modified Gold Electrodes and Adsorbed Cytochrome C," *Journal of Electroanalytic Chemistry*, **410** (1996) 9–13.

117. M. E. Orazem, P. Shukla, and M. A. Membrino, "Extension of the Measurement Model Approach for Deconvolution of Underlying Distributions for Impedance Measurements," *Electrochimica Acta*, **47** (2002) 2027–2034.

118. M. Durbha, *Influence of Current Distributions on the Interpretation of the Impedance Spectra Collected For Rotating Disk Electrode*, Ph.D. thesis, University of Florida, Gainesville, Florida (1998).

119. J. S. Newman, "Effect of Ionic Migration on Limiting Currents," *I & EC Fundamentals*, **5** (1966) 525–528.

120. J. S. Newman, "The Effect of Migration in Laminar Diffusion Layers," *International Journal of Heat and Mass Transfer*, **10** (1967) 983–997.

121. R. de Levie, "On Porous Electrodes in Electrolyte Solutions," *Electrochimica Acta*, **9** (1964) 1231–1245.

122. O. E. Barcia, E. D'Elia, I. Frateur, O. R. Mattos, N. Pébère, and B. Tribollet, "Application of the Impedance Model of de Levie for the Characterization of Porous Electrodes," *Electrochimica Acta*, **47** (2002) 2109–2116.

123. P. K. Shukla and M. E. Orazem, "Hydrodynamics and Mass-Transfer-Limited Current Distribution for a Submerged Stationary Hemispherical Electrode Under Jet Impingement," *Electrochimica Acta*, **49** (2004) 2901–2908.

124. A. Anderko, S. J. Sanders, and R. D. Young, "Real-Solution Stability Diagrams: A Thermodynamic Tool for Corrosion Modeling," *Corrosion*, **53** (1997) 43–53.

125. A. Anderko and P. J. Shuler, "A Computational Approach to Predicting the Formation of Iron Sulfide Species Using Stability Diagrams," *Computers & Geosciences*, **23** (1997) 647–658.

BIOGRAPHICAL SKETCH

Pavan Kumar Shukla grew up in Kanpur, India. He attended the Indian Institute of Technology, Kanpur, for his undergraduate and master's degree in chemical Engineering. He finished his undergraduate degree in Spring 1994 and his mastrer's degree in Spring 1996. He came to the U.S. in July 1996 to work on a NASA project. He started his Ph.D. program in the fall of 1998 at the University of Florida under the direction of Professor Mark E. Orazem. He graduated in the summer of 2004 after spending six years being educated in chemical and electrochemical engineering.